APPLICATION OF THE LATTICE BOLTZMANN METHOD IN SOLVING ENERGY EQUATIONS OF HEAT TRANSFER PROBLEMS INVOLVING THERMAL RADIATION

A THESIS

submitted by

BITTAGOPAL MONDAL

for the award of the degree

of

DOCTOR OF PHILOSOPHY

DEPARTMENT OF MECHANICAL ENGINEERING

INDIAN INSTITUTE OF TECHNOLOGY GUWAHATI

APRIL 2008

CERTIFICATE

It is certified that the work contained in the thesis entitled **Application of the Lattice Boltzmann Method in Solving Energy Equations of Heat Transfer Problems Involving Thermal Radiation** by Bittagopal Mondal, a student in the Department of Mechanical Engineering, Indian Institute of Technology Guwahati, India, for the award of the degree of the Doctor of Philosophy has been carried out under my supervision and that this work has not been submitted elsewhere for a degree.

Dr. Subhash C. Mishra
Professor
Department of Mechanical Engineering
Indian Institute of Technology Guwahati
Assam, India
April 2008

Dedicated to

My Parents

Late Billeswar Mondal

Late Puspa Mondal

Acknowledgements

First of all, I would like to express my deepest gratitude to my supervisor, Prof. Subhash C. Mishra, for his invaluable guidance, steady encouragement, inspiration and support throughout my Ph.D. work. In the past few years I worked under his guidance to achieve this state of my work. I can never forget the vigor and attention bestowed by him in taking my research ahead during tough times. He has contributed immensely in the formulation of the problems, identifying new problems and interpretations of the solutions. He helped me with the most innovative significant ideas, good books and journals that were very supportive in successfully completing the present thesis. I have benefited from each and every moment of my association with him. As my supervisor, his personal character with great spirit and enthusiasm will remain a source of inspiration for the rest of my life.

I am thankful to my doctoral committee members, namely, Prof. A.K. Dass, Dr. P. Mahanta and Dr. D.C. Dalal for providing insightful comments and valuable suggestions during my progress seminars, and on other occasions too.

I would like to express my sincere thanks to Prof. U.S. Dixit and other faculty members of the Department of Mechanical Engineering for their encouragement and support. I would like to express my special thanks to Dr. P. Mahanta for providing me his departmental room to carry out my research work. I am thankful to the other faculty members and staff of IIT Guwahati who directly or indirectly motivated me to complete my thesis work.

I am extremely grateful to Prof. Romano Borchiellini and Dr. Pietro Asinari of Politecnico Di Torino, Torino, Italy for their support and guidance to carry out a part of my research work there. I spent 4 wonderful months and got good exposure in the area of practical oriented heat transfer problems. I would like to express my sincere thanks to all of faculty members and staff members of Department of Energy, Politecnico Di Torino, Torino, Italy for their kind cooperation and help during my stay.

I am extremely thankful to all of my family members for their patience and the enormous trust they repose in my abilities. Without their moral support and wishes it would have been difficult for me to reach this position.

Muthu was a helping hand and an academic partner in many discussions ranging from the basics of radiation to CFD -related stuff. Vijay indeed played the role of the friend in need. The company of my friends in IIT G made my life colorful. Their contribution towards my living in IIT G made me "complete." Because of them, I really "lived a life" here. Everybody of them deserves a special thank for being with me when I was in distress and when I was happy.

And last, but not least, I am thankful to Dr. S. Choudhury, Mr. P. K. Dutta, Mr. A. Kalita and Mr. P. Kalita for their kind help and encouragement.

Bittagopal Mondal
IIT Guwahati

April 2008

List of Publications from this thesis work

International Journals

1. B. Mondal and S. C. Mishra, Lattice Boltzmann method applied to the solution of the energy equations of the transient conduction and radiation problems on non-uniform lattices, International Journal of Heat and Mass Transfer, 51, 68-82, 2008.

2. B. Mondal, S. C. Mishra, P. Asinari and R. Borchiellini, Analysis of a localized fire in a 3-D tunnel using a hybrid solver: Lattice Boltzmann method, finite volume method and fully explicit upwind scheme, Numerical Heat Transfer, Part A, 53 (4): 392-417, 2008.

3. B. Mondal and S.C. Mishra, The lattice Boltzmann method and the finite volume method applied to conduction-radiation problems with heat flux boundary conditions, International Journal for Numerical Methods in Engineering, (Revised manuscript submitted) July 2008.

4. B. Mondal and S. C. Mishra, Analysis of transient conduction-radiation in a 3-D cubical enclosure using the lattice Boltzmann method and finite volume method on non-uniform lattices, Journal of Thermophysics and Heat Transfer (Revised manuscript submitted) April 2008.

5. B. Mondal and S.C. Mishra, Numerical Analysis of Liquid-Solid Phase Transition in Presence of Volumetric Radiation in a 3-D Semitransparent Medium using the Lattice Boltzmann Method, International Journal of Thermal Sciences (Revised manuscript submitted) July 2008.

6. B. Mondal and S. C. Mishra, Simulation of natural convection in the presence of volumetric radiation using the lattice Boltzmann method and the finite volume method, Numerical Heat Transfer, Part-A (Submitted) April 2008.

International Conferences

1. B. Mondal and S. C. Mishra, Analysis of 1-D transient conduction and radiation heat transfer using the variable relaxation time lattice Boltzmann method and the finite volume method, 13th International Heat Transfer Conference, 13-18 August 2006, Sydney, NSW, Australia.

2. B. Mondal and S. C. Mishra, Application of variable relaxation time lattice Boltzmann method in 2-D transient conduction and radiation heat transfer problems, International Congress on Computational Mechanics and Simulation , 8-10 December 2006, IIT Guwahati, India, Vol. 2, pp. 1877-1883.

3. B. Mondal and S. C. Mishra, Analysis of 3-D transient conduction-radiation heat transfer problems using lattice Boltzmann method and finite volume method, 19th National & 8th ISHMT-ASME Heat and Mass Transfer Conference, Hyderabad 3-5 January 2008.

4. B. Mondal and S. C. Mishra, Analysis of Solid-Liquid Phase Transition in 3-D Semitransparent Medium using Lattice Boltzmann Method and Finite Volume Method, 19th National & 8th ISHMT-ASME Heat and Mass Transfer Conference, Hyderabad 3-5 January 2008.

5. B. Mondal and S. C. Mishra, Analysis of Transient Conduction and Radiation Heat Transfer with Flux boundary condition using the Lattice Boltzmann Method and Finite Volume Method, 19th National & 8th ISHMT-ASME Heat and Mass Transfer Conference, Hyderabad 3-5 January 2008.

Symposium

1. S. C. Mishra and B. Mondal, Lattice Boltzmann method - A new CFD tool to handle fluid flow and heat transfer problems, as a Keynote Paper in Indo-Australian Workshop on "A CFD Approach on Fluid Flow, Heat and Mass Transfer and Symposium on "CFD Applications in Multidisciplinary Areas, IIT Roorkee, 12-14 April 2007**.**

Synopsis

In the recent past, the lattice Boltzmann method (LBM) has received much attention in science and engineering as a potential computational tool to analyze a large class of problems. Among many other types of problems, the LBM has been successfully used to simulate a wide range of fluid flow and heat transfer problems. Examples include but are not limited to analysis of porous media flows, multiphase flows, chemically reacting flows and turbulent flows in simple to complex physical systems.

Owing to its mesoscopic origin, the LBM is emerging as a versatile computational tool having many advantages over conventional computational fluid dynamics (CFD) solvers such as the finite difference method (FDM), the finite volume method (FVM) and the finite element method (FEM). A clear physical meaning, a simple calculation procedure, simple and efficient implementation for parallel computation, straightforward and efficient handling of complex geometries and boundary conditions, high computational performance with regard to stability and precision are some of the advantages of the LBM. Proponents of the LBM consider this method to have the potential to become a versatile CFD platform.

Compared to its application to fluid dynamics, the usage of the LBM has received less attention in the field of heat transfer. With problems involving thermal radiation, its application is very recent.

The FVM for computation of radiative information is a robust method. The drawbacks like the false scattering of the widely used discrete ordinates method (DOM) is absent in the FVM. And, the method is also less prone to ray effect. Thus, the FVM is considered an improved version of the DOM. Since it inherits some features of the FVM of the CFD too, the FVM for radiative heat transfer is fully conservative and is applicable to complex geometry and participating medium.

Very recently, the LBM has been used to solve the energy equations of conduction-radiation problems in which the radiative information was computed using the FVM. The LBM in conjunction with other radiative transfer methods such as the collapsed

dimension method, the discrete transfer method (DTM) and the DOM has been used to analyze some heat transfer problems involving thermal radiation. However, with FVM as the solver for the radiative information and LBM as a tool for solving the energy equation not much study has been made for many complex problems.

Analysis of combined radiation, conduction and/or convection mode heat transfer problems find applications in design of boilers, furnaces, combustion chambers of IC engines, fire analysis, insulation systems, solidification and melting of semitransparent materials such as glass and salt crystals, fibrous and foam insulations, heating and cooling devices, etc. In these, for accurate analyses, a right choice of methods to solve conservation equations is desirable. The LBM and the FVM being the efficient solvers, they are the appropriate choice to solve the conservation equations.

In the present work, to extend the usage of the LBM to different class of heat transfer problems involving thermal radiation, 6 problems have been considered. The energy and/or momentum equations of problems have been solved using the LBM. In all the problems, the FVM has been used to compute the radiative information.

This thesis is organized in 9 chapters. A brief discussion of each chapter is presented below:

Chapter 1 entitled Introduction starts with a brief historical background of the LBM. Applications along with some of developments in the LBM are discussed next. Importance of thermal radiation in heat transfer problems is included in this chapter. Widely used numerical radiative transfer methods such as the DTM, the DOM and the FVM for computation of radiative information have also been briefly reviewed.

The Chapter 2 contains a general formulation of a radiation, conduction and convection problem. The formulation in the LBM along with implementation of initial and boundary conditions are discussed. Formulation in the FVM to compute radiative information is provided. The solution procedure for a problem is provided at the end.

In Chapter 3, a transient conduction-radiation problem in a 1-D planer absorbing, emitting and scattering medium is considered. Cases of both constant temperature and

flux boundary conditions are taken up. The FVM is used to compute the radiative information. Application of the LBM to a conduction-radiation problem on non-uniform lattices is extended. Volumetric heat generation in the medium is also considered. Effects of different radiative parameters such as the extinction coefficient, the scattering albedo and the emissivity on temperature and heat flux are studied. Different types of lattices/control volumes clustering are used to test the workability of the LBM-FVM.

To study the performance of the LBM-FVM combination on non-uniform lattices/control volumes, 2-D transient conduction-radiation problems in the presence of volumetric heat generation are considered in Chapter 4. Medium boundaries are maintained at either constant temperature or prescribed heat flux. Different radiative parameters are considered to study their effect on temperature distributions. Results are compared with the benchmark solutions and also with those obtained from uniform lattices/control volumes.

Chapter 5 contains applications of the LBM to solve the energy equation of a conduction-radiation problem in a 3-D cubical geometry having absorbing, emitting and isotropically-scattering medium. Both uniform and non-uniform lattices are used. Effect of volumetric heat generation is also considered. In case of heat flux boundary condition, the results are compared between direct and inverse methods. Effects of various parameters such as the extinction coefficient, the scattering albedo, the conduction-radiation parameter, the boundary emissivity, and the total heat flux are studied on temperature distributions.

In Chapter 6, analysis of liquid-solid phase transition of a 3-D cubical semitransparent absorbing and scattering medium in the presence of volumetric radiation is considered. The solidification process is analyzed by an enthalpy based LBM. The FVM is used to compute the radiative information required to solve the energy equation. Over a range of temperatures, a distinct liquid-, mushy- and solid- zones are considered. The analyses of liquid-solid phase transition are done considering both the constant temperature as well as the constant heat flux boundary conditions. The liquid fraction and the temperature distributions in the medium are analyzed for the effects of various

parameters such as the extinction coefficient, the scattering albedo, the conduction-radiation parameter and the latent heat.

The localized fire in a 3-D tunnel is analyzed by solving a combined mode natural convection and radiation problem in Chapter 7. Non-local thermal equilibrium between air and smoke is considered. Separate energy equations are used for the two species. The density and temperature fields required for the solution of the energy equation are computed using the LBM. The FVM is used to compute the radiative information. The energy equations are solved using the fully explicit upwind scheme. Boussinesq approximation is used to account for the buoyancy effect. Effects of the scattering albedo, the convection-radiation parameter and the wall emissivity on temperature profiles in the tunnel have been studied.

In Chapter 8, the analysis of natural convection in the presence of volumetric radiation in a square cavity containing an absorbing, emitting and scattering medium is presented. The LBM is used to compute the velocity and the temperature fields. Separate equations dealing with different particle distribution functions in the LBM are used to calculate the density and velocity fields and the thermal field. The FVM is used to compute the radiative term of the energy equation. Velocity, temperature, stream function and Nusselt number are analyzed for different parameters such as Rayleigh number, conduction-radiation parameter, extinction coefficient and scattering albedo.

Summary of the research work and conclusions are made in Chapter 9. Future scope and recommendations are also made in this chapter.

• • •

Contents

List of Figures

List of Tables

Nomenclature

A	-	area
a	-	anisotropy factor
$\mathbf{b}$	-	External force field vector
C	-	lattice speed/heat capacity
c_i	-	microscopic velocity vector
c_p	-	specific heat
D	-	single – species diffusion coefficient
e	-	internal energy
F	-	external force term
f_i	-	particle distribution function in the i direction for velocity field
f_i	-	liquid fraction
$f_i^{(eq)}$	-	equilibrium particle distribution function in the i direction for velocity field
$\mathbf{g}$	-	gravitational field vector
g_i	-	particle distribution function in the i direction for thermal field
$g_i^{(eq)}$	-	equilibrium particle distribution function in the i direction for thermal field
G	-	incident radiation
$\vec{G}$	-	external force acting per unit mass
g_0	-	gravitational acceleration
H	-	height and width of the cavity/total enthalpy
I	-	intensity
k	-	thermal conductivity
L	-	latent heat
M	-	molecular weight
Ma	-	Mach number
M_θ	-	number of discrete θ directions
M_ϕ	-	number of discrete ϕ directions
m	-	particle mass
N	-	conduction-radiation parameter
$\vec{N}u$	-	Nusselt number
$\hat{n}$	-	outer normal
p	-	pressure

P	-	cell center
Pr	-	Prandtl number
$\vec{q}_R$	-	radiative heat flux
R	-	ideal gas constant
Ra	-	Rayleigh number
R_C	-	convection-radiation parameter
$\vec{r}$	-	position vector
S	-	source term
T	-	temperature
T_m	-	mean temperature/melting temperature
t	-	time
U	-	macroscopic velocity component
$\vec{u}$	-	macroscopic velocity vector
$\mathbf{V}$	-	microscopic velocity tensor
V	-	volume of the cell
$\mathbf{v}$	-	microscopic velocity vector
w_i	-	weight in the LBM
X, Y, Z	-	lenth of rectangular enclosure in x-,y- and z- direction.
x	-	mass concentration
y	-	volume (or molar) concentration

Greek Symbols

α, χ	-	thermal diffusivity
β	-	extinction coefficient
β_t	-	Coefficient of thermal expansion
ν	-	kinematics viscosity
γ	-	finite-difference weighing factor
ε	-	emissivity
θ	-	polar angle
κ_a	-	absorption coefficient
ρ	-	density
σ	-	Stefan-Boltzmann constant

σ_s	-	scattering coefficient
τ	-	relaxation time
τ_t	-	relaxation time for thermal field
τ_v	-	relaxation time for velocity field
Φ	-	scattering phase function
ϕ	-	azimuthal angle
ω	-	scattering albedo
Ω	-	direction in the FVM
$\Delta\Omega$	-	elemental solid angle

Subscripts

E,W, N, S, F,B	-	east, west, north, south, front and back
b	-	boundary
C	-	cold
H	-	hot
m	-	mixture
l	-	liquid phase
f	-	freezing
P	-	value at the cell centre
s	-	solid phase
x, y,z	-	x-, y- and z- direction
σ	-	index for species
0	-	reference value

Superscript

eq	-	equilibrium
m	-	index for direction

Abbreviations

1-D/2-D/ 3-D	one/two/three- dimensional
BGK	Bhatnagar-Gross- Krook
CA	cellular automata
CDM	collapsed dimension method
CFD	computational fluid dynamics
DOM	discrete ordinate method
D1Q2	one dimensional and 2 direction model
D2Q9	two dimensional and 9 direction model
D3Q15	three dimensional and 15 direction model
DTM	discrete transfer method
FDM	finite difference method
FEM	finite element method
FVLBM	finite volume lattice Boltzmann method
FVM	finite volume method
LB	lattice Boltzmann
LBE	lattice Boltzmann equation
LBM	lattice Boltzmann method
LGA	lattice gas automata
LHS	left hand side
MCM	Monte Carlo method
RTE	radiative transfer equation

CHAPTER 1

Introduction

1.1 Overview of the Lattice Boltzmann Method

Concerning the historical origins of lattice Boltzmann method (LBM), it is quite usual to introduce the cellular automata (CA) and the lattice gas cellular automata (LGCA) as their ideal forerunners [1]. A cellular automaton is an idealization of a physical system in which space, time and the physical quantities i.e. states of the automation take only a finite set of values. Since its invention by Von Neuman in the late 1940s, the concept of a CA has been applied to a large class of scientific problems [2-5].

A very important feature of CAs is that they provide simple models of complex systems. They exemplify the fact that a collective behaviour can emerge from the sum of many simple components. Even if the basic and local interactions are perfectly known, it is possible that the global behaviour of a system obeys new laws which are not obviously extrapolated from the microscopic properties. This fact makes cellular automata very interesting candidates to model physical processes and, in particular, to simulate the non-equilibrium systems.

Many phenomena in science and engineering can be studied at different levels of description [6]. For instance, at a microscopic level, a fluid can be viewed as a large collection of particles interacting in a complicated way whereas, at a macroscopic level, the same fluid is described by its local density (ρ), local velocity (u) and local

temperature (T). Of course, the macroscopic level is linked to the microscopic one by some coarse graining procedure and the explicit link can be worked out using the concept of statistical physics. The interesting point is that, in general, the macroscopic behaviour depends very little on the microscopic details of the interaction and the most relevant features that remain after coarse graining are the conservation laws and basic symmetries of the interaction.

Using these symmetries and conservations, it is possible to device a microscopic universe made of fictitious components which can be easily programmed on a computer and has the same macroscopic behaviour as the real system [7]. In this way, a CA model is a fully discrete molecular dynamics where only simple but essential interactions are considered among fictitious particles moving in a regular lattice.

The first LGCA i.e. a special kind of CA for the simulation of fluid flow and other physical problems was proposed by Hardy et al. [8]. Frish *et al.* [9] introduced simple lattice gas automata (LGA) obeying nothing but conservation laws at a microscopic level and was able to reproduce the complexity of real fluid flows. This discovery caused great excitement in the fluid dynamics community. The prospects were promising like a round-off free, intrinsically parallel computational paradigm for fluid flows, perhaps even more, the analogous of the Ising model for turbulence. The two major drawbacks of the LGA were intrinsic noise and very limited range of transport coefficient, both due to the Boolean nature of the LGA method. In order to solve these problems, McNamara and Zanetti [10] pointed out that the hydrodynamic properties of the lattice-gas automata can be determined very efficiently by using an alternative technique named as lattice Boltzmann equation (LBE). Shortly it became apparent that all other anomalies plaguing LGA could also be naturally disposed off by the LBM. As a result the LBM rapidly evolved into a self standing research subject bearing an increasingly fainter relation to its LGA predecessor.

1.2 Literature Review on Lattice Boltzmann Method

In the end of 20th century, the usage of the LBM to analyze problems in science and engineering has increased significantly. As a different approach from the conventional computational fluid dynamics (CFD), the LBM has been demonstrated to be successful in simulation of fluid dynamical problems, including flows in porous media [11], multiphase flow [11,12], magnetohydrodynamics [13,14], immiscible fluids [11], chemically reacting flows [15], turbulence [16,17] and heat transfer problems [18-22] and other types of complex physical systems. Proponents of the LBM consider this method to have the potential to become a versatile CFD platform that is superior over the existing continuum-based CFD methods.

The LBM is a mesoscopic approach that incorporates microscopic physics with affordable computational expense. Unlike the conventional CFD based methods that directly simulate the continuum based governing equations (for example the Navier-Stokes equations), the LBM is based on a mesoscopic kinetic equation. This bottom-up approach of the LBM assures by construction, the conservation of the relevant macroscopic quantities such as mass and momentum [23]. One hypothesis for using this simplified kinetic type method for macroscopic phenomena is that the macroscopic properties are the result of collective behaviour of many microscopic particles and the macroscopic dynamics are not sensitive to the details of the microscopic mechanism.

The LBM is based on the microscopic models and mesoscopic kinetic equation. It has many advantages over the conventional numerical scheme based on the discretizations of macroscopic continuum equations. The fundamental idea of the LBM is to construct simplified kinetic models that incorporate the essential physics of microscopic or mesoscopic processes so that the macroscopic averaged properties obey the desired macroscopic equations. Eventhough the LBM is based on a particle picture, its principal focus is averaged macroscopic performance. The kinetic equation provides many of the advantages of molecular dynamics, including a clear physical meaning, a simple calculation, simple implementation on a computer, ease in parallel computation, easy handling of complex geometries, easy implementation of boundary conditions, capability

of stable and accurate simulation, etc. [23-28]. The LBM is second-order accurate in time and space [23], which is sufficient for most engineering applications.

MaNamara and Zanetti [10] proposed the LBM as an alternative technique to the lattice-gas automata for the study of hydrodynamic properties. This approach completely eliminates the statistical noise that infects the usual lattice-gas simulations and therefore permits simulations that demand much less computer time. Succi *et al*. [29] have shown that the LBE arising from the basic of lattice-gas scheme for Navier-Stokes equation can be extended in such a way as to include the effects of a two dimensional magnetic field. A numerical method based on the Boltzmann equation was presented for solving the equations of magneto-hydrodynamics by Chen *et al*. [13]. Alexander *et al.* [30] first introduced a lattice Boltzmann scheme capable of modelling thermo hydrodynamic flows of monatomic gases. They used a small number of discrete velocity states and a linear, single-time relaxation collision operator. The numerical simulations of the LBM were tested on several problems with exact solutions and were also compared to an explicit finite difference projections method by Skordos [31]. Chen *et al.* [32] introduced the basic principles of the LBM and its application to pattern formation in chemical reaction-diffusion systems, multiphase fluid flows and polymeric dynamics.

Until 1995, the bulk of LBM simulations had utilized heuristic techniques to model stationary walls. A hydrodynamic boundary condition was developed by Noble *et al*. [33] to replace the heuristic bounce back boundary condition used in the majority of the LBM. To demonstrate the accuracy of this approach, the technique was applied to the two dimensional, steady flow of an incompressible fluid between two infinite, parallel plates. From these results, it was shown that the LBM is truly a second-order schemes as long as the boundary conditions were accurately modelled. A detailed analysis was presented to demonstrate the capabilities of the LBM by Hou *et al*. [34]. Thorough comparisons with other numerical solution for the two dimensional, driven cavity flow show that the LBM gives accurate results over a wide range of Reynolds number. Miller [35] checked the ability of the LBM to compute the velocity and the pressure of an incompressible fluid flow in a two dimensional lid driven cavity with Dirichlet and Neumann boundary

conditions and results were compared with analytical solutions. Inamuro *et al*. [36] introduced the non-slip boundary condition at a wall for the fluid flow problem. In their method, unknown distribution functions at the wall were assumed to be an equilibrium distribution function with a counter slip velocity which was determined so that fluid velocity at the wall was equal to the wall velocity. Eggles and Somers [37] incorporated the convective and dissuasive scalar transport into the lattice-Boltzmann discretizations scheme. Their ultimate objective was to include heat and mass transport capabilities into lattice Boltzmann large eddy simulation tool to study engineering problems encountered in complex turbulent flows.

A new lattice Boltzmann algorithm was proposed to simulate the Navier-Stokes equation on arbitrary non-uniform mesh grids by He *at al*. [38]. A simulation of flow in a two dimensional symmetric channel with sudden expansion was carried out using that algorithm on a non-uniform mesh.

Shan [39] simulated Rayleigh-Benard convection in two and three dimensions using a two-component LB equation method. A body force proportional to the temperature was applied and the system satisfied the Boussinesq equation except for a slight compressibility. A no slip, isothermal boundary condition was imposed in the vertical directions and periodic boundary conditions were used in horizontal directions. He *et al*. [40] proposed a new LB algorithm used to simulate flows with high Reynolds number. Not only was the Reynold number enhanced in their simulation study using the new algorithm, but also the numerical stability improved significantly. The interpolation-supplemented lattice Boltzmann equation [ISLBE] method was used to simulate the two dimensional vortex shedding behind a circular cylinder with a low Reynolds number by He and Doolen [41]. The interpolation step, which didn't exist in the previous LBE models, was introduced to reconstruct the distribution function at grid nodes at the next time step. Regular space lattices were used in the LBM and they couldn't handle curved boundaries with desirable flexibility.

To overcome such difficulties, Mei and Shyy [42] proposed a finite difference based LBM in curvilinear coordinates using body fitted coordinates with non-uniform grids. An interpolation based LBM was extended to apply in general curvilinear coordinate systems by He and Doolen [43]. Two dimensional flows around a circular cylinder were simulated to check the workability of the interpolation based LBM. Compared with previous LB simulations of the same problems, their new approach greatly enhanced the computational efficiency. Peng *et al.* [44] described a finite volume scheme for the LBM (FVLBM). A finite volume formulation based on triangular elements in two dimensions was used and the scheme was implemented assuming that velocity space was isotropically discretized at each node in position space. The FVLBM scheme was applicable to irregular two dimensional regions which contained both exterior and interior boundaries of arbitrary shape.

He et al. [24] proposed a novel LB thermal model for studying thermo-hydrodynamics in incompressible limit. The new model introduced an internal energy density distribution function to simulate the temperature field. It also incorporated viscous heat dissipation and compression work done by pressure. Soe *et al*. [45] presented a thermal LB equation model for two dimensional free decaying turbulence induced by a strongly perturbed double velocity shear layer for various Prandtl numbers. Sun [46] formulated a LB model to solve supersonic flows. The particle velocities were determined by the mean velocity and internal energy. The adaptive nature of particle velocities permitted the mean flow to have a high Mach number. The introduction of a particle potential energy caused the model to be suitable for a perfect gas with an arbitrary specific heat ratio. A grid refinement scheme for the lattice BGK model was proposed by Filippova and Hanel [47]. The refinement scheme and a boundary fitting scheme for complicated geometries were applied to simulate a benchmark problem of flow past a cylinder in a channel with small and moderate Reynolds number. Pavlo *et al*. [48] presented the numerically stability of thermo LB models. The thermo LB algorithm was linearized and represented in matrix form. In particular, the numerical stability of two 2-speed 13-bit thermal LB models was examined.

Xi and Duncan [49] used the promising LBM numerical scheme to simulate single droplet deformation and break up under simple shear flow. Karlin *et al*. [50] extended the LBM to a class of irregular lattices without interpolation. Verberg and Ladd [51] presented a numerical method based on the LBM to solve the equation for low Reynolds number flow in porous media. A second order accurate treatment of the boundary condition in the LBM was developed by Mei *et al*. [52] for a curved geometry. The proposed boundary condition behaved stability characteristics when the relaxation time was close to 0.5. The improvement could make a substantial contribution toward simulating practical fluid flow problems using the LBM. The application of the LBM was extended to simulate the bubble flow by Sankaranarayanan [53].

Palmer and Rector [54] developed an algorithm for incorporating the effects of temperature into LB simulation. They modelled the internal energy as a scalar field using a second distribution. Qi [55] simulated fluidization of two-dimensional rectangular multi-particles falling against gravity using LBM. Sun [56] presented an adaptive LBM of higher accuracy for viscous compressible flows with heat conduction. The proper heat conduction term in energy equation was recovered by a modification of the kinetic energy transported by particles. The advantage of the proposed method over the standard one was that the particle velocities were no longer constant, varying with the mean velocity and internal energy.

Yu and Zhao [57] applied LBM to simulate compressible flows with high Mach number up to 5 introducing an attractive force. An extended LBM was presented for the simulation of low Mach number combustion with significant density changes by Filippova and Hanel [58]. Lin and Lai [59] proposed a composite block structured LBM to simulate the two dimensional incompressible fluid flows. They demonstrated that more accurate results were obtained on fine grids with a considerable saving in CPU time. Mei *et al*. [60] investigated two issues that were important to computational efficiency and reliability in fluid dynamics application of the LBM. These two issues were (a) computational stability and accuracy of different models and (b) the treatment of the boundary conditions on curved solid boundaries and their 3-D implementation. They

found that $D3Q15$ model was more prone to numerical instability and $D3Q27$ was more computationally intensive and $D3Q19$ model provided a balance between computational reliability and efficiency.

Kono *et al*. [61] extended the application of the LBM to simulate the multi-phase fluids flow with phase transition by taking into account the mass exchange process in the LB equation. Bernsdorf *et al*. [62] used the LBM for a detailed study on the origins of the pressure drop in porous media flow. Takada *et al*. [63] examined the applicability of the LBM to the numerical analysis of bubble motions, two and three dimensional two-phase fluid motions.

Zhang *et al*. [64] proposed an efficient fractional volumetric scheme for the LBM. The scheme possessed much better stability particularly for thermal the LBM by reducing the effective time step. Miller [65] extended the LBM on a face centred hyperbolic lattice by a phase field model to calculate the interaction between the liquid-solid phase transition and the melt-convection. Denniston *et al*. [66] developed a modified LBM to simulate liquid crystal subject to Poiseuille flow.

An extended LBM was developed by Jiaung *et al*. [18] for the simulation of the phase change problem governed by the heat conduction equation incorporating enthalpy formation. Yang *et al*. [67] performed a numerical study to investigate the hydrodynamic aspects of the pool boiling. Filippova *et al*. [68] discussed the viability of multiscale LBM for the numerical simulation of turbulent flows and they numerically demonstrated its applications to turbo axial machine.

Desplat *et al*. [69] developed a general purpose parallel LB code named as LUDWIG, capable of simulating the hydrodynamics of complex fluids in 3D on cubic lattice. LUDWIG is able to handle multi-components fluids, amphiphilic systems and flow in porous media as well as colloidal particles and polymers. Shu *et al*. [70] proposed a new LBM which was derived from standard LBM by using Taylor series expansion and optimised using the least square method. The method was meshless and applied to

complex geometry and non-uniform grids. A multi-relaxation LBM on two- dimensional rectangular geometry was constructed by Bouzidi *et al*. [71]. The method was tested for three different cases and numerical results of these tests were compared with either analytic solutions or the results obtained by other methods. Lai *et al*. [72] investigated the accuracy and efficiency of the LBM for steady –state flow simulations.

He and Doolen [73] demonstrated the thermodynamically consistent LBM for single-component multiphase flows derived from kinetic equation using both Enskog's theory for dense fluids and mean field theory for long range molecular interaction. They analyzed the strength and weakness of previous LBM for multiphase flow. The standard LBM was extended to solve the practical thermo-hydrodynamics in the incompressible limit to an arbitrary geometry by Shu *et al*. [74]. They carried out numerical simulation of natural convection in a square cavity on both uniform and non-uniform grids.

Chew *et al*. [75] proposed a new technique for implementing boundary condition based on the half covolume and bounce back rule for the non-equilibrium distribution function for the FVLBM. Zhang *et al*. [76] proposed a mirror-image method to implement the boundary condition in the LBM for the advection and anisotropic dispersion of solute transport in porous media. The accuracy of the proposed method was verified against benchmark problems and finite difference method. Numerical stability of FDLBM was analyzed by Seta and Takahashi [77].

A non-uniform grid LB technique was extended to simulate 3-D flows in complex geometries by Lu *et al*. [78]. The technique was applied to solve the turbulent flow problem in a stirred tank driven by a standard Rushtan turbine. Ho *et al*. [19] developed an extended LBM with a source term for the system of equations governing the hyperbolic heat conduction equation. They demonstrated that their proposed scheme was stable and free of numerical oscillation. Inamuro *et al*. [79] proposed a LBM for an isothermal binary miscible fluid mixture. Their proposed LBM scheme was useful for the simulation of fluid flows with heat as well as mass transfer.

Ginzburg and Steiner [80] proposed a generalized LBM to simulate free surface in both two and three dimensions. Interfacial boundary conditions were accurately satisfied by the proposed model. The method included an anti-diffusion algorithm to maintain a sharp interfacial front. Sofonea and Sekerka [81] discussed about the 2D FDLBM for single complex fluids and corresponding macroscopic equations for mass and momentum conservation were derived by performing a Chapman-Enskog expansion. Peng *et al*. [82] proposed a simplified thermal LBM to simulate the natural convection in a square cavity for a wide range of Reyleigh numbers. This simplified thermal model was established neglecting the compression work done by pressure and viscous heat dissipation. Ho *et al*. [20] studied dual-phase-lag based heat conduction equation by the LBM. The transmission-reflection phenomenon induced by pulsed thermal energy passing the interface of a two layered structure was analyzed in their study.

Inamuro *et al*. [83] proposed a LBM for two-phase immiscible fluid with large density differences. The projection method was used to overcome the difficulty in the treatment of large density difference. To validate the proposed method, they applied it in simulation of capillary waves, binary droplet collusion and bubble flows. The local time step method was applied to the LBM on non-uniform grid for steady flow simulation by Inamura *et al*. [84]. Two dimensional flow simulations around an airfoil were performed in order to validate the code using the local time step method and the results were compared with the global time step solutions.

Mishra and Lankadasu [22] used the LBM to solve the energy equation of a 1-D problem involving conduction and radiation heat transfer with and without heat generation. The radiative information for the governing energy equation was computed using the discrete transfer method (DTM) and the LBM was used to solve the energy equation. Mishra *et al*. [85] applied LBM to solve the transient conduction-radiation problem in a 2-D rectangular enclosure filled with an optically absorbing, emitting and scattering medium. Liu *et al*. [86] used multiple-relaxation time LBM to simulate cross flow for a long slender rigid circular cylinder to examine three-dimensional wake effect on the flow induced forces.

Raj *et al*. [87] analyzed 1-D solidification problem of a semitransparent material using the LBM and the DTM. The solidification was assumed to occur over a range of temperatures and thus the presence of a mushy zone was considered. Gupta *et al*. [88] extended the application of the LBM to solve the energy equation of a problem involving temperature dependent thermal conductivity.

LBM was used to analysis of heat transfer characteristics of fluid flow in micro channel by Hung and Ru [89]. They used the internal energy thermal model to predict the temperature distribution in micro-channel flow. Onishi *et al.* [90] developed a discrete model for multi-component visco-elastic fluids based on the LBM. To validate the current model, three dimensional simulations of a Newtonian drop in shear flow of a visco-elastic fluid were performed. Ansumali *et al*. [91] proposed a new method for the computation of flows at the micrometer scale. The new method was based on the minimal entropic kinetic models. It was used to study extensively in the simulation of the two dimensional Poiseille channel flow.

Chen *et al*. [92] applied the LBM to simulate 2-D incompressible backward-facing step flows at low Reynolds number. The field synergy principle was applied to demonstrate that an interruption within fluid results in decreased intersection angle between the velocity and temperature gradients. Seta *et al*. [93] studied the confirmation of reliability and the computational efficiency of the LBM in simulating natural convection in porous media. Temperature field was simulated by a simplified thermal energy distribution function which neglected the compression work done by the pressure and viscous heat dissipation. A new computational tool based on the LBM for the simulation of two phase flow and heat transfer phenomena in boiling water fuel bundles was described by Tentner *et al*. [94].

Zhou *et al*. [95] used the LBM for the analysis of high and moderate Knudsen number phenomena. Simulation results were presented for micro-scale Couette and Poiseille flows. Dixit and Babu [96] used a thermal LBM based on the BGK model to simulate

high Rayleigh number natural convection in a square cavity. To avoid the requirement of an unreasonably high uniform grid for higher Rayleigh number, the interpolation supplemented LBM was used in their study. Yu and Girimaji [97] presented a multi block LBM for 3-D problems. In this application, interpolation scheme were carefully addressed to avoid the inconsistency when information was transferred from coarse to fine blocks. Yamamoto and Takada [98] studied simulation of soot formation during combustion in porous media. Results showed that the combustion reaction was well simulated to observe the decrease of soot attached to the porous wall.

A LB algorithm for fluid-solid conjugate heat transfer was developed by Wang *et al*. [99]. A half lattice division treatment for the fluid-solid interaction and energy transport was proposed to ensure the temperature and heat flux continuity at the interface. Mishra and Roy [100] used the LBM to solve the energy equation of transient conduction-radiation heat transfer problems in 1-D planar and 2-D rectangular enclosures. The finite volume method (FVM) was used to compute the radiative information.

Yan and Zu [101] studied a viscous fluid flowing past a rotating isothermal cylinder. The convective heat transfer performance was further studied and validated. Tian *et al*. [102] simulated gaseous flow and heat transfer in micro-channels using the LBM. Viscous heat dissipation was adopted in the simulation for thermal LB model. To capture the velocity slip and temperature jump, a new boundary treatment was proposed based on macro variables. Kao *et al*. [103] studied the LBM based simulations to examine fluid flows through a fixed-bed micro-reactor comprising a micro-array of porous solids. The model was proposed to evaluate the chemical reactive efficiency of the micro-reactor based on the steady state temperature field.

A double population thermal LBM was proposed by Kuznik *et al*. [104] to solve the problem of the heated cavity with imposed temperatures. A non-uniform mesh was used to reduce the computational cost at higher order Rayleigh numbers (up to10^8). A numerical investigation of laminar convective flows in a differentially heated, square enclosure with heat conducting cylinder in its centre was carried out by Jami *et al*. [105].

The flow and temperature were computed respectively using the LBM and finite difference method with suitable coupling to take into account natural convection.

Very recently, application of the LBM was extended to simulate blood clotting based on a simple residence time model by Bernsdrof *et al*. [106]. Semma *et al*. [107] applied the LBM to solve melting and solidification problems. The phase interface was traced by using partial or probabilistic bounce back approach. The predicted solutions for the phase change problems were compared with the prediction of conventional method. Sun and Munn [108] developed a LB model that considered blood as a suspension of particle in plasma, accounting explicitly for cell-cell and cell-wall interactions. The LB approach was used to analyze the interaction of red and white blood cells as they flow through vascular networks digitized from normal and tumor tissue. The red and white blood cell forces, particle trajectories, the pressure changes in each segment and the forces felt by the vessel wall at any location were determined using the same approach.

1.3 Modes of Heat Transfer

Heat transfer or heat is energy in transit due to a temperature difference. Heat transfer must occur if temperature difference exists in a medium. There are three different modes of heat transfer, namely conduction, convection and radiation. In case of conduction in a solid, it takes place by a combination of lattice vibration and electron transport. In liquid and gases conduction takes place due to the transport of energy by molecular motion i.e. the faster molecules losses some of its kinetic energy to the slower one. In case of convection heat transfer, it occurs between a surface and a moving fluid with temperature difference. In this process, many of the molecules with raised kinetic energy are carried away by the fluid flow and are replaced by low kinetic energy molecules, which increase the rate of heat transfer. A medium is required for the transfer of energy in both conduction and convection. On the other hand, the third mode of heat transfer namely thermal radiation is due to continuous emission of energy in the form of electromagnetic waves or photons. Emission of energy is caused by the molecular and atomic agitation

associated with their internal energy. Thermal radiation differs from the other forms of electromagnetic radiation such as radio, television, X-ray and Υ-rays which are not dependent on temperature. Thermal radiation falls in the wavelength range 0.1 μm to 1000 μm. Within this wave length range, the medium emits electromagnetic waves/photons due to its temperature only.

1.4 Importance of Thermal Radiation

Conductive and convective heat transfer rates are proportional to the temperature difference whereas radiative heat transfer rates are generally proportional to differences in absolute temperature to the forth power. Thus, thermal radiation becomes more important with rising temperature levels and more dominant over other two modes of heat transfer in very high temperature application. Thermal radiation is important in combustion applications such as fires, power plant, engines and heat reactors, during atmospheric re-entry of space vehicles, etc.

Analysis of combined radiation, conduction and/or convection mode heat transfer problems find applications in design of boilers, furnaces, combustion chambers of IC engines, fire analysis, insulation systems, solidification and melting of semitransparent materials such as glass and salt crystals, fibrous and foam insulations, fire protection, high temperature porous insulating materials, heat exchanger, electronic chips and to many industrial heating, cooling and drying process etc. In these, for accurate analyses, a right choice of methods to solve conservation equations is desirable.

1.5 Radiation in Participating Medium

Radiation is the energy emitted by matter in the form of electromagnetic waves as a result of the changes in the electronic configuration of the atoms or molecules. Without attenuation, electromagnetic waves travel in a vacuum. At the time of energy exchange

between two surfaces, the intervening medium may or may not be participating depending on the nature of medium. There are two types of thermal radiation i.e. surface radiation and gas radiation.

Surface radiation is defined as the radiation energy exchange between two surfaces without attenuation its intensity. The intervening medium does not take part while exchanging the radiation energy. Radiation is usually considered to be surface phenomena for solid that are opaque to thermal radiation such as metal, wood etc. In surface radiation, the radiation is emitted from such bodies originates from molecules that are within a distance of approximately 1 μm from the exposed surface. Surface radiation is having following features:

1. It is a surface phenomena
2. In this there is no change in radiation intensity
3. In this emissive power is the basic radiation quantity.
4. Analysis is simple

If the intervening medium takes part in the radiation energy exchange, it is known as gas radiation. The intensity emitting from the matter undergos changes inside the medium due to absorption, emission and scattering by the medium before it reaches the other boundary. Gas radiation is having the following features:

1. It is a volumetric phenomena
2. In this there is a change in radiation intensity
3. In this, the basic radiation quantity is Intensity
4. Analysis is complex.

The practical application of radiation in participating medium is very important in glass manufacturing process, combustion phenomena, burning of pulverised coal, propellants of solid rocket, power plant, processing of semitransparent material etc.

1.6 Numerical Methods for Solving Participating Medium Radiative Heat Transfer

The governing equation for radiative transfer in an absorbing, emitting and scattering participating medium is a third order integro-differential equation. Radiative intensity has five independent variables viz. three space co-ordinates and two co-ordinates for describing the direction of photon travel [109,110]. An additional variable such as frequency of radiation comes into the equation for a non-gray medium and it makes the equation non-linear. Another variable included is time for transient thermal radiation. The presence of other modes of heat transfer makes it necessary to solve simultaneously for overall conservation of energy. For this situation, the divergence of radiative heat flux appearing in the energy equation is the contribution of radiative mode of heat transfer and its intensity is related in a non-linear way. Therefore, an efficient and cost effective numerical method is required for predicting the radiative heat flux for solving the governing energy equation.

Due to complexity for solving divergence of radiative heat flux, exact analytical solutions are available for only some simple cases. Analytical solutions for such simple problems have been studied extensively. A number of numerical methods have been developed to calculate radiative heat flux in participating media for different situations. Some methods work very well for a particular situation. Some methods are compatible in presence of other modes heat transfer. So depending upon the problems, one can choose a particular method.

The following methods are found in literature:

1. Exact analytical method [111]
2. Diffusion approximation method [112]
3. Zonal method [113]
4. Monte Carlo method [114]
5. Multi-flux method [115]
6. Moment method [116]

7. P_N approximation method [117]
8. Discrete ordinate method [109]
9. Discrete transfer method [109]
10. Finite element method [111]
11. Finite volume method [118-120]
12. Collapsed dimension method [121,122]

Some methods have been found to be more applicable for difficult situations involving multidimensionality, variable properties, anisotropic scattering, non-gray effects and coupled with other modes of heat transfer. According to Howell [123] and Yang [124], any practical numerical method should have the following features:

1. Capability to handle multidimensional and complex geometry.
2. Good accuracy under all condition: non-scattering and anisotropic scattering, gray and non-gray, isothermal or non-isothermal participating media.
3. Ease to application.
4. Ease of generalization: flexibility in choosing the different order of approximations.
5. Availability of the accurate intensity field and the integrated quantity.
6. Computational compatibility with conductive and/or convective heat transfer modes.
7. Low computational cost.
8. Stable solution.

In the following pages, advantage and disadvantages of some important methods have been given.

Monte Carlo method (MCM) is having following features [109,110]:

1. Highly accurate.
2. Computationally very expensive.

3. Applicable to three dimensional enclosures with anisotropically scattering inhomogeneous media at constant temperature.
4. A benchmark solution for two dimensional enclosures with absorbing, emitting and isotropically media at a radiative equilibrium.
5. Always gives results very close to the exact analytical solution.
6. Owing to the statistical nature of the method, falls within a narrow band around the exact analytical solution.
7. Inability to match the required grid size needed for computation of conjugate problem
8. Large appetite for computer time.
9. Statistical fluctuation of result.
10. Limitation of its use to benchmarking of only pure radiation problems.

Discrete ordinate method (DOM) is having following features [109,110]:

1. Presence of ray effect.
2. Radiation can be lost if it does not fall into one of the discrete ordinate directions.
3. Unless an infinite number of directions are used, ray effect can not be totally eliminated.
4. As the single scattering albedo increase, the radiation field becomes more isotropic and the ray effects become less noticeable.
5. With increasing single scattering albedo/optical thickness of the medium, the convergence rate may become very slow.
6. The computer time and memory requirement of this method are relatively high as compared to P_N approximation and zonal method.
7. Consequence of spatial discretizations error can be reduced with finer mesh of control volume (false scattering).
8. Very difficult to apply to irregular geometries.
9. Basic principle of this method and the multi-flux methods are the same, but the difference is in the evaluation of the integral. The flux method uses a trapezoidal

rule for the angular integral, whereas the DOM uses a higher order Gaussian type quadrature formula, which is more accurate.

Discrete transfer method (DTM) is having following features [109,110]:

1. Very accurate results could be obtained using this method in one and two dimensional geometries by increasing the number of rays.
2. It is applicable to three dimensional rectangular enclosures also and DTM shows reasonably good agreements.
3. It is capable to accounting for anisotropic scattering in the medium.
4. It is more time consuming than DOM.
5. DTM has less ray effect.
6. DTM does not suffer from false scattering.

Collapsed dimension method (CDM) is having following features [111]:

1. This method collapses the 3-D radiative information into its 2-D solution plane.
2. Eliminates the use of solid angle and reduces both the complexity and computational expense involved in the solution of problem.
3. It gives near analytical result for all ranges of optical thickness, including optically very thin cases where most of the existing methods fail to perform well.
4. Computational time taken by this method for solution of any particular problem will be least, since this method views all radiative phenomena in the 2-D solution plane.
5. This method has not yet been tested for complicated situation.

Finite volume method (FVM) is having following features [109,110]:

1. It is fully conservative: exact satisfaction of all- and half-moments can be achieved for arbitrary geometries and there is no loss of radiative energy.
2. Ray effect is minimal.

3. False scattering is completely absent.
4. Angular grid can be adapted to each special situation.
5. Same grid systems can be used for solving convection-diffusion problem.
6. Very accurate results could be obtained using this method in one, two and three dimensional geometries by increasing the number of rays.
7. It can be used in uniform, non-uniform, unstructured and in any type of complex geometry.
8. Very fast and compatible with other numerical methods.

1.7 Objective and Organization of the Thesis

In the recent past, the LBM has received much attention in science and engineering as a potential computational tool to analyze a large class of problems. Among many other types of problems, the LBM has been successfully used to simulate a wide range of fluid flow and heat transfer problems. Examples include but are not limited to analysis of porous media flows, multiphase flows, chemically reacting flows and turbulent flows in simple to complex physical systems.

Owing to its mesoscopic origin, the LBM is emerging as a versatile computational tool having many advantages over conventional CFD solvers such as the finite difference method (FDM), the FVM and the finite element method (FEM). A clear physical meaning, a simple calculation procedure, simple and efficient implementation for parallel computation, straightforward and efficient handling of complex geometries and boundary conditions, high computational performance with regard to stability and precision are some of the advantages of the LBM. Proponents of the LBM consider this method to have the potential to become a versatile CFD platform.

Compared to its application to fluid dynamics, the usage of the LBM has received less attention in the filed of heat transfer. With problems involving thermal radiation, its application is very recent.

The FVM for computation of radiative information is a robust method. The drawbacks like the false scattering of the widely used the DOM is absent in the FVM. And, the method is also less prone to ray effect. Thus, the FVM is considered an improved version of the DOM. Since it inherits some features of the FVM of the CFD too, the FVM for radiative heat transfer is fully conservative and is applicable to complex geometry and participating medium.

Very recently, the LBM has been used to solve the energy equations of conduction-radiation problems in which the radiative information was computed using the FVM. The LBM in conjunction with other radiative transfer methods such as the collapsed dimension method, the DTM and the DOM has been used to analyze some heat transfer problems involving thermal radiation. However, with FVM as the solver for the radiative information and LBM as a tool for solving the energy equation not much study has been made for many complex problems.

Analysis of combined radiation, conduction and/or convection mode heat transfer problems find applications in design of boilers, furnaces, combustion chambers of IC engines, fire analysis, insulation systems, solidification and melting of semitransparent materials such as glass and salt crystals, fibrous and foam insulations, heating and cooling devices, etc. In these, for accurate analyses, a right choice of methods to solve conservation equations is desirable. The LBM and the FVM being the efficient solvers, they are the appropriate choice to solve the conservation equations.

In the present work, to extend the usage of the LBM to different class of heat transfer problems involving thermal radiation, 6 problems have been considered. The energy and/or momentum equations of problems have been solved using the LBM. In all the problems, the FVM has been used to compute the radiative information.

This thesis is organized in nine chapters. A brief discussion of each chapter is discussed here.

Chapter 1 entitled Introduction starts with a brief historical background of the LBM. Applications along with some of developments in the LBM are discussed next. Importance of thermal radiation in heat transfer problems is included in this chapter. Widely used numerical radiative transfer methods such as the DTM, the DOM and the FVM for computation of radiative information have also been briefly reviewed.

The Chapter 2 contains a general formulation of a radiation, conduction and convection problem. The formulation in the LBM along with implementation of initial and boundary conditions are discussed. Formulation in the FVM to compute radiative information is provided. The solution procedure for a problem is provided at the end.

In Chapter 3, a transient conduction-radiation problem in a 1-D planer absorbing, emitting and scattering medium is considered. Cases of both constant temperature and flux boundary conditions are taken up. The FVM is used to compute the radiative information. Application of the LBM to a conduction-radiation problem on non-uniform lattices is extended. Volumetric heat generation in the medium is also considered. Effects of different radiative parameters such as the extinction coefficient, the scattering albedo and the emissivity on temperature and heat flux are studied. Different types of lattices/control volumes clustering are used to test the workability of the LBM-FVM.

To study the performance of the LBM-FVM combination on non-uniform lattices/control volumes, 2-D transient conduction-radiation problems in the presence of volumetric heat generation are considered in Chapter 4. Medium boundaries are maintained at either constant temperature or prescribed heat flux. Different radiative parameters are considered to study their effect on temperature distributions. Results are compared with the benchmark solutions and also with those obtained from uniform lattices/control volumes.

Chapter 5 contains applications of the LBM to solve the energy equation of a conduction-radiation problem in a 3-D cubical geometry having absorbing, emitting and

isotropically-scattering medium. Both uniform and non-uniform lattices are used. Effect of volumetric heat generation is also considered. In case of heat flux boundary condition, the results are compared between direct and inverse methods. Effects of various parameters such as the extinction coefficient, the scattering albedo, the conduction-radiation parameter, the boundary emissivity, and the total heat flux are studied on temperature distributions.

In Chapter 6, analysis of liquid-solid phase transition of a 3-D cubical semitransparent absorbing and scattering medium in the presence of volumetric radiation is considered. The solidification process is analyzed by an enthalpy based LBM. The FVM is used to compute the radiative information required to solve the energy equation. Over a range of temperatures, a distinct liquid-, mushy- and solid- zones are considered. The analyses of liquid-solid phase transition are done considering both the constant temperature as well as the constant heat flux boundary conditions. The liquid fraction and the temperature distributions in the medium are analyzed for the effects of various parameters such as the extinction coefficient, the scattering albedo, the conduction-radiation parameter and the latent heat.

The localized fire in a 3-D tunnel is analyzed by solving a combined mode natural convection and radiation problem in Chapter 7. Non-local thermal equilibrium between air and smoke is considered. Separate energy equations are used for the two species. The density and temperature fields required for the solution of the energy equation are computed using the LBM. The FVM is used to compute the radiative information. The energy equations are solved using the fully explicit upwind scheme. Boussinesq approximation is used to account for the buoyancy effect. Effects of the scattering albedo, the convection-radiation parameter and the wall emissivity on temperature profiles in the tunnel have been studied.

In Chapter 8, the analysis of natural convection in the presence of volumetric radiation in a square cavity containing an absorbing, emitting and scattering medium is presented. The LBM is used to compute the velocity and the temperature fields. Separate equations

dealing with different particle distribution functions in the LBM are used to calculate the density and velocity fields and the thermal field. The FVM is used to compute the radiative term of the energy equation. Velocity, temperature, stream function and Nusselt number are analyzed for different parameters such as Rayleigh number, conduction-radiation parameter, extinction coefficient and scattering albedo.

Summary of the research work and conclusions are made in Chapter 9. Future scope and recommendations are also made in this chapter.

1.8 Summary

Historical origin of the lattice Boltzmann method was discussed. Details of the literature review on the LBM were reported. Different modes of heat transfer and importance of thermal radiation were addressed briefly. Types of thermal radiation and some features of different important numerical methods to calculate the radiative heat flux were discussed. Objectives and organization of the thesis were presented.

CHAPTER 2

Formulation

2.1 Introduction

In fluid flow and heat transfer problems, continuity, momentum, species conservation and energy equations are the governing equations. These equations can be solved simultaneously. The solution of the energy equation becomes complicated in presence of radiation. If the temperature is high and the enclosed medium is absorbing, emitting and scattering, then volumetric radiation is considered within the energy equation.

The governing equations can be solved by any of the conventional CFD tools like FDM, FEM, FVM. etc. In the recent past, the LBM has been used successfully to simulate the fluid flow and heat transfer problems and other types of complex physical systems. It has many advantages over conventional CFD methods as specified in the previous chapter. In the present work, the governing equations are solved by LBM. The radiative information required to solve the energy equation is calculated using the FVM.

In this chapter, a general procedure to solve a heat transfer problem involving thermal radiation has been described. In the following pages, the FVM to calculate radiative information and the LBM to solve governing energy equation are described briefly.

2.2 Energy Equation

For a single component radiatively participating compressible fluid, the general form of the overall energy equation can be written as [109,110]

$$\rho c_v \left(\frac{\partial T}{\partial t} + v.\nabla T \right) = \nabla.\left(k \nabla T \right) - p\nabla.v + \Phi_d + Q''' - \nabla \cdot \vec{q}_R \qquad (2.1)$$

where ρ is the density, c_v is the specific heat, k is the thermal conductivity, p is the pressure term, v is the velocity vector, Φ_d is the source of energy due to viscous dissipation, Q''' is the local energy source per unit volume and time and $\vec{q}_R$ is the radiative heat flux.

The energy equation is simultaneously solved with the continuity and momentum equations in a general problem which involves all three modes of heat transfer. At any solution steps, with the known velocity field v, the pressure field p, energy due to heat dissipation Φ_d and local energy source Q''', the solution of Eq. (2.1) requires information about the divergence of radiative heat flux $\nabla.\vec{q}_R$. In the following sections, we briefly discuss the methodology of the FVM for the computation of $\nabla \cdot \vec{q}_R$ and the procedure in the LBM to solve the energy equation (Eq. (2.1)). The formulation is provided for 3-D Cartesian geometry.

2.3 The Finite Volume Method (FVM)

2.3.1 Introduction

The FVM for radiative heat transfer was first proposed by Raithby and Chui [118]. A slightly modified FVM scheme has been proposed by Chai *et al*. [119]. The FVM uses exact integration over both spatial control volume and angular control (solid) angle. This method is fully conservative. There is no loss of radiative energy in the FVM.

The governing radiative transfer equation (RTE) equation for the intensity field in an absorbing, emitting and scattering medium is given by [110]

$$I(s+ds,\Omega)-I(s,\Omega)\equiv\frac{\partial I}{\partial s}ds=\overbrace{\kappa I_b(s)ds}^{emission}-\overbrace{\kappa I(s,\Omega)ds}^{absorption}-\overbrace{\sigma_s I(s,\Omega)ds}^{out-scattering}+\underbrace{\left(\frac{\sigma_s}{4\pi}\right)\int_{\Omega'=4\pi}I(s,\Omega')p(\Omega'\to\Omega)d\Omega'}_{in-scattering} \tag{2.2}$$

where the left hand side (LHS) of the above equation is change of the magnitude of intensity from the location s to $s+ds$, 1st term in the right hand side (RHS) is intensity due to emission, 2nd term in RHS is intensity for the absorption by the particle, 3rd term of RHS represents the intensity scattered from the medium and last term of RHS is the intensity increase due to in-scattering. In Eq. (2.2), I is the intensity, s is the location, Ω represents direction, κ is the absorption coefficient, I_b is the boundary intensity, σ_s is the scattering coefficient and p is the phase function and $d\Omega'$ is the elemental solid angle.

Eq. (2.2) can be written in the form of

$$\frac{dI(s,\Omega)}{ds}=\kappa I_b(s)-\beta I(s,\Omega)+\left(\frac{\sigma_s}{4\pi}\right)\int_{\Omega'=4\pi}I(s,\Omega')p(\Omega'\to\Omega)d\Omega' \tag{2.3}$$

where β is the extinction coefficient of the medium. According to the Bouger-Beer relation, it is equal to $\kappa+\sigma_s$.

The differential form of the RTE in any direction $\hat{s}$ identified by the solid angle Ω about an elemental solid angle $d\Omega$ is given by

$$\frac{dI}{ds}=-\beta I+S \tag{2.4}$$

where S is the source term given by

$$S=\kappa\left(\frac{\sigma T^4}{\pi}\right)+\frac{\sigma_s}{4\pi}\int_{\Omega'=4\pi}I(\Omega')\Phi(\Omega,\Omega')\,d\Omega' \tag{2.5}$$

Resolving Eq. (2.4) along the Cartesian coordinate directions and integrating it over the elemental solid-angle $\Delta\Omega^m$ (Fig. 2.1), we get

$$\frac{\partial I^m}{\partial x}D_x^m + \frac{\partial I^m}{\partial y}D_y^m + \frac{\partial I^m}{\partial z}D_z^m = -\beta I^m \Delta\Omega^m + S^m \Delta\Omega^m \tag{2.6}$$

If $\hat{n}$ is the outward normal to a surface, then D^m is given by

$$D^m = \int_{\Delta\Omega^m} \left(\hat{n}\cdot\hat{s}^m\right) d\Omega \tag{2.7}$$

where the direction $\hat{s}^m = \left(\sin\theta^m\cos\phi^m\right)\hat{i} + \left(\sin\theta^m\sin\phi^m\right)\hat{j} + \left(\cos\theta^m\right)\hat{k}$. When $\hat{n}$ is pointing towards one of the positive coordinate directions, D_x^m, D_y^m and D_z^m are given by

$$\begin{aligned} D_x^m &= \int_{\Delta\Omega^m} \sin\theta\cos\phi\, d\Omega = \int_{\phi^m-\frac{\Delta\phi^m}{2}}^{\phi^m+\frac{\Delta\phi^m}{2}} \int_{\theta^m-\frac{\Delta\theta^m}{2}}^{\theta^m+\frac{\Delta\theta^m}{2}} \cos\phi\sin^2\theta\, d\theta\, d\phi \\ &= \cos\phi^m \sin\left(\frac{\Delta\phi^m}{2}\right)\left[\Delta\theta^m - \cos 2\theta^m \sin\left(\Delta\theta^m\right)\right] \end{aligned} \tag{2.8a}$$

$$\begin{aligned} D_y^m &= \int_{\Delta\Omega^m} \sin\theta\sin\phi\, d\Omega = \int_{\phi^m-\frac{\Delta\phi^m}{2}}^{\phi^m+\frac{\Delta\phi^m}{2}} \int_{\theta^m-\frac{\Delta\theta^m}{2}}^{\theta^m+\frac{\Delta\theta^m}{2}} \sin\phi\sin^2\theta\, d\theta\, d\phi \\ &= \sin\phi^m \sin\left(\frac{\Delta\phi^m}{2}\right)\left[\Delta\theta^m - \cos 2\theta^m \sin\left(\Delta\theta^m\right)\right] \end{aligned} \tag{2.8b}$$

$$\begin{aligned} D_z^m &= \int_{\Delta\Omega^m} \cos\theta\, d\Omega = \int_{\phi^m-\frac{\Delta\phi^m}{2}}^{\phi^m+\frac{\Delta\phi^m}{2}} \int_{\theta^m-\frac{\Delta\theta^m}{2}}^{\theta^m+\frac{\Delta\theta^m}{2}} \cos\theta\sin\theta\, d\theta\, d\phi \\ &= \sin\theta^m\cos\theta^m \sin\left(\Delta\theta^m\right)\Delta\phi^m \end{aligned} \tag{2.8c}$$

For $\hat{n}$ pointing towards the negative coordinate directions, signs of D_x^m, D_y^m and D_z^m are opposite to what are obtained from Eq. (2.8). In Eq. (2.7), $\Delta\Omega^m$ is given by

$$\Delta\Omega^m = \int_{\Delta\Omega^m} d\Omega = \int_{\phi^m-\frac{\Delta\phi^m}{2}}^{\phi^m+\frac{\Delta\phi^m}{2}} \int_{\theta^m-\frac{\Delta\theta^m}{2}}^{\theta^m+\frac{\Delta\theta^m}{2}} \sin\theta d\theta d\phi = 2\sin\theta^m \sin\left(\frac{\Delta\theta^m}{2}\right)\Delta\phi^m \tag{2.9}$$

Integrating Eq. (2.6) over the control volume and using the concept of the FVM for the CFD, we get

$$\left[I_E^m - I_W^m\right]A_{EW}D_x^m + \left[I_N^m - I_S^m\right]A_{NS}D_y^m + \left[I_F^m - I_B^m\right]A_{FB}D_z^m = \left[-\beta V I_P^m + V S_P^m\right]\Delta\Omega^m \tag{2.10}$$

where A_{EW}, A_{NS} and A_{FB} are the areas of the x-, y- and z-faces of the 3-D control volume, respectively. In Eq. (2.10), I with suffixes E, W, N, S, F and B designate east, west, north, south, front and back control surface average intensities, respectively. On the right-hand side of Eq. (2.10), $V = dx \times dy \times dz$ is the volume of the cell and I_P^m and S_P^m are the intensities and source terms at the cell centre P, respectively.

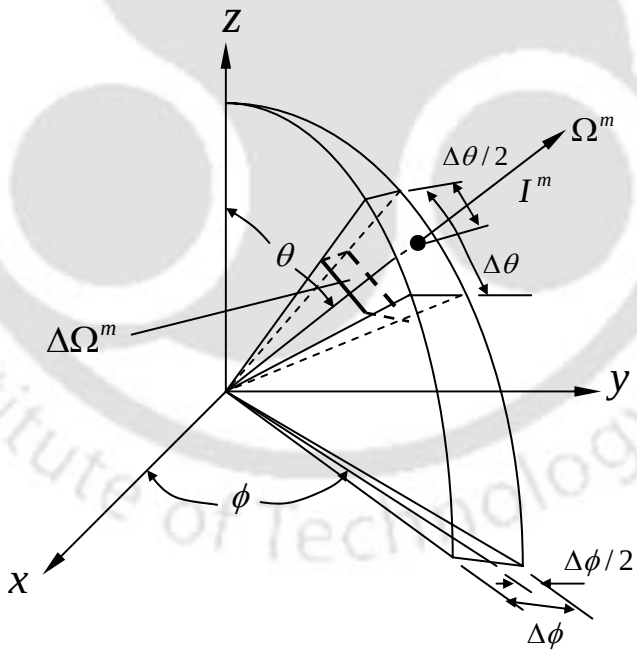

Figure 2.1: Intensity I^m in direction Ω^m in the center of the elemental sub-solid angle $\Delta\Omega^m$.

In any discrete direction Ω^m, if a linear relationship among the two cell-surface intensities and cell-centre intensity I_P^m is assumed, then

$$I_P^m = \gamma_x I_E^m + (1-\gamma_x) I_W^m = \gamma_y I_N^m + (1-\gamma_y) I_S^m = \gamma_z I_F^m + (1-\gamma_z) I_B^m \tag{2.11}$$

where γ is the finite-difference weighting factor and its value is normally considered to be 0.5. While marching from the first octant of a 3-D enclosure, for which D_x^m, D_y^m and D_z^m are all positive, I_P^m in terms of known cell-surface intensities can be written as

$$I_P^m = \frac{\frac{D_x^m A_{EW}}{\gamma_x} I_W^m + \frac{D_y^m A_{NS}}{\gamma_y} I_S^m + \frac{D_z^m A_{FB}}{\gamma_z} I_B^m + \left(V \Delta\Omega^m\right) S_P^m}{\frac{D_x^m A_E}{\gamma_x} + \frac{D_y^m A_N}{\gamma_y} + \frac{D_y^m A_F}{\gamma_z} + \beta V \Delta\Omega^m} \tag{2.12}$$

where

$$A_{EW} = (1-\gamma_x) A_E + \gamma_x A_W, \quad A_{NS} = (1-\gamma_y) A_N + \gamma_y A_S, \quad A_{FB} = (1-\gamma_z) A_F + \gamma_z A_B \tag{2.13}$$

are the averaged areas. When any one of the D_x^m, D_y^m or D_z^m is negative, marching starts from other corners. In this case, a general expression of I_P^m in terms of known intensities and source term can be written as

$$I_P^m = \frac{\frac{\left|D_x^m\right| A_x}{\gamma_x} I_{x_i}^m + \frac{\left|D_y^m\right| A_y}{\gamma_y} I_{y_i}^m + \frac{\left|D_z^m\right| A_z}{\gamma_z} I_{z_i}^m + \left(V \Delta\Omega^m\right) S_P^m}{\frac{\left|D_x^m\right| A_{x_e}}{\gamma_x} + \frac{\left|D_y^m\right| A_{y_e}}{\gamma_y} + \frac{\left|D_z^m\right| A_{z_e}}{\gamma_z} + \beta V \Delta\Omega^m} \tag{2.14}$$

where in Eq. (2.14), x_i, y_i and z_i suffixes over I^m are for the intensities entering the control volume through x-, y- and z-faces, respectively and A_x, A_y and A_z are given by

$$A_x = (1-\gamma_x) A_{x_e} + \gamma_x A_{x_i}, \quad A_y = (1-\gamma_y) A_{y_e} + \gamma_y A_{y_i}, \quad A_z = (1-\gamma_z) A_{z_e} + \gamma_z A_{z_i} \tag{2.15}$$

In Eq. (2.15) A with suffixes x_i, y_i and z_i represent control surface areas through which intensities enter the control volume, while A with suffixes x_e, y_e and z_e represent control surface areas through which intensities leave the control volume.

For a linear anisotropic phase function $\Phi(\Omega,\Omega') = 1 + a\cos\theta\cos\theta'$, the source term S at any location $\vec{r}$ is given by

$$S = \kappa_a\left(\frac{\sigma T^4}{\pi}\right) + \left(\frac{\sigma_s}{4\pi}\right)\int_0^{2\pi}\int_0^{\pi} I(\theta',\phi')(1 + a\cos\theta\cos\theta')\sin\theta' d\theta' d\phi' \tag{2.16}$$

which in terms of the incident radiation G and net radiative heat flux q_R is written as

$$S = \frac{\sigma_s}{4\pi}[G + a\cos\theta q_R] \tag{2.17}$$

In Eq. (2.17), G and q_R are given by and numerically computed from the following

$$\begin{aligned} G &= \int_{\Omega=0}^{4\pi} I(\Omega)\, d\Omega = \int_{\phi=0}^{2\pi}\int_{\theta=0}^{\pi} I(\theta,\phi)\sin\theta\, d\theta\, d\phi \\ &\approx \sum_{k=1}^{M_\phi}\sum_{l=1}^{M_\theta} I^m(\theta_l^m,\phi_k^m)2\sin\theta_l^m \sin\left(\frac{\Delta\theta_l^m}{2}\right)\Delta\phi_k^m \end{aligned} \tag{2.18}$$

where M_θ and M_ϕ are the number of discrete points considered over the complete span of the polar angle $(0 \le \theta \le \pi)$ and azimuthal angle $(0 \le \phi \le 2\pi)$, respectively. Therefore, $M_\theta \times M_\phi$ constitute the number of discrete directions in which intensities are considered at any point

$$\begin{aligned} q_R &= \int_{\Omega=0}^{4\pi} I(\Omega)\cos\theta\, d\Omega = \int_{\phi=0}^{2\pi}\int_{\theta=0}^{\pi} I(\theta,\phi)\cos\theta\sin\theta\, d\theta\, d\phi \\ &\approx \sum_{k=1}^{M_\phi}\sum_{l=1}^{M_\theta} I^m(\theta_l^m,\phi_k^m)2\sin\theta_l^m\cos\theta_l^m\sin(\Delta\theta_l^m)\Delta\phi_k^m \end{aligned} \tag{2.19}$$

While marching from any of the corners, evaluation of Eq. (2.14) requires knowledge of the boundary intensity. For a diffuse-gray boundary/wall having temperature T_b and emissivity ε_b, the boundary intensity I_b is computed from

$$I_b = \frac{\varepsilon_b\sigma T_b^4}{\pi} + \left(\frac{1-\varepsilon_b}{\pi}\right)\sum_{k=1}^{M_\phi}\sum_{l=1}^{M_\theta/2} I^m\left(\theta_l^m,\phi_k^m\right)\sin\theta_l^m\cos\theta_l^m\sin\Delta\theta_l^m\Delta\phi_k^m \tag{2.20}$$

In Eq. (2.20), the first and the second terms represent the emitted and the reflected components of the boundary intensity, respectively.

Once the intensity distributions are known, radiative information $\nabla\cdot\vec{q}_R$ required for the energy equation is computed from

$$\nabla \cdot \vec{q}_R = \beta(1-\omega)\left(4\pi\frac{\sigma T^4}{\pi} - G\right) \tag{2.21}$$

where in Eq. (2.21), $\omega = \sigma_s / \beta$ is the scattering albedo.

2.4 Lattice Boltzmann Method (LBM)

In the recent past, the LBM has received much attention in science and engineering as a potential computational too to analyze a large class of problems. Among many other types of problems, the LBM has been successfully used to simulate a wide range of fluid flow and heat transfer problems. In the following section, the derivation of lattice Boltzmann equation is described in details.

2.4.1 Derivation of the Lattice Boltzmann Equation

For the sake of simplicity and without loosing generality, the Bhatnagar-Gross-Krook (BGK) equation [125] is used in this derivation. Using the single relaxation time approximation, the Boltzmann equation can be written as

$$\frac{\partial f}{\partial t} + c.\nabla f = -\frac{1}{\lambda}\left(f - f^{(eq)}\right) \tag{2.22}$$

Eq. (2.22) can be written in the form of an ordinary differential equation

$$D_t f + \frac{1}{\lambda} f = \frac{1}{\lambda} f^{(eq)} \tag{2.23}$$

where $D_t \equiv \frac{\partial}{\partial t} + c.\nabla$ is the Lagrangian derivative along the microscopic velocity vector c, $f = f(x,t)$ is the single-particle distribution function, λ is the relaxation time due to collision and $f^{(eq)}$ is the Maxwell-Boltzmann distribution function which is given by

$$f^{(eq)} = \frac{\rho}{(2\pi RT)^{D/2}} \exp\left(-\frac{(c-u)^2}{2RT}\right) \tag{2.24}$$

in which R is the ideal gas constant, D is the dimension of the space, ρ is the macroscopic density, u is the macroscopic velocity vector and T is the macroscopic temperature.

The macroscopic variables are the moments of the distribution function f

$$\rho = \int f\, dc \qquad \rho u = \int cf\, dc \qquad \rho e = \int \frac{(c-u)^2}{2} f\, dc \tag{2.25}$$

where $e = D_0 RT/2$ and D_0 is the number of freedom of a particle.

Multiplying both side of Eq. (2.23) by an integral factor $e^{\int \frac{1}{\lambda} dt}$, Eq. (2.23) takes the form of

$$\begin{aligned} &\frac{df}{dt} e^{\int \frac{1}{\lambda} dt} + \frac{1}{\lambda} f\, e^{\int \frac{1}{\lambda} dt} = \frac{1}{\lambda} f^{(eq)} e^{\int \frac{1}{\lambda} dt} \\ &\Rightarrow d\left(f e^{\int \frac{1}{\lambda} dt} \right) = \frac{1}{\lambda} f^{(eq)} e^{\int \frac{1}{\lambda} dt} \end{aligned} \tag{2.26}$$

Eq. (2.26) can be integrated over a time interval Δt:

$$\begin{aligned} &\int_0^{\Delta t} d\left(f e^{\int \frac{1}{\lambda} dt} \right) = \frac{1}{\lambda} \int_0^{\Delta t} \left(f^{(eq)} e^{\int \frac{1}{\lambda} dt} \right) dt \\ &\Rightarrow \left[f\left(r + c\Delta t, t + \Delta t\right) \right] e^{\Delta t/\lambda} - \left[f\left(r,t\right) \right] = \frac{1}{\lambda} \int_0^{\Delta t} \left(f^{(eq)} e^{\int \frac{1}{\lambda} dt} \right) dt \end{aligned} \tag{2.27}$$

for $0 \le t' \le 1$, the above equation can be written as

$$\left[f\left(r + c\Delta t, t + \Delta t\right) \right] = e^{-\Delta t/\lambda} \left[f\left(r,t\right) \right] + \frac{1}{\lambda} e^{-\Delta t/\lambda} \int_0^{\Delta t} \left(e^{t'/\lambda} f^{(eq)}\left(r + ct', t + t'\right) \right) dt' \tag{2.28}$$

Assuming that Δt is small enough and $f^{(eq)}$ is smooth enough locally, the following approximation can be made [126]:

$$f^{(eq)}\left(r + ct', t + t'\right) = \left(1 - \frac{t'}{\Delta t}\right) f^{(eq)}\left(r,t\right) + \left(\frac{t'}{\Delta t}\right) f^{(eq)}\left(r + c\Delta t, t + c\Delta t\right) + o\left(\Delta t^2\right) \tag{2.29}$$

Neglecting the higher order term and subtracting $f\left(r,t\right)$ from both side of Eq. (2.29), it can be modified as

$$f\left(r+c\Delta t,t+\Delta t\right)-f\left(r,t\right)=e^{-\Delta t/\lambda}f\left(r,t\right)-f\left(r,t\right)$$
$$+\frac{1}{\lambda}e^{-\Delta t/\lambda}\int_0^{\Delta t}\left(e^{t'/\lambda}\left(1-\frac{t'}{\Delta t}\right)f^{(eq)}\left(r,t\right)\right)dt' \tag{2.30}$$
$$+\frac{1}{\lambda}e^{-\Delta t/\lambda}\int_0^{\Delta t}\left(e^{t'/\lambda}\frac{t'}{\Delta t}f^{(eq)}\left(r+c\Delta t,t+\Delta t\right)\right)dt'$$

After simplification of Eq. (2.30),

$$f\left(r+c\Delta t,t+\Delta t\right)-f\left(r,t\right)=\left(e^{-\Delta t/\lambda}-1\right)f\left(r,t\right)+\frac{1}{\lambda}e^{-\Delta t/\lambda}\int_0^{\Delta t}\left(e^{t'/\lambda}f^{(eq)}\left(r,t\right)\right)dt'$$
$$-\frac{1}{\lambda}e^{-\Delta t/\lambda}\int_0^{\Delta t}\left(e^{t'/\lambda}\frac{t'}{\Delta t}f^{(eq)}\left(r,t\right)\right)dt' \tag{2.31}$$
$$+\frac{1}{\lambda}e^{-\Delta t/\lambda}\int_0^{\Delta t}\left(e^{t'/\lambda}\frac{t'}{\Delta t}f^{(eq)}\left(r+c\Delta t,t+\Delta t\right)\right)dt'$$

Now,

$$\int_0^{\Delta t}e^{t'/\lambda}t'dt'=\left[\lambda t'e^{t'/\lambda}-\lambda^2e^{t'/\lambda}\right]_0^{\Delta t}$$
$$=\lambda\left[\Delta te^{t'/\lambda}-\lambda e^{t'/\lambda}+\lambda\right] \tag{2.32}$$

The second term of R.H.S. of Eq. (2.31) can be simplified as:

$$\frac{1}{\lambda}e^{-\Delta t/\lambda}\int_0^{\Delta t}\left(e^{t'/\lambda}f^{(eq)}\left(x,t\right)\right)dt'=e^{-\Delta t/\lambda}f^{(eq)}\left(x,t\right)\left[e^{\Delta t/\lambda}-1\right] \tag{2.33}$$

The third term of R.H.S. of Eq. (2.31) can be simplified as

$$\frac{1}{\lambda}e^{-\Delta t/\lambda}\int_0^{\Delta t}\left(e^{t'/\lambda}\frac{t'}{\Delta t}f^{(eq)}\left(x,t\right)\right)dt'=e^{-\Delta t/\lambda}\frac{f^{(eq)}\left(x,t\right)}{\Delta t}\left[\Delta te^{\Delta t/\lambda}-\lambda e^{\Delta t/\lambda}+\lambda\right] \tag{2.34}$$

The last term of R.H.S. of Eq. (2.31) can be simplified as:

$$\frac{1}{\lambda}e^{-\Delta t/\lambda}\int_0^{\Delta t}\left(e^{t'/\lambda}\frac{t'}{\Delta t}f^{(eq)}\left(r+c\Delta t,t+\Delta t\right)\right)dt'$$
$$=e^{-\Delta t/\lambda}\frac{f^{(eq)}\left(r+c\Delta t,t+\Delta t\right)}{\Delta t}\left[\Delta te^{\Delta t/\lambda}-\lambda e^{\Delta t/\lambda}+\lambda\right] \tag{2.35}$$

Thus, the Eq. (2.32) can be written as

$$f\left(r+c\Delta t,t+\Delta t\right)-f\left(r,t\right)=\left(e^{-\Delta t/\lambda}-1\right)f\left(r,t\right)+e^{-\Delta t/\lambda}f^{(eq)}\left(r,t\right)\left[e^{\Delta t/\lambda}-1\right]$$
$$-e^{-\Delta t/\lambda}\frac{f^{(eq)}\left(x,t\right)}{\Delta t}\left[\Delta te^{\Delta t/\lambda}-\lambda e^{\Delta t/\lambda}+\lambda\right] \qquad (2.36)$$
$$+e^{-\Delta t/\lambda}\frac{f^{(eq)}\left(r+c\Delta t,t+\Delta t\right)}{\Delta t}\left[\Delta te^{\Delta t/\lambda}-\lambda e^{\Delta t/\lambda}+\lambda\right]$$

Now, the above equation can be simplified as

$$f\left(r+c\Delta t,t+\Delta t\right)-f\left(r,t\right)=\left(e^{-\Delta t/\lambda}-1\right)\left\{f\left(r,t\right)-f^{(eq)}\left(r,t\right)\right\}$$
$$+\left(1+\frac{\lambda}{\Delta t}\left(e^{-\Delta t/\lambda}-1\right)\right)\left\{f^{(eq)}\left(r+c\Delta t,t+\Delta t\right)-f^{(eq)}\left(r,t\right)\right\} \qquad (2.37)$$

By Taylor series expansion,

$$e^{-\Delta t/\lambda}-1=-\frac{\Delta t}{\lambda}+\frac{\Delta t^2}{2!\lambda^2}-\frac{\Delta t^3}{3!\lambda^3}+\cdots \qquad (2.38)$$

and neglecting the second and higher order terms of Eq.(2.38)

$$1+\frac{\lambda}{\Delta t}\left(e^{-\Delta t/\lambda}-1\right)=1+\frac{\lambda}{\Delta t}\left(-\frac{\Delta t}{\lambda}\right)=0 \qquad (2.39)$$

Thus, substituting Eqs. (2.38) and (2.39) in Eq. (2.37),

$$f\left(r+c\Delta t,t+\Delta t\right)-f\left(r,t\right)=-\frac{\Delta t}{\lambda}\left\{f\left(r,t\right)-f^{(eq)}\left(r,t\right)\right\}$$
$$=-\frac{1}{\tau}\left\{f\left(r,t\right)-f^{(eq)}\left(r,t\right)\right\} \qquad (2.40)$$

where $\tau=\frac{\lambda}{\Delta t}$ is the relaxation time. Eq. (2.40) is the evolution equation of the distribution function f with discrete time.

2.4.2 LBM formulation for Heat Transfer Problems

The starting point of the LBM is the kinetic equation (Eq. (2.40)) which for a 3-D geometry can be written as [1, 23-28, 39, 127]

$$\frac{\partial f_i\left(\vec{r},t\right)}{\partial t}+\vec{c}_i\cdot\nabla f_i\left(\vec{r},t\right)=\Omega_i \qquad (2.22)$$

where f_i is the particle distribution function denoting the number of particles at the lattice node $\vec{r} = (\vec{r}(x, y, z))$ and time t moving in direction i with velocity $\vec{c}_i$ along the lattice link $\Delta\vec{r} = \vec{c}_i \Delta t$ connecting the nearest neighbors. The term Ω_i represents the local change in f_i due to particle collisions. Using the single time relaxation of the Bhatanagar-Gross-Krook (BGK) approximation, the discrete Boltzmann equation given by [1, 23-28, 39, 127]:

$$\frac{\partial f_i(\vec{r},t)}{\partial t} + \vec{c}_i \cdot \nabla f_i(\vec{r},t) = -\frac{1}{\tau}\left[f_i(\vec{r},t) - f_i^{(eq)}(\vec{r},t)\right] \tag{2.23}$$

where τ is the relaxation time and $f_i^{(eq)}$ is the equilibrium distribution function. In the LBM, lattices depend upon the geometries. D1Q2 and D1Q3 are the lattices used in 1-D geometries, while D2Q7 and D2Q9 are the lattices used in 2-D geometries. In 3-D geometries, normally D3Q15 and D3Q19 lattices are used. In all these lattices, the number following D denotes the dimension and the number following Q denotes the number of directions through which the particle distribution function f_i propagates to the nearest neighbours. In the lattice having odd number of directions, one particle distribution function remains at rest at the lattice centre.

For a given application, relaxation time τ is different for different lattices. In heat transfer problems, the relaxation time τ for the D1Q2 lattice (Fig. 2.2) is computed from [1, 23-28, 39, 127]

$$\tau = \frac{\alpha}{\left|\vec{c}_i\right|^2} + \frac{\Delta t}{2} \tag{2.24}$$

For the D1Q2 lattice (Fig. 2.2) the two velocities $\vec{c}_i$ and their corresponding weights w_i are calculated from

$$c_1 = C, \quad c_2 = -C \tag{2.25}$$

$$w_1 = w_2 = \frac{1}{2} \tag{2.26}$$

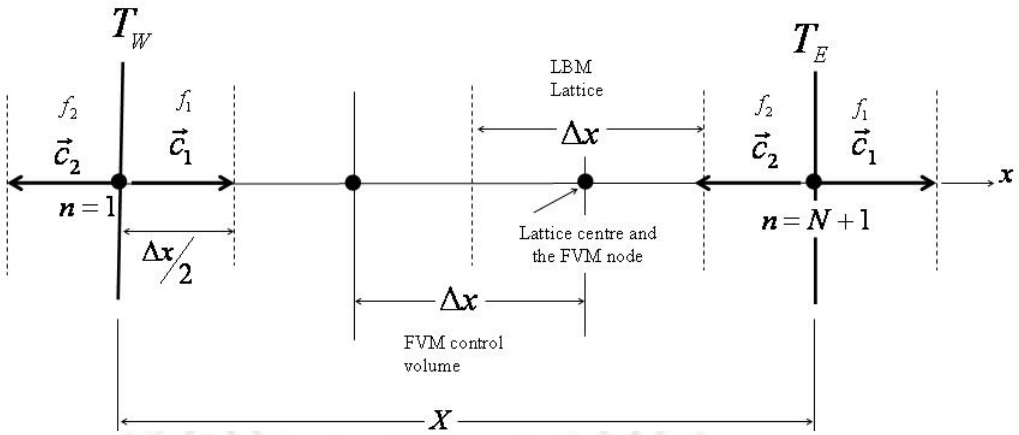

Figure 2.2: D1Q2 lattice of the LBM and control volume of the FVM used in 1-D planar geometry**.**

The relaxation time τ for the D2Q9 (Fig. 2.3) and the D3Q15 (Fig. 2.4) lattices is given by [1, 23-28, 39, 127]

$$\tau = \frac{3\alpha}{\left|\vec{c}_i\right|^2} + \frac{\Delta t}{2} \tag{2.27}$$

The 9 velocities $\vec{c}_i$ and their corresponding weights w_i in the D2Q9 lattice are the following:

$$\begin{aligned} c_0 &= (0,0) \\ c_{1,3} &= (\pm 1,0)\cdot C \\ c_{2,4} &= (0,\pm 1)\cdot C \\ c_{5,6,7,8} &= (\pm 1,\pm 1)\cdot C \end{aligned} \tag{2.28}$$

$$w_0 = \frac{4}{9}, w_{1,2,3,4} = \frac{1}{9}, w_{5,6,7,8} = \frac{1}{36} \tag{2.29}$$

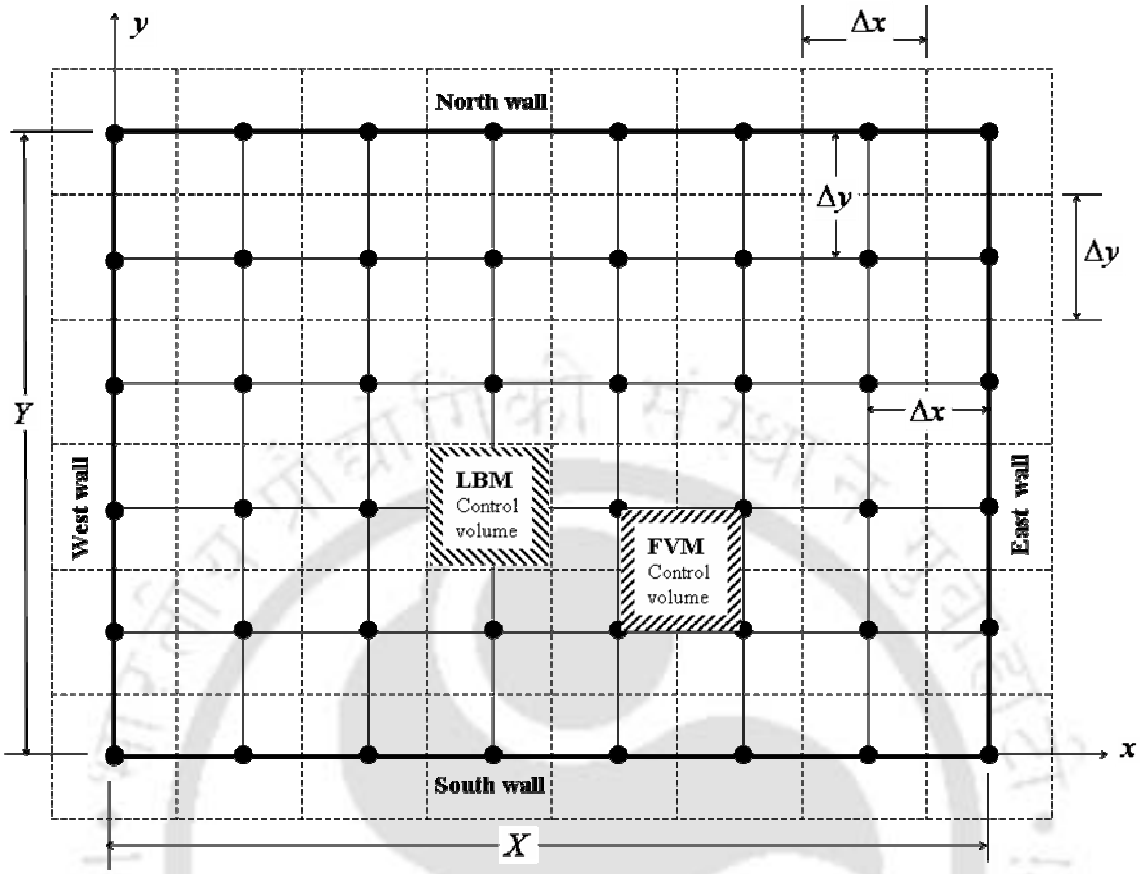

(a)

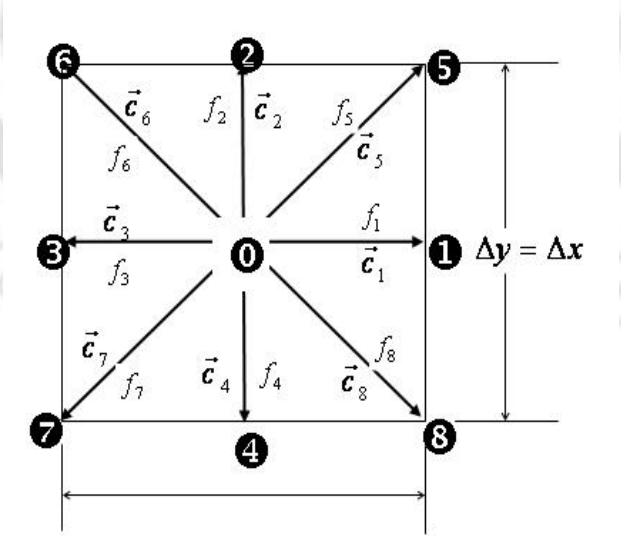

(b)

Figure 2.3: (a) Arrangement of lattices and control volumes in a 2-D rectangular geometry and (b) D2Q9 lattice used in 2-D geometry.

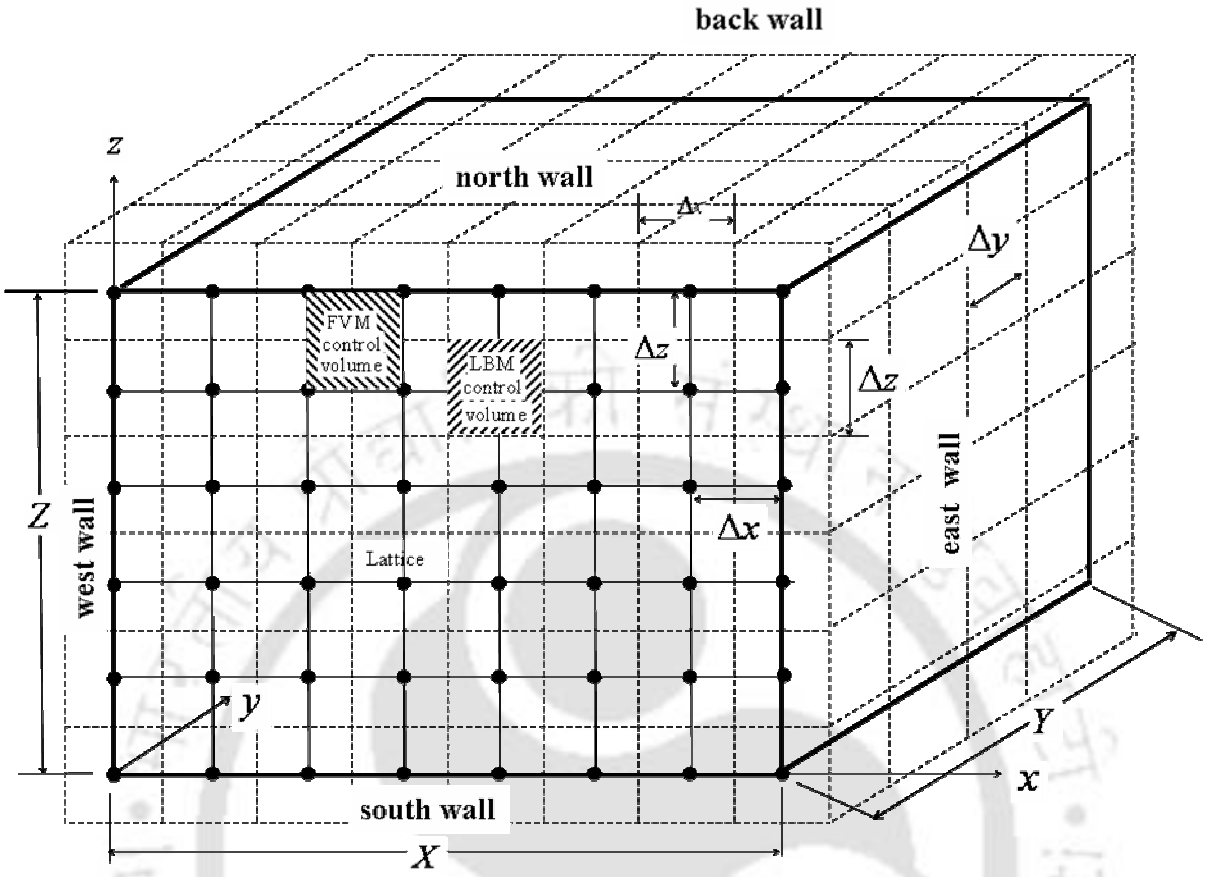

(a)

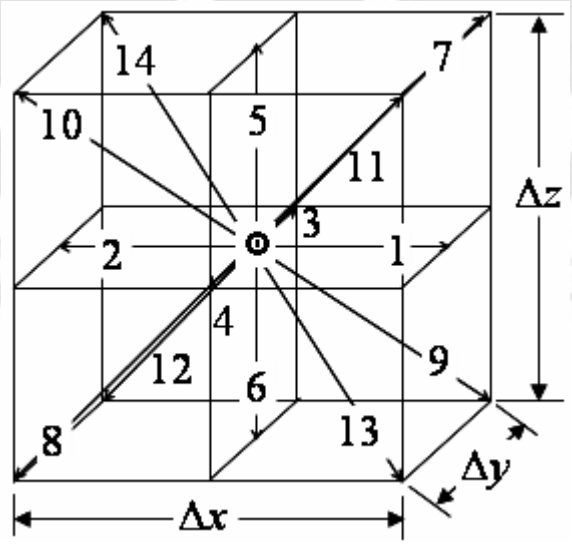

(b)

Figure 2.4: (a) Arrangement of lattices and control volumes in a 3-D Cartesian geometry (b) D3Q15 lattice in a 3-D geometry.

For the D3Q15 lattice (Fig. 2.4), the same are given by

$$\begin{aligned} c_0 &= (0,0,0) \\ c_{1,2} &= (\pm 1,0,0)\cdot C \\ c_{3,4} &= (0,\pm 1,0)\cdot C \\ c_{5,6} &= (0,0,\pm 1)\cdot C \\ c_{7,\cdots 14} &= (\pm 1,\pm 1,\pm 1)\cdot C \end{aligned} \tag{2.30}$$

$$w_0 = \frac{2}{9}, w_{1,\cdots\cdots 6} = \frac{1}{9}, w_{7,\cdots\cdots 14} = \frac{1}{72} \tag{2.31}$$

It is to be noted that in the above equations, $C = \Delta x/\Delta t = \Delta y/\Delta t = \Delta z/\Delta t$ and the weights satisfy the relation $\sum_{i=1}^{b} w_i = 1$.

After discretization, Eq. (2.23) can be written as [1, 23-28, 39, 127]

$$f_i\left(\vec{r}+\vec{c}_i\Delta t, t+\Delta t\right) = f_i\left(\vec{r},t\right) - \frac{\Delta t}{\tau}\left[f_i\left(\vec{r},t\right) - f_i^{(eq)}\left(\vec{r},t\right)\right] \tag{2.32}$$

This is the LB equation with the BGK approximation that describes the evolution of the particle distribution function f_i. The algorithm for Eq. (2.32) can be divided into two essential parts per time step:

- The calculation of new distribution functions f_i with respect to the right-hand-side of Eq. (2.32), usually referred to as collision.
- The streaming of the distribution functions to the next neighbouring nodes usually referred to as propagation.

In case of heat transfer problems, temperature is obtained after summing f_i over all direction [1, 23-28, 39, 127], i.e.,

$$T(\vec{r},t) = \sum_{i=0}^{b} f_i\left(\vec{r},t\right) \tag{2.33}$$

To process Eq. (2.32), an equilibrium distribution function is required. For heat conduction problems, this is given by

$$f_i^{(eq)}(\vec{r},t) = w_i T(\vec{r},t) \tag{2.34}$$

From Eqs. (2.33) and (2.34), we also have

$$\sum_{i=0}^{b} f_i^{(eq)}(\vec{r},t) = \sum_{i=0}^{b} w_i T(\vec{r},t) = T(\vec{r},t) = \sum_{i=0}^{b} f_i(\vec{r},t) \qquad (2.35)$$

Equation (2.32), with definitions of temperature $T(\vec{r},t)$ and equilibrium function $f_i^{(eq)}(\vec{r},t)$ given in Eqs. (2.33) and (2.34), respectively, provide solution of a transient heat conduction problem in the LBM. To incorporate the volumetric radiation, Eq. (2.31) gets modified to

$$f_i(\vec{r}+\vec{c}_i\Delta t, t+\Delta t) = f_i(\vec{r},t) - \frac{\Delta t}{\tau}\left[f_i(\vec{r},t) - f_i^{(eq)}(\vec{r},t)\right] - \left(\frac{\Delta t}{\rho c_p}\right) w_i \nabla\cdot\vec{q}_R \qquad (2.36)$$

Equation (2.36) is the desired equation to be used in the LBM. It is to be noted that Eq. (1) can be obtained from Eq. (2.35) using the Chapman-Enskog multiscale expansion.

2.5 Solution Procedure

The medium is divided into a finite number of lattices/control volumes. The control volumes of the FVM for computing the radiative information $\nabla\cdot\vec{q}_R$ and lattices in the LBM are staggered as shown in Figs. 2.2-2.4. Sizes of the lattices in the LBM and the control volumes in the FVM are taken the same.

In solving Eq. (2.36), $\nabla\cdot\vec{q}_R$ information is required at the lattice centres (Figs. 2.2-2.4). In the FVM for the radiative heat transfer, in any control volume, intensity distributions are computed at the mid-points of the control surfaces and at the centre of the FVM control volume. Thus $\nabla\cdot\vec{q}_R$ is known only at these points (3 points in 1-D, 5 points in 2-D and 7 points in 3-D control volumes in Figs. 2.2-2.4, respectively). It is seen from Figs. 2.2-2.4 that none of these points coincide with the lattice centres. Therefore, $\nabla\cdot\vec{q}_R$ value at any lattice centre is computed from the average of the $\nabla\cdot\vec{q}_R$ values of the control-surfaces surrounding that lattice centre. For the lattice centres along the corners, average of the $\nabla\cdot\vec{q}_R$ values are based on $\nabla\cdot\vec{q}_R$ of the corner faces. For any other points except the corner points along a boundary, the $\nabla\cdot\vec{q}_R$ at the lattice centre is the average of $\nabla\cdot\vec{q}_R$ values of the neighbouring points, that are collinear for 2-D geometries and

coplanar for 3-D geometries, with the lattice center. The procedure to solve the energy equation (Eq. (2.36)) is the following:

1. Depending upon the type of geometry, choose the lattice and accordingly compute the relaxation time τ .
2. With initial temperature field known, in the first iteration, calculate the equilibrium particle distribution function $f_i^{(eq)}(\vec{r},0)$ from Eq. (2.34).
3. With initial temperature field known, calculate $\nabla \cdot \vec{q}_R$ using the FVM (Eq. (2.21)).
4. Calculate now the particle distribution functions $f_i(\vec{r}+\vec{c}_i\Delta t, t+\Delta t)$ using Eq. (2.36).
5. Propagate the particle distributions to the neighboring lattice centers.
6. Calculate the new temperature field $T(\vec{r},t)$ using Eq. (2.33).
7. Check for convergence and terminate the process, if appropriate.
8. Modify the particle distribution functions locally, to satisfy the boundary conditions.
9. Compute the equilibrium particle distribution functions $f_i^{(eq)}(\vec{r},t)$ from the new temperature field using Eq. (2.34) for every lattice.
10. Go to step 2

2.6 Summary

In this chapter, a general procedure to solve a heat transfer problem involving thermal radiation was described. A detailed formulation of the FVM for the computation of $\nabla \cdot \vec{q}_R$ in a 3-D Cartesian geometry was presented. The kinetic equation of the LBM from Boltzmann equation was derived. Different LB models and the solution procedure in the LBM to solve energy equation involving thermal radiation were discussed. The next chapter deals with the 1-D conduction-radiation problems

CHAPTER 3

1-D Conduction-Radiation Problems

3.1 Introduction

Analysis of combined conduction-radiation problem with flux boundary condition finds applications in furnace design, fire protection systems, foam insulations, solidification/melting of semitransparent materials, high temperature porous insulating materials, glass-fluidized bed, electronics chip and power plants etc.. Radiation being a volumetric phenomenon, its treatment in such problems is relatively difficult. In the presence of volumetric radiation, the governing energy equation turns out to be an integro-differential one and its solution requires efficient methods to compute radiative information and to solve the governing energy equation.

Combined conduction and radiation heat transfer problem with steady [122,131-133] or unsteady [134-137] condition has got wide practical applications. Problems having constant temperature boundary conditions have been analyzed in many studies [122, 136-138]. A few papers have discussed the problems with flux boundary conditions [132-134, 139]. Talukdar and Mishra [122] used the collapsed dimension method to analyze a conduction radiation problem in an absorbing, emitting and anisotropically scattering medium. Viskanta and Grosh [131] analyzed heat transfer by simultaneous conduction and radiation in an absorbing medium. Fernandes and Francis [132] used the finite element method in a combined conduction-radiation heat transfer problem in a planer

medium. They considered a constant temperature at one boundary and a constant total heat flux at the other boundary. Lin and Tsai [133] analyzed the steady conduction-radiation heat transfer problem for a planer, anisotropically scattering medium with flux boundary condition. Barker and Sutton [134] studied transient conduction radiation problem for a gray participating medium with externally heated semitransparent boundaries. Viskanta [138] solved the conduction-radiation heat transfer problem in absorbing and scattering materials for temperature boundary condition. Ho and Ozisik [139] also discussed the combined conduction-radiation problem in a two layer planer medium with flux boundary condition.

Normally, the LBM is constructed on a special class of uniform and regular lattices. This limitation of using uniform lattices becomes particularly severe in many practical applications where the complex geometry of boundaries cannot be well fitted by regular lattices and sharply varying information has to be captured in a given region. During the past few years, a few researchers motivated by such considerations have used irregular lattices. Succi *et al.* [128] and Ubertini and Succi [129] were the first to propose a finite volume formulation of the lattice Boltzmann equation (LBE). Quite recently, another elegant finite volume scheme was developed by Chen [130]. In a way similar to the conventional LBM, He *et al.* [38] proposed a model for an arbitrary rectangular mesh. All applications of the LBM with non-uniform/irregular lattices were those for the fluid mechanics problems. However, as far as its application to a conduction and radiation heat transfer problem is concerned, no work has been reported so far.

Towards the above objective, in the present chapter, the LBM is used to solve the energy equations of transient conduction and radiation problems in a 1-D planar geometry on non-uniform lattices. The variable relaxation time and the maximum relaxation time have been used in the LBM formulation. To check the performance of the LBM-FVM on non-uniform lattices/control volumes, the same problems are also solved for the uniform lattices/control volumes. The application of the LBM is extended to combined conduction-radiation problems with heat flux boundary conditions. An effect of heat generation is also considered.

3.2 Formulation

Let us consider a 1-D radiating and conducting homogeneous planar medium that is initially at temperature T_E (Figure 3.1). For time $t > 0$, the west boundary is maintained at temperature $T_W > T_E$. In the presence of heat generation, energy equation for the problem under consideration is given by

$$\rho c_p \frac{\partial T}{\partial t} = k\nabla^2 T - \nabla \vec{q}_R + Q''' \tag{3.1}$$

where the density of the medium is ρ, c_p is the specific heat at constant pressure, T is the dimensional temperature of the medium, t is the time, k is the thermal conductivity, $\vec{q}_R$ is the radiative heat flux and Q''' is the volumetric heat generation.

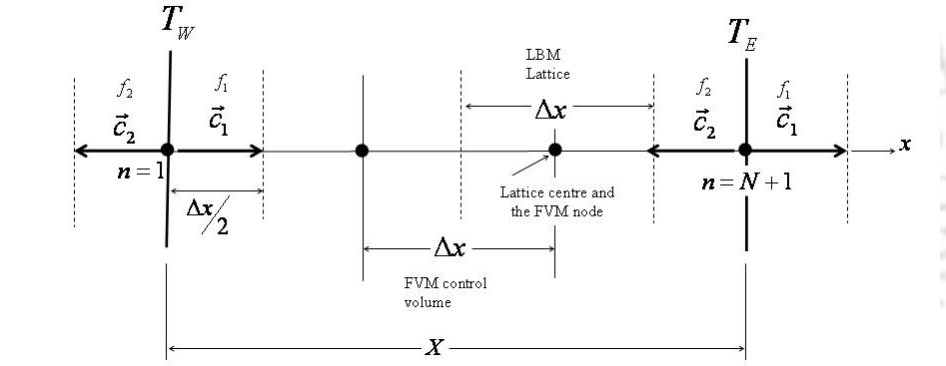

(a)

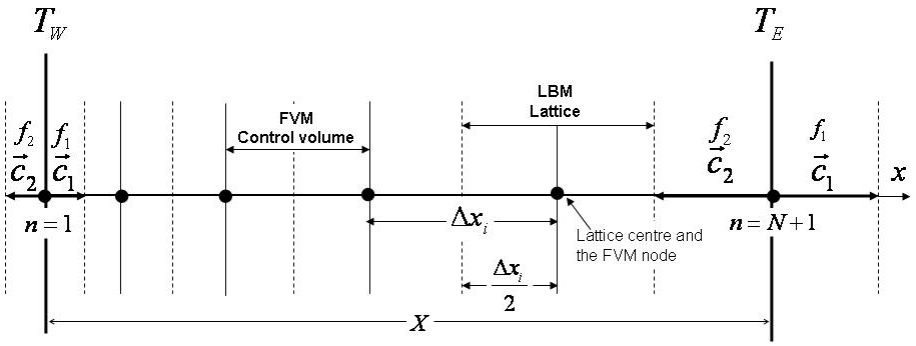

(b)

Figure 3.1: LBM and FVM with (a) uniform lattices/control volumes and (b) non-uniform lattices/control volumes.

Let us consider the west boundary temperature as the reference temperature and the non-dimensional parameters are taken as

$$\theta = \frac{T}{T_{ref}},\quad \Psi_R = \frac{q_R}{\sigma T_{ref}^4},\quad \xi = \frac{t}{\frac{\rho c_p}{k\beta^2}} = \frac{k\beta^2 t}{\rho c_p} = \alpha\beta^2 t,\quad Q^* = \frac{Q'''}{k\beta^2 T_{ref}} \tag{3.2}$$

where θ is the non-dimensional temperature, ψ_R is the non-dimensional radiative heat flux, ξ is the non-dimensional time and Q^* is the non-dimensional volumetric heat generation.

Using these non-dimensional parameter in Eq. (3.1), the resulting dimensionless equation can be written as

$$\frac{\partial\theta}{\partial\xi} = \frac{\partial^2\theta}{\partial x^2} - \frac{1}{4N}\frac{\partial\Psi_R}{\partial x} + Q^* \tag{3.3}$$

where the non-dimensional conduction-radiation parameter is defined as $N = \frac{k\beta}{4\sigma T_{ref}^3}$. To solve the above equation, information about the divergence of radiative heat flux is calculated using the FVM. Using the Eq. (2.21), the Eq.(3.3) can be written as

$$\frac{\partial\theta}{\partial\xi} = \frac{\partial^2\theta}{\partial x^2} - \frac{(1-\omega)}{N}\left[\theta^4 - \frac{G^*}{4\pi}\right] + Q^* \tag{3.4}$$

where ω is the scattering albedo and G^* is the non-dimensional irradiation. This governing transient energy equation is solved by LBM. So the desired equation to be used in the LBM is given by

$$\begin{aligned} f_i(r+\Delta r, \xi+\Delta\xi) = {} & f_i(r,\xi) - \frac{\Delta\xi}{\tau}\left[f_i(r,\xi) - f_i^{(eq)}(r,\xi)\right] \\ & - \Delta\xi \times w_i \frac{(1-\omega)}{N}\left[\theta^4 - \frac{G^*}{4\pi}\right] + \Delta\xi \times w_i \times Q^* \end{aligned} \tag{3.5}$$

3.3 Results and Discussion

The following four cases have been considered to validate the usage of the LBM on non-uniform lattices/control volumes in solving the energy equation of transient conduction and radiation heat transfer problem.

- **Conduction-radiation in a 1-D planar medium with variable relaxation time**: Initially the 1-D planar conducting and radiating participating medium is at a temperature T_E equal to that of the east boundary. Suddenly the west boundary is brought to a temperature T_W and for all times $t \geq 0$, it is maintained at this temperature. The boundaries of the absorbing, emitting and scattering medium are diffuse gray. Thermo-physical and optical properties are considered constant. The relaxation time for the LBM is variable.

- **Conduction-radiation in a 1-D planar medium with maximum relaxation time**: The same problem has been considered. In this case, the relaxation time is calculated based on the minimum velocity. This minimum velocity corresponds to the smallest size lattice.

- **Conduction-radiation in a 1-D planar medium with flux boundary condition:** Initially the 1-D planar-participating medium is at temperature T_N and for time $t > 0$, its south boundary is maintained at heat flux $q_{in} = q_{T,S}$. The gray homogeneous medium is absorbing, emitting and isotropically scattering. Its boundaries are diffuse-gray.

- **Conduction-radiation in a 1-D planar medium with heat generation:** Initially the 1-D planar conducting and radiating participating medium is at a temperature T_E equal to that of the east boundary. Suddenly the west boundary is brought to a temperature T_W and for all times $t \geq 0$, it is maintained at this temperature. The boundaries of the absorbing, emitting and scattering medium are diffuse gray. Thermo-physical and optical properties are considered constant. The non-dimensional heat generation rate is taken as unity.

3.3.1 Conduction-radiation in a 1-D planar medium with variable relaxation time: In this case, non-uniform lattices (Fig. 3.2) were generated using the following expression

$$x_n = \left\{ \frac{n-1}{n_{max}} + \frac{C_x}{\pi} \sin\left(\frac{\pi(n-1)}{n_{max}} \right) \right\} \tag{3.6}$$

where x_n is the location of the lattice centre in the LBM, n_{max} is the total number of lattices and C_x is a constant $\left(0 \le |C_x| \le 1\right)$ that determines clustering. For $C_x = 0$, uniform size lattices are obtained (Fig. 3.2a). For lattices/control volumes in Fig. 3.2b, $C_x = 0.5$ and that for Fig. 3.2c, $C_x = -0.5$. The type of lattices/control volumes in Figs. 3.2d and 3.2e are generated by dividing the solution domain in four zones and considering positive or negative values of C_x .

To establish the workability of the LBM-FVM with non-uniform lattices/control volumes, runs were taken for different types of clustering as shown in Figs. 3.2c-d. In all the cases, results of the non-uniform lattices/control volumes were compared against LBM-FVM with uniform lattices/control volumes (Fig. 3.2a). The number of uniform and non-uniform lattices/control volumes in the LBM-FVM was taken the same.

While generating the results, non-dimensional time step $\Delta\zeta = 1.0 \times 10^{-4}$ $\left(\zeta = \alpha\beta^2 t\right)$ was considered and steady-state condition was assumed to have been achieved when the maximum variation in temperature $\theta = \frac{T}{T_W}$ at any location between two consecutive time levels did not exceed 1.0×10^{-6}. In both non-uniform and uniform lattices/control volumes, beyond 101 lattices in the LBM and 100 control volumes and 10 directions in the FVM, no significant changes in results were observed.

It is to be noted that in case of a 1-D planar medium, radiation is azimuthally symmetric. Thus, 10 equally spaced directions in the FVM were considered by discretizing the polar angle θ $\left(0 \le \theta \le \pi\right)$. The variable relaxation time τ_n which depends upon the Δx_n under consideration is computed from

$$\tau_n = \frac{\alpha}{\left|\vec{C}_{n,i}\right|^2} + \frac{\Delta t}{2} \tag{19}$$

where α is the thermal diffusivity.

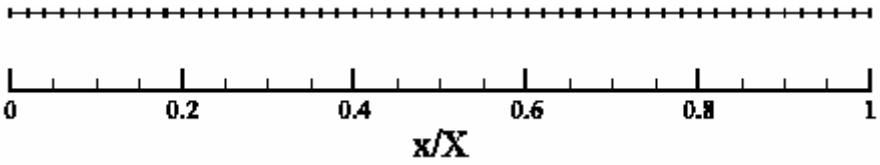

(a) $C_x = 0$

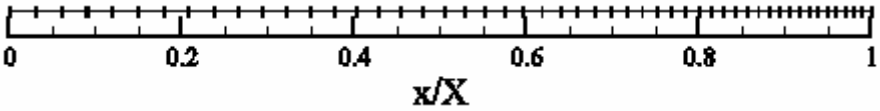

(b) $C_x = 0.5$

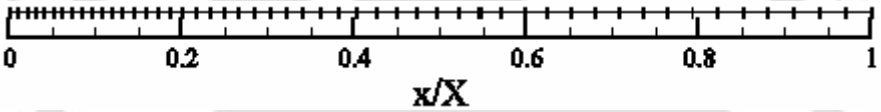

(c) $C_x = -0.5$

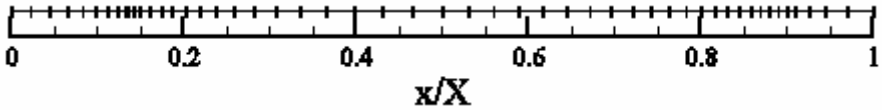

(d) $C_x = 0.5, 0 \le \left(\frac{x}{X}\right) \le 0.15$ and $0.5 \le \left(\frac{x}{X}\right) \le 0.9$

$C_x = -0.5, 0.15 \le \left(\frac{x}{X}\right) \le 0.5$ and $0.9 \le \left(\frac{x}{X}\right) \le 1.0$

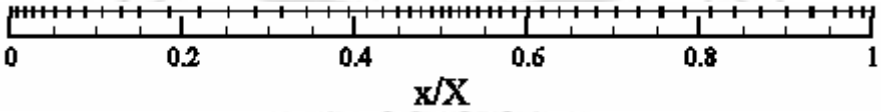

(e) $C_x = -0.5, 0 \le \left(\frac{x}{X}\right) \le 0.15$ and $0.5 \le \left(\frac{x}{X}\right) \le 0.9$

$C_x = 0.5, 0.15 \le \left(\frac{x}{X}\right) \le 0.5$ and $0.9 \le \left(\frac{x}{X}\right) \le 1.0$

Figure 3.2: Different types of non-uniform lattices for the 1-D planar medium.

Two velocities $\vec{c}_{n,i}$ and their corresponding weights w_i for the D1Q2 lattice are given by

$$c_1 = \frac{\Delta x_n}{\Delta t}, c_2 = -\frac{\Delta x_n}{\Delta t},\ w_1 = w_2 = \frac{1}{2} \tag{20}$$

To establish the workability of the LBM-FVM with non-uniform size lattices/control volumes with variable relaxation time, some sample results are presented in Figs 3.2-3.4. For comparison purpose, in these figures, results generated from the LBM-FVM with uniform lattice/control volumes single relaxation time have also been plotted and these results were first benchmarked against those available in the literature Mishra and Lankadasu [22].

In Figure 3.3, for extinction coefficient $\beta = 1.0$ and conduction-radiation parameter $N = \frac{k\beta}{4\sigma T_W^3} = 0.01$, non-dimensional temperature θ computed from the LBM-FVM with uniform and non-uniform lattices/control volumes have been compared for the effects of the scattering albedo ω. It can be seen from the figure that at all times ζ, the results of the two cases match very well with each other. The number of iterations for the steady-state solutions in the LBM-FVM with non-uniform lattices/control volumes (variable relaxation time) for ω = 0.0, 0.5 and 0.9 were 729, 1077 and 2915. The same in case of the LBM-FVM with uniform lattices/control volumes were found to be 739, 1112 and 3066. It is observed here that the LBM-FVM with non-uniform lattices/control volumes reaches steady-state faster.

In Figure 3.4, for $\omega = 0.0$ and $\beta = 1.0$, comparisons have been shown for two values of the conduction-radiation parameter N. It is seen that for both radiation dominated $(N = 0.01)$ and conduction dominated $(N = 0.1)$ cases, the results with non-uniform lattices/control volumes match well with those with uniform lattices/control volumes. For non-uniform lattices/control volumes the numbers of iterations for the steady-state

results were found to be 727 and 3675 for $N = 0.01$ and 0.1, respectively. The same for uniform lattices/control volumes were found to be 739 and 3932.

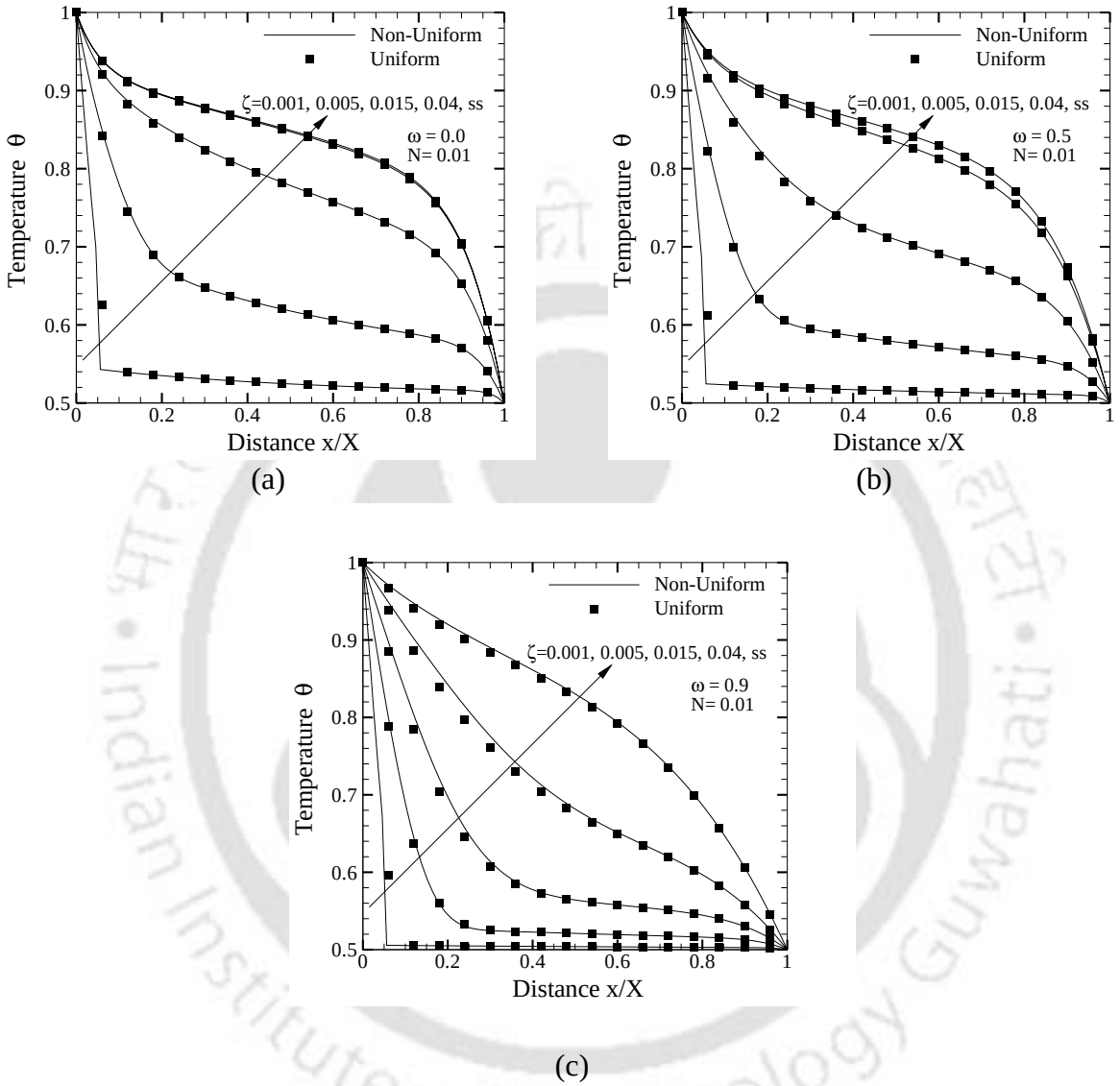

Figure 3.3: Comparison of non-dimensional temperature θ at different instants ζ for (a) scattering albedo ω = 0.0, (b) 0.5 and (c) 0.9.

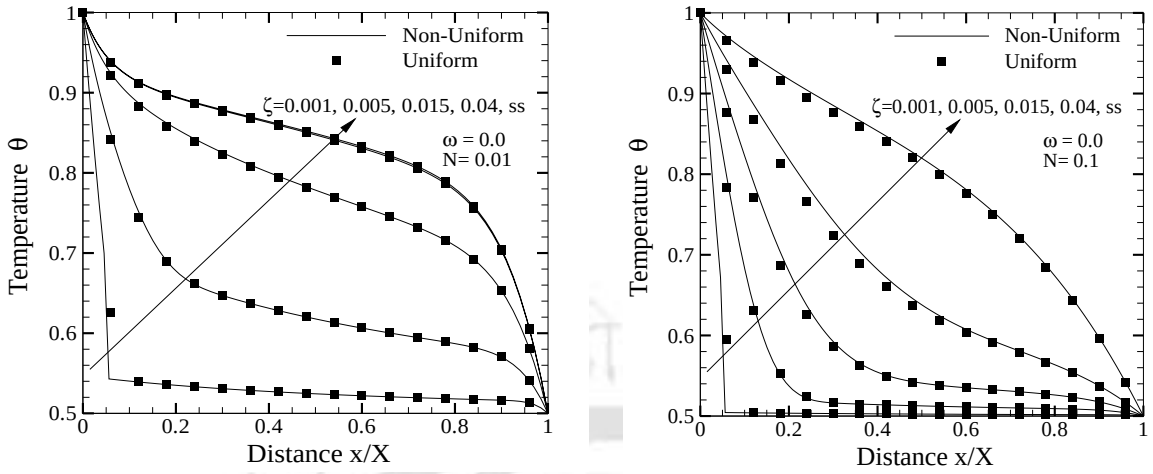

(a) (b)

Figure 3.4: Comparison of non-dimensional temperature θ in a planar medium at different instants ζ for conduction-radiation parameter N = (a) 0.01 and (b) 0.1.

In Figure 3.5, for $\beta = 1.0, \omega = 0.0$ and $N = 0.01$, with east boundary as black ε_E =1.0, comparisons of the temperature results have been made for the effect of west boundary emissivity ε_W. It is seen that at all times, results with non-uniform lattices/control volumes compare very well with those of the uniform lattices/control volumes. In this case too, the LBM-FVM with non-uniform lattices/control volumes were found to converge fast. For ε_W =0.1, 0.5 and 0.9, number of iterations with LBM-FVM with non-uniform lattices/control volumes were 1079, 876 and 747 respectively. The same for the other case were 1098, 909 and 779.

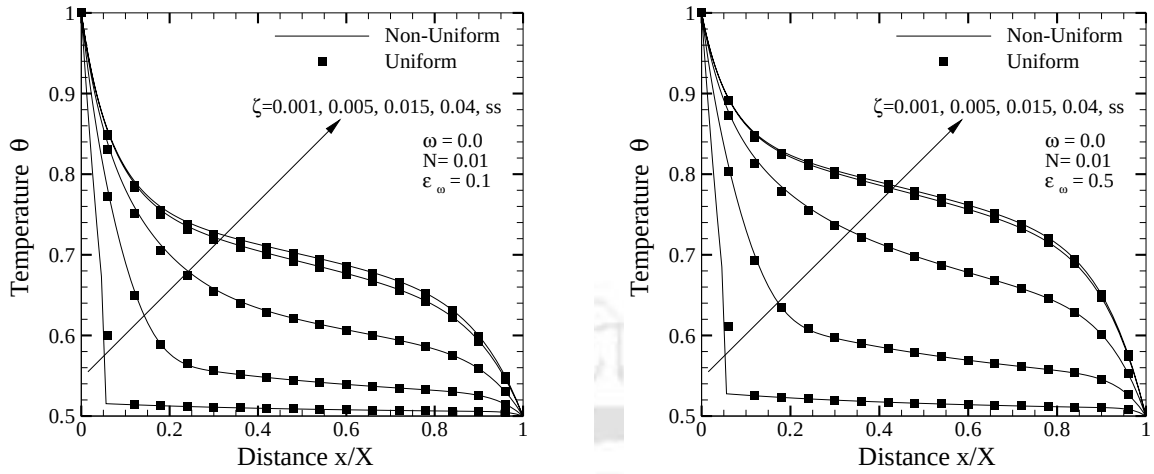

(a)

(b)

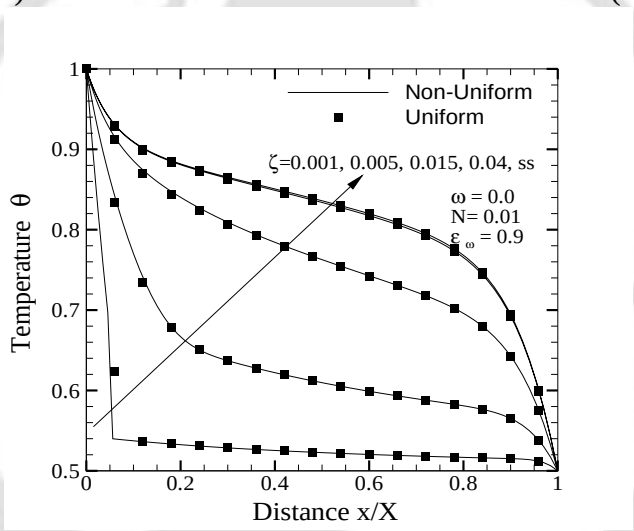

(c)

Figure 3.5: Comparison of non-dimensional temperature T/T_W in a planar medium at different instants ζ for emissivity of the south boundary ε_W = 0.1, (b) 0.5 and (c) 0.9.

3.3.2 Conduction-radiation in a 1-D planar medium with maximum relaxation time: With the LBM on non-uniform lattices, lattices are not of the same size, and if the velocities are calculated based on the respective lattice sizes, all the particle distribution functions f_i will not be available for collision at the same instant which is a pre-requisite in the LBM. To obviate this difficulty, all the particle distribution functions f_i from all the lattice centres are allowed to move with the same velocity which corresponds to the smallest size lattice. However with this, the f_i from a given lattice centre are not equidistant from the neighboring lattice centres. To allow the collision at the same instant, and thus to have a single relaxation time, the f_i in a given direction are interpolated to make them reach the neighboring lattice centres and thus remain available for collision at the same instant. This very interpolation concept has been recently used for fluid mechanics problems by Lu *et al*. [78], Ubertini and Succi [129] and Imamura *et al.* [84]. In case of a 1-D planar medium problem, in which we have used the D1Q2 lattice, linear interpolation of f_i have been done as suggested by Ubertini and Succi [129].

To compare results of the LBM-FVM on non-uniform lattices/control volumes with that of the LBM-FVM on uniform lattices/control volumes, in Table 3.1, at time $\zeta = 0.05$, temperature $\theta = \frac{T}{T_W}$ results are compared with those reported in the literature [133-135]. With clustering parameter $C = 0.5$, extinction coefficient $\beta = 1.0$, scattering albedo $\omega = 0.5$, conduction-radiation parameter $N = \frac{\kappa\beta}{4\sigma T_W^3} = 0.1$ and $T_E = 0.0$, at three locations in the medium *viz.* $x/X = 0.25, 0.50$ and 0.75, this comparison has been made for two sets of boundary

Table 3.1: Comparison of transient temperature θ at time $\zeta = 0.05$ for $\beta = 1.0$, $T_E = 0.0$, $\omega = 0.5$, and $N = 0.1$ and two sets of wall reflectivities.

ε_W	ε_E	Investigators	Transient temperature $\frac{T}{T_W}$		
			$x/X = 0.25$	$x/X = 0.50$	$x/X = 0.75$
1.0	1.0	Barker and Sutton [134]	0.4893	0.1775	0.0588
		Sutton [135]	0.4888	0.1778	0.0591
		Tsai and Lin [133]	0.4889	0.1773	0.0588
		Talukdar and Mishra [122]	0.4892	0.1768	0.0585
		Uniform lattices (present)	0.4898	0.1771	0.0581
		Non-uniform lattices (present)	0.4898	0.1771	0.0581
1.0	0.0	Barker and Sutton [134]	0.5035	0.2003	0.0831
		Sutton [135]	0.5030	0.2005	0.0833
		Tsai and Lin [133]	0.5031	0.2001	0.0830
		Talukdar and Mishra [122]	0.5033	0.1995	0.0824
		Uniform lattices (present)	0.5035	0.1996	0.0823
		Non-uniform lattices (present)	0.5036	0.1997	0.0823

emissivities ε_W and ε_E. It is observed from Table 1 that the results for the both uniform and non-uniform lattices/control volumes are in good agreements with each other and they are closely matching with those reported in the literature [131-133].

In Figs. 3.6-3.8, comparisons of temperature $\theta = \frac{T}{T_W}$ results with uniform $(C = 0.0)$ lattices / control volumes have been made for non-uniform lattices/control volumes with $C = 0.5$. In Fig. 6, results have been compared for different values of C.

In Fig. 3.6, for extinction coefficient $\beta = 1.0$ and conduction-radiation parameter $N = 0.01$, temperature θ computed from the LBM-FVM with uniform and non-uniform lattices/control volumes have been compared for the effects of the scattering albedo ω. It can be seen from the figure that results for the both cases are matching very well. The number of iterations for the steady-state (SS) solutions in the LBM-FVM with non-uniform lattices/control volumes for ω = 0.0, 0.5 and 0.9 were 869, 1144 and 2492. The same in case of the LBM-FVM with uniform lattices/control volumes were found to be 881, 1163 and 2639.

In Fig. 3.7, for $\omega = 0.0$ and $\beta = 1.0$, comparisons have been shown for three values of the conduction-radiation parameter N. It is seen that for both radiation dominated $(N = 0.01)$ and conduction dominated $(N = 1.0)$ cases, the result for the steady state condition with non-uniform lattices/control volumes match well with those with uniform lattices/control volumes. It can be seen from the figure that at all times ζ, the results with non-uniform lattices/control volume give slightly higher value with those with uniform lattices/control volumes. For non-uniform lattices/control volumes, the numbers of iterations for the steady-state results were found to be 869, 3450 and 4887 for $N = 0.01$, 0.01 and 0.1, respectively. The same for uniform lattices/control volumes were found to be 881, 3706 and 5764.

In Fig. 3.8, for $\beta = 1.0, \omega = 0.0$ and $N = 0.01$, with east boundary as black ε_E =1.0, comparisons of the temperature results have been made for the effect of west boundary emissivity ε_W. It is seen that at all times, results with non-uniform lattices/control volumes compare very well with those of the non-uniform lattices/control volumes. In

this case too, the LBM-FVM with non-uniform lattices/control volumes were found to converge fast. For ε_W =0.1, 0.5 and 0.9, number of iterations with LBM-FVM with non-uniform lattices/control volumes were 1162, 995 and 892 respectively. The same for the other case were 1193, 1024 and 905.

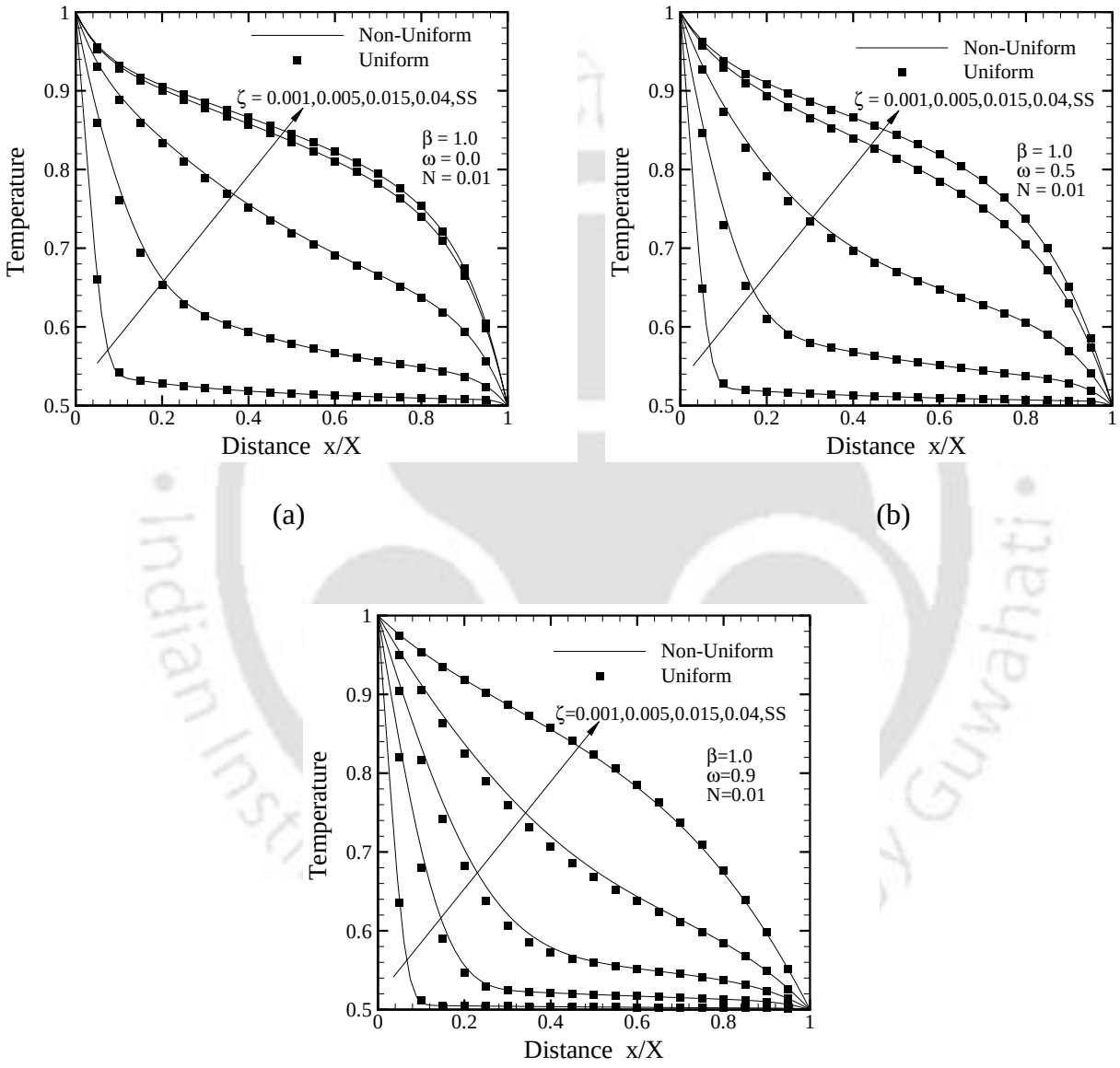

Figure 3.6: Comparison of temperature θ in a planar medium at different instants ζ for scattering albedo ω = (a) 0.0, (b) 0.5 and (c) 0.9.

In Fig. 3.9, for $\beta = 1.0, \omega = 0.0, N = 0.01, \varepsilon_W = \varepsilon_E = 1.0$, temperature θ results for different cluster values C have been compared at ζ = 0.015, 0.040 and steady-state. It is seen from this figure for different clustering values, results are in good agreement with each other.

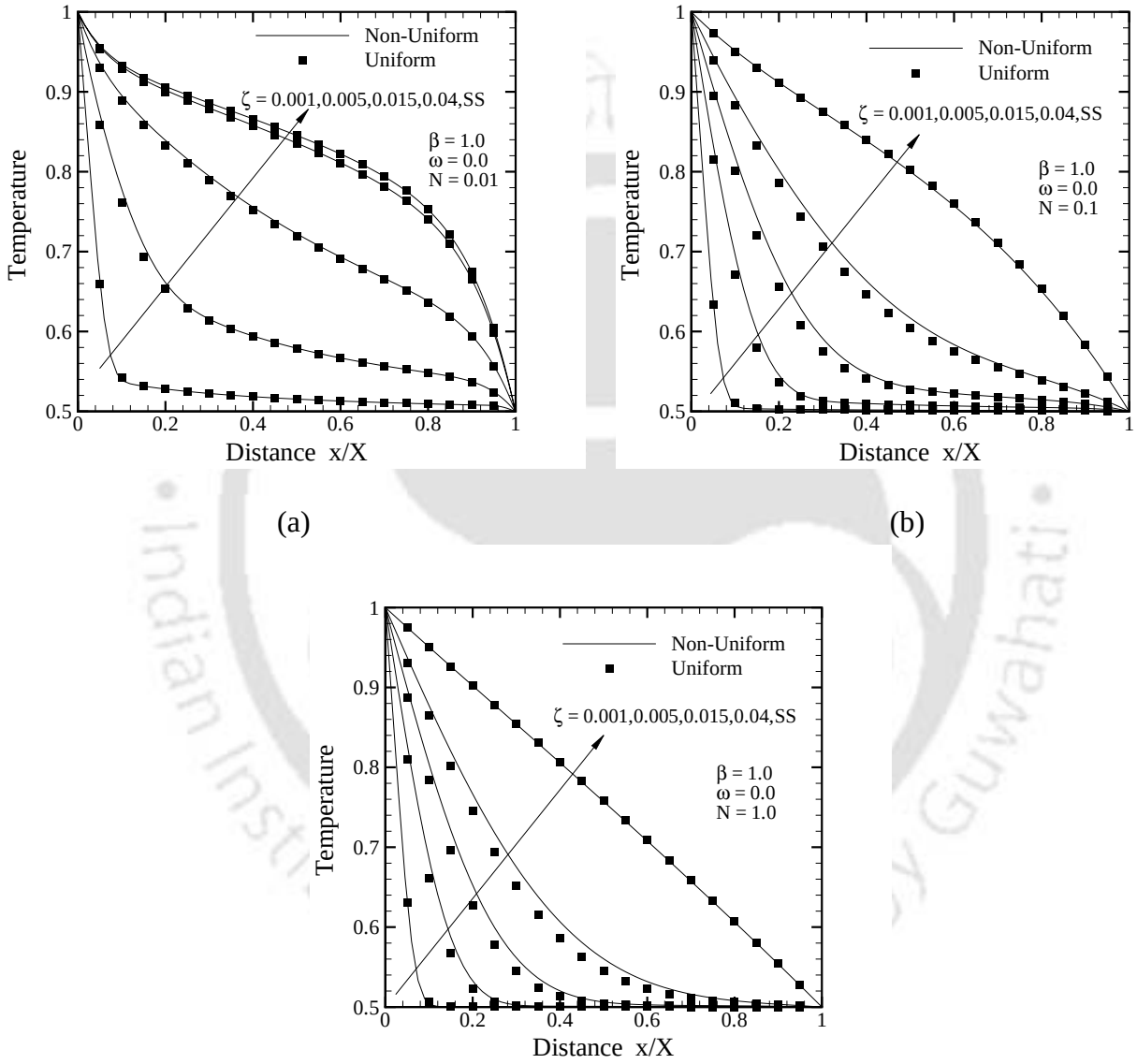

Figure 3.7: Comparison of temperature θ in a planar medium at different instants ζ for conduction-radiation parameter N = (a) 0.01, (b) 0.1 (c) 1.0.

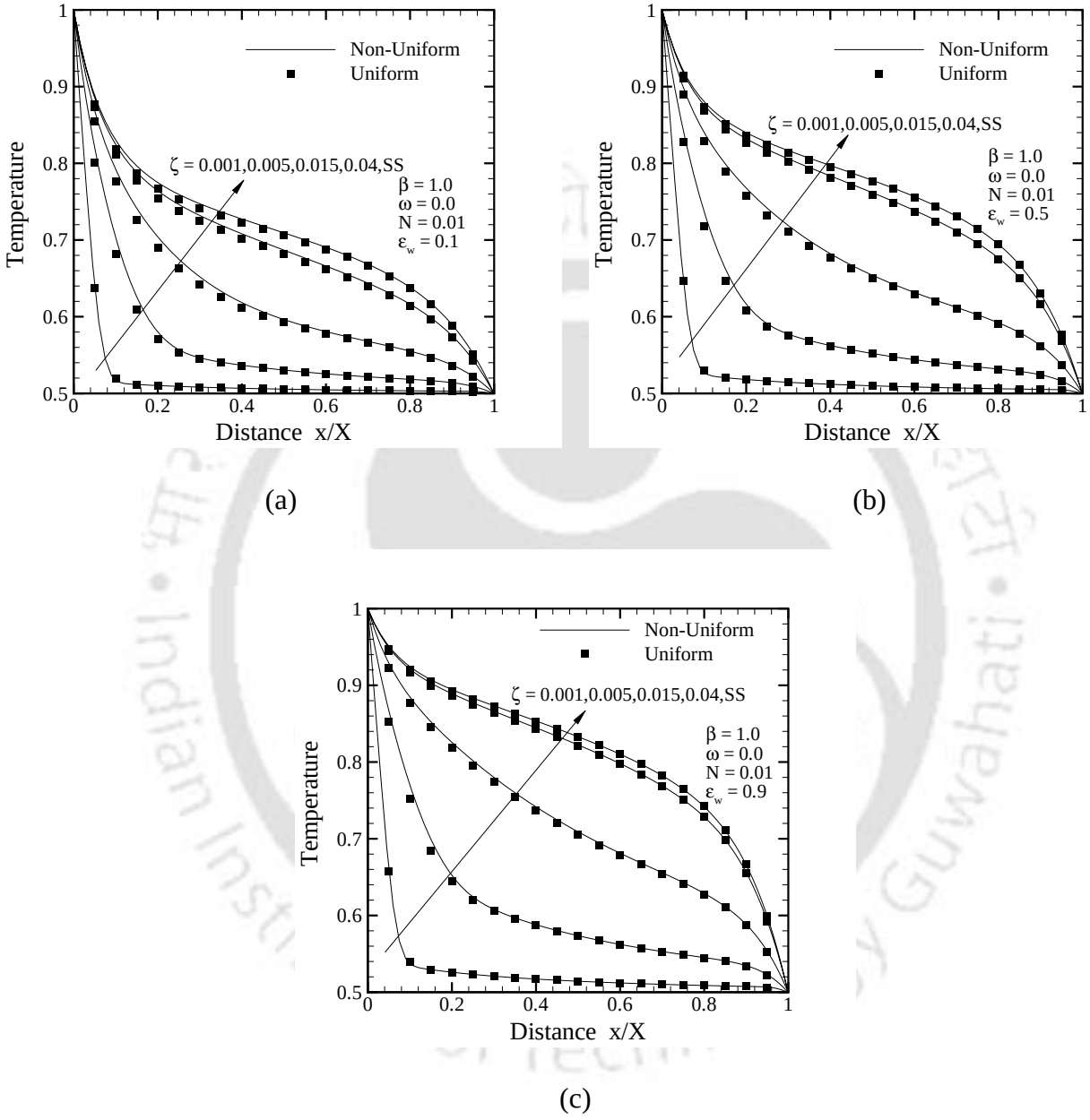

Figure 3.8: Comparison of temperature θ in a planar medium at different instants ζ for emissivity of the south boundary ε_W = (a) 0.1, (b) 0.5 and (c) 0.9.

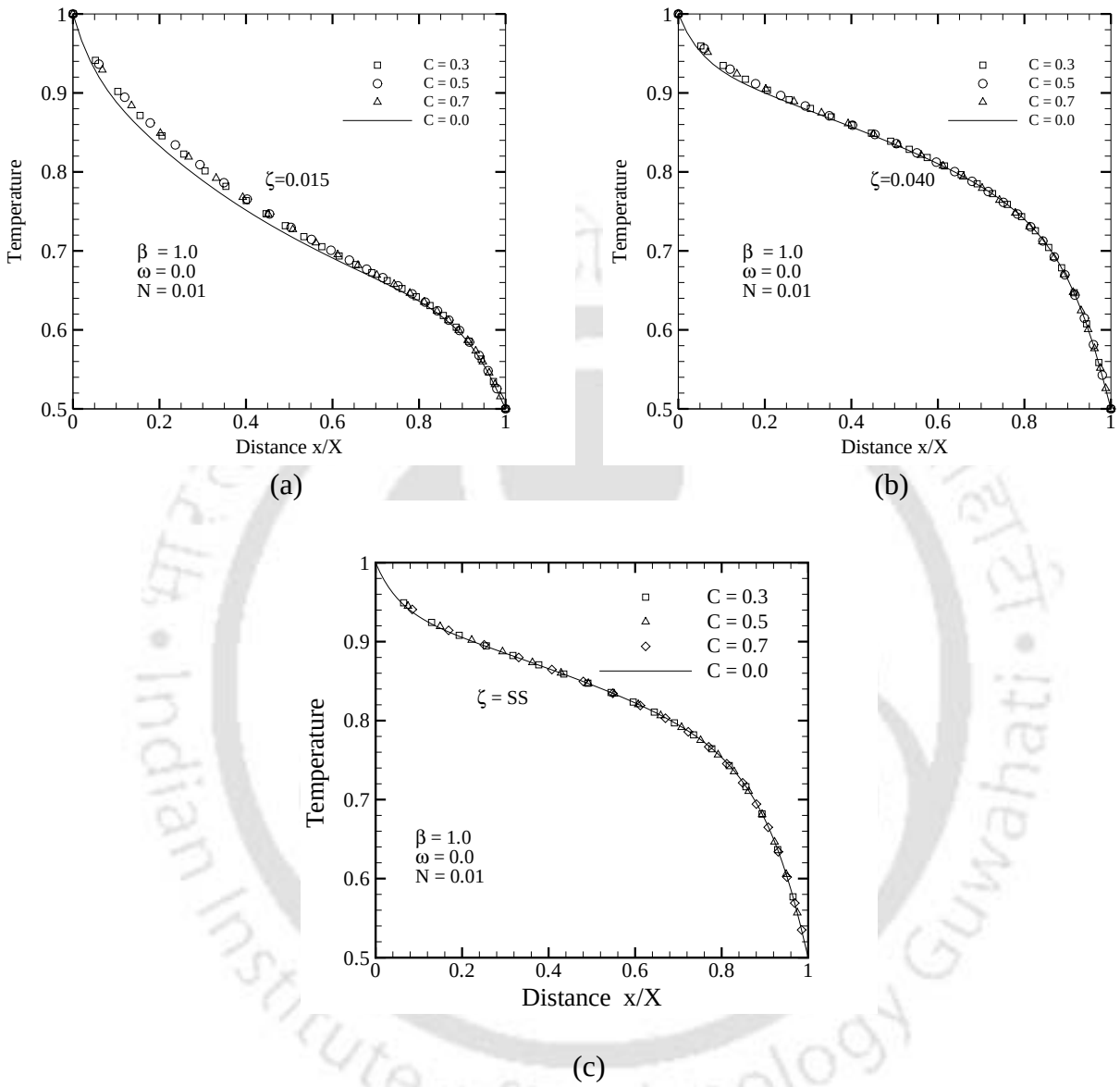

Figure 3.9: Comparison of temperature θ in a planer medium for different cluster values $C = 0.0, 0.3, 0.5$ and 0.7 at time (a) $\zeta = 0.015$, (b) $\zeta = 0.040$ and (c) steady state.

3.3.3 Conduction-radiation in a 1-D planar medium with flux boundary condition: To extend the applicability of the LBM to combined conduction-radiation problems with heat flux and temperature boundary conditions, we consider a 1-D planar geometry. The contained medium is assumed absorbing, emitting and scattering. In a 1-D planar medium, one boundary is at prescribed flux. The energy equation is solved using the LBM, and the FVM is used to compute the volumetric radiative information. Correctness of the formulation and implementation of the boundary conditions is established by comparing results of the direct and inverse methods, and also by comparing with those available in the literature. Effects of some important parameters on temperature and heat flux distributions are also analyzed.

3.3.3.1 Implementation of Flux Boundary Conditions in the LBM: In applications of the LBM to heat transfer problems involving thermal radiation, boundaries of the geometries were at prescribed temperatures, and implementation of temperature boundary condition has been explained in Mishra and Lankadasu [22]. In the present work, we have extended the application of the LBM to a conduction-radiation problem with flux boundary condition. With volumetric radiation, the total heat flux on a boundary comprises of conductive and radiative heat fluxes. All intensities incident at any point on the boundary contribute to the radiative heat flux. Below we briefly describe implementation of the heat flux boundary condition in the LBM. For the sake of simplicity, we explain this for the south boundary of a 1-D planar medium (Fig. 3.10) which is subjected to total heat flux q_{in}.

In implementing the flux boundary condition in the LBM, conservation of energy is applied to the half-size boundary lattice (Fig. 3.10). This conservation of energy over time Δt to the half-size lattice (Fig. 3.10) at the south boundary ($j=1$) yields,

$$\rho c_p \int_0^{\left(\frac{\Delta x}{2}\right)} \left(\int_t^{t+\Delta t} \frac{\partial T}{\partial t} dt \right) dx = \int_t^{t+\Delta t} \left(q_{in} - q_{out} \right) dt \tag{3.9}$$

where q_{in} is the prescribed total heat flux at the south boundary and $q_{out} = q_C + q_R$ is the heat flux leaving the half-size boundary lattice. Using Fourier's law for q_C and after discretizations of terms in Eq. (3.9), we get

$$\rho c_p \left(T_j^{k+1} - T_j^k\right)\frac{\Delta x}{2} = \int_t^{t+\Delta t}\left(\left(q_{in} - q_R\right) - k\left[\frac{T_j^k - T_{j+1}^k}{\Delta x}\right]\right)dt \tag{3.10}$$

where k and $k+1$ represent the time levels at t and $t+\Delta t$, respectively.

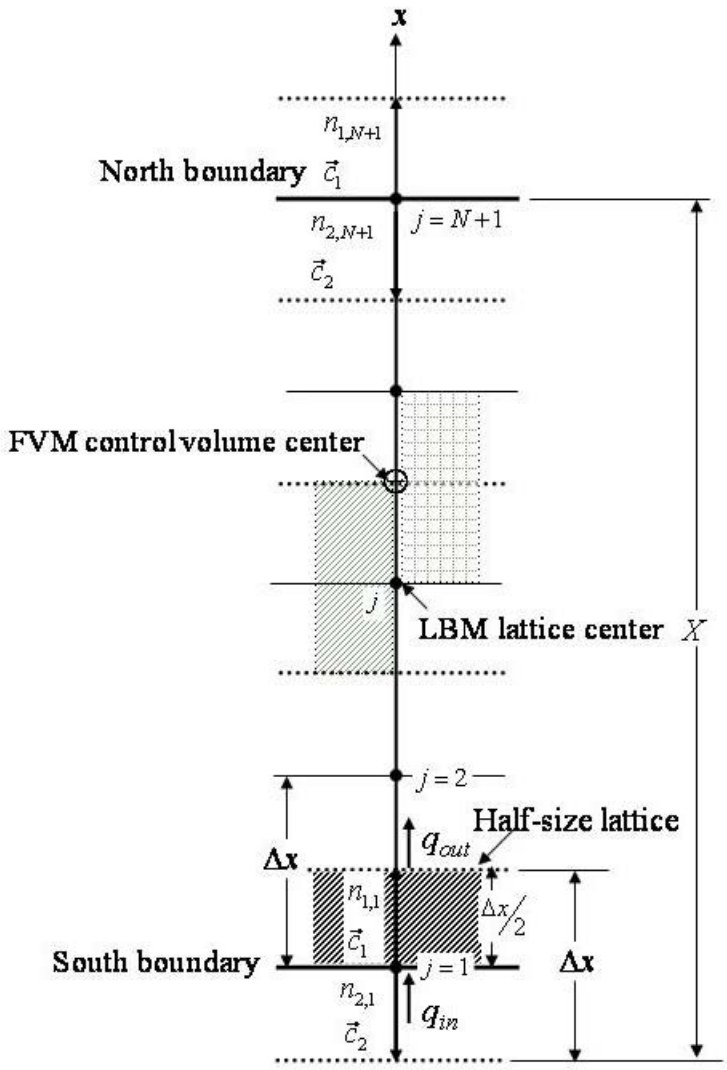

Figure 3.10: 1-D planar medium with D1Q2 lattice.

If an explicit scheme for the time discretization on the right hand side of Eq. (3.10) is employed, we obtain

$$T_j^{k+1} = (1-A)T_j^k + AT_{j+1}^k + B\left(q_{in} - q_R\right) \tag{3.11}$$

where $A = \frac{2\alpha\Delta t}{(\Delta x)^2}$ and $B = \frac{2\Delta t}{\rho c_p \Delta x}$. Once temperature T_j^{k+1} at the boundary is known in terms of prescribed flux q_{in}, the unknown particle distribution function n_i at any point of the boundary can be calculated easily by the procedure described in references [100] for the constant boundary condition.

It is to be noted that with flux prescribed at any boundary, temperature remains an unknown quantity. With iterations, a correct value of temperature evolves. Thus, while using Eq. (3.11), radiative heat flux q_R at the boundary, which too depends on the temperature field of the entire system, gets updated with iterations. Thus, in Eq. (3.11), T_j^{k+1} keeps on updating with iterations.

3.3.3.2 Results for conduction-radiation problem in a 1-D planar medium: To access the correctness of the LBM-FVM formulation and its implementation for the flux boundary condition of a transient conduction-radiation problem, we first solved a direct problem. In this, for a prescribed south-boundary temperature $\theta_S = 1.0$ and north boundary temperature $\theta_N = 0.5$, we predicted the total heat flux $\Psi_{T,S} = \Psi_C + \Psi_R$ at the south boundary. Then in the inverse problem, the computed value of the heat flux $\Psi_{T,S}$ became the flux boundary condition at the south boundary. We then computed the temperature field θ in the medium and compared them with that of the direct method. For other conditions and parameters remaining the same, the validation of the LBM-FVM with flux boundary condition is established if both the direct method and inverse method would yield the same results.

With extinction coefficient $\beta = 1.0$, conduction-radiation parameter $N = 0.1$, scattering albedo $\omega = 0.0$ and both boundaries black, the total heat flux $\Psi_{T,S}$ at the south boundary was found to be 0.7632. This is the result from the direct method. Keeping other parameters the same and the south boundary now subjected to $\Psi_{T,S}$=0.7632, in the inverse method, the temperature at the south boundary θ_S was found to be 0.9997 which is very close to unity, the prescribed temperature ($\theta_S = 1.0$) in the direct method.

In Fig 3.11, for three different values of the conduction-radiation parameter N, scattering albedo ω and boundary emissivity ε, the non-dimensional temperature θ computed using direct and inverse methods have been compared. The results of the direct method have been benchmarked against the results given in Mishra and Talukdar [122]. It is seen from Fig. 3.11 that at all locations including the south boundary, results of the direct and inverse methods are in excellent agreement with each other.

To further validate our LBM-FVM results, in Tables 3.2 and 3.3, we compare temperature θ and radiative heat flux $\frac{\Psi_R}{4N}$, respectively with those given in Fernandes and Francis [132], Lin and Tsai [133] and Mishra and Talukdar [122] for constant heat flux boundary condition. It is to be noted that in these references [122, 132, 133], both radiative transfer method and the energy equation solver were different than what we have used in the present work.

Table 3.2: Comparison of temperature for isotropic scattering with $\omega = 0.5$, $\beta = 1.0$, $\varepsilon_S = \varepsilon_N = 0.5$ and $N = 0.5, 0.1, 0.05$

	Temperature θ at							
	$x/X = 0.0$				$x/X = 0.5$			
$N = 0.5$								
$\Psi_{T,S}$	Ref. [132]	Ref. [133]	Ref. [122]	Present	Ref. [132]	Ref. [133]	Ref. [122]	Present
2	0.961	0.961	0.961	0.959	0.546	0.546	0.546	0.544
4	1.425	1.425	1.426	1.427	0.835	0.835	0.835	0.835
6	1.706	1.707	1.708	1.710	1.043	1.044	1.044	1.045
8	1.909	1.910	1.911	1.914	1.211	1.212	1.213	1.215
$N = 0.1$								
0.4	0.786	0.786	0.786	0.786	0.475	0.475	0.475	0.474
0.8	1.059	1.060	1.060	1.062	0.677	0.677	0.677	0.678
1.2	1.226	1.227	1.228	1.230	0.821	0.822	0.822	0.823
1.6	1.350	1.351	1.351	1.354	0.937	0.937	0.937	0.939
$N = 0.05$								
0.2	0.701	0.701	0.701	0.702	0.439	0.439	0.439	0.439
0.4	0.919	0.919	0.920	0.921	0.610	0.611	0.611	0.612
0.6	1.054	1.055	1.055	1.057	0.732	0.733	0.733	0.734
0.8	1.155	1.157	1.156	1.159	0.828	0.830	0.829	0.831

With $\omega = 0.5$, $\beta = 1.0$, $\varepsilon_S = \varepsilon_N = 0.5$ and $\theta_N = 0.1$, for three values of $N = 0.5, 0.1, 0.05$, in Table 3.2, temperature θ at two locations, viz. $x/X = 0.0$ and 0.5 are compared for different values of heat flux Ψ_T imposed on the south boundary. For the same sets of parameters as taken in Table 3.2, in Table 3.3, comparison of radiative heat flux $\frac{\Psi_R}{4N}$ has been shown at three locations, viz. $x/X = 0.0$, 0.5 and 1.0. The results of the present work are found to compare very well with those available in [122,132,133].

Table 3.3: Comparison of radiative heat flux distribution for isotropic scattering with $\omega = 0.5$, $\beta = 1.0$, $\varepsilon_S = \varepsilon_N = 0.5$ and $N = 0.5, 0.1$ and 0.05

	Radiative heat flux $\frac{\Psi_R}{4N}$ at											
	$x/X = 0.0$				$x/X = 0.5$				$x/X = 1.0$			
	$N = 0.5$											
$\Psi_{T,S}$	Ref. [132]	Ref. [133]	Ref. [122]	Pres-ent	Ref. [132]	Ref. [1133]	Ref. [122]	Pres-ent	Ref. [132]	Ref. [133]	Ref. [122]	Present
2	0.143	0.144	0.143	0.142	0.153	0.153	0.153	0.152	0.064	0.064	0.064	0.063
4	0.687	0.689	0.689	0.689	0.747	0.747	0.747	0.749	0.314	0.313	0.314	0.315
6	1.394	1.398	1.398	1.403	1.552	1.552	1.553	1.562	0.661	0.661	0.661	0.665
8	2.158	2.165	2.164	2.174	2.452	2.451	2.454	2.470	1.060	1.060	1.061	1.068
	$N = 0.1$											
0.4	0.314	0.315	0.315	0.314	0.349	0.348	0.348	0.346	0.149	0.149	0.148	0.148
0.8	1.019	1.022	1.022	1.025	1.164	1.164	1.165	1.171	0.507	0.506	0.507	0.509
1.2	1.799	1.805	1.805	1.814	2.106	2.106	2.108	2.122	0.939	0.939	0.940	0.946
1.6	2.604	2.613	2.612	2.627	3.097	3.096	3.096	3.122	1.414	1.414	1.414	1.426
	$N = 0.05$											
0.2	0.393	0.394	0.393	0.393	0.445	0.445	0.445	0.444	0.193	0.193	0.192	0.192
0.4	1.135	1.139	1.139	1.143	1.326	1.326	1.326	1.334	0.590	0.590	0.590	0.594
0.6	1.932	1.938	1.938	1.948	2.303	2.302	2.305	2.321	1.056	1.056	1.058	1.064
0.8	2.748	2.755	2.757	2.773	3.313	3.312	3.317	3.340	1.563	1.563	1.567	1.576

Effects of the scattering albedo ω, the conduction-radiation parameter N, the south boundary heat flux $\Psi_{T,S}$ and the boundary emissivity $\varepsilon_S = \varepsilon_N = \varepsilon$ on temperature θ distribution have been shown in Fig 3.12 and Fig. 3.13. In Figs. 3.12a-c, for $\beta = 1.0, \varepsilon = 0.5, N = 0.05, \theta_N = 0.5$ and $\Psi_{T,S}$ = 0.4, effect of the scattering albedo ω on variation of θ has been shown at different times steps $\zeta = 0.005, 0.03, 0.05$ and SS. The radiative contribution is less as effects of scattering albedo ω increases. So non-linearity in θ profile is observed to be more for lower values of ω. The south boundary temperature increases for the higher values of scattering albedo ω. In Figs. 3.12d-f, the effects of N on θ profile are shown for $\beta = 1.0$, $\omega = 0.5$, $\theta_N = 0.5$, $\varepsilon = 0.5$ and $\Psi_{T,S} = 0.4$ at transient as well as steady state condition. In Fig 4d, the transient results of non-dimensional temperature θ distribution have been shown for the radiation dominated ($N = 0.02$) cases. Therefore, the steady state temperature distribution is more non-linear. On the other hand, in case of conduction dominated ($N = 1.0$), steady state θ distribution is completely linear.

In Fig. 3.13, effects of $\Psi_{T,S}$ and ε on θ profile are shown for $\beta = 1.0, \omega = 0.5, N = 0.05, \theta_N = 0.5$ at different time steps $\zeta = 0.005, 0.03, 0.05$ and SS. In Figs. 3.13a-c, effects of $\Psi_{T,S}$ are considered. With increase in $\Psi_{T,S}$ at the south boundary, energy input to the medium is more, the radiation becomes more prominent. Non-linearity in the θ profile increases and at any location, θ value is more for higher $\Psi_{T,S}$. In Figs. 3.13d-e, when walls become more reflecting, the boundary reflects more energy back to the medium and thus effect of radiation becomes more and non-linearity in θ profile is found to be more, and at any location, θ value is more for lower ε.

In Figs. 3.14a-h, variations of radiative heat flux Ψ_R and conductive heat flux $\Psi_C = -4N\left(\frac{\partial\theta}{\partial x}\right)$ have been plotted for the effects of various parameters. In Figs. 3.14a

and 3.14b, for $\beta = 1.0, \varepsilon = 0.5, N = 0.05, \theta_N = 0.5$ and $\Psi_{T,S}$ = 0.4, effect of the scattering albedo ω on Ψ_R and conductive heat flux Ψ_C have been shown. With $\beta = 1.0$, $\omega = 0.5$, $\theta_N = 0.5$, $\varepsilon = 0.5$ and $\Psi_{T,S} = 0.4$, effect of the conduction-radiation parameter N on Ψ_R and Ψ_C have been shown in Figs. 3.14c and 3.14d, respectively. Effect of $\Psi_{T,S}$ on Ψ_R and Ψ_C have been shown in Figs. 3.14e and 3.14f, respectively for $\beta = 1.0, \omega = 0.5, N = 0.05, \theta_N = 0.5, \varepsilon = 0.5$. Figs. 3.14g and 3.14h show the effect of ε on Ψ_R and Ψ_C, respectively for $\beta = 1.0, \omega = 0.5, N = 0.05, \theta_N = 0.5, \Psi_{T,S} = 0.4$.

With $\omega = 1.0$, $\nabla \cdot \Psi_R = 0.0$ and Ψ_R = constant (Fig. 3.14a). This will also lead to a constant value of Ψ_C in the medium (Fig. 3.14b), because in the steady-state, as seen from Fig. 4a, for $\omega = 1.0$, temperature θ profile is a linear one. Further, with decrease in ω, medium absorbs more radiative energy, radiative heat flux Ψ_R some distance away from the boundaries increases (Fig. 3.14a). An opposite trend will be for the conductive heat flux Ψ_C and this is observed in Fig. 3.14b.

When the imposed heat flux $\Psi_{T,S}$ on the south boundary increases, radiative contribution to the medium increases and thus as seen from Fig. 3.14e, radiative heat flux Ψ_R increases with increase in $\Psi_{T,S}$. Conductive heat flux Ψ_C too increases and near the north boundary, effect of $\Psi_{T,S}$ on Ψ_C is more prominent.

When the boundaries become more reflecting, boundaries retain less radiative energy. Thus, as seen from Fig. 3.14g, radiative heat flux Ψ_R decreases with decrease in the emissivity ε of the south and the north boundaries. An apposite trend is seen in case of Ψ_C profile (Fig. 3.14h). It is further seen that in the middle portion of the medium, effect of the emissivity ε of the boundaries is negligible.

It is to be noted that for the 1-D planar medium problem under consideration, in the steady-state, the total heat flux $\Psi_T = \Psi_C + \Psi_R$ throughout the medium will be constant. Thus, as seen from Figs. 3.14a-h, radiative heat flux Ψ_C and conductive heat flux Ψ_R varies in the medium in such as way that for any given set of parameters, the total heat flux $\Psi_T = \Psi_C + \Psi_R$ remains constant. The values of the constant total heat flux Ψ_T increase or decrease depending upon the chosen set of parameters.

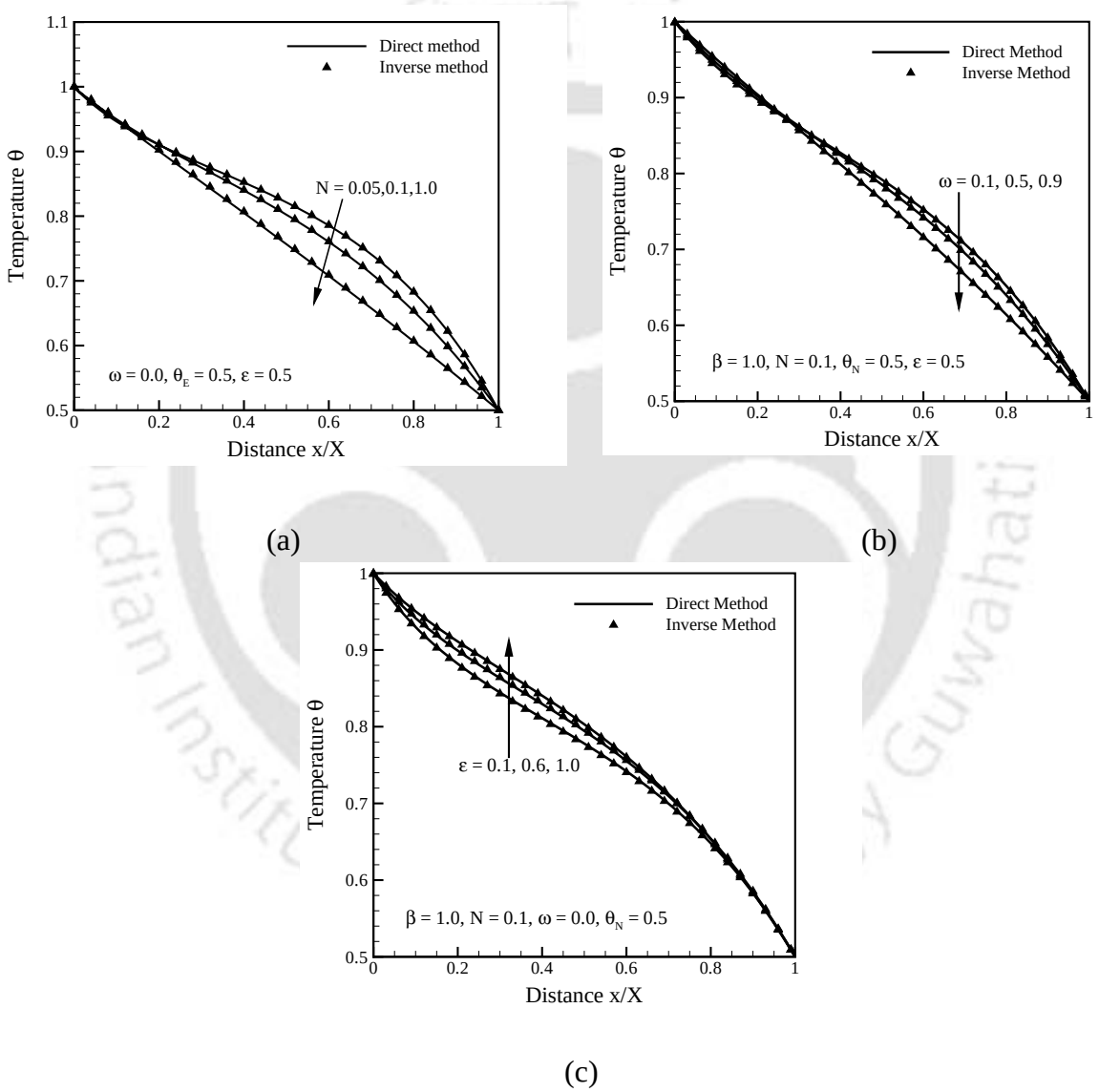

Figure 3.11: Comparison of variation of non-dimensional temperature θ with distance x/X computing using direct method and inverse method for different values of (a) conduction-radiation parameter N, (b) scattering albedo ω and (c) boundary emissivity ε.

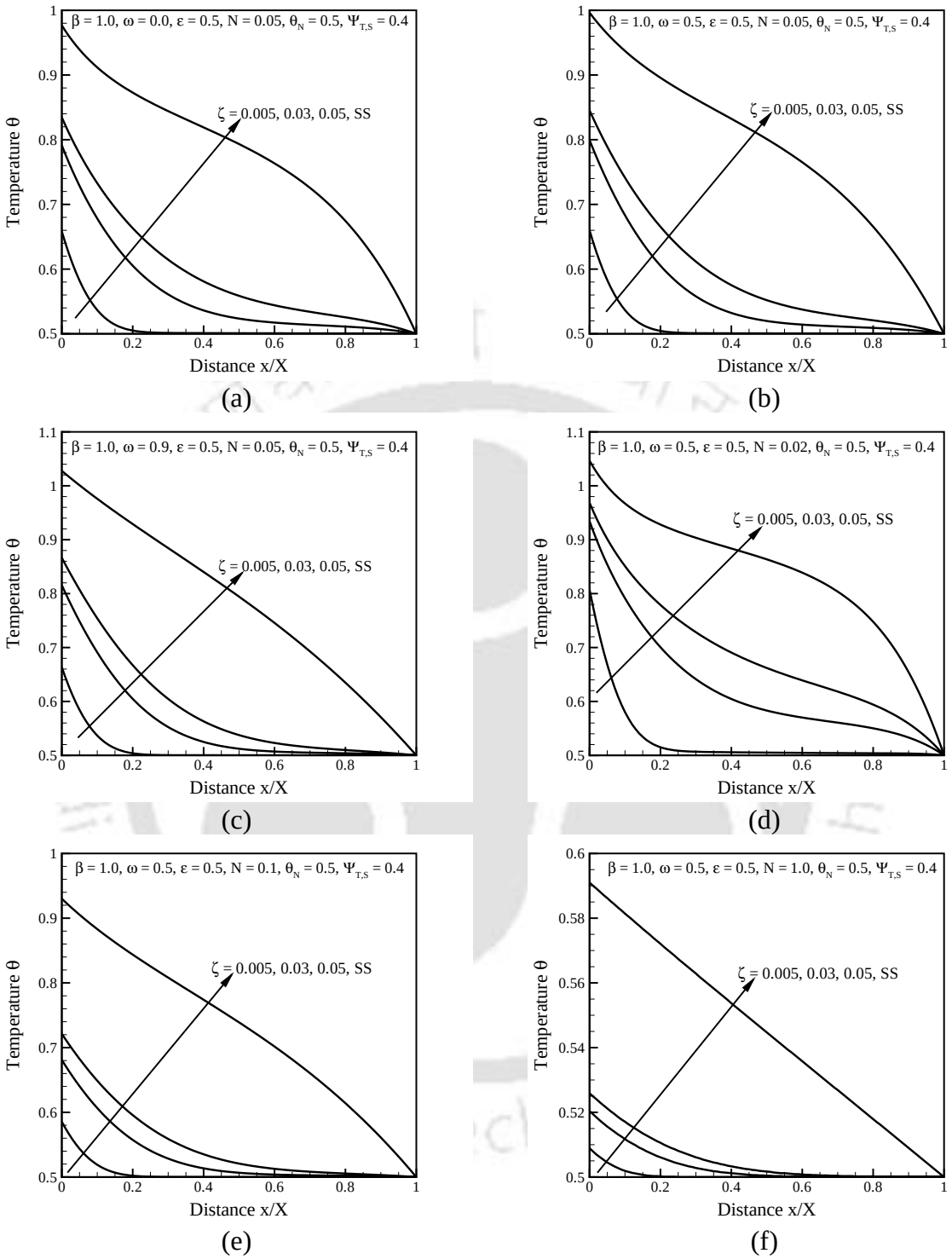

Figure 3.12: Variation of transient non-dimensional temperature θ in the medium for scattering albedo ω (a) 0.0, (b) 0.5 and (c) 0.9; and for conduction-radiation parameter N (a) 0.02, (b) 0.1 and (c) 1.0.

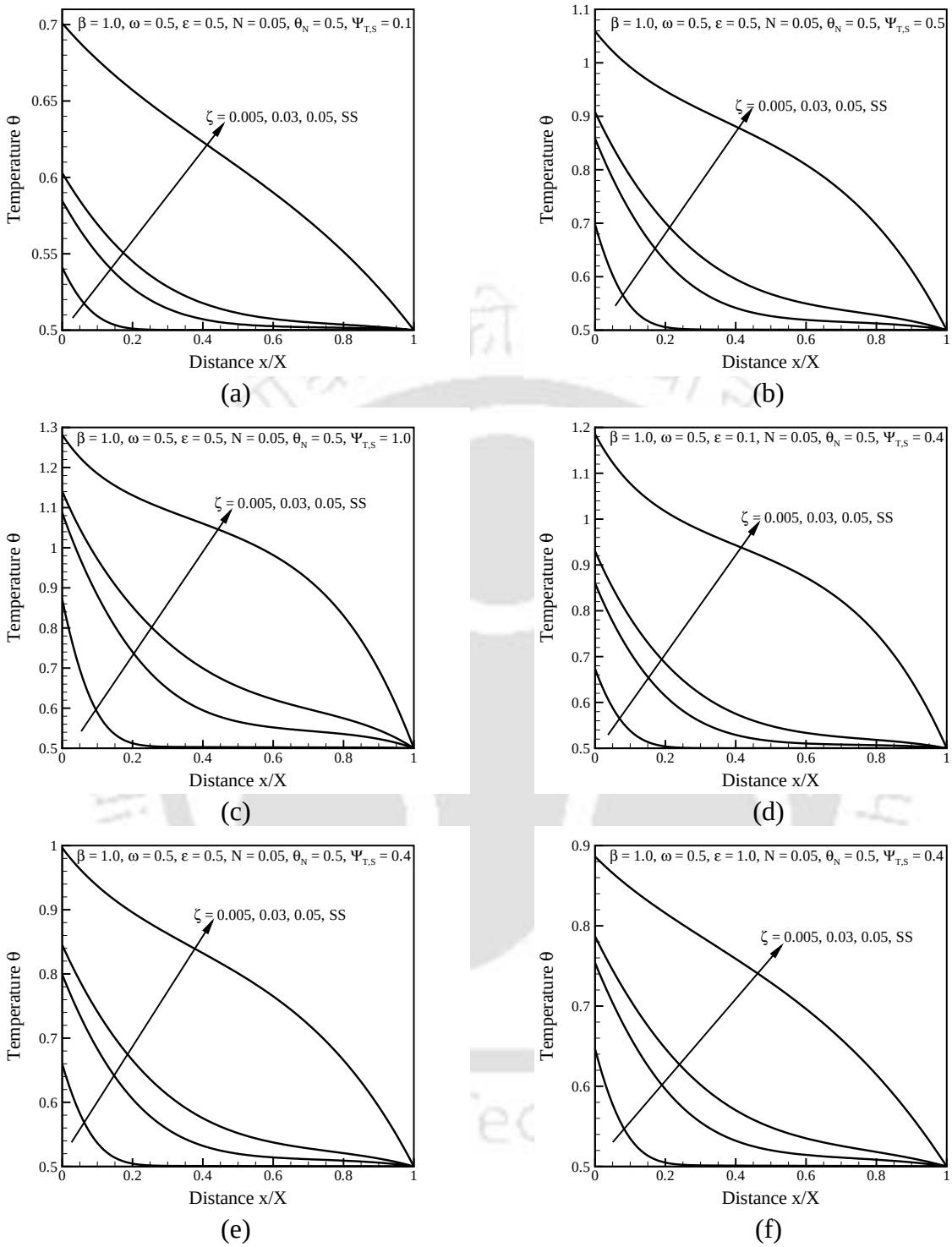

Figure 3.13: Variation of transient non-dimensional temperature θ in the medium for south boundary heat flux $\Psi_{T,S}$ (a) 0.1, (b) 0.5 and (c) 1.0; and for boundary emissivity ε (a) 0.1, (b) 0.5 and (c) 1.0.

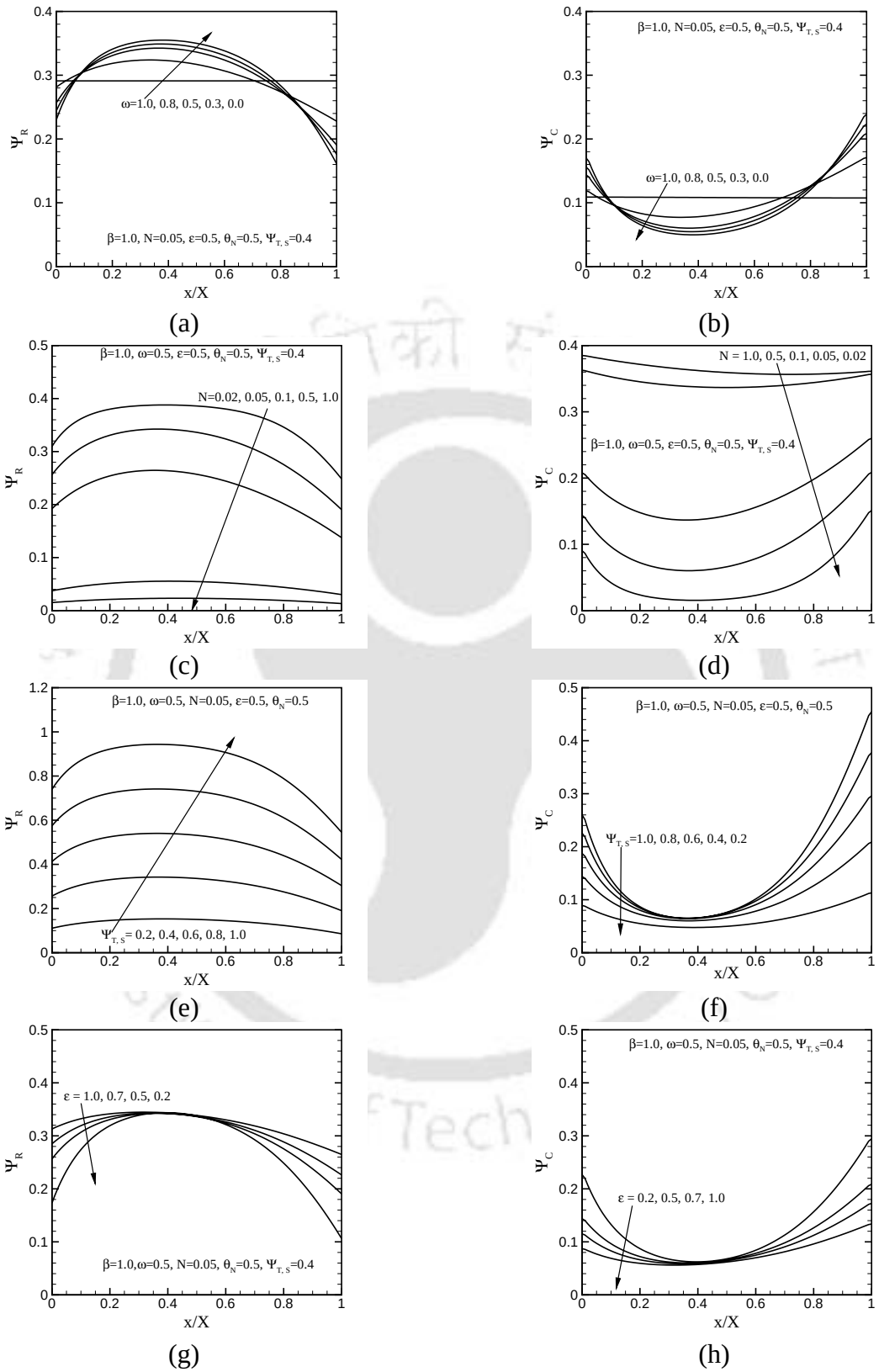

Figure 3.14: Effects of various parameters on radiative heat flux Ψ_R and conductive heat flux Ψ_C.

3.3.4 Conduction-radiation in a 1-D planar medium with heat generation: The effects of heat generation on temperature distribution θ, conductive heat flux ψ_C, radiative heat flux ψ_R and total heat flux ψ_T for various radiative parameters like scattering albedo, conduction-radiation parameter and boundary emissivity are discussed. The boundary conditions are same as the problem considered in case of without heat generation. The non-dimensional heat generation rate is taken as unity.

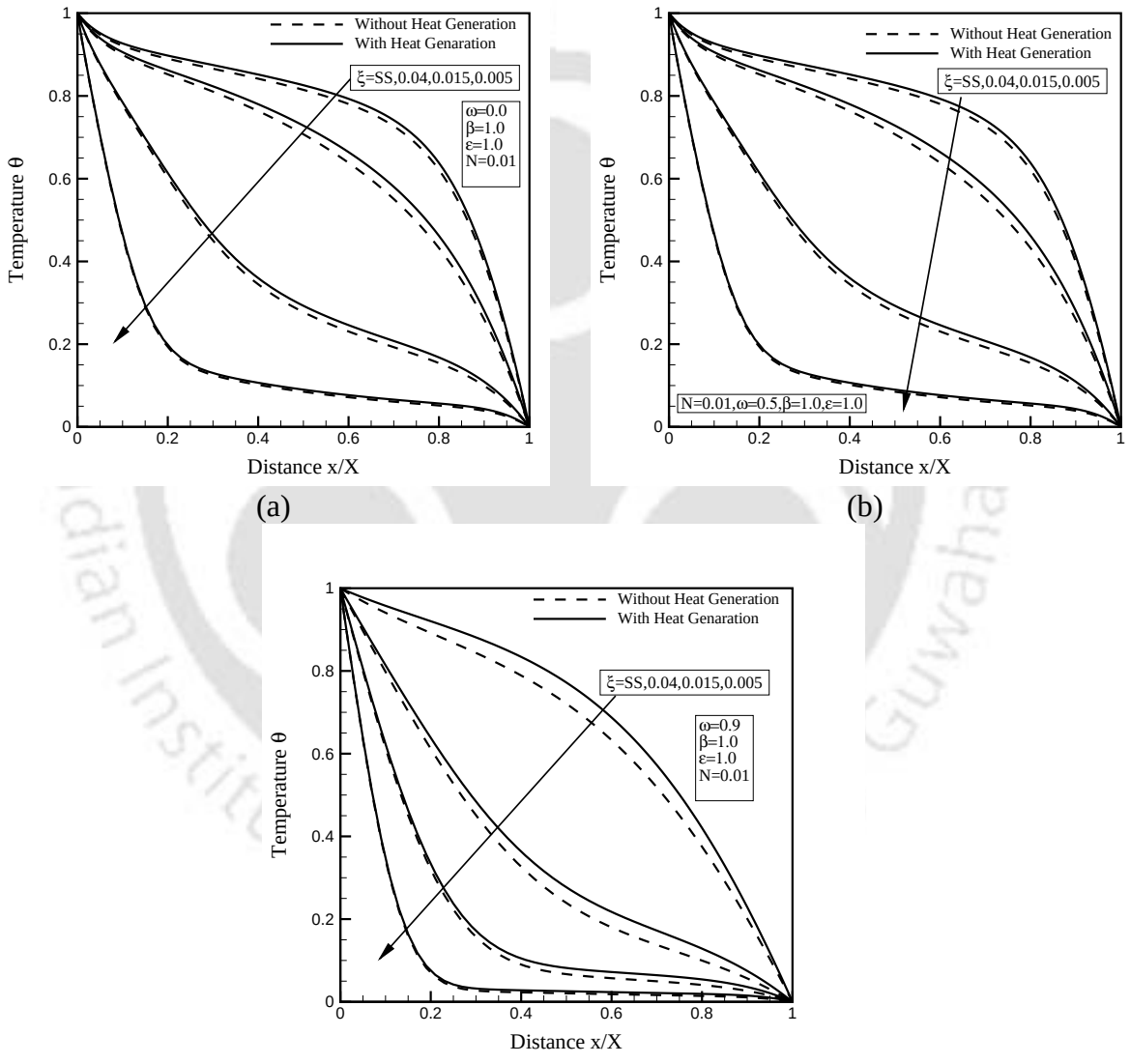

Figure 3.15: Effects of heat generation on temperature θ in a planar medium at different instants ξ for scattering albedo ω = (a) 0.0, (b) 0.5 and (c) 0.9.

In Fig.3.15, The effects of heat generation on temperature distribution at different time ξ have been shown for different values of scattering albedo ω. All other radiative parameters are considered as conduction-radiation parameter $N = 0.01$, extinction coefficient $\beta = 1.0$ and boundaries are black. For higher values of ω, the temperature gradient is high.

The effects of heat generation on temperature distribution for different values of conduction-radiation parameter N are shown in Fig. 3.15 at different time ξ. All other radiative parameters are considered as scattering albedo $\omega = 0.5$, extinction coefficient $\beta = 1.0$ and boundaries are black. For higher values of N (conduction dominated), the third term of Eq. (3.5) is small and effects of heat generation is dominated on temperature distribution. For lower values of N (radiation dominated), the temperature profile does not depend much on heat generation.

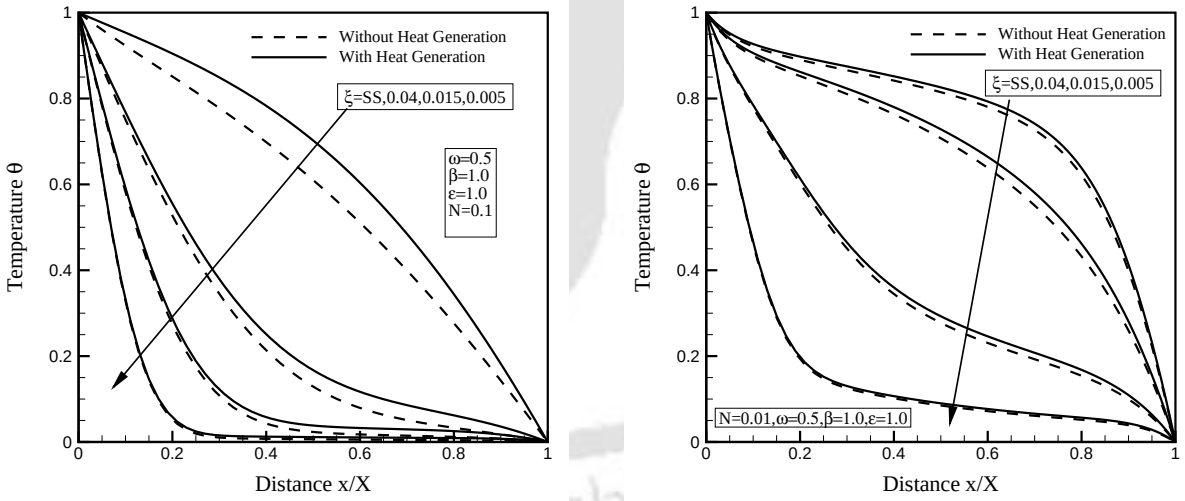

Figure 3.16: Effects of heat generation on temperature θ in a planar medium at different instants ξ for conduction-radiation parameter N = (a) 0.1, (b) 0.01.

The effects of heat generation on temperature distribution for different values of west boundary emissivity ε_W are shown in Fig. 3.17 at different time ξ. All other radiative parameters are considered as $\omega = 0.5$, $\beta = 1.0$, $N = 0.01$ and east boundary is black. As

time increases, the deviation in temperature profile with and without heat generation increases. For lower value of ε_W , the temperature gradient is more near the hot boundary.

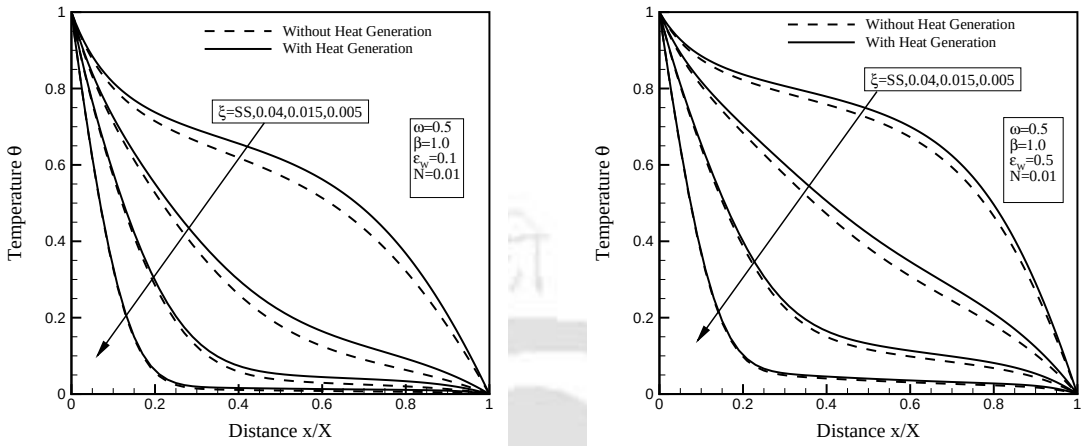

Figure 3.17: Effects of heat generation on temperature θ in a planar medium at different instants ξ for west boundary emissivity ε_W = (a) 0.1, (b) 0.5.

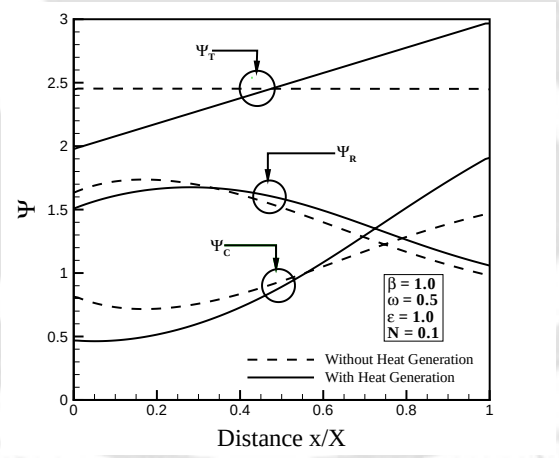

Figure 3.18: Variation of conductive heat flux Ψ_C , radiative heat flux Ψ_R and total heat flux Ψ_T at steady state with and without heat generation.

In Fig.3.18, The effect of heat generation on conductive heat flux ψ_C , radiative heat flux ψ_R and total heat flux ψ_T at steady state condition has been shown for conduction-radiation parameter $N = 0.1$, extinction coefficient $\beta = 1.0$, scattering albedo $\omega = 0.5$ and boundaries are black. Considering the heat generation, conductive heat flux decreases near the hot boundary and increases near the cold boundary because of ψ_C is proportional to the temperature gradient. Similar effect is seen on radiative heat flux also. For without

heat generation, the total heat flux is constant. Since the non-dimensional heat generation is taken as constant throughout the control volume, the total heat flux should be linear variation as increases from hot boundary to cold boundary as shown in Fig 3.17.

3.3 Summary

The LBM was used to solve the energy equation of transient conduction and radiation in a 1-D planar geometry. Four different cases were considered to validate the usage of the LBM in solving the energy equation of transient conduction and radiation heat transfer problems. The variable relaxation time and smallest size lattice based relaxation time were used in the LBM formulation for non-uniform lattices/control volumes. To facilitate collisions to take place at the same instant, linear interpolations of the particle distribution functions were done.

The results with non-uniform size lattices/control (variable relaxation time) volumes were found to compare very well with those with the uniform size lattices/control volumes (constant relaxation time). For various parameters including the clustering parameter, results of the uniform and non-uniform lattices/control volumes were found in good agreements.

LBM-FVM with non-uniform lattices/control volumes were found to take less number of iterations for the steady-state solutions. Transient conduction-radiation problem with heat generation was solved by LBM. The effects of heat generation on temperature distribution θ, conductive heat flux Ψ_C, radiative heat flux Ψ_R and total heat flux Ψ_T for various radiative parameters like scattering albedo, conduction-radiation parameter and boundary emissivity were analyzed. It was shown that with heat generation, it took less time to converge. Comparison of results showed very good agreement with those available in literature. The next chapter deals with the 2-D conduction-radiation problems.

CHAPTER 4

2-D Conduction-Radiation Problems

4.1 Introduction

Application of the LBM in solving energy equations of heat transfer problems involving thermal radiation was extended by Mishra and co-workers [22, 87, 88, 100, 140, 141]. Mishra and Lankadasu [22] applied the LBM to solve the energy equation of transient conduction and radiation heat transfer in a planar medium with or without heat generation. They used the DTM to compute the radiative information. Raj *et al.* [87] used the LBM to analyze the solidification of a semitransparent planer layer. They used the DTM to compute the radiative information. Parida *et al.* [140] extended the work of Raj *et al.* [87] by considering radiative and convective cooling along the boundaries and used the DOM for the radiative information. Gupta *et al.* [88] used a variable relaxation time LBM to solve the energy equation of a temperature dependent transient conduction and radiation heat transfer in a planer medium. They used the DOM to compute the radiative information. Mishra and Roy [100] used the LBM to solve conduction-radiation problems in 1-D and 2-D rectangular geometries and used the FVM to compute the radiative information. Mondal and Mishra [141] solved the same problems as those of [100] using the LBM and the DOM. In all the previous applications of the LBM to heat transfer problems [18-23, 39, 87, 88, 100, 140-142], uniform size lattices/control volumes were used in the LBM.

In this chapter, the LBM is used to solve the energy equations of transient conduction and radiation problems in a 2-D rectangular geometry on non-uniform lattices. Different types of lattice clustering are used to test the workability of the LBM to this class of problems with both Dirichlet and Neumann boundary conditions. Since the FVM [100, 109] is more suitable to all types of control volumes than other methods like the DTM, the DOM etc. of the radiative transfer, in the present work, we too have adopted the FVM to compute the radiative information for the energy equation. To check the performance of the LBM-FVM on non-uniform lattices/control volumes, the same problems are also solved for the uniform lattices/control volumes. Effects of heat generation are also considered. Results have been compared for different values of the scattering albedo, the boundary emissivity, the conduction radiation parameter and the clustering parameter.

4.2 Formulation

Let us consider a 2-D radiating and conducting homogeneous rectangular medium that is initially at temperature T_E (Figure 4.1). For time $t > 0$, its south boundary is maintained at temperature $T_S > T_E$. In the presence of heat generation, energy equation for the problem under consideration is given by

$$\rho c_p \frac{\partial T}{\partial t} = k\nabla^2 T - \nabla \vec{q}_R + Q''' \tag{4.1}$$

where the density of the medium is ρ, c_p is the specific heat at constant pressure, T is the dimensional temperature of the medium, t is the time, k is the thermal conductivity, $\vec{q}_R$ is the radiative heat flux and Q''' is the volumetric heat generation.

If the west boundary temperature is considered as the reference temperature and the non-dimensional parameters are defined as

$$\theta = \frac{T}{T_{ref}}, \quad \Psi_R = \frac{q_R}{\sigma T_{ref}^4}, \quad \xi = \frac{t}{\frac{\rho c_p}{k\beta^2}} = \frac{k\beta^2 t}{\rho c_p} = \alpha\beta^2 t, \quad Q^* = \frac{Q'''}{k\beta^2 T_{ref}} \tag{4.2}$$

where θ is the non-dimensional temperature, Ψ_R is the non-dimensional radiative heat flux, ξ is the non-dimensional time and Q^* is the non-dimensional volumetric heat generation.

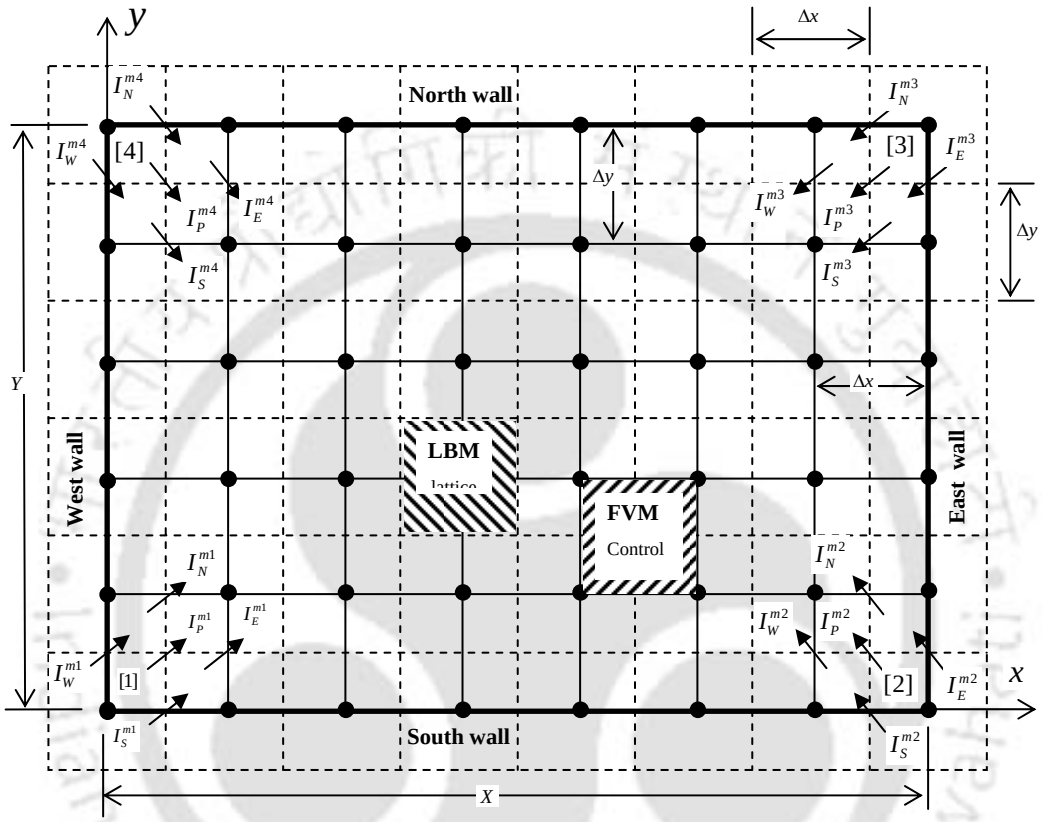

(a)

Figure 4.1: Arrangement of lattices in the LBM and control volumes in the FVM in a 2-D rectangular geometry along with marching scheme in the FVM for four equally spaced sample directions with one in every quadrant.

Using these non-dimensional parameter in Eq. (4.1), the resulting dimensionless equation can be written as

$$\frac{\partial \theta}{\partial \xi} = \frac{\partial^2 \theta}{\partial x^2} + \frac{\partial^2 \theta}{\partial y^2} - \frac{1}{4N} \nabla \vec{\Psi}_R + Q^* \qquad (4.3)$$

where the non-dimensional conduction-radiation parameter is defined as $N = \frac{k\beta}{4\sigma T_{ref}^3}$. To solve the above equation, information about the divergence of radiative heat flux is calculated using the FVM. Thus, the Eq.(4.3) can be written as

$$\frac{\partial \theta}{\partial \xi} = \frac{\partial^2 \theta}{\partial x^2} + \frac{\partial^2 \theta}{\partial y^2} - \frac{(1-\omega)}{N}\left[\theta^4 - \frac{G^*}{4\pi}\right] + Q^* \tag{4.4}$$

where ω is the scattering albedo and G^* is the non-dimensional irradiation. This governing transient energy equation is solved by the LBM. So the desired equation to be used in the LBM is given by

$$\begin{aligned} f_i(\vec{r}+\Delta\vec{r}, \xi+\Delta\xi) = {} & f_i(\vec{r},\xi) - \frac{\Delta\xi}{\tau}\left[f_i(\vec{r},\xi) - f_i^{(eq)}(\vec{r},\xi)\right] \\ & - \Delta\xi \times w_i \frac{(1-\omega)}{N}\left[\theta^4 - \frac{G^*}{4\pi}\right] + \Delta\xi \times w_i \times Q^* \end{aligned} \tag{4.5}$$

The procedure to calculate radiative information using the FVM has been discussed in chapter 2. For solving the energy equation (Eq. (4.5)) on non-uniform lattices, the maximum relaxation time is calculated in the same way as calculated in case of 1-D planer medium.

4.3 Results and Discussion

The following three cases are considered to validate the usage of the LBM on non-uniform lattices in solving the energy equations of transient conduction and radiation heat transfer problems:

- **Conduction-radiation in a 2-D square medium with non-uniform lattices:** Initially the 2-D square enclosure is cold. Suddenly the temperature of the south boundary is raised to T_S and for all times $t \geq 0$ it is maintained at this temperature. The boundaries of the

absorbing, emitting and scattering medium are diffuse gray. Thermo-physical and optical properties are considered constant.

- **Conduction-radiation in a 2-D square medium with flux boundary condition:** The gray homogeneous 2-D square absorbing, emitting and isotropically scattering participating medium (Fig. 2a) is initially at temperature T_E. Its boundaries are diffuse-gray. At time, $t > 0$,
    - the south boundary is kept at heat flux $q_{T,S}$ and rest of the three boundaries remain at temperature T_E.
    - the heat flux at the south and the north boundaries are $q_{T,S}$ and $q_{T,N}$, respectively, and rest of the two boundaries remain at temperature T_E.
- **Conduction-radiation in a 2-D square medium with heat generation:** Initially the 2-D planar conducting and radiating participating medium is at a temperature T_0. Suddenly the south boundary is brought to a temperature $T_S = 2T_0$ and for all times $t \geq 0$, it is maintained at this temperature. The boundaries of the absorbing, emitting and scattering medium are diffuse gray. Thermo-physical and optical properties are considered constant. The non-dimensional heat generation rate is taken as unity.

4.3.1 Conduction-radiation in a 2-D square medium with non-uniform lattices: To validate the LBM-FVM on non-uniform lattices/control volumes, next we consider transient conduction and radiation heat transfer in a 2-D square enclosure (Fig. 4.1). In this case, initially the entire system is at a temperature $T_0 = T_N = T_W = T_E$. For $t > 0$, the south boundary temperature is raised to $T_S = 2T_0$. The enclosed gray-homogeneous medium is absorbing, and isotropically scattering.

The non-uniform size lattices/control volumes were generated from the following expressions

$$x_n = \left\{ \frac{\text{n-1}}{\text{N}_x} + \frac{C_x}{\pi} \sin\left(\frac{\pi(\text{n-1})}{\text{N}_x} \right) \right\} \tag{26}$$

$$y_n = \left\{ \frac{\text{n-1}}{\text{N}_y} + \frac{C_y}{\pi} \sin\left(\frac{\pi(\text{n-1})}{\text{N}_y} \right) \right\} \tag{27}$$

where x_n and y_n are the location of the lattice centre in the LBM and the control volume corner in the FVM in the $x-$ and $y-$ directions, respectively. N_x and N_y are the total number of lattices/control volumes in the $x-$ and $y-$ directions, respectively and $C_x \left(0 \le |C_x| \le 1\right)$ and $C_y \left(0 \le |C_y| \le 1\right)$ are parameter that determines clustering. For the four different sets of C_x and C_y, the 2-D lattices are shown in Fig. 4.2a-d. With $C_x = 0$ and $C_y = 0$, uniform size lattices/control volumes are obtained (Fig. 4.2a). In the present work, numerical experiments were performed for the four different types of lattices shown in Fig. 4.2a-d.

In the 2-D case too, like the 1-D case, the non-dimensional time step $\Delta\zeta = 1.0 \times 10^{-4}$ was considered and steady-state condition was assumed to have been achieved when the maximum variation in temperature $\theta = \frac{T}{T_S}$ at any location between two consecutive time levels did not exceed 1.0×10^{-6}. No significant changes in results were observed beyond 21×21 lattices in the LBM and 20×20 control volumes and 8×8 directions over the spherical space in the FVM. The numbers of lattices/control volumes and directions were same in both LBM-FVM with uniform and non-uniform lattices/control volumes.

In Table 4.1, for the three values of the extinction coefficient $\beta = 0.1, 1.0$ and 5.0, and the three values of the conduction-radiation parameter $N = 0.01, 0.1$ and 1.0, with scattering albedo $\omega = 0.0$, the LBM-FVM centerline $\left(\frac{x}{X} = 0.5\right)$ non-dimensional temperature θ results at three $\frac{y}{Y}$ locations for uniform and non-uniform lattices/control volumes of the

LBM-FVM are compared with those of Yuen and Takara [143], Wu and Ou [144] and Mishra *et al*. [145]. It can be seen that the LBM-FVM results for uniform and non-uniform lattices/control volumes are in good agreement with those available in the literature [143-145].

Table 4.1: Comparison of steady-state centerline $\left(x/X = 0.5\right)$ temperature at three locations in a black square enclosure; $\omega = 0.0, \beta = 1.0$.

β	N	Centreline T/T_S at y/Y	Wu and Ou [144]	Yuen and Takara [143]	Mishra *et al.* [145]	Uniform lattices / control volumes	Non-uniform lattices / control volumes
0.1	0.1	0.3	0.733	0.733	0.734	0.734	0.741
		0.5	0.626	0.630	0.626	0.626	0.633
		0.7	0.561	0.563	0.561	0.561	0.566
1.0	1.0	0.3	0.733	0.737	0.737	0.737	0.734
		0.5	0.630	0.630	0.630	0.630	0.638
		0.7	0.560	0.560	0.564	0.564	0.570
1.0	0.1	0.3	0.760	0.763	0.759	0.759	0.766
		0.5	0.663	0.661	0.663	0.664	0.674
		0.7	0.590	0.589	0.594	0.596	0.604
1.0	0.01	0.3	0.791	0.807	0.789	0.784	0.784
		0.5	0.725	0.726	0.725	0.726	0.728
		0.7	0.663	0.653	0.666	0.678	0.682
5.0	0.1	0.3	0.834	0.802	0.802	0.800	0.803
		0.5	0.689	0.707	0.708	0.706	0.711
		0.7	0.585	0.626	0.628	0.625	0.631

In the following paragraphs, centerline $\left(\frac{x}{X}=0.5\right)$ non-dimensional temperature θ along $\frac{y}{Y}$ and for the steady state solutions, the numbers of iterations with uniform and non-uniform lattices/control volumes of the LBM-FVM are compared for the effects of various parameters including the clustering value. In Figs. (4.3-4.5), the results are shown for cluster value 0.5 and the fine grids are used near the each boundary.

In Fig. 4.3, for $\beta=1.0$ and $N=0.01$, temperature $\theta\left(T/T_S\right)$ computed from the LBM-FVM with uniform and non-uniform lattices/control volumes have been compared for the effects of the scattering albedo ω. It can be seen from the figure that at all times ζ, the results of the non-uniform and uniform lattices are in good agreements. The number of iterations for the steady-state solutions with non-uniform lattices/control volumes for ω = 0.0, 0.5 and 0.9 were 881, 1220 and 2477. The same with uniform lattices/control volumes were found to be 872, 1204 and 2418.

In Fig. 4.4, for $\omega=0.0$ and $\beta=1.0$, comparisons of temperature θ have been shown for three values of the conduction-radiation parameter N. It is seen that for both radiation dominated $(N=0.01)$ and conduction dominated $(N=1.0)$ cases, result for the steady state condition with non-uniform lattices/control volumes match well with those with uniform lattices/control volumes. For non-uniform lattices/control volumes, the numbers of iterations for the steady-state results were found to be 881, 2837 and 3566 for $N=0.01$, 0.01 and 0.1, respectively. The same for uniform lattices/control volumes were found to be 872, 2764 and 3469.

In Fig. 4.5, for $\beta=1.0, \omega=0.0$ and $N=0.01$, comparisons of temperature θ have been made for different values of the south boundary emissivity ε_S. Other three boundaries are taken black. It is seen that at all times, results with non-uniform lattices/control volumes compare very well with those of the non-uniform lattices/control volumes. For ε_W =0.1,

0.5 and 0.9, number of iterations with non-uniform lattices/control volumes were 1060, 974 and 898 respectively. The same for the uniform lattices/control volumes case were 1048, 963 and 888.

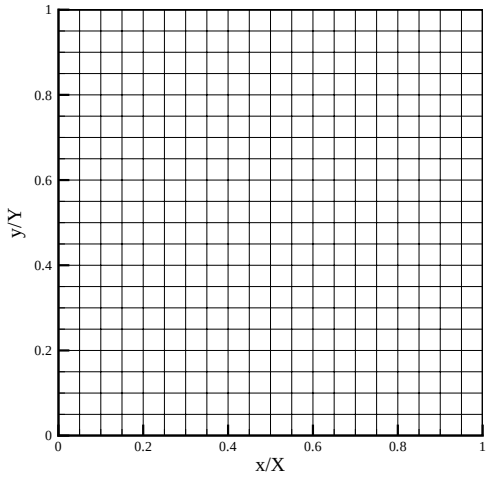

(a) $C_x = 0.0 \text{ and } C_y = 0.0$

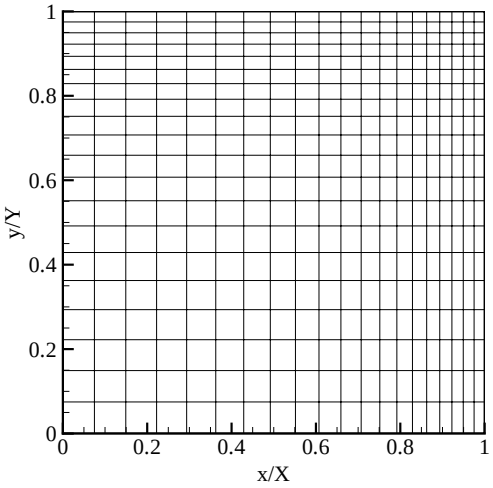

(b) $C_x = 0.5 \text{ and } C_y = 0.5$

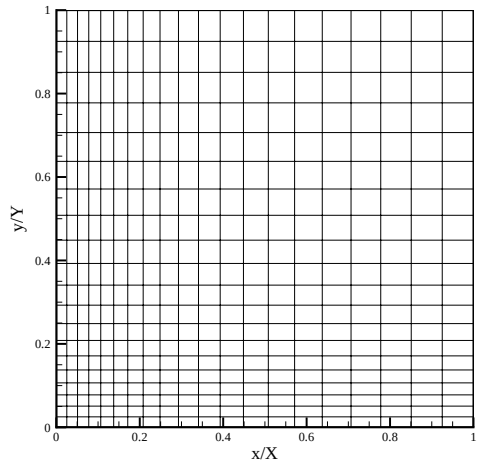

(c) $C_x = -0.5 \text{ and } C_y = -0.5$

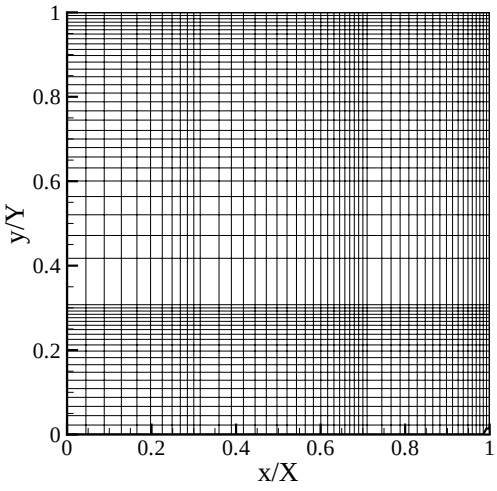

(d)

$$C_x = C_y = 0.5 \begin{cases} 0.0 \le \frac{x}{X}, \frac{y}{Y} \le 0.3, N_x = N_y = 10 \\ 0.3 \le \frac{x}{X}, \frac{y}{Y} \le 0.7, N_x = N_y = 20 \\ 0.7 \le \frac{x}{X}, \frac{y}{Y} \le 1.0, N_x = N_y = 20 \end{cases}$$

Figure 4.2: Different types of non-uniform lattices for 2-D geometry

With $\beta = 1.0, \omega = 0.0$ and $N = 0.01$ with all four boundaries black, in Fig. 4.6, temperature θ results have been compared for the four sets of clustering parameter $C_x = C_y = C$. In this figure, C = 0.0, stands for uniform lattices/control volumes. It is observed at three time levels including the steady-state, results for all values of C are in good agreements.

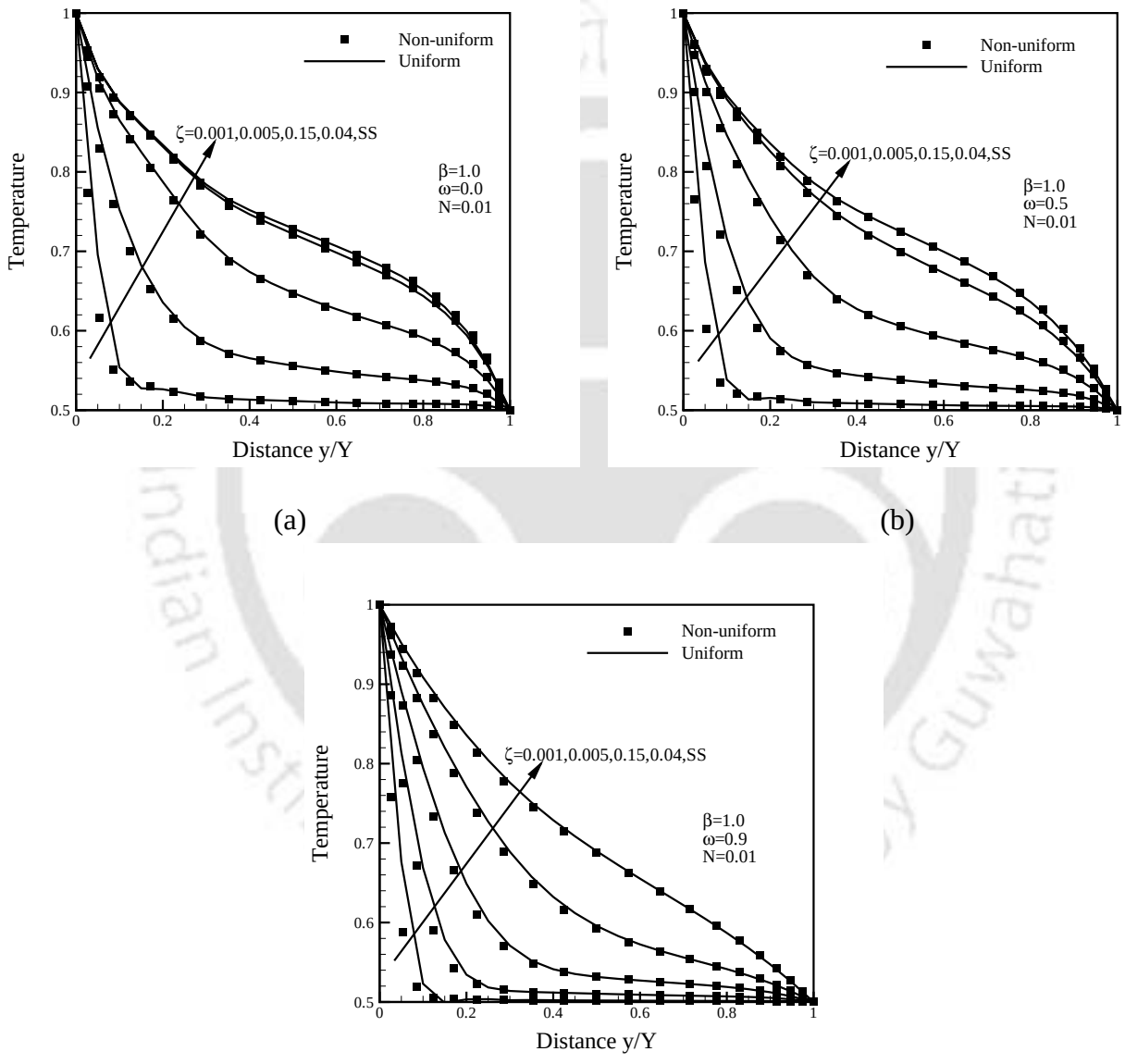

Figure 4.3: Comparison of centreline temperature θ in a 2-D square enclosure at different instants ζ for scattering albedo ω = (a) 0.0, (b) 0.5 and (c) 0.9.

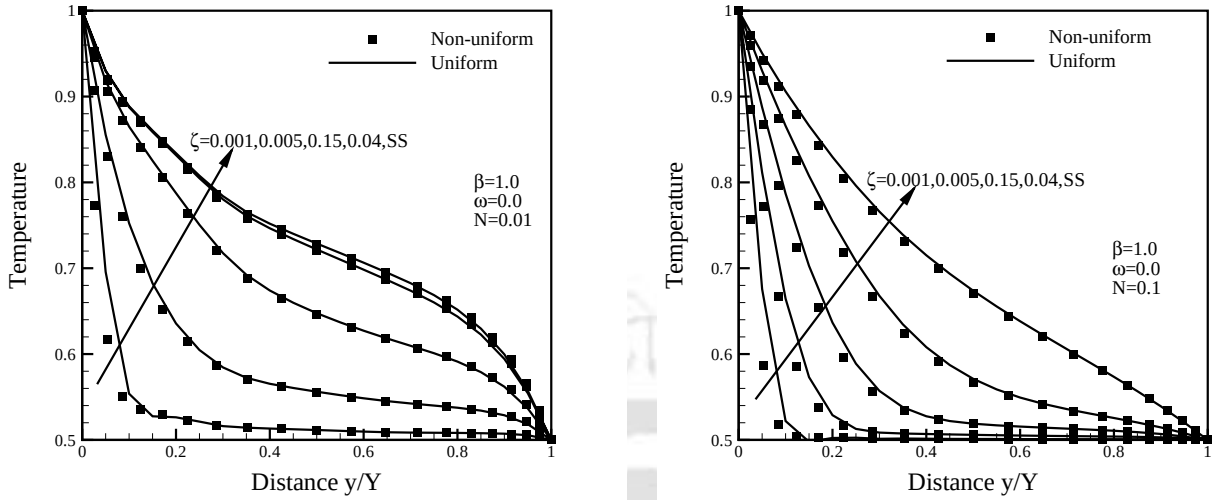

(a)

(b)

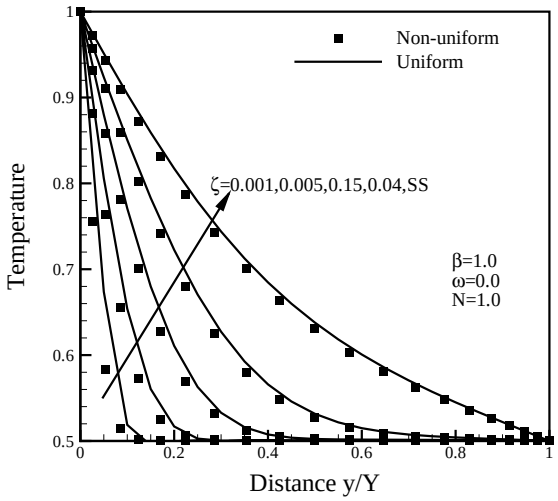

(c)

Figure 4.4: Comparison of centreline temperature θ in a 2-D square enclosure at different instants ζ for conduction-radiation parameter N = (a) 0.01, (b) 0.1 and (c) 1.0.

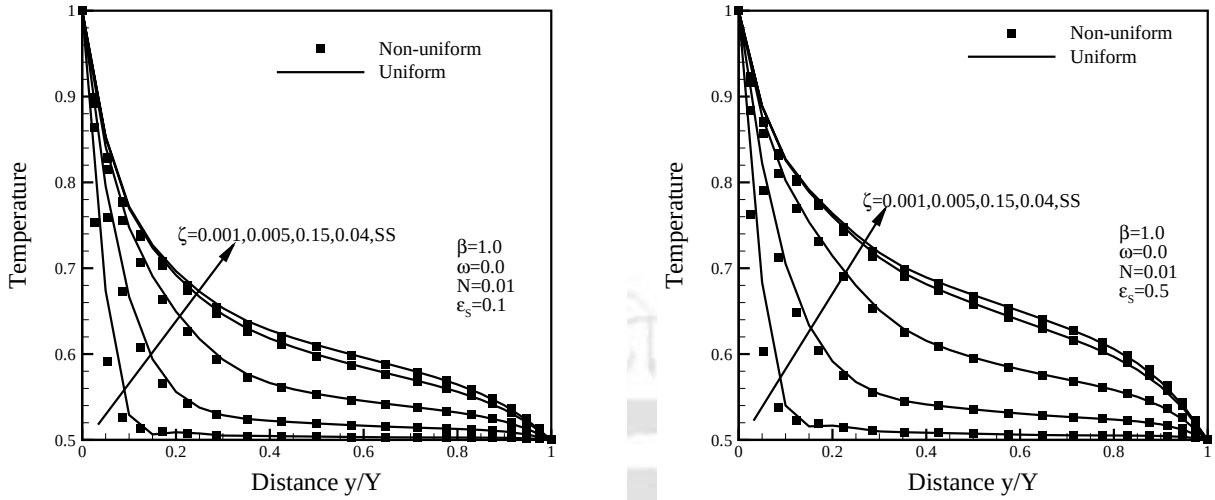

(a)

(b)

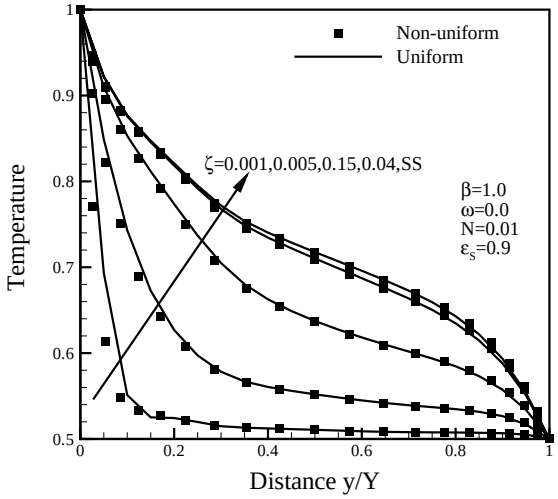

(c)

Figure 4.5: Comparison of centreline temperature θ in a 2-D square enclosure at different instants ζ for (a) emissivity of the south boundary ε_S = 0.1, (b) 0.5 and (c) 0.9.

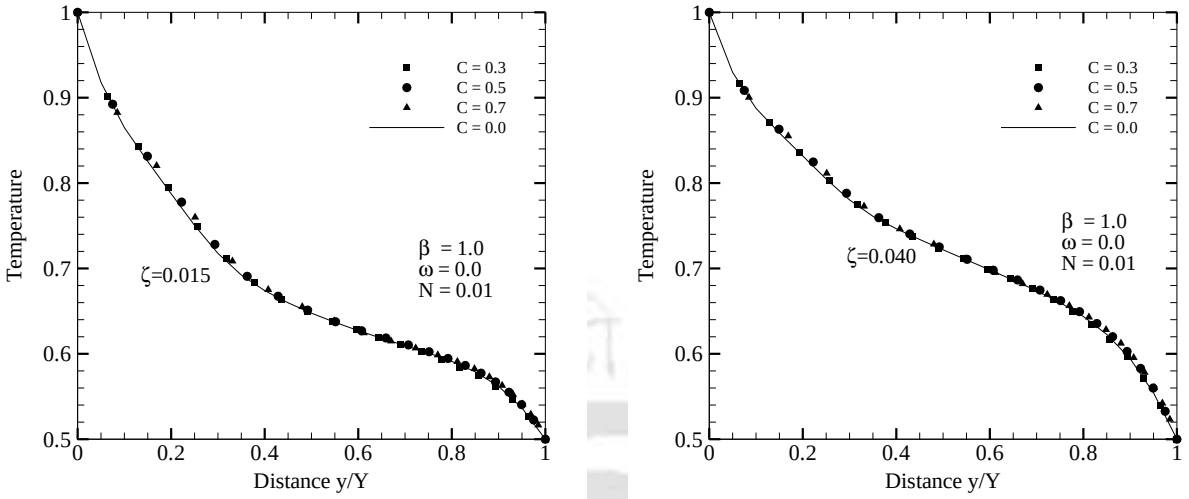

(a)

(b)

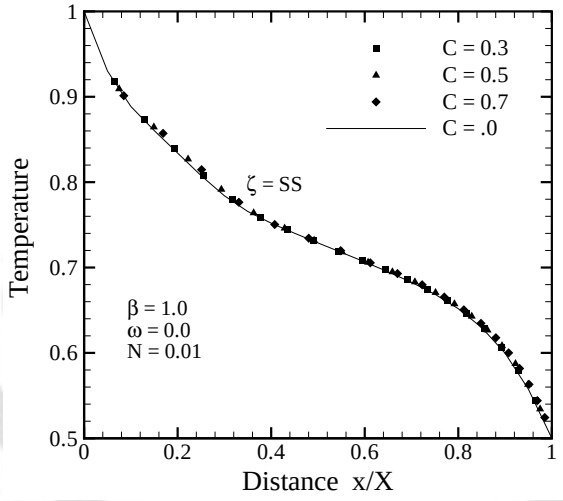

(c)

Figure 4.6: Comparison of centreline temperature θ in a 2-D square enclosure at steady state for different types of lattices using quadratic interpolation scheme at non-dimensional time (a) $\zeta = 0.015$, (b) $\zeta = 0.040$ and (c) steady state.

4.3.2 Results of conduction-radiation problem in a 2-D square medium: In Figs. 4.7a-e, we establish the validity of our formulation by comparing results of centerline $\left(\frac{x}{X}=0.5,\frac{y}{Y}\right)$ temperature $\theta=\frac{T}{T_{ref}}$ of the direct and inverse methods. Results of the direct method in all the cases have been validated against benchmark results given in references [143-145]. In each of the Figs. 4.7a-e, for a given set of parameters, the south boundary heat flux $\Psi_{T,S}$ distribution is computed using the direct method, which in the inverse method serves as the imposed heat flux boundary condition at the south boundary.

In Figs. 4.7a and 4.7b, for conduction-radiation parameter $N=0.1$ and 0.01, respectively, comparison of the centreline temperature θ in the direct and inverse methods have been shown for the effect of the extinction coefficient β. Fig. 4.7c shows the comparison for the effect of the scattering albedo ω. In Figs. 4.7d and 4.7e, results of the direct and inverse methods have been compared for the effects of the conduction-radiation parameter N and emissivity of the south boundary ε_S. It is to be noted that for results in Fig. 4.7e, except the south boundary, rest all three boundaries are black. It is seen from Figs. 4.7a-e that in all the cases, results of the centreline temperature θ from the inverse and direct methods match with each other very well.

In Fig. 4.8, effects the imposed heat flux $\Psi_{T,S}$ at the south boundary on centreline temperature θ are shown for $\beta=1.0,\omega=0.0,N=0.01$. In this case, all boundaries are black and temperatures of the west, east and north boundaries are at constant, $\theta_N=\theta_E=\theta_W=0.5$. With increase in $\Psi_{T,S}$, medium gets more energy and hence at all locations including the south boundary, temperature increases. Further, non-linearity in the temperature profile is more for a higher value of $\Psi_{T,S}$. In Fig 4.8a and 4.8b, the transient

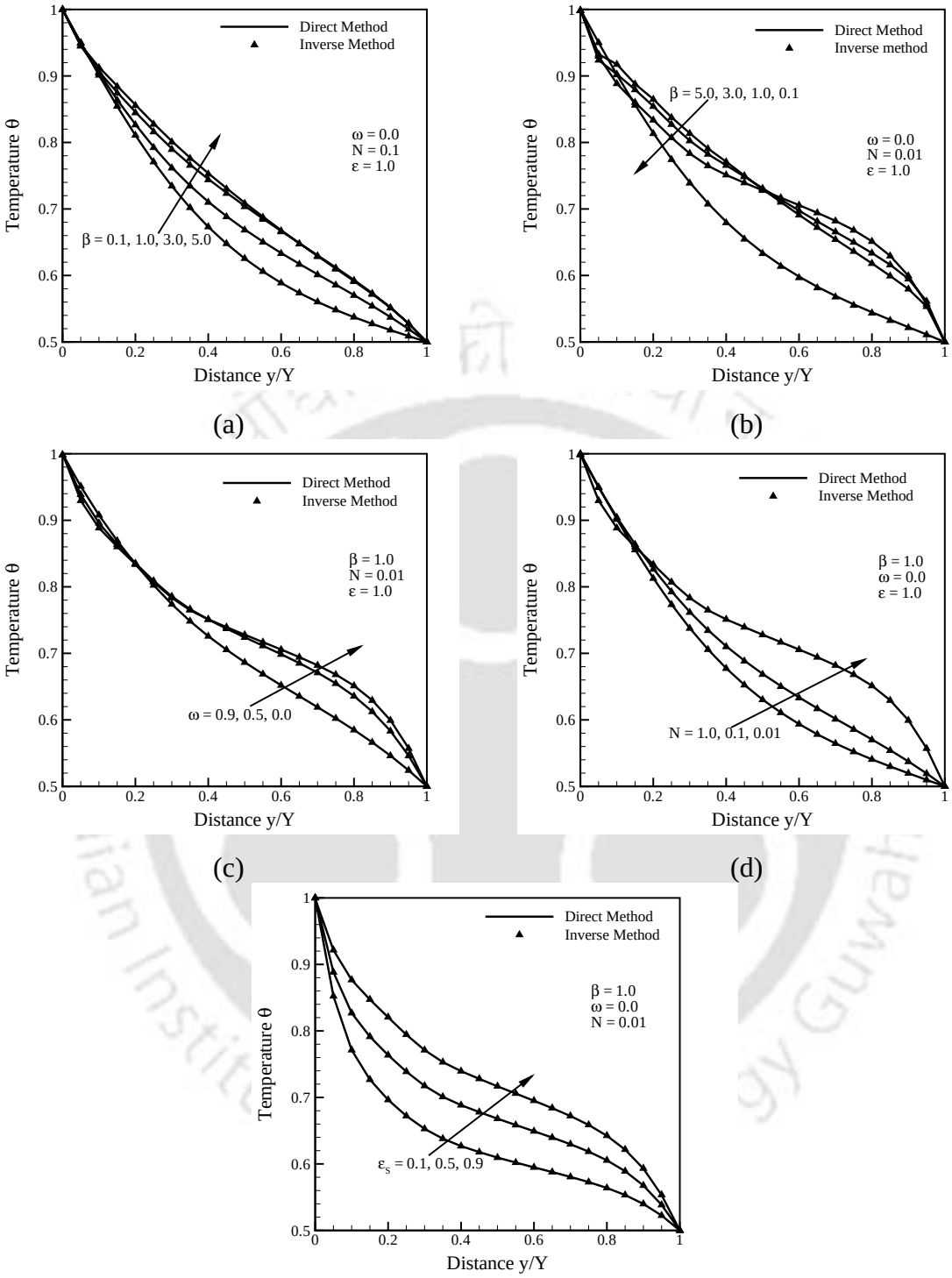

Figure 4.7: Comparison of on centreline $\left(\frac{x}{X}=0.5,\frac{y}{Y}\right)$ temperature θ in direct and inverse methods for various parameters in a 2-D square geometry.

temperatures at $\zeta = 0.05$ reach very close to the steady state. When the imposed heat flux increases, the transient temperatures at $\zeta = 0.05$ converge with the steady state condition (Figs. 4.8c-e).

By keeping the value of the imposed heat flux at the south boundary constant $\Psi_{T,S} = 1.0$, in Fig. 4.9, effect of the imposed heat flux on the north boundary $\Psi_{T,N}$ on centreline temperature θ are shown for $\beta = 1.0, \omega = 0.0, N = 0.01$. In this case too, the four boundaries are black. Temperature θ profiles have been plotted at time $\zeta = 0.005, 0.03$ and SS. It is observed from Fig. 4.9b that when $\Psi_{T,S} = \Psi_{T,N} = 1.0$, the centreline temperature profile θ is symmetric about the horizontal mid-plane $\left(\frac{x}{X}, \frac{y}{Y} = 0.5\right)$. Since in this case, east and the west boundaries are at constant temperature, $\theta_E = \theta_W = 0.5$, the above observation is correct. When $\Psi_{T,N} > \Psi_{T,S}$ (Figs. 4.9c-e), temperature at the north boundary will be more than that at the south boundary. Opposite is the case when $\Psi_{T,N} < \Psi_{T,S}$ (Fig. 4.9a).

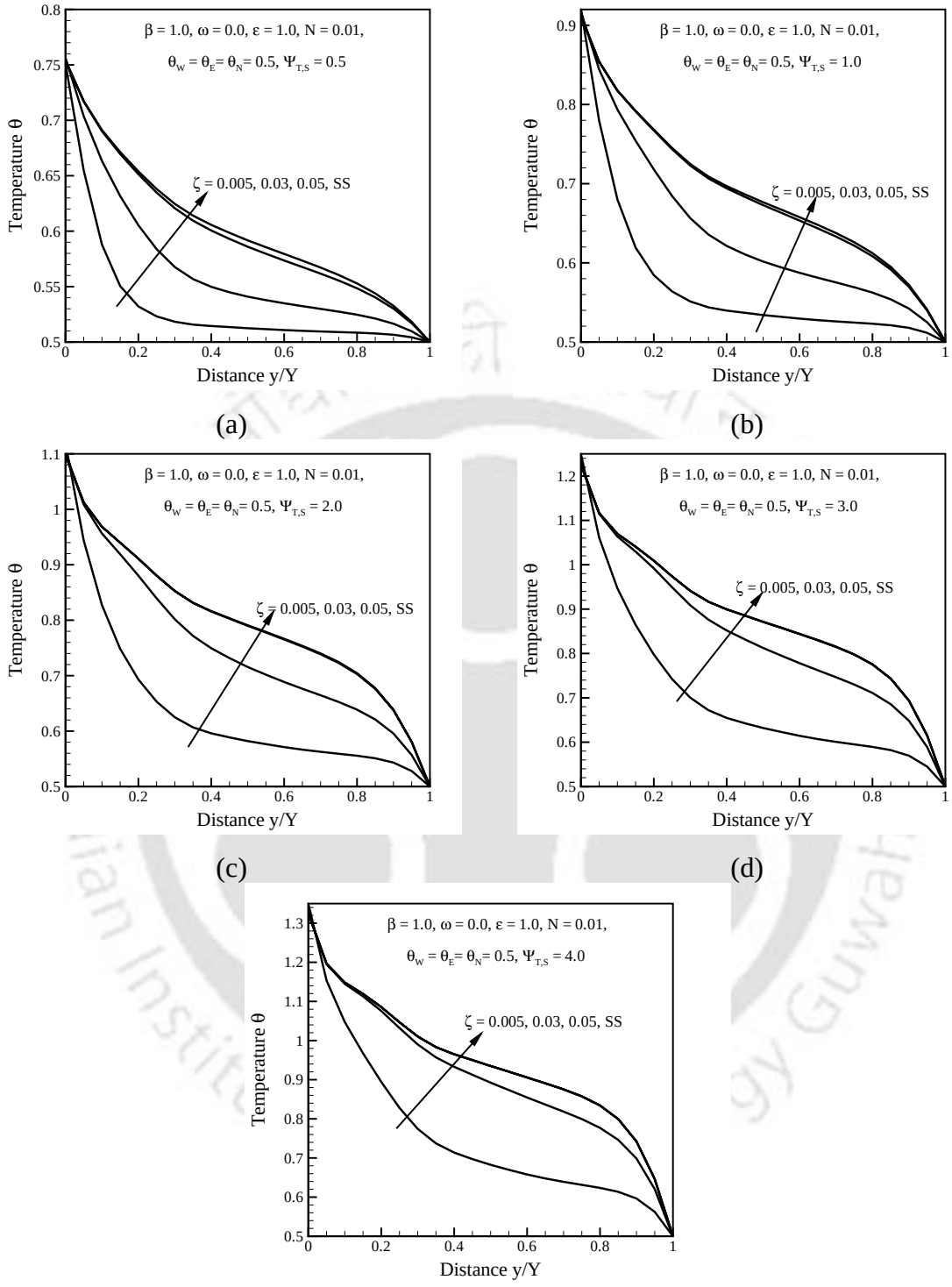

Figure 4.8: Effects of imposed south boundary heat flux ($\Psi_{T,S}$) on centreline $\left(\frac{x}{X}=0.5,\frac{y}{Y}\right)$ temperature θ in a 2-D square geometry.

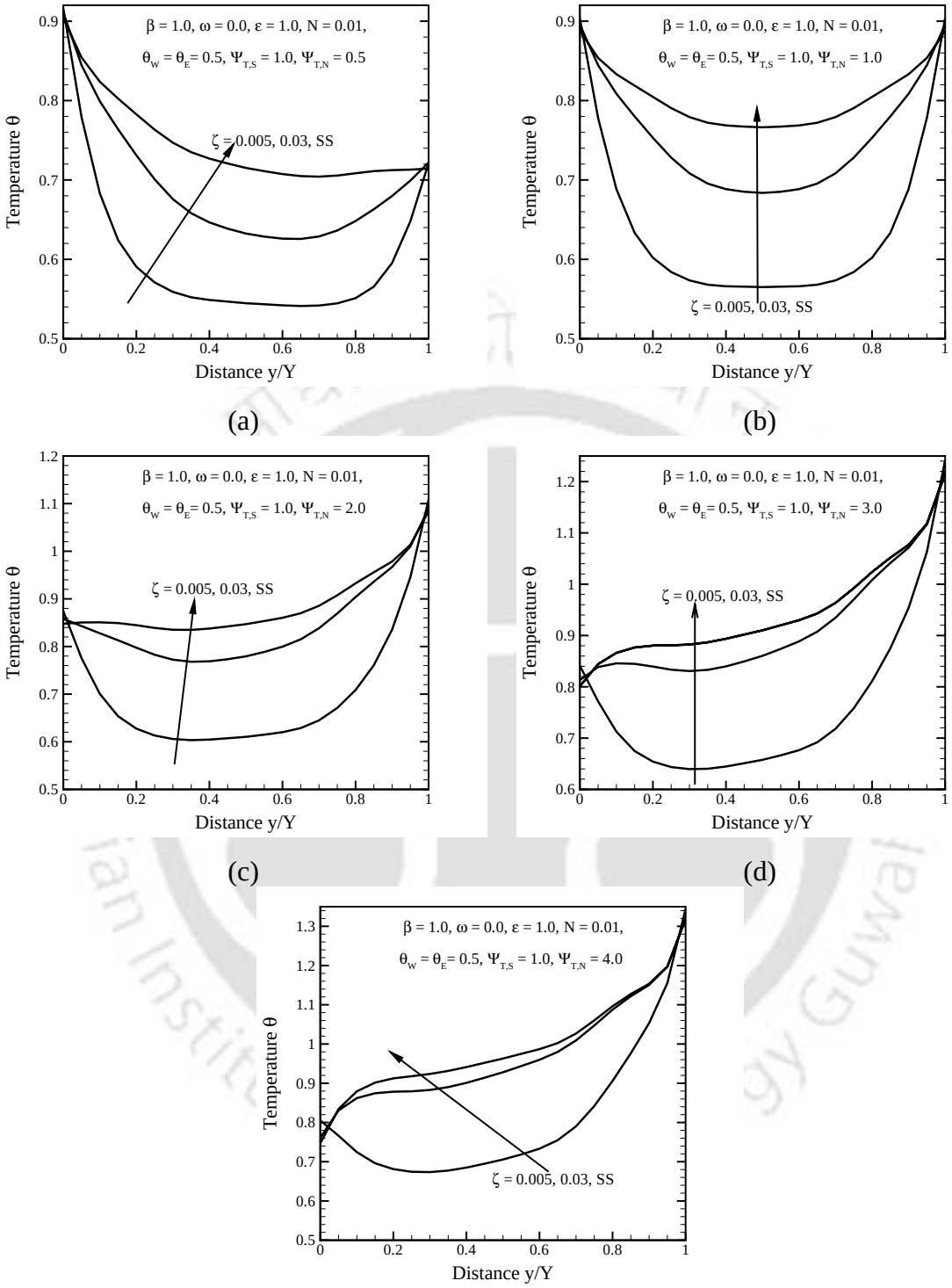

Figure 4.9: Effects of imposed north boundary heat flux ($\Psi_{T,N}$) on centreline $\left(\frac{x}{X}=0.5,\frac{y}{Y}\right)$ temperature θ in a 2-D square geometry.

4.3.3 Conduction-radiation in a 2-D square medium with heat generation: The effects of heat generation on temperature distribution for various radiative parameters like scattering albedo, conduction-radiation parameter and boundary emissivity are discussed. The boundary conditions are same as the problem considered in case of non-uniform lattices. The non-dimensional heat generation rate is taken as unity.

In Fig.4.10, The effects of heat generation on temperature distribution at different time ξ have been shown for different values of conduction-radiation parameter N . All other radiative parameters are considered as scattering albedo $\omega = 0.0$, extinction coefficient $\beta = 1.0$ and boundaries are black. For higher values of N (conduction dominated), the third term of Eq. (4.5) is small and effects of heat generation is dominated on temperature distribution. For lower values of N (radiation dominated), the temperature profile does not depend much on heat generation.

The effects of heat generation on temperature distribution for different values of scattering albedo ω are shown in Fig. 4.11(a) and Fig. 4.11(b) at different time ξ. All other radiative parameters are considered as $\beta = 1.0$, $N = 0.01$ and all boundaries are black. As time increases, the deviation in temperature profile with and without heat generation increases. For higher value of ω, the temperature gradient is more and effects of heat generation on centreline temperature is more.

The effect of heat generation on temperature distribution for the south boundary emissivity $\varepsilon_S = 0.5$ is shown in Fig. 4.11(c) at different time ξ. All other radiative parameters are considered as $\omega = 0.0$ $\beta = 1.0$, $N = 0.01$ and rest of the boundaries are black. As time increases, the deviation in temperature profile with and without heat generation increases.

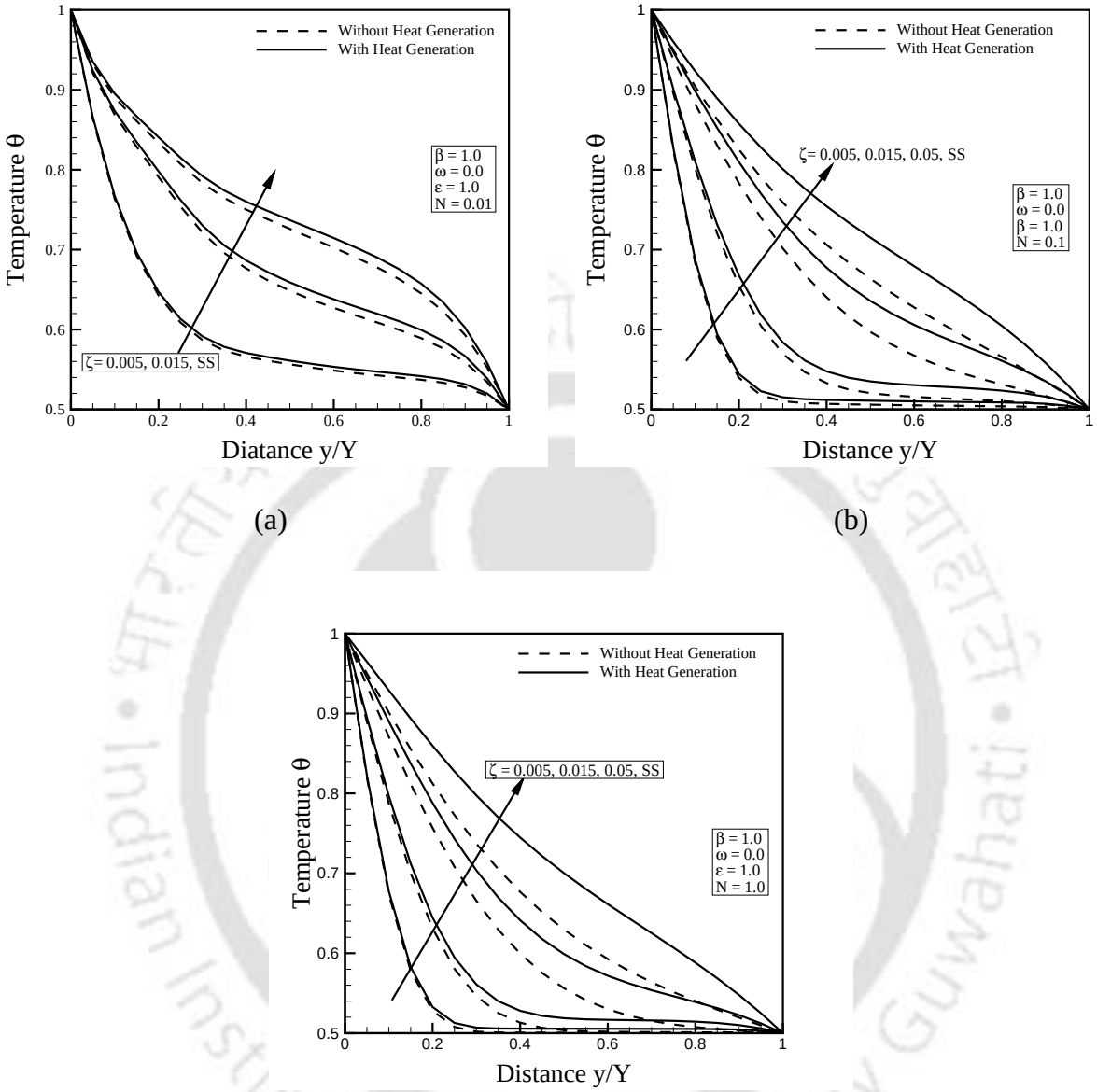

Figure 4.10: Comparison of centreline temperature θ in a 2-D square enclosure at different instants ζ for (a) emissivity of the south boundary ε_S = 0.1, (b) 0.5 and (c) 0.9.

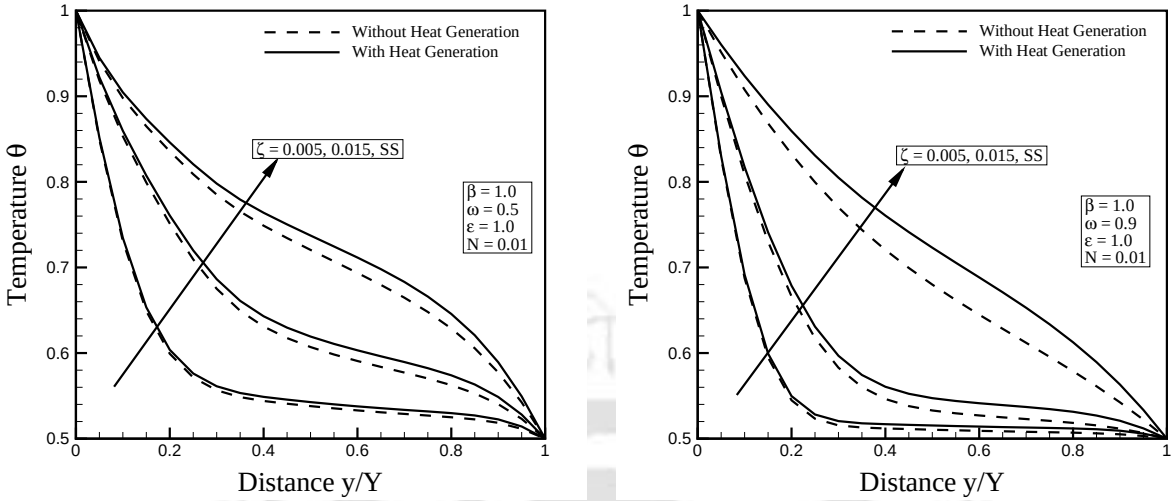

(a)

(b)

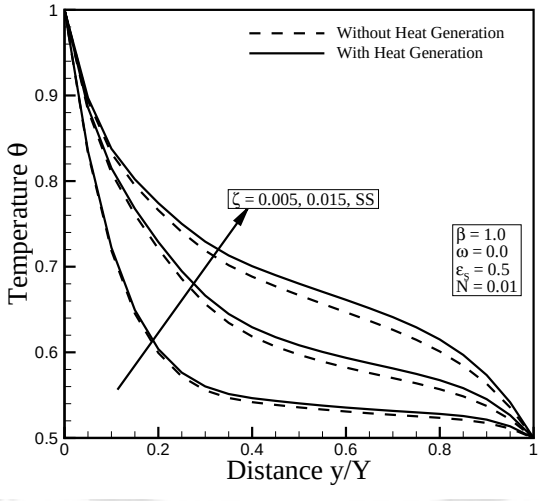

(c)

Figure 4.11: Comparison of centreline temperature θ in a 2-D square enclosure at different instants ζ for (a) emissivity of the south boundary ε_S = 0.1, (b) 0.5 and (c) 0.9.

4.4 Summary

The LBM was used to solve a transient conduction and radiation heat transfer problem in a 2-D rectangular enclosure containing absorbing, emitting and scattering medium. Three different cases were considered. To facilitate collisions to take place at the same instant for non-uniform lattices, quadratic interpolations of the particle distribution functions were done.

The results with non-uniform size lattices/control volumes were found to compare very well with those with the uniform size lattices/control volumes. For various parameters including the clustering parameter, results of the uniform and non-uniform lattices/control volumes were found in good agreements. The LBM in conjunction with the FVM was implemented for the solution of combined conduction-radiation problems with flux boundary conditions. The validity of the formulation was established first by comparing the results of the inverse problems with that of the direct ones. For different sets of parameters, temperature distributions were analyzed. The effects of heat generation were also analyzed. The next chapter deals with the 3-D conduction-radiation problems.

CHAPTER 5

3-D Conduction-Radiation Problems

5.1 Introduction

Analysis of heat transfer problems involving thermal radiation finds applications in many areas such as boilers, furnaces, phase change of semitransparent materials, fire safety analysis, fibrous and foam insulations.

Over the last two decades, a good amount of work [137, 139, 144, 146, 147] has been devoted to the study of transient conduction-radiation heat transfer problems in different geometries. Tsai and Ozisik [137] analyzed transient conduction and radiation heat transfer in an absorbing, emitting and isotropically scattering solid sphere. Chu and Tseng [146] studied conduction-radiation in an absorbing, emitting and scattering planar medium with variable thermal conductivity. Combined conduction-radiation heat transfer problem in a 2-D rectangular enclosure with absorbing and emitting medium was studied by Sokman and Razzaque [147] and Ho and Ozisik [139] using the finite element method. Wu and Ou [144] analyzed the transient conduction-radiation problem in a participating medium using the integral-equation method.

Non-Fourier effects on transient temperature response in a semitransparent medium with black surfaces caused by laser pulse were considered by Liu *et al*. [148]. Solidification of a planar medium using the LBM was analyzed by Jiaung *et al*. [18]. Ho *et al.* [19] solved a non-Fourier heat conduction problem in a planar medium using the LBM. Heat transfer in a multilayered structured with the dual phase lag heat conduction model using

the LBM was studied by Ho *et al*. [20]. Application of the LBM in solving heat transfer problems involving thermal radiation was extended by Mishra and co-workers [22, 88, 100, 141]. Mishra and Lankadasu [22] solved the energy equation of a transient conduction-radiation heat transfer problem of 1-D planer medium using the LBM. They used the DTM to calculate the radiative information. Mishra and Roy [100] used the LBM to solve transient conduction-radiation problems in 1-D planer and 2-D rectangular geometries and used the FVM to compute the radiative information. Gupta *et al.* [88] used a variable relaxation time based LBM to solve the energy equation of a temperature dependent transient conduction and radiation heat transfer in a planer medium. In their study, the radiative information was calculated by the DOM. Mondal and Mishra [141] extended the application of LBM to solve the energy equation of conduction-radiation problem 1-D planar and 2-D rectangular geometries on non-uniform lattices. Chatterjee and Chakraborty [21, 149] used the LBM for simulating conduction dominated phase change problem. They [150, 151] developed a hybrid LBM for simulating the solid-liquid phase transitions in the presence of fluid flow. In the above studies, only 1-D and 2-D geometries were considered.

From the literature, it has been found that not much attention has been paid to the study of conduction-radiation heat transfer in 3-D rectangular geometries. Very recently, Talukdar et al. [152] used the FVM to solve conduction-radiation problem in a 3-D enclosure. Wellele et *al.* [153] have also analyzed several problems with non-uniform heating for conduction-radiation problem in a 3-D rectangular enclosure. However, as far as analysis of conduction-radiation problems in 3-D geometries using the LBM is concerned, so far no study has been reported. The present work is, therefore, aimed at extending the application of the LBM to solve transient conduction-radiation problems in a 3-D cubical enclosure containing an absorbing, emitting and scattering medium. The FVM is used to compute the radiative information. To generalize the usage of the LBM, the problem is solved on both uniform and non-uniform lattices/control volumes. Further, cases of constant temperature as well as heat flux boundary conditions are also considered. The effect of heat generation is taken into account. To check the performance of the LBM-FVM on non-uniform lattices/control volumes, comparisons of

temperature results have been made for various parameters like the extinction coefficient, the scattering albedo, the boundary emissivity and the conduction radiation parameter.

5.2 Formulation

Let us consider a 3-D cubical enclosure containing an absorbing, emitting and scattering homogeneous participating medium as shown in Fig 5.1a. Thermo-physical and optical properties of the medium are constant. The system is initially at temperature T_E. For time $t > 0$, the south boundary is subjected to a constant temperature T_S or constant heat flux $q_{T,S}$. The rest of the boundaries are kept at initial temperature T_E. For the problem under consideration, the energy equation is

$$\rho c_p \frac{\partial T}{\partial t} = k \frac{\partial^2 T}{\partial x^2} + k \frac{\partial^2 T}{\partial y^2} + k \frac{\partial^2 T}{\partial z^2} - \nabla \cdot \vec{q}_R + Q''' \tag{5.1}$$

where ρ is the density, c_p is the specific heat, k is the thermal conductivity, $\vec{q}_R$ is the radiative heat flux and Q''' is the heat generation per unit volume.

In Eq. (5.1), the divergence of radiative heat flux $\nabla \cdot \vec{q}_R$ that accounts for the volumetric radiation is given by

$$\nabla \cdot \vec{q}_R = (1 - \omega)\beta \left[4\pi \left(\frac{\sigma T^4}{\pi} \right) - G \right] \tag{5.2}$$

where ω is the scattering albedo, β is the extinction coefficient and G is the incident radiation. In the present work, $\nabla \cdot \vec{q}_R$ is computed using the FVM and the LBM is employed to solve the energy equation. Below we provide a brief formulation of the FVM and the LBM. Details of the FVM methodology used in the present work can be found in chapter 2.

To account for volumetric radiation, applying LBM, Eq. (5.1) takes the form of

$$f_i\left(\vec{r}+\vec{c}_i\Delta t, t+\Delta t\right) = f_i\left(\vec{r},t\right) - \frac{\Delta t}{\tau}\left[f_i\left(\vec{r},t\right) - f_i^{(eq)}\left(\vec{r},t\right)\right] - \left(\frac{\Delta t w_i}{\rho c_p}\right)\nabla\cdot q_R + \Delta t w_i Q''' \qquad (5.3)$$

Equation (5.3) is the equivalent form of the energy equation (Eq. (5.1)) in the LBM formulation. It describes a transient conduction-radiation problem.

5.3 Results and Discussion

The following cases have been considered:

- **Transient conduction-radiation in a 3-D cubical enclosure with constant temperature boundary condition:** Initially the 3-D cubical participating medium is at temperature T_E and for time $t>0$, its south boundary is maintained at constant temperature $T_S > T_E$ and rest all boundaries are at temperature T_E. The homogeneous medium is absorbing, emitting and isotropically scattering. Its boundaries are diffuse-gray. This problem is solved on both uniform and non-uniform lattices/control volumes.

- **Transient conduction-radiation in a 3-D cubical enclosure with one of its boundaries at constant heat flux:** The 3-D cubical absorbing, emitting and isotropically scattering medium is initially at temperature T_E. Its boundaries are diffuse-gray. For time, $t>0$, its south boundary is kept at heat flux $q_{T,S}$ and rest of the boundaries remain at temperature T_E.

- **Transient conduction-radiation in a 3-D cubical enclosure in presence of volumetric heat generation:** Initially the 3-D cubical absorbing, emitting and isotropically scattering medium is at temperature T_E and for time $t>0$, its south boundary is maintained at constant temperature $T_S > T_E$ and rest of the boundaries are at temperature T_E. In this case, volumetric heat generation is considered within the medium.

For grid and ray independency tests, numerical experiments were performed with $21\times21\times21, 31\times31\times31, 41\times41\times41, 51\times51\times51$ lattices/control volumes and 4×8, 6×8, 8×8 and 10×8 ray directions over the spherical space in the FVM. No significant changes in results were observed beyond $31\times31\times31$ lattices 8×8 ray direction. In all the cases, non-dimensional time step $\Delta\xi=\alpha\beta^2t=1.0\times10^{-4}$ were used, and the steady-state condition was assumed to have been achieved when the maximum variation in temperature $\theta=\dfrac{T}{T_{\text{ref}}}$ at any location between two consecutive time levels did not exceed 1.0×10^{-6}.

5.3.1 Transient conduction-radiation in a 3-D cubical enclosure with constant temperature boundary condition: Initially the entire system is at a temperature θ_0. For $t>0$, the south boundary temperature is raised to $\theta_S=2\theta_0$. The enclosed gray-homogeneous medium is absorbing, emitting and isotropically scattering. The problem was also solved for the uniform and non-uniform lattices/control volumes.

The non-uniform size lattices/control volumes were generated from the following expressions

$$\mathrm{x_n}=\left\{\frac{\mathrm{n\text{-}1}}{\mathrm{N_x}}+\frac{C_x}{\pi}\sin\left(\frac{\pi(\mathrm{n\text{-}1})}{\mathrm{N_x}}\right)\right\} \tag{5.4}$$

$$\mathrm{y_n}=\left\{\frac{\mathrm{n\text{-}1}}{\mathrm{N_y}}+\frac{C_y}{\pi}\sin\left(\frac{\pi(\mathrm{n\text{-}1})}{\mathrm{N_y}}\right)\right\} \tag{5.5}$$

$$\mathrm{z_n}=\left\{\frac{\mathrm{n\text{-}1}}{\mathrm{N_z}}+\frac{C_z}{\pi}\sin\left(\frac{\pi(\mathrm{n\text{-}1})}{\mathrm{N_z}}\right)\right\} \tag{5.6}$$

where x_n, y_n and z_n are the coordinates of the lattice centre in the LBM and the control volume corner in the FVM in $x-$, $y-$ and $z-$ directions, respectively. N_x, N_y and N_z are the total number of lattices/control volumes in the $x-$, $y-$ and $z-$ directions, respectively

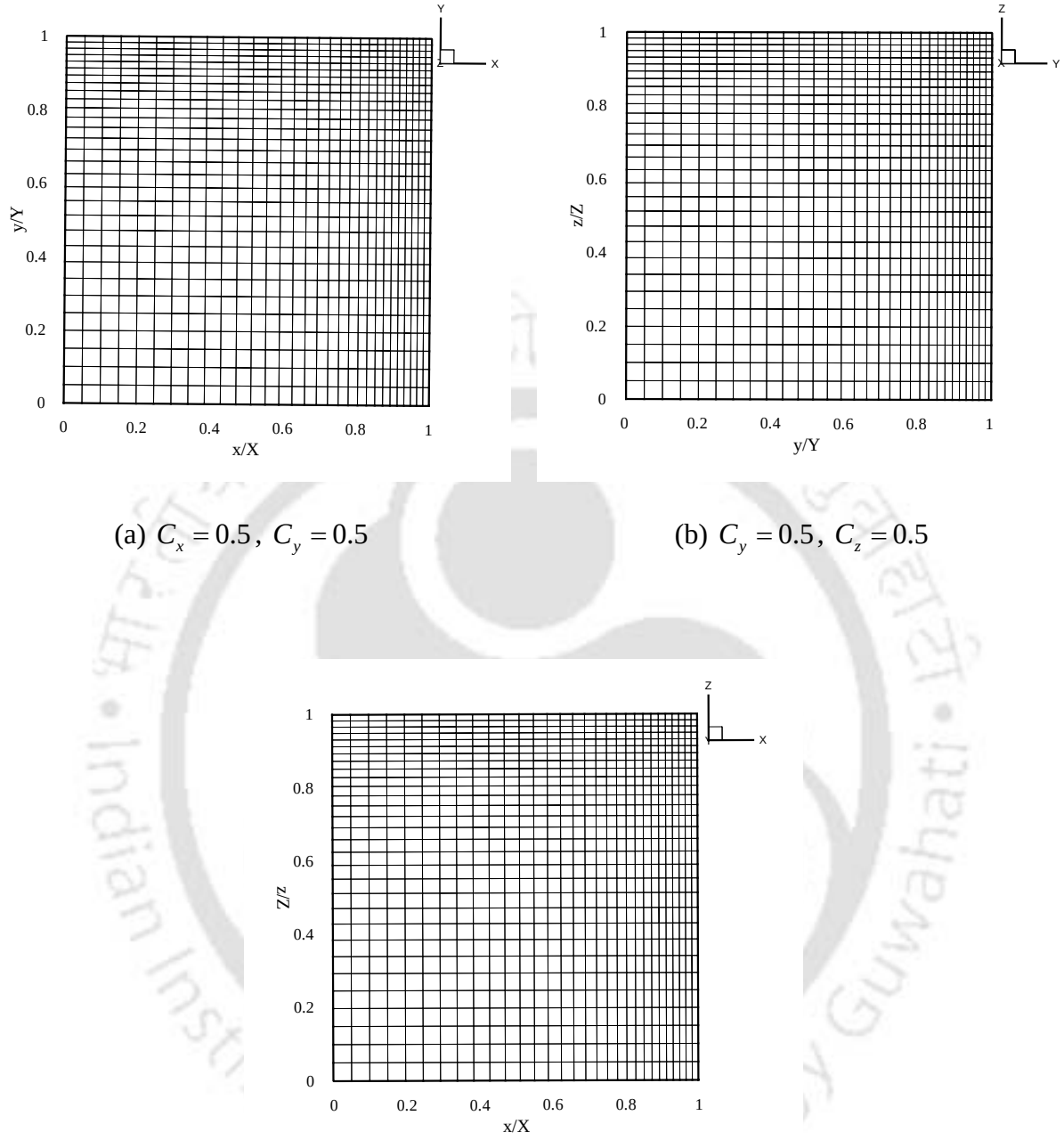

(a) $C_x = 0.5$, $C_y = 0.5$

(b) $C_y = 0.5$, $C_z = 0.5$

(c) $C_x = 0.5$, $C_z = 0.5$

Figure 5.1: A sample of non-uniform lattices in different planes of a 3-d cubical geometry used in the numerical experiment.

and $C_x \left(0 \le |C_x| \le 1\right)$, $C_y \left(0 \le |C_y| \le 1\right)$ and $C_z \left(0 \le |C_z| \le 1\right)$ are parameter that determine clustering. With $C_x = 0$, $C_y = 0$ and $C_z = 0$, uniform size lattices/control volumes are obtained. For $C_x = 0.5$, $C_y = 0.5$ and $C_z = 0.5$, the non-uniform lattices in three different planes are shown in Fig. 5.1.

A 3-D cubical enclosure with absorbing, emitting and isotropic scattering medium of unit length is considered. The south $\left(\frac{y}{Y} = 0\right)$ boundary is at a finite temperature θ_S and other all boundaries are at a lower temperature $\theta_E < \theta_S$. The south boundary temperature T_S is taken as the reference temperature, thus non-dimensional temperature $\theta = \frac{T}{T_S}$. In non-dimensional form, the south boundary temperature $\theta_S = 1.0$ and rest all boundary temperature are $\theta_0 = \theta_N = \theta_W = \theta_E = \theta_F = \theta_B = 0.5$.

In Fig. 5.2, for scattering albedo $\omega = 0.0$, conduction radiation parameter $N = 0.01$ and considering all boundaries black ($\varepsilon = 1.0$), the steady state temperature θ computed from the LBM-FVM with uniform and non-uniform lattices/control volumes have been compared with Talukdar *et al.* [152] for the effects of three different values of the extinction coefficient β. It can be seen from the Fig. 5.2 that at all times ζ, results of the non-uniform and uniform lattices/control volumes are in good agreements. The number of iteration for the steady state solutions with non-uniform lattices/control volumes for $\beta = 0.1, 1.0$ and 5.0 were found 2573, 870 and 200 respectively. The same with uniform lattices/control volumes were found to be 2553, 872 and 203.

In Fig. 5.3, comparison of centreline $\left(\frac{x}{X} = 0.5, \frac{y}{Y}, \frac{z}{Z} = 0.5\right)$ temperature θ along y-direction has been made for the effects of different radiative parameters. With $\beta = 1.0$, conduction-radiation parameter $N = 0.01$ and considering all boundaries black $\left(\varepsilon = 1.0\right)$,

effects of the scattering albedo $\omega = 0.5$ and 0.9 have been shown in Figs. 5.3a and 5.3b. For non-uniform

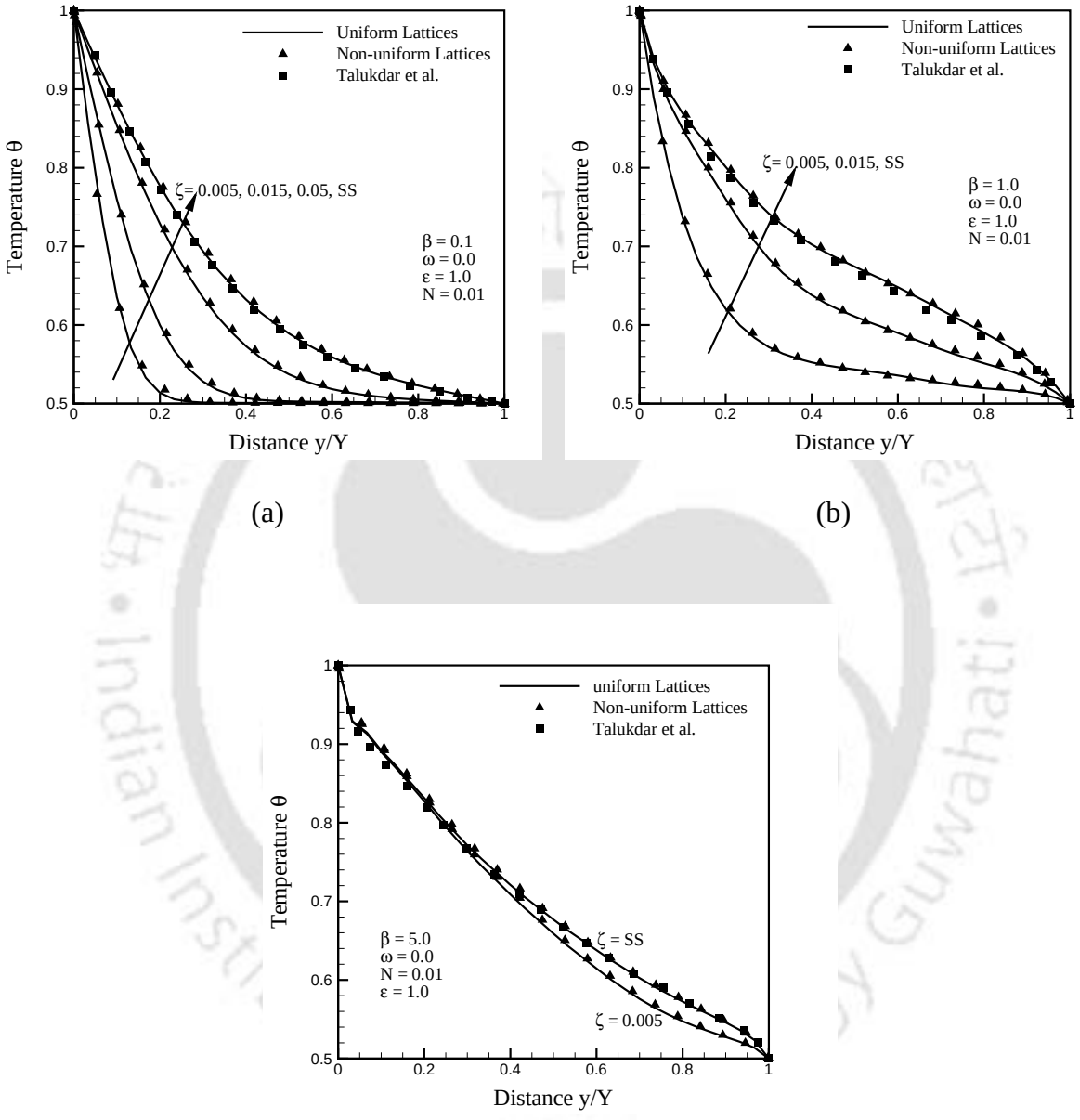

Figure 5.2: Comparison of centre line temperature θ at different instants ξ for extinction coefficient β = (a) 0.1, (b) 1.0 and (c) 5.0 for non-uniform and uniform lattices/control volumes.

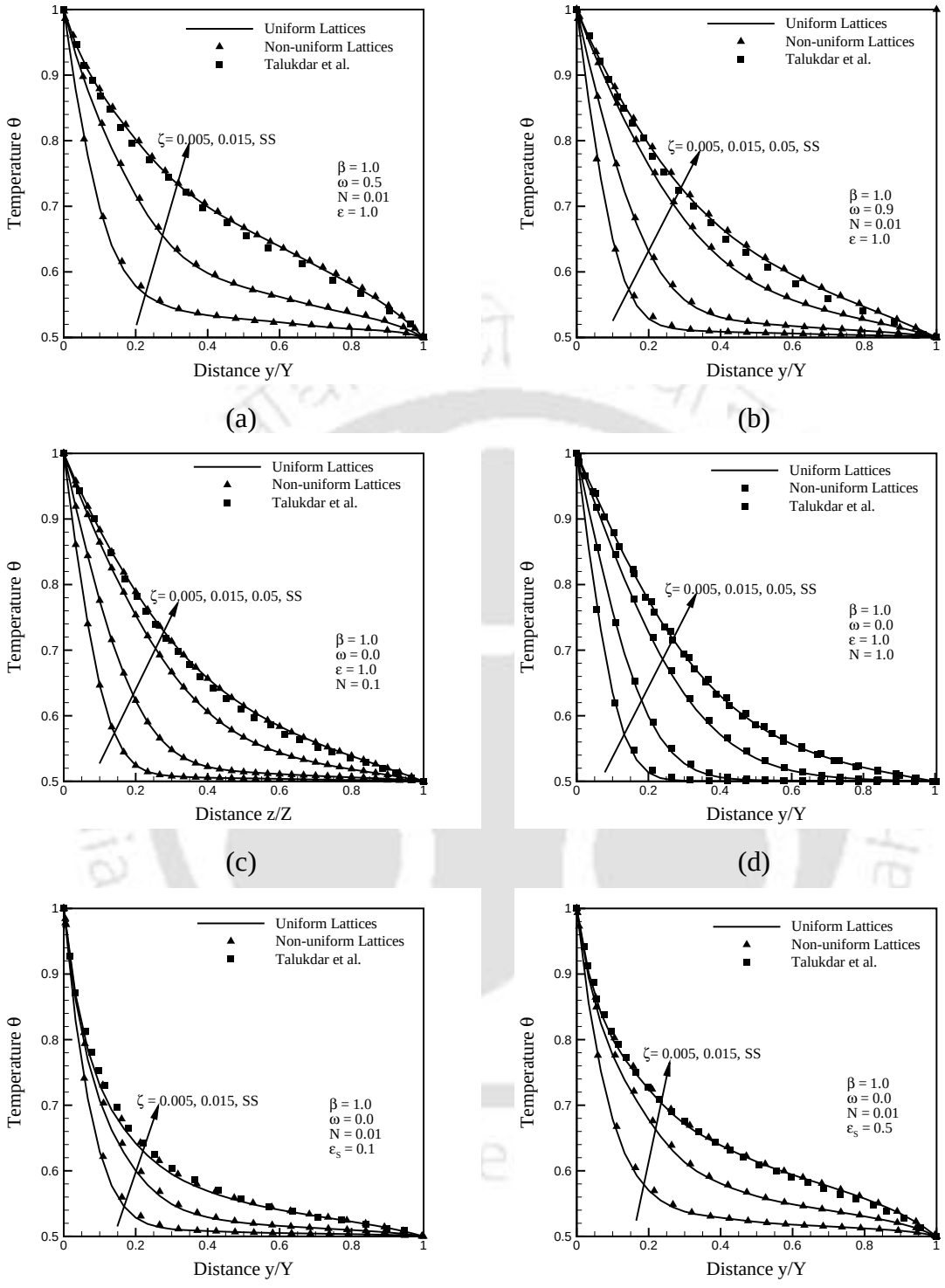

Figure 5.3: Comparison of centre line temperature θ at different instants ξ with different combination of radiative parameters for non-uniform and uniform lattices/control volumes.

lattices /control volumes, the number of iterations for the steady state solution were found to be 1230 and 2078 for $\omega = 0.5$ and 0.9, respectively. The same for uniform lattices/control volumes were 1219 and 2073, respectively. The steady state results for non-uniform and uniform lattices/control volumes are very close to the results available in the literature [152].

In Figs. 5.3c and 5.3d, results have been shown for the conduction-radiation parameter $N = 0.1$ and 1.0, respectively. Other radiative parameters are $\beta = 1.0, \omega = 0.0$ and $\varepsilon = 1.0$. It can be seen from these two figures that the results for non-uniform and uniform lattices/control volumes at all times are in good agreement. The steady state results are also very close to each other and they compare well with the results of Talukdar *et al.* [152]. In case of non-uniform lattices/control volumes, for $N = 0.1$ and 1.0, the number iterations for steady state solutions were found to be 2225 and 2590, respectively. The same for the uniform lattices/control volumes were 2217 and 2569, respectively.

In Figs. 5.3e and 5.3f, with $\beta = 1.0$, $\omega = 0.0$ and $N = 0.01$, results are shown for the south boundary emissivity $\varepsilon_S = 0.1$ and 0.5, respectively. Rest all boundaries are considered black. In these cases too, the centreline $\left(\frac{x}{X} = 0.5, \frac{y}{Y}, \frac{z}{Z} = 0.5\right)$ temperature θ along y-direction at different times, for uniform and non-uniform lattices/control volumes are found in good agreement with each other. The steady state results are very close to the results of Talukdar *et al.*[152]. For non-uniform lattices/control volumes, the number of iterations for the steady state results were found to be 993 and 941, respectively. The same for the uniform lattices/control volumes were found to be 993 and 944, respectively.

5.3.2 Conduction-radiation in a 3-D cubical enclosure with one boundary at a prescribed heat flux: To validate the LBM-FVM formulation and its implementation for the flux boundary condition for a transient conduction-radiation problem, we first solved the direct problem. In the direct problem, for a prescribed boundary temperature,

the total heat flux $\Psi_{T,S} = \Psi_C + \Psi_R$ at the south boundary is calculated. Then in the inverse problem, the computed value of heat flux $\Psi_{T,S}$ became imposed heat flux at the south boundary. The rest

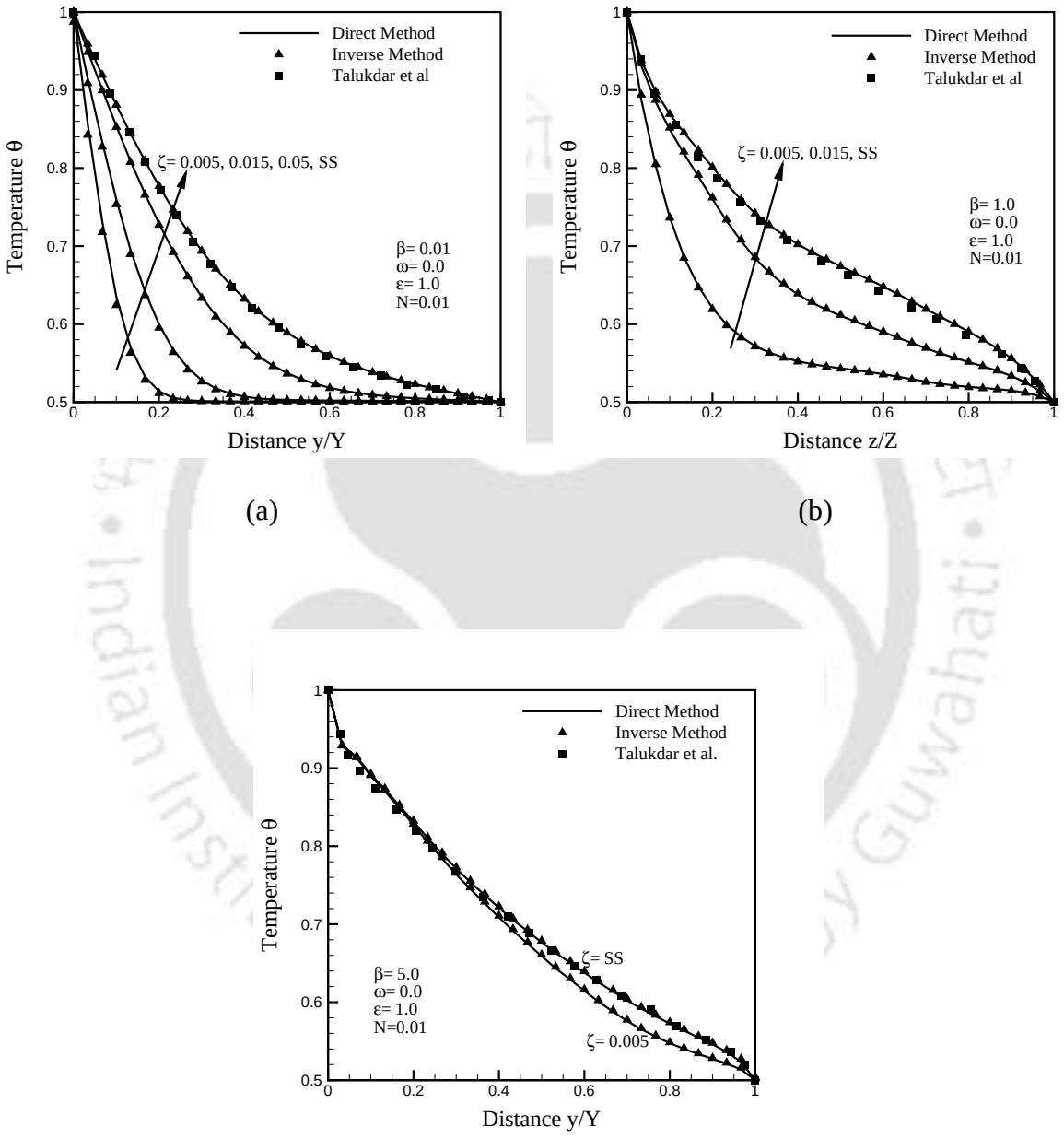

Figure 5.4: Comparison of centre line temperature θ at different instants ξ for extinction coefficient β = (a) 0.1, (b) 1.0 and (c) 5.0 in direct and inverse method.

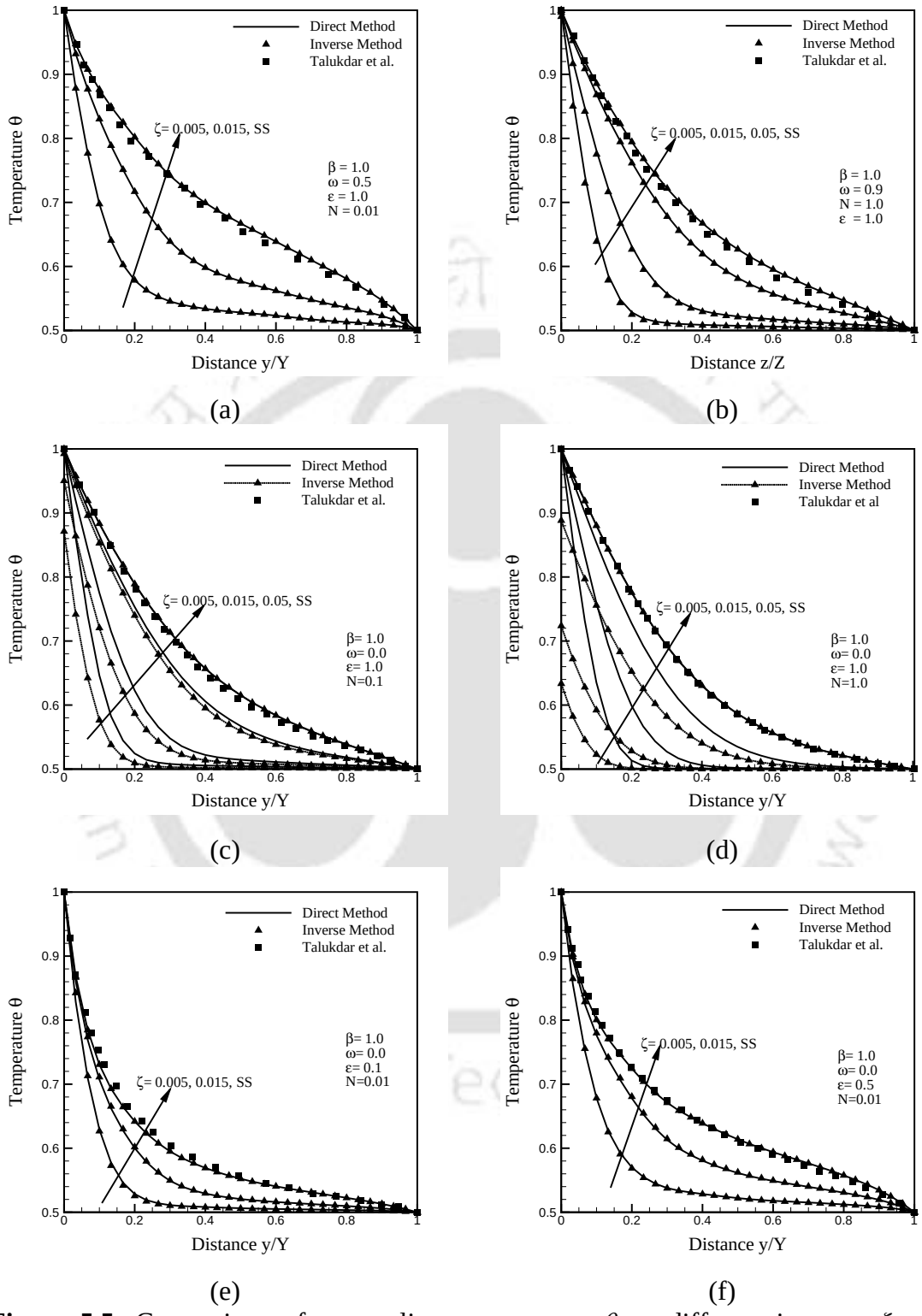

Figure 5.5: Comparison of centre line temperature θ at different instants ξ with different combination of radiative parameters for the direct and inverse method.

all boundaries are at prescribed temperature as in the case of the direct problem. With other parameters and conditions remaining the same, the validation of the LBM-FVM with flux boundary condition is established if both the direct method and inverse method yield the same results.

In Figs. 5.4 and 5.5, we have validated the LBM-FVM formulation by comparing the centreline $\left(\frac{x}{X}=0.5,\frac{y}{Y},\frac{z}{Z}=0.5\right)$ temperature θ obtained from the direct method and the inverse method. With $\omega=0.0$, $N=0.01$ and all boundaries black $\varepsilon=1.0$, in Figs. 5.4a-c, results have been compared for the extinction coefficient $\beta=0.1,1.0$ and 5.0, respectively. Comparisons have been made at 4 time ζ levels including the steady state. Results of the direct and the inverse methods match with each other well and the steady state results compare well with those given in [152]. For $\beta=0.1,1.0$ and 5.0, in the inverse method, the number of iterations for the steady state results were found to be 2073, 812 and 200, respectively. The same in the direct method were 2563, 866 and 204, respectively.

With $\beta=1.0$, $N=0.01$ and $\varepsilon=1.0$, in Figs. 5.5a and 5.5b, centreline θ results are compared for the scattering albedo $\omega=0.5$ and 0.9, respectively. At all times, results from the direct method and inverse method are found in good agreement with each other and the steady state results match well with those given in [152]. In the inverse method, for $\omega=0.5$ and 0.9, the numbers of iterations for steady state solution were found to be 1086 and 1759, respectively. The same for the direct method were 1219 and 2073, respectively.

In Fig. 5.5c and 5.5d, θ results are shown for conduction radiation parameter $N=0.1$ and 1.0, respectively. In conduction dominated case ($N=1.0$) (Fig. 5.5d), temperature θ evolution is slow in case of inverse method. In the inverse method, with prescribed heat flux $\Psi_{T,S}$ at the south boundary, temperature θ at the south boundary is calculated. At

this boundary, θ evolves from a low value to the correct value which is unity. On the other hand, in the direct method, non-dimensional temperature θ of the south boundary is unity. In radiation dominated case ($N = 0.1$) (Fig. 5.5c), radiation augments temperature evolution and thus, unlike Fig. 5.5d, in this case, in the inverse method, θ profiles do not lag much behind those of the direct method.

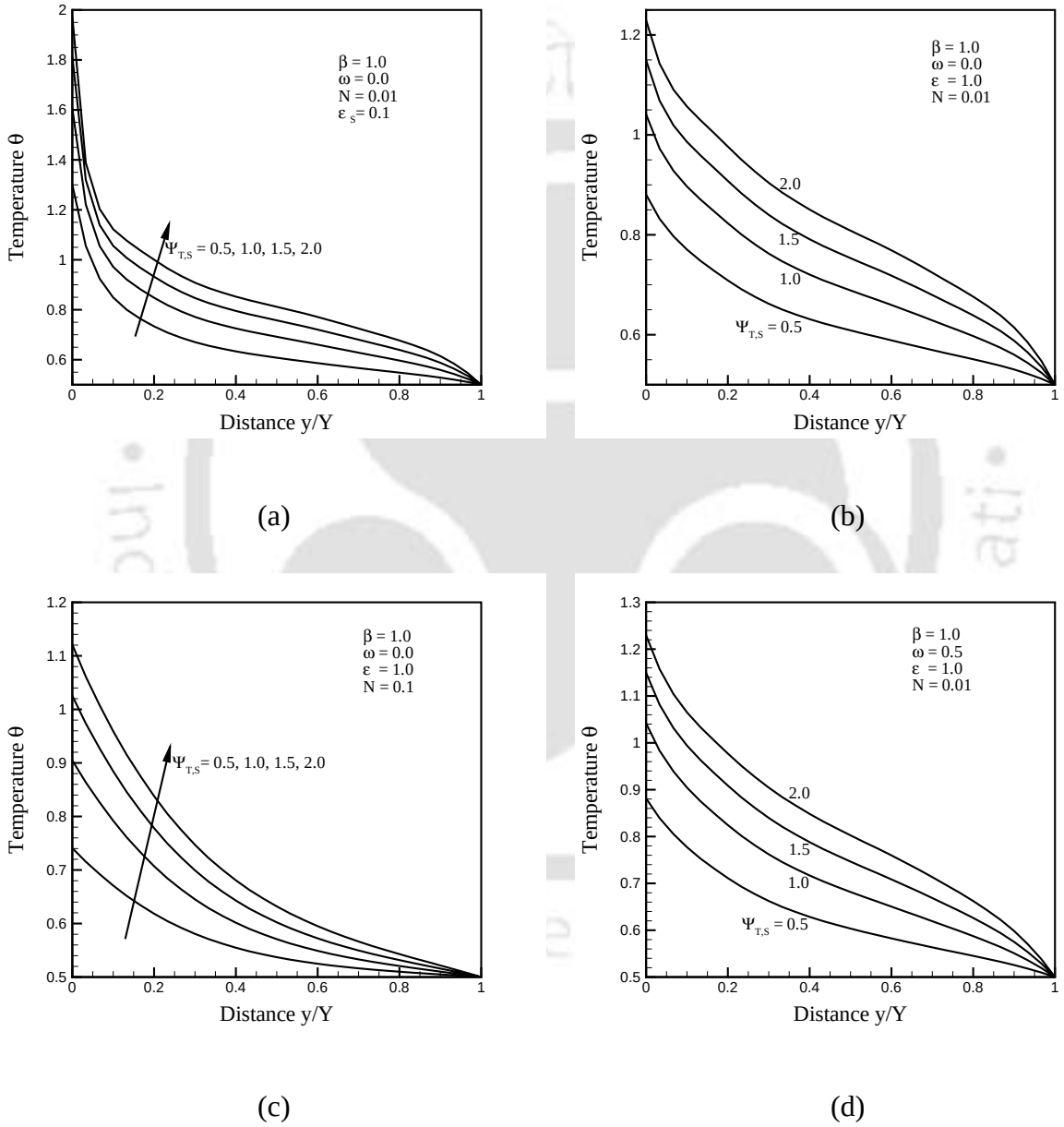

Figure 5.6: Comparison of centre line temperature θ at steady state solution with different combination of radiative parameters for imposed heat flux at the south boundary.

Steady state results of both inverse and direct methods compare well with those of [152]. For $N = 0.1$ and 1.0, in the inverse method, the numbers of iterations for the steady state results were found to be 1921 and 2567 respectively. The same in the direct method were 2217 and 2569, respectively.

With $\beta = 1.0$, $\omega = 0.0$ and $N = 0.01$, in Figs. 5.5e and 5.5f, centreline temperature θ results computed from the direct and inverse methods have been compared for the two values of the south boundary emissivity $\varepsilon_S = 0.1$ and 0.5, respectively. At all time levels, results of the two methods match and the steady-state results compare well with that of [152]. In the inverse method, for $\varepsilon_S = 0.1$ and 0.5, the numbers of iterations for the steady state results were found to be 890 and 858, respectively. The same in case of the direct method were 993 and 944, respectively.

Effects of the imposed heat flux $\Psi_{T,S}$ on centreline temperature θ distributions have been shown in Figs. 5.6a-d. Values of $\Psi_{T,S}$ imposed on the south boundary are 0.5, 1.0, 1.5 and 2.0. Rest all boundaries are maintained at non-dimensional temperature 0.5. For results in Fig. 5.6a-d, the reference temperature was taken as unity.

In Fig. 5.6a, with $\beta = 1.0$, $\omega = 0.0$, $N = 0.01$ and the south boundary emissivity $\varepsilon_S = 0.1$, effects $\Psi_{T,S} = 0.5$, 1.0, 1.5 and 2.0 on centreline temperature θ has been shown. For results in Fig. 5.6b, all boundaries are considered black and other radiative parameters are the same as for the results given in Fig 5.6a. For results in Fig. 5.6a, the south boundary is reflecting more $(\varepsilon_S = 0.1)$ and thus near this boundary a sharp temperature gradient is observed. With increase in $\Psi_{T,S}$, temperature θ at any location increases.

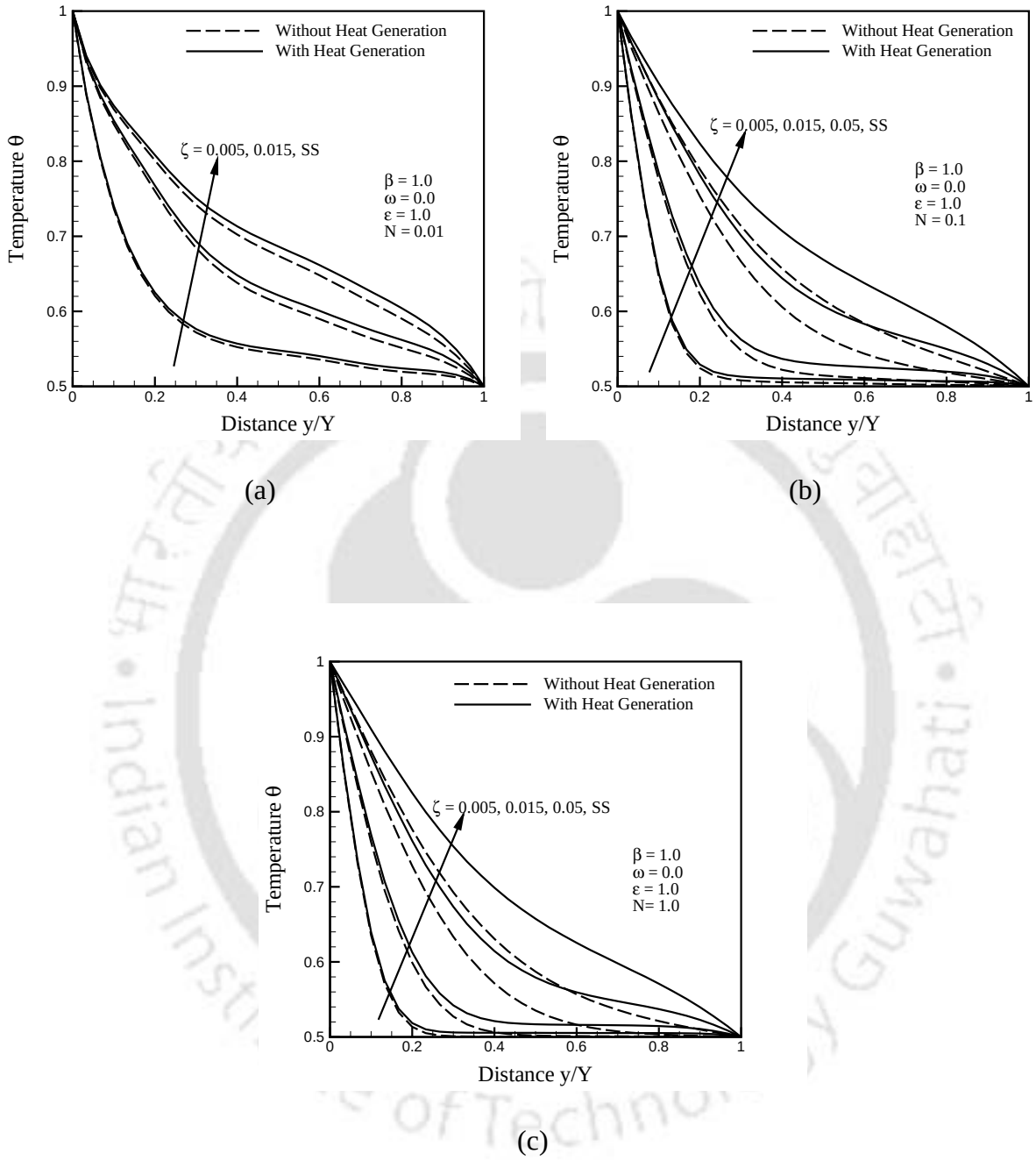

Figure 5.7: Effects of conduction radiation parameter (N) on centre line temperature θ at different instants ξ with and without heat generation.

With $\beta = 1.0$ and all boundaries black $(\varepsilon = 1.0)$, effects of $\Psi_{T,S}$ on temperature θ have been shown for $\omega = 0.0$ and $N = 0.1$ in Fig. 5.6c and for $\omega = 0.5$ and $N = 0.01$ n in Fig. 5.6d. A comparison of Figs. 5.6b and 5.6c show that in radiation dominated case $(N = 0.01)$ (Fig. 5.6b), for a given value of $\Psi_{T,S}$, θ at any location is more. A comparison of Figs. 5.6b and 5.6d show that scattering albedo ω has not much effect on θ profile.

5.3.3 Conduction-radiation in a 3-D cubical enclosure in presence of volumetric heat generation: Centreline $\left(\frac{x}{X} = 0.5, \frac{y}{Y}, \frac{z}{Z} = 0.5\right)$ temperature θ distributions in the medium with and without heat generation have been compared in Figs. 5.7 and 5.8. The value of the non-dimensional heat generation rate has been taken as unity.

With $\beta = 1.0, \omega = 0.0$ and $\varepsilon = 1.0$, in Figs. 5.7a-c, results have been compared for the conduction-radiation parameter $N = 0.01, 0.1$ and 1.0. It is observed from Figs. 5.7a-c that in the radiation dominated case $(N = 0.01)$ (Fig. 5.7a), heat generation has not much effect on θ. At any time, θ in the medium is more homogeneous. In conduction-dominated case $(N = 1.0)$ (Fig. 5.7c), θ profile is steeper compared to radiation dominated case $(N = 0.01)$ (Fig. 5.7a).

In Figs. 5.8a and 5.8b, for $\omega = 0.5$ and 0.9, with and without heat generation, θ distributions have been studied. For results in both these figures, $\beta = 1.0, N = 0.01$ and $\varepsilon = 1.0$. It is observed from these figures that the effect of heat generation on θ distribution is more pronounced when medium is more scattering $(\omega = 0.9)$. In Fig. 5.8c, with south boundary emissivity $\varepsilon_s = 0.5$, with and without heat generation, θ distributions have been studied. For results in this figure $\beta = 1.0, N = 0.01$ and $\omega = 0.0$. A comparison of Figs. 5.7a and 5.8c shows that when the south boundary is more reflecting $(\varepsilon_s = 0.5)$, effect of heat generation is slightly more.

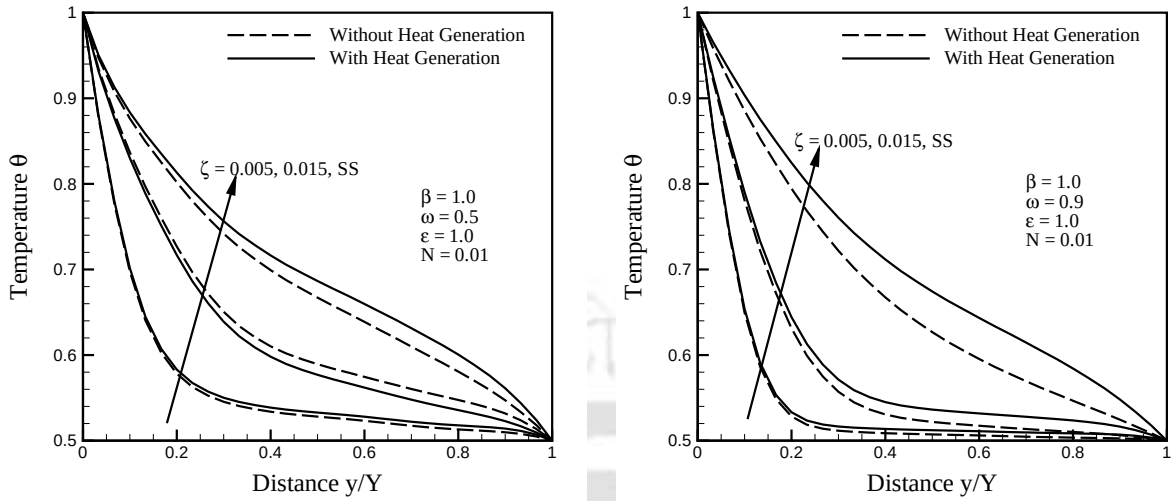

(a)

(b)

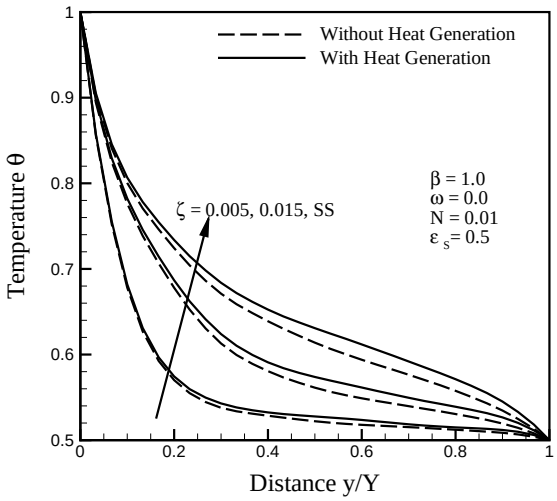

(c)

Figure 5.8: Effects of scattering albedo (ω) (a) = 0.5, (b) = 0.9 and south boundary emissivity (ε_S) (c) = 0.5 on centre line temperature θ at different instants ξ with and without heat generation.

5.4 Summary

The application of the LBM to solve transient conduction-radiation problems in a 3-D cubical geometry was extended on both uniform and non-uniform lattices/control volumes. Cases of both constant temperature and flux boundary conditions were considered. The radiating-conducting participating medium was considered as absorbing, emitting and isotropically-scattering. Effect of volumetric heat generation was also considered. To validate results of heat flux boundary condition, results from direct and inverse methods were compared. In the direct method, by prescribing temperatures at the boundaries, the temperature profile and heat flux were calculated. The computed heat flux values were imposed at the same boundary to establish the correctness of the numerical code in the inverse method. Effects of various parameters such as the extinction coefficient, the scattering albedo, the conduction-radiation parameter, the boundary emissivity, and the total heat flux were studied on the distributions of temperature. Results of the LBM in conjunction with the FVM were found to compare very well with those available in the literature.

CHAPTER 6

3-D Phase Transition Problems

6.1 Introduction

Mathematical modelling of phase change of semitransparent materials is an important field of research. It has relevance in various engineering applications such as films used in solar energy, crystal growth, alloy processing, nuclear engineering and laser material processing [154-160]. Semitransparent materials such as oxides, fluorides and silicon find applications as single- and poly-crystals, glasses, ceramics, composites, etc. [161-165].

One of the early numerical studies of melting and solidification has been reported by Co and Sunderland [154]. Habib [155] considered solidification of semitransparent materials. In his study, he considered the effects of conduction and radiation. Abrams and Viskanta [156] considered effects of radiative heat transfer in melting and solidification of semitransparent crystals. Effects of scattering on melting and solidification of a semi-infinite semitransparent medium was taken into account by Oruma et al. [157]. Morphological stability during directional solidification due to radiative heat transfer was analyzed by Yuferev et al. [158]. Shu et al. [159] studied effects of internal radiation and solidification in semitransparent melts in the presence of magnetic fields.

In the presence of volumetric radiation, solidifications of 1-D planar and 2-D square geometries were analyzed by Raj et al. [87] and Mishra et al. 160]. In [87, 160], the LBM was used to analyze the solidification process. The DTM was applied to compute

radiation information in case of a 1-D planar medium in [87]. In [160], in case of a 2-D square geometry, the FVM was used to compute the radiative information.

Chatterjee and Chakraborty [21] have formulated an enthalpy based lattice Boltzmann model for the simulation of melting of a 3-D cubical medium. However, their analysis was limited to materials which did not require consideration of volumetric radiation.

From the literature review it has been found that none of the studies reported so far has analyzed solidification of a 3-D semitransparent medium considering effects of volumetric radiation. The present work, therefore, is aimed at the analysis of solidification of a 3-D absorbing, emitting and scattering semitransparent medium involving radiation. An enthalpy based formulation in the LBM is employed to simulate the solidification process. Solidification is assumed to take place over a range of temperatures, and accordingly distinct liquid-, mushy- and solid-zones are considered. The FVM [120, 109] is used to compute the radiative information. Analyses are done considering both Dirichlet and Neumann boundary conditions. The liquid fraction and temperature profiles in the medium are analyzed for the effects of various parameters such as the extinction coefficient, the scattering albedo, the conduction-radiation parameter and the latent heat.

6.2 Formulation

Solidification of a 3-D cubical semi-transparent absorbing, emitting and scattering medium is considered. Initially at time $t = 0$, the liquid pool is at temperature T_0. The freezing temperature of the material is T_f which is lower than the initial temperature T_0. For time $t > 0$, the north boundary and south boundary are maintained at temperatures T_N and T_S, respectively. These temperatures are below its freezing temperature T_f. The remaining four boundaries are maintained at the initial temperature T_0. Since temperatures of the north and south boundaries are lower than the freezing temperature of the material, the solidification starts from these boundaries. Prior to solidification, a

mushy zone appears within the material. For the material under consideration, solidification is considered over a range of temperatures. Since the material is semitransparent, thermal radiation pervades the material and its consideration becomes paramount in the energy equation.

For the problem under consideration, energy equation with volumetric radiation in terms of total enthalpy can be written as

$$\frac{\partial(\rho H)}{\partial t} = \nabla \cdot (k \nabla T) - \nabla \cdot \vec{q}_R \tag{6.1}$$

where ρ is the density, H is the total enthalpy, k is the thermal conductivity, T is the temperature and $\vec{q}_R$ is the radiative heat flux.

In Eq. (6.1), the total enthalpy H consists of two parts i.e. sensible enthalpy $C_P T$ and latent enthalpy $f_l L$. C_P is the specific heat at constant pressure, f_l is the liquid fraction and L is the latent heat of fusion. Different zones, viz. solid-, liquid- and mushy-zones are identified with the values of the liquid fraction f_l. For liquid-zone, $f_l = 1$. If $f_l = 0$, then it is a solid-zone and for the mushy-zone, $0 < f_l < 1$. Using the definition of the total enthalpy $H = C_p T + f_l L$, the energy equation is written as

$$\frac{\partial(\rho c_P T)}{\partial t} = \nabla \cdot (k \nabla T) - L \frac{\partial(\rho f_l)}{\partial t} - \nabla \cdot \vec{q}_R \tag{6.2}$$

If ρ, C_P and k are assumed constant over a particular zone and also independent of time, Eq. (6.2) for a specific zone (solid-, mushy- and liquid) can be written as

$$\frac{\partial T}{\partial t} = \alpha \nabla^2 T - \frac{L}{C} \frac{\partial(\rho f_l)}{\partial t} - \frac{1}{C} \nabla \cdot \vec{q}_R \tag{6.3}$$

where $\alpha = k / \rho c_P$ is the thermal diffusivity and $C = \rho c_p$ is the heat capacity. In the solid-, mushy- and liquid-zones, the liquid fraction f_l and enthalpy are related as

$$f_l = \begin{cases} 0, & H < H_s \\ \dfrac{H - H_s}{H_l - H_s}, & H_s \le H \le H_l \\ 1, & H > H_l \end{cases} \tag{6.4}$$

In Eq. (6.4), subscripts *s* and *l* stand for solid- and liquid-zones, respectively. The enthalpy based energy equation (6.3) can be solved by any of the conventional CFD tools, such as the FVM.

Recently solidification problems have also been analyzed by the LBM [87, 160]. Jiaung et al. [18], Raj et al. [87], Mishra et al. [160] and Chatterjee and Chakraborty [21] have used the LBM to analyze phase change problems. Like fluid dynamics, use of the LBM is also gaining momentum in solving heat transfer problems [18-22]. Proponents [24, 25, 28, 63,] of the LBM claim that this method has the potential to be a robust CFD platform. In the present work, therefore, we analyze the 3-D solidification problem using the LBM.

The FVM for computation of radiative information is a robust method [109,110]. Unlike the DOM, it is less prone to ray effect and in this method, the false scattering is absent. Because of its construction, the method is fully conservative. In [100], compatibility of the LBM and FVM for solving conduction-radiation problems in 1-D and 2-D Cartesian geometries has been demonstrated. In the present work, therefore, the solidification problem which is analyzed by the LBM, the radiative information is computed using the FVM.

Considering the liquid fraction and the volumetric radiation, the energy equation (Eq.(6.3)) gets modified to

$$\begin{aligned} f_i\left(\vec{r} + \vec{c}_i\Delta t, t + \Delta t\right) = f_i\left(\vec{r}, t\right) - \frac{\Delta t}{\tau}\left[f_i\left(\vec{r}, t\right) - f_i^{(eq)}\left(\vec{r}, t\right)\right] \\ - \Delta t w_i \Phi_i - \left(\frac{\Delta t}{C}\right) w_i \nabla \cdot \vec{q}_R \end{aligned} \tag{6.5}$$

where

$$\Phi_i = \frac{L\rho}{C}\left[\frac{f_l(\vec{r}, t+\Delta t) - f_l(\vec{r}, t)}{\Delta t}\right] \tag{6.6}$$

It is to be noted that the relaxation time τ, the density ρ and the heat capacity C are different for different zones. With f_i known, temperature is obtained after summing f_i over all directions.

6.3 Results and Discussion

The following two cases have been considered:

- **Solidification of a 3-D semitransparent medium with all boundaries at specified temperatures:** Initially the 3-D cubical semitransparent participating medium is at temperature T_0 and for time $t > 0$, its south and north boundaries are maintained at constant temperature $T_S = T_N < T_f$. The remaining four boundaries are at initial temperature T_0.
- **Solidification of a 3-D semitransparent medium with one of its boundaries at constant heat flux:** Initially the 3-D cubical semitransparent participating medium is initially at temperature T_0. At time $t > 0$, the constant heat flux $q_{T,S}$ is extracted from the south boundary. The north boundary is kept at constant temperature $T_N < T_f$. All other four boundaries are maintained at initial temperature T_0.

The computer code for the present 3-D solidification problem has been validated against the results given in [152]. In [152], conduction-radiation problem in a 3-D cubical enclosure has been considered without any phase change. The FVM has been used to compute radiative information and also to solve the energy equation.

In Fig. 6.1, with $\beta = 1.0$ and $\omega = 0.0$, for conduction-radiation parameter $N = 1.0$, 0.1 and 0.01, along $\frac{z}{Z}$ direction at $\frac{x}{X} = 0.5$ and $\frac{y}{Y} = 0.5$ the centreline non-dimensional temperature $\theta = \frac{T}{T_0}$ have been compared. Results of the present work have been compared with those given in [152]. A very good agreement is observed.

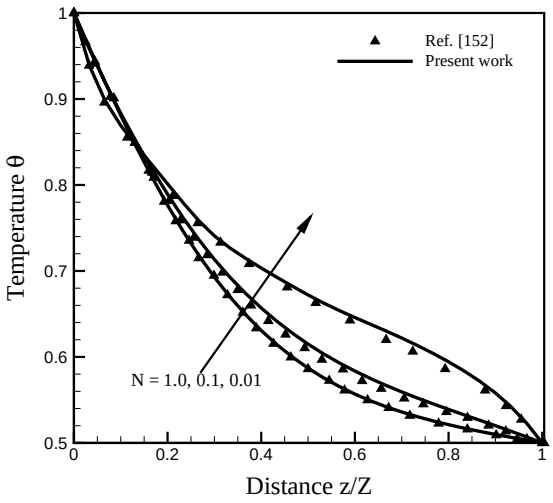

Figure 6.1: Comparison of results of the present work with those of Talukdar et al.[152] for $\beta = 1.0$ and $\omega = 0.0$.

For a cubical medium undergoing solidification, grid independence results are shown in Figs. 6.2a and 6.2b. With 4×8 rays, Figs 3a and 3b respectively show centreline liquid fraction f_l and temperature $\theta = \frac{T}{T_0}$ along $\frac{z}{Z}$ direction at $\frac{x}{X} = 0.5$ and $\frac{y}{Y} = 0.5$ of the cubical medium for $21 \times 21 \times 21$, $31 \times 31 \times 31$ and $41 \times 41 \times 41$ lattices/control volumes. It is seen from the Figs. 6.2a and 6.2b that the results of f_l have a slight variation in the mushy zone and the centreline temperature θ profiles are independent of the lattices/control volumes. It is found that $41 \times 41 \times 41$ lattices/ control volumes are optimum since there is no significant improvement even for $41 \times 41 \times 41$ lattices/control volumes.

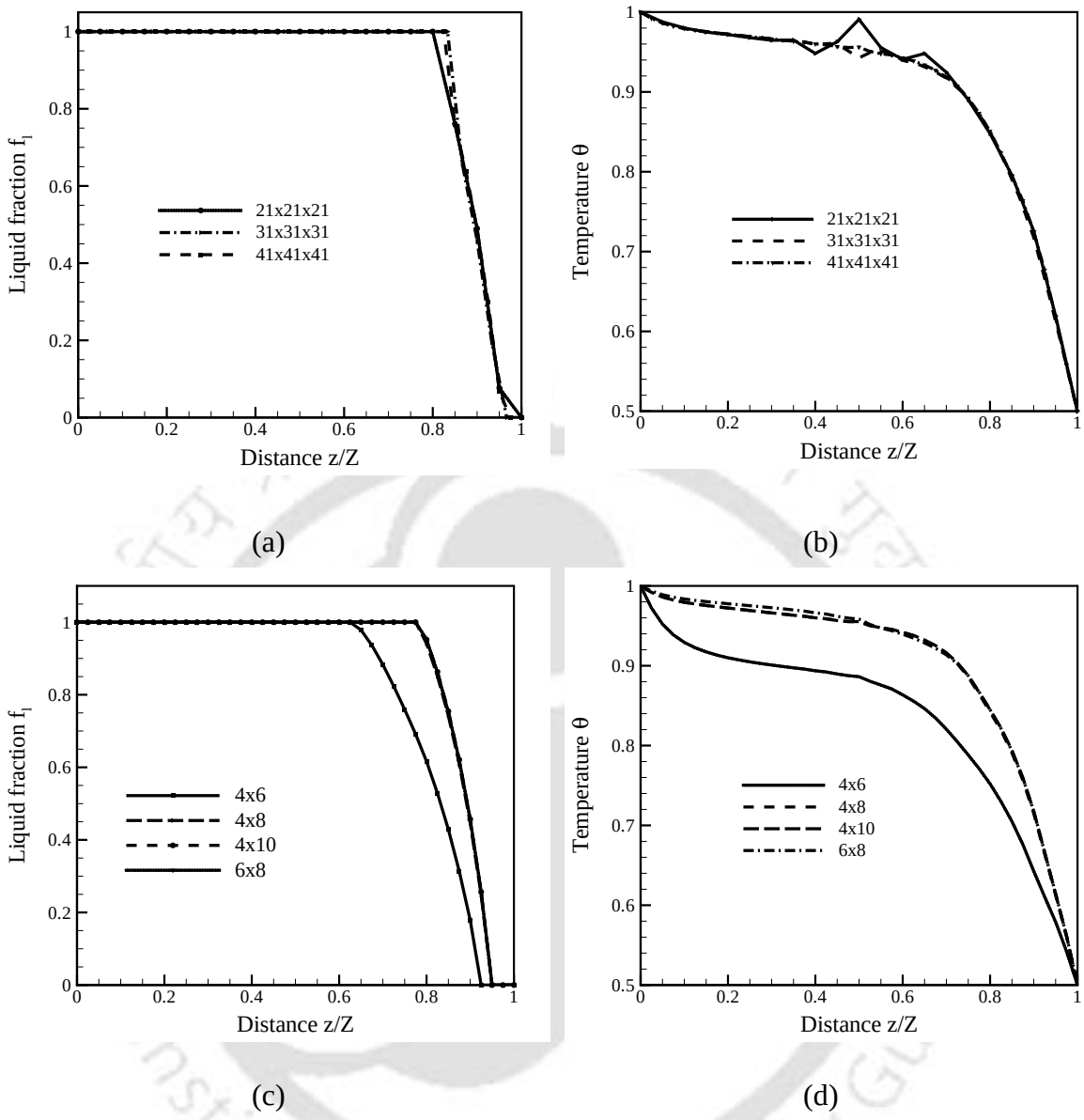

Figure 6.2: Grid- and ray- independency tests: effects of number of lattices/control volumes on centre line (a) liquid fraction (b) temperature distribution for 4×8 rays; Effects of number of rays on centerline (c) liquid fraction (d) temperature distribution for 41×41 lattices/control volumes.

With $41\times41\times41$ lattices/control volumes, effects of different number of rays on centerline ($\frac{x}{X}=0.5$, $\frac{y}{Y}=0.5$) liquid fraction f_l and the temperature θ distributions along

$\frac{z}{Z}$ are shown in Figs. 6.2c and 6.2d, respectively. No significance change is observed in f_l and θ distributions beyond 4×8 rays.

For the problem under consideration, all results are, therefore, presented for $41\times41\times41$ lattices/control volumes and 4×8 rays.

In present study, material properties considered are those given in [1, 8]. The ratio of the thermal conductivity of materials in liquid-zone and solid-zone is $k_l/k_s = 0.6$, mushy-zone to solid-zone is $k_{mz}/k_s = 0.76$, the ratio of heat capacity of liquid-zone to solid-zone is $C_l/C_s = 1.2$ and mushy-zone to solid-zone is $C_{mz}/C_s = 1.12$. The numerical values of thermal diffusivity α for the three regions are calculated from the knowledge of the above ratios. The temperatures $\theta = \frac{T}{T_0}$ at the solid-mushy and mushy-liquid interfaces were set at 0.6 and 0.8, respectively.

6.3.1 Solidification of a 3-D semitransparent medium with all boundaries at specified temperatures: Effects of the scattering albedo ω on liquid fraction f_l and temperature θ distributions along the centreline $\left(\frac{x}{X}=0.5, \frac{y}{Y}=0.5, \frac{z}{Z}\right)$ are shown in Figs. 6.3a-f. These results are given for the extinction coefficient $\beta = 1.0$, the conduction radiation parameter $N = 0.1$ and the latent heat $L = 1.0$. For every value of ω, results are shown at 4 different time levels. In Figs. 6.3a and 6.3b, results are given for an absorbing-emitting medium $\omega = 0.0$. It is seen from Fig 4a that with time t, the mushy zone thickness increases. With $\omega = 0.0$, radiation effect is more, thus in Fig. 6.3b, temperature gradient is more. For an absorbing, emitting and isotropically scattering medium with $\omega = 0.5$ and 0.9, f_l and θ profiles at different times are shown in Fig 6.3c,

6.3d and Fig. 6.3e, 6.3f, respectively. From Figs. 6.3a, 6.3c and 6.3e, it is observed that with increase in ω, thickness of the mushy-zone increases and from Figs. 6.3b, 6.3d and 6.3f, it is seen that temperature gradient decreases. When $\omega = 0.9$, along the centerline $\left(\frac{x}{X} = 0.5, \frac{y}{Y} = 0.5, \frac{z}{Z} \right)$, at time $t = 5.0$ s, no liquid-zone is observed. This is because of the fact that with increase in ω, the medium scatters more energy (Eq. (19)), and thus it is able to hold less radiation.

With $\beta = 1.0$, $\omega = 0.5$ and $L = 1.0$, effects of conduction-radiation parameter N on centreline $\left(\frac{x}{X} = 0.5, \frac{y}{Y} = 0.5, \frac{z}{Z} \right)$ liquid fraction f_l and temperature θ distributions at different instants t are shown in Fig. 6.4a-f. In Figs. 6.4a and 6.4b, results are given for $N = 0.01$. Here, thickness of the mushy-zone is less (Fig. 6.4a) and high temperature gradients are observed (Fig. 6.4b). $N = 0.01$ corresponds to radiation dominated case and thus the movement of the mushy-zone is slow. For $N = 0.1$ and $N = 1.0$, the liquid fraction f_l profiles are shown in Fig 6.4c and Fig. 6.4e, respectively. For $N = 0.1$ and $N = 1.0$, the θ profiles are shown in Fig 6.4d and 6.4f, respectively. The mushy zone thickness is more for higher values of N (conduction dominated situation) and its movement is also fast. In the mushy zone, the temperature gradient is less in the conduction dominated ($N = 1.0$) case. It is to be noted that in the case of conduction dominated situation ($N = 1.0$), the f_l and θ profiles do not change as time progresses from for $t = 1.0$ s to $t = 5.0$ s (Figs. 6.4e and 6.4f).

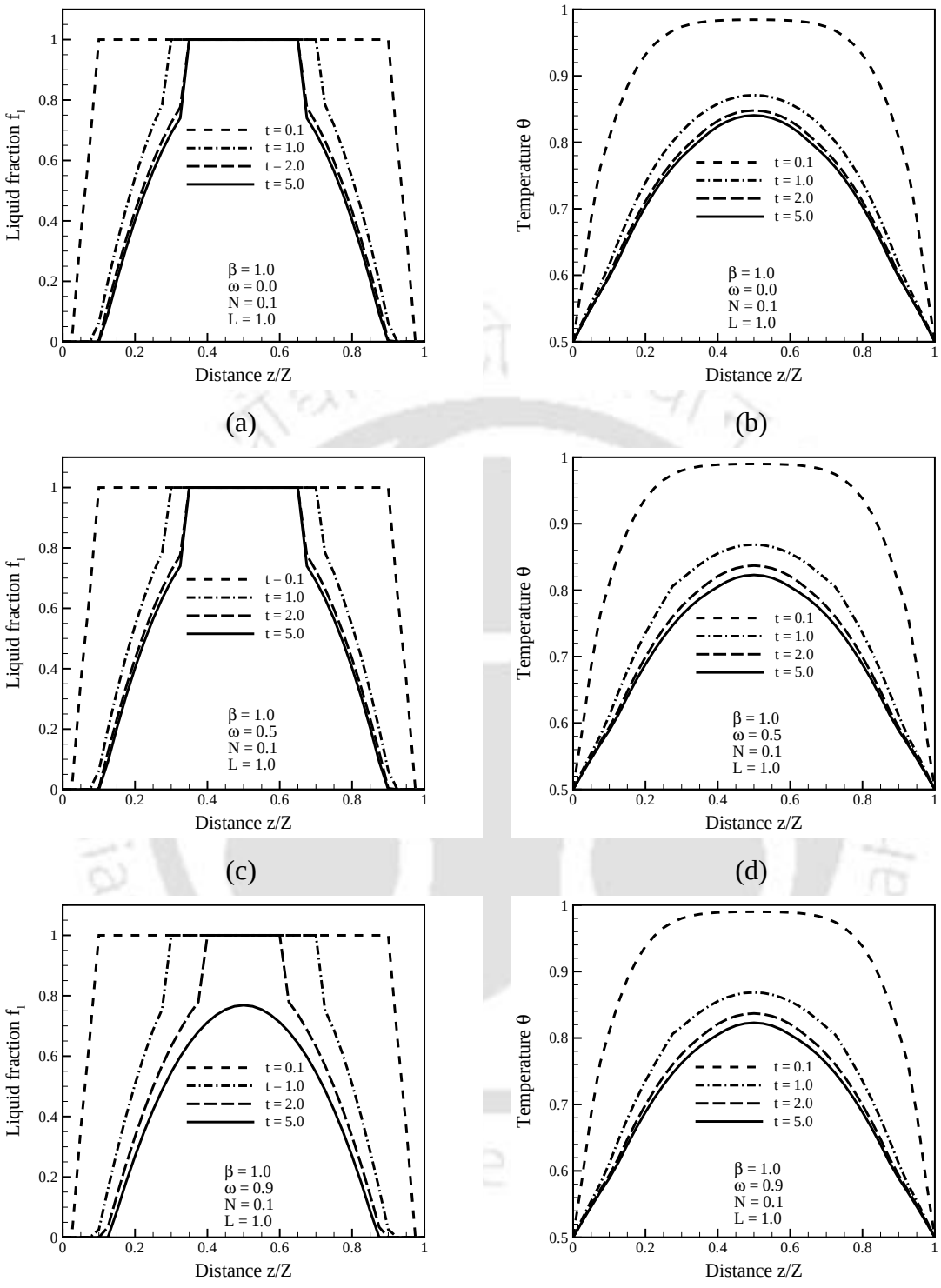

Figure 6.3: Transient value of centre line liquid fraction and temperature variations of the cubical enclosure for $\beta = 1.0$, $N = 0.1, L = 1.0$ and (a), (b) $\omega = 0.0$, (c), (d) $\omega = 0.5$ and (e), (f) $\omega = 0.9$.

Effects of the extinction coefficient β on centerline $\left(\frac{x}{X}=0.5,\frac{y}{Y}=0.5,\frac{z}{Z}\right)$ liquid fraction f_l and temperature θ profiles at different times are shown in Figs. 6.5a-f. In this case, the other parameters are taken as $\omega=0.0$, $N=0.1$ and $L=1.0$. The liquid fraction f_l profiles are shown in Fig. 6.5a, 6.5c and 6.5e for $\beta=0.1$, $\beta=1.0$ and $\beta=3.0$, respectively. In case of a radiatively less participating medium ($\beta=0.1$), it is found that f_l and θ profiles do not change after $t=1.0$ s. With increase in β, the mushy-zone thickness is found to decrease. From Figs. 6.5b, 6.5d and 6.5f, it is observed that θ profiles become steeper with increase in β. In case of a radiatively more participating medium (higher values of β), the mushy-zone thickness is less and temperature gradient is high. The movement of mushy-zone is fast in case of a radiatively less participating medium ($\beta=0.1$). This is because, in this case, radiation penetrates to a higher depth.

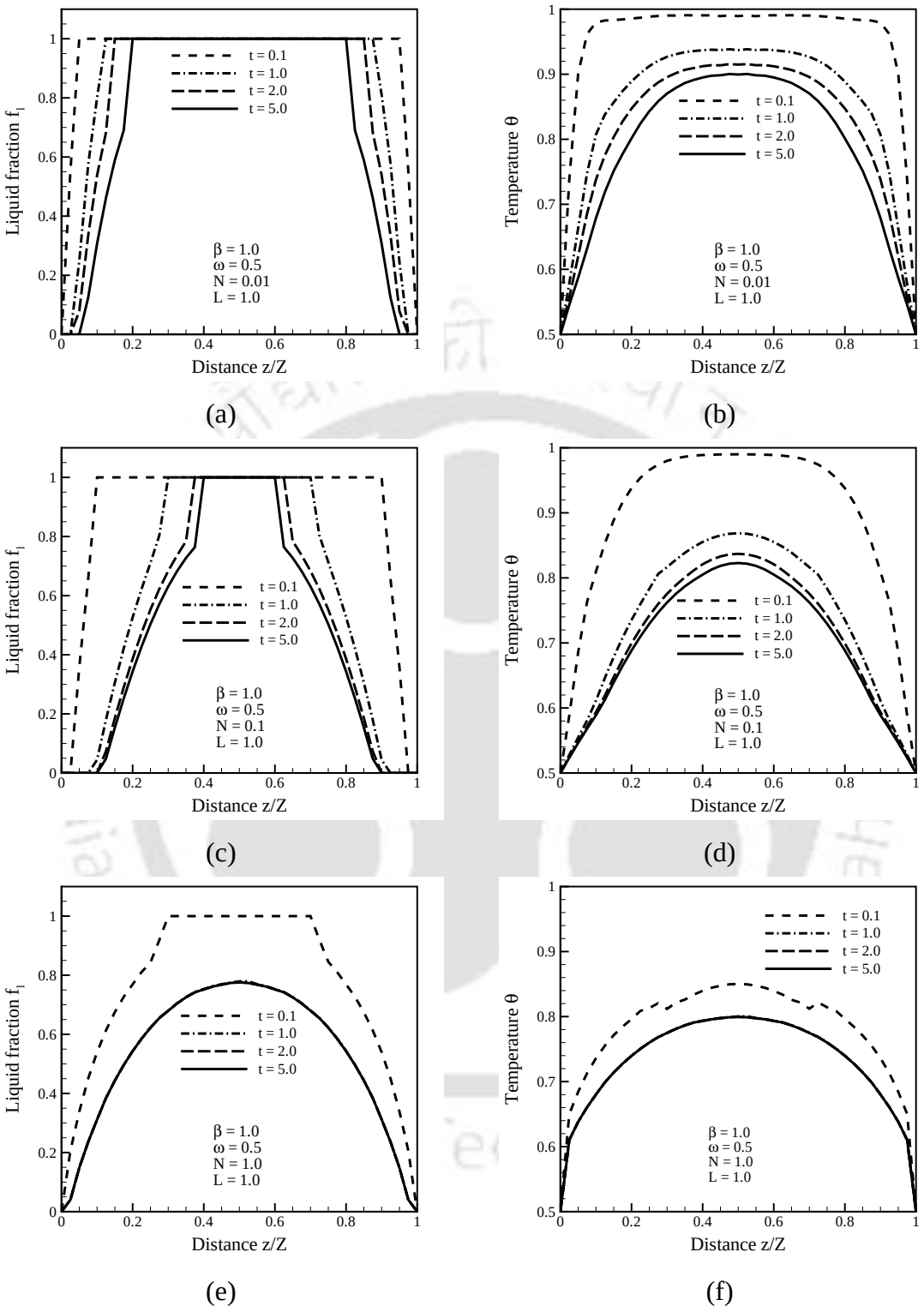

Figure 6.4: Transient value of centre line liquid fraction and temperature variations of the cubical enclosure for $\beta = 1.0$, $\omega = 0.5$, $L = 1.0$ and (a), (b) $N = 0.01$, (c), (d) $N = 0.1$ and (e), (f) $N = 1.0$.

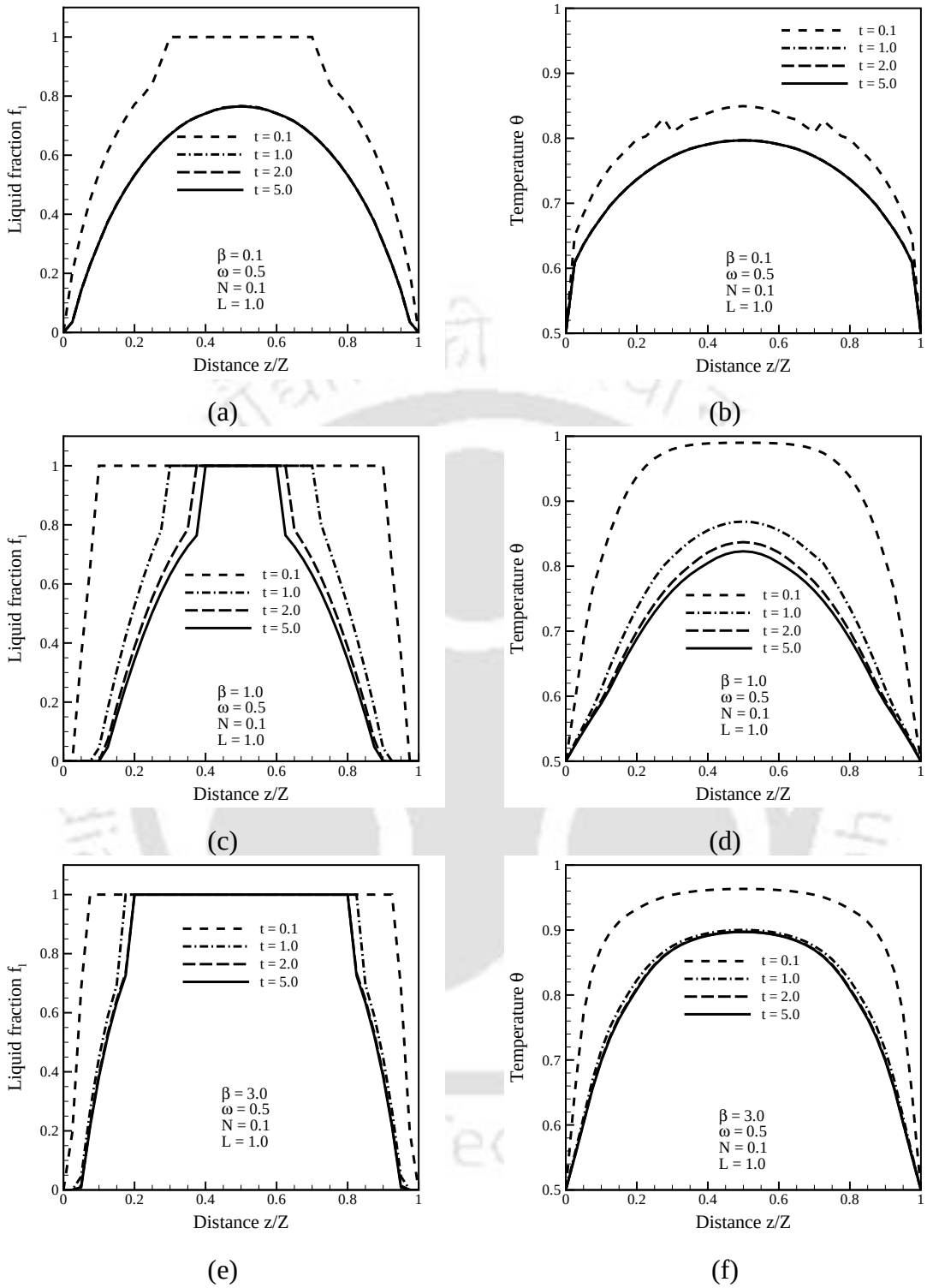

Figure 6.5: Transient value of centre line liquid fraction and temperature variations of the cubical enclosure for $\omega = 0.5$, $N = 0.1$, $L = 1.0$ and (a), (b) $\beta = 0.1$, (c), (d) $\beta = 1.0$ and (e), (f) $\beta = 3.0$.

Effects of the latent heat L on centreline $\left(\frac{x}{X}=0.5,\frac{y}{Y}=0.5,\frac{z}{Z}\right)$ liquid fraction f_l and temperature θ distributions at different times are shown in Fig. 6.6. These results are shown for $\beta=1.0$, $\omega=0.0$ and $N=0.1$. For $L=1.0$, in Figs. 6.6a and 6.6b, results are shown for liquid fraction f_l and temperature θ, respectively. For $L=10.0$ and $L=100.0$, f_l and θ profiles are given in Fig. 6.6c-f. For a higher values of L, the mushy-zone thickness decreases and temperature gradient is steeper in the mushy-zone. This trend is attributed to the fact that when L is large, a phase change from liquid to solid requires more energy.

In Figs. 6.7a-d, liquid fraction f_l contours are shown for $\beta=1.0$, $N=0.1$, $\omega=0.5$ and $L=1.0$. At four different time t levels, these contours are plotted in the $y-z$ plane at $\frac{x}{X}=0.5$. In Figs. 6.7a-d, liquid fraction f_l contours are shown at time $t=0.1,1.0,2.0$ and 5.0s, respectively. The mushy-zone thickness is found to increase with time. It is observed from Figs. 6.7a and 6.7b that in the early stage, the mushy-zone grows at a faster rate but its movement becomes slow at later stages (Fig 6.7c and 6.7d).

For $\beta=1.0$, $N=0.1$, $\omega=0.5$ and $L=1.0$, temperature θ contours in the $y-z$ plane at $\frac{x}{X}=0.5$ are shown in Figs. 6.8a-d at four different time t levels. At an early stage (Fig. 6.8a, $t=0.1$s), temperature of the medium is very high. Very close to the south and the north boundaries, the temperature is less. In Fig 6.8b, for at $t=1.0$ s, it is seen that near the south and the north boundaries, temperature decrease is fast. With the passage of time, temperature gradient decreases (Figs. 6.8c and 6.8d). Since the south and the north boundaries are maintained at the same temperature, which is lower than the freezing temperature T_f, the solidification starts from these boundaries and gives the symmetrical temperature profiles in the $y-z$ plane at $\frac{x}{X}=0.5$.

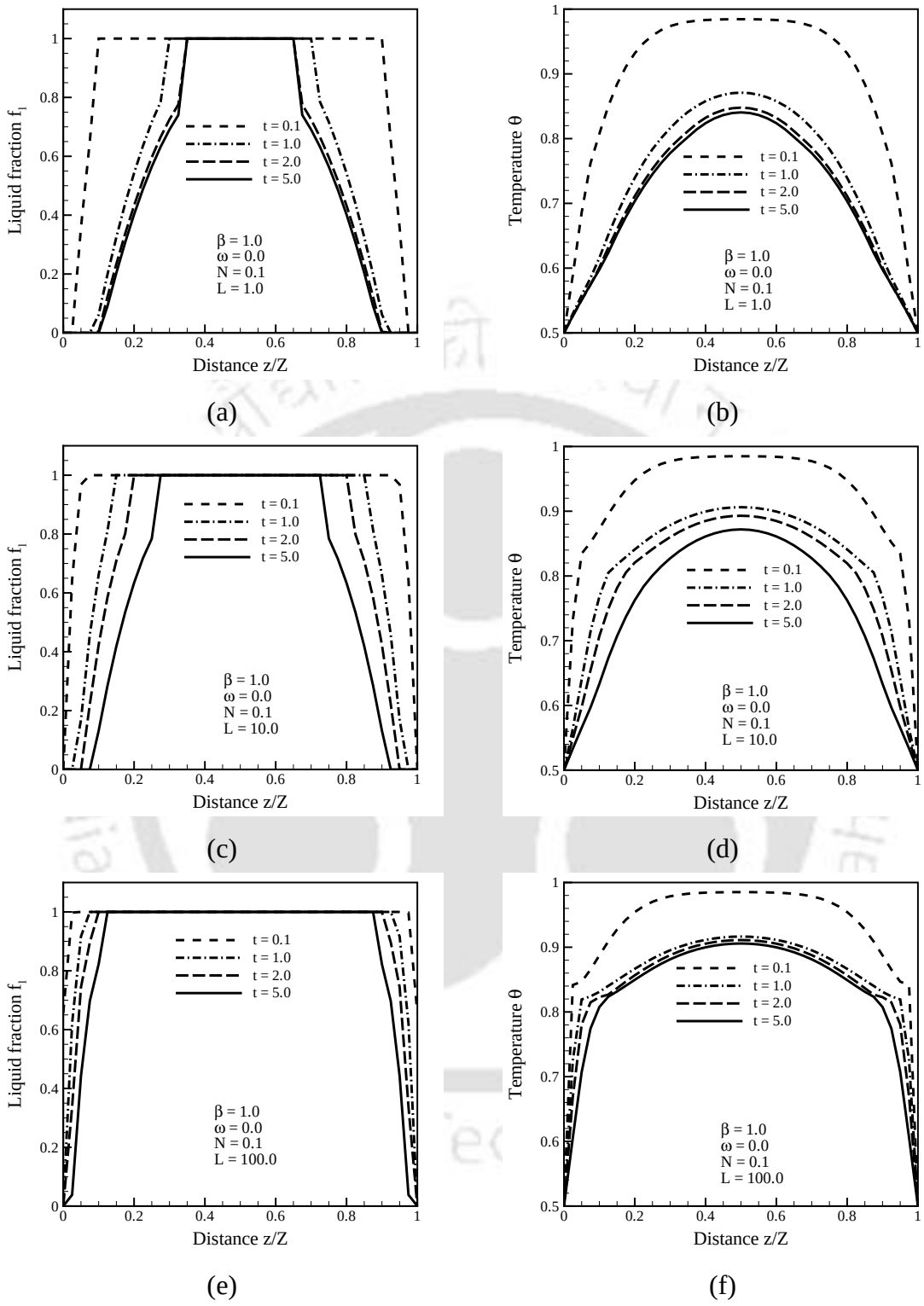

Figure 6.6: Transient value of centre line liquid fraction and temperature variations of the cubical enclosure for $\beta = 1.0$, $N = 0.1$, $\omega = 0.5$ and (a), (b) $L = 1.0$, (c), (d) $L = 10.0$ and (e), (f) $L = 100.0$.

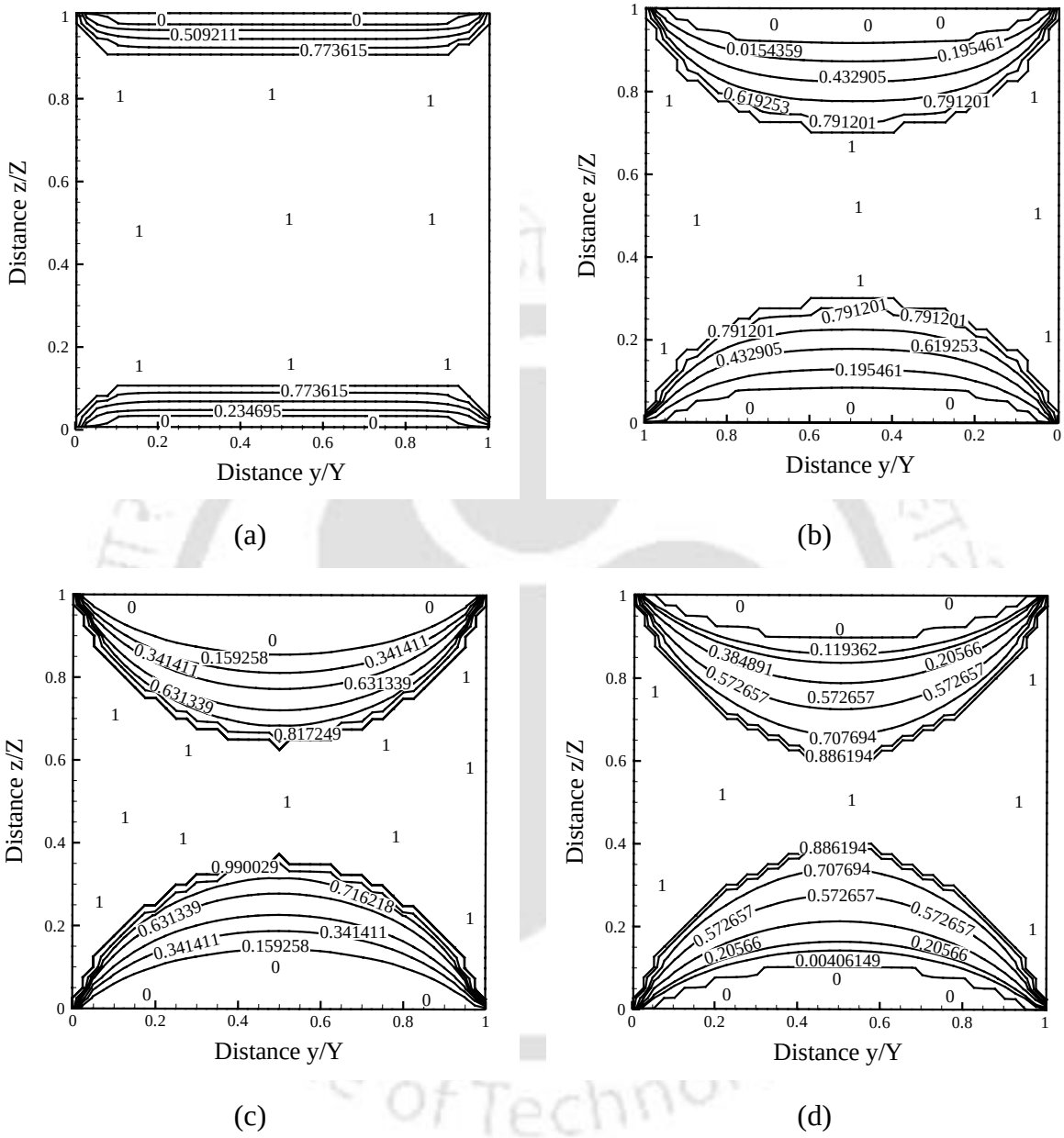

Figure 6.7: Liquid fraction f_l contours at time (a) $t = 0.1\,\text{s}$ (b) $t = 1.0\,\text{s}$ (c) $t = 2.0\,\text{s}$ (d) $t = 5.0\,\text{s}$ for $\beta = 1.0, \omega = 0.5, N = 0.1, L = 1.0$.

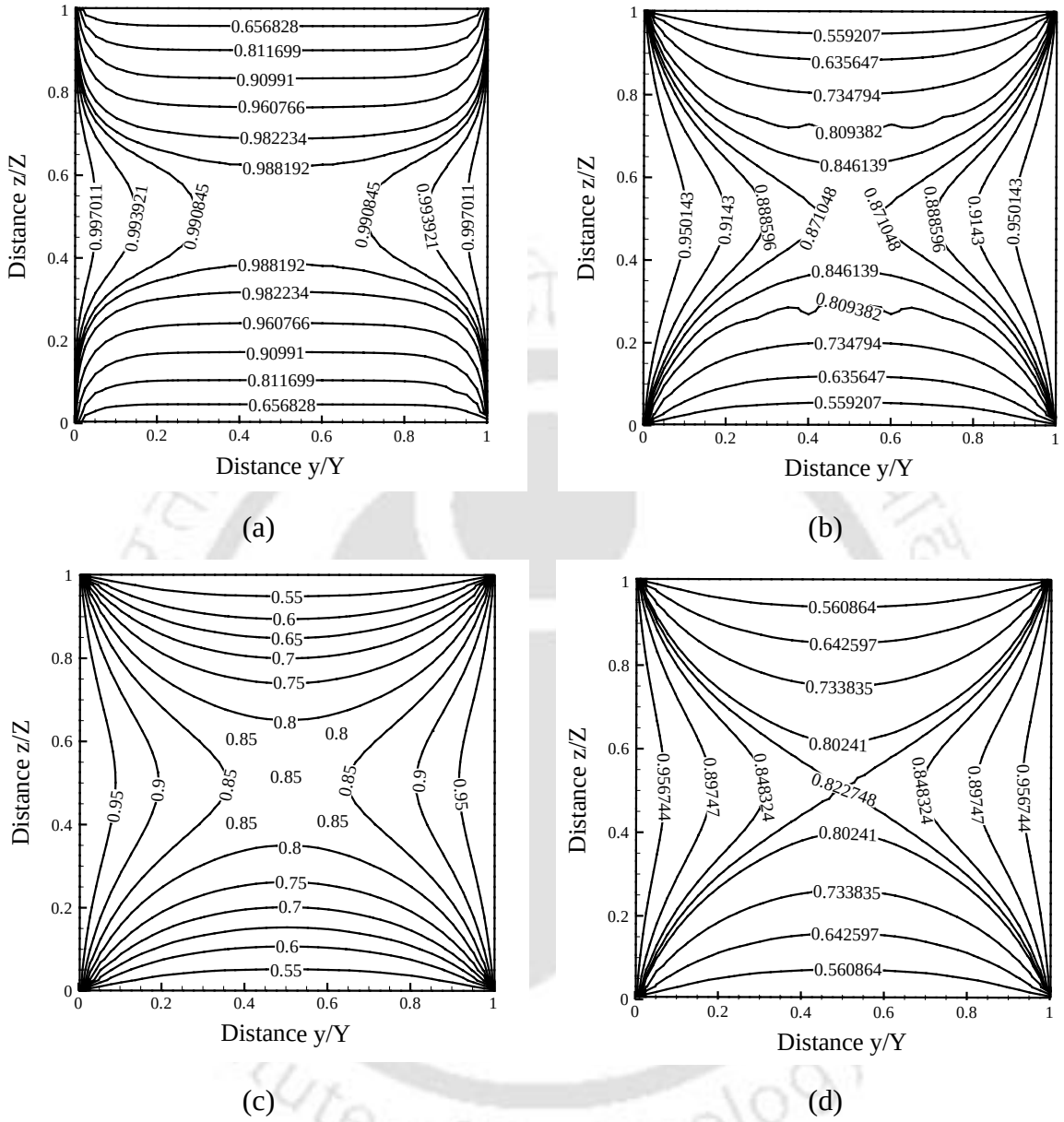

Figure 6.8: Temperature θ contours at time (a) $t = 0.1$s (b) $t = 1.0$s (c) $t = 2.0$s (d) $t = 5.0$s for $\beta = 1.0, \omega = 0.5, N = 0.1, L = 1.0$.

6.3.2 Solidification of a 3-D semitransparent medium with one of its boundaries at constant heat flux: Effects of heat flux $q_{T,S}$ extraction from south boundary on centreline $\left(\frac{x}{X}=0.5,\frac{y}{Y}=0.5,\frac{z}{Z}\right)$ liquid fraction f_l and temperature θ profiles are shown in Figs. 6.9a-f. These results are shown at four different time levels. For these results, parameters are taken as $\beta=1.0$, $N=0.1$, $\omega=0.5$ and $L=1.0$. For results in Figs. 6.9a and 6.9b, $q_{T,S}=1.0$. $q_{T,S}=2.0$ and 3.0 have been taken for results in Figs. 6.9c, 6.9d and 6.9e, 6.9f, respectively. It is observed from Figs. 6.9a, 6.9c and 6.9e, it is observed that with passage of time, thickness of the mushy-zone increases. It is further observed that with increase in the value of the extracted heat flux $q_{T,S}$, the solidification is more rapid. It is seen from Figs. 6.9b, 6.9d and 6.9f that with increase in $q_{T,S}$, temperature θ gradient increases. For a given value of $q_{T,S}$, with time, temperature θ gradient decreases. When heat extraction is more, solidification becomes fast and thus at a given instant, temperature variation in the medium will be more.

All computations in the present work were carried out with $\Delta t=0.001$. In every case, transience was observed for 5 s. Thus, all the runs were taken for 5000 iterations. On a computer with CPU (512 MB, 2.8 GHz with hyper threading), a typical run took about 10 hours. For various cases, runs ranged from 10-12 hours.

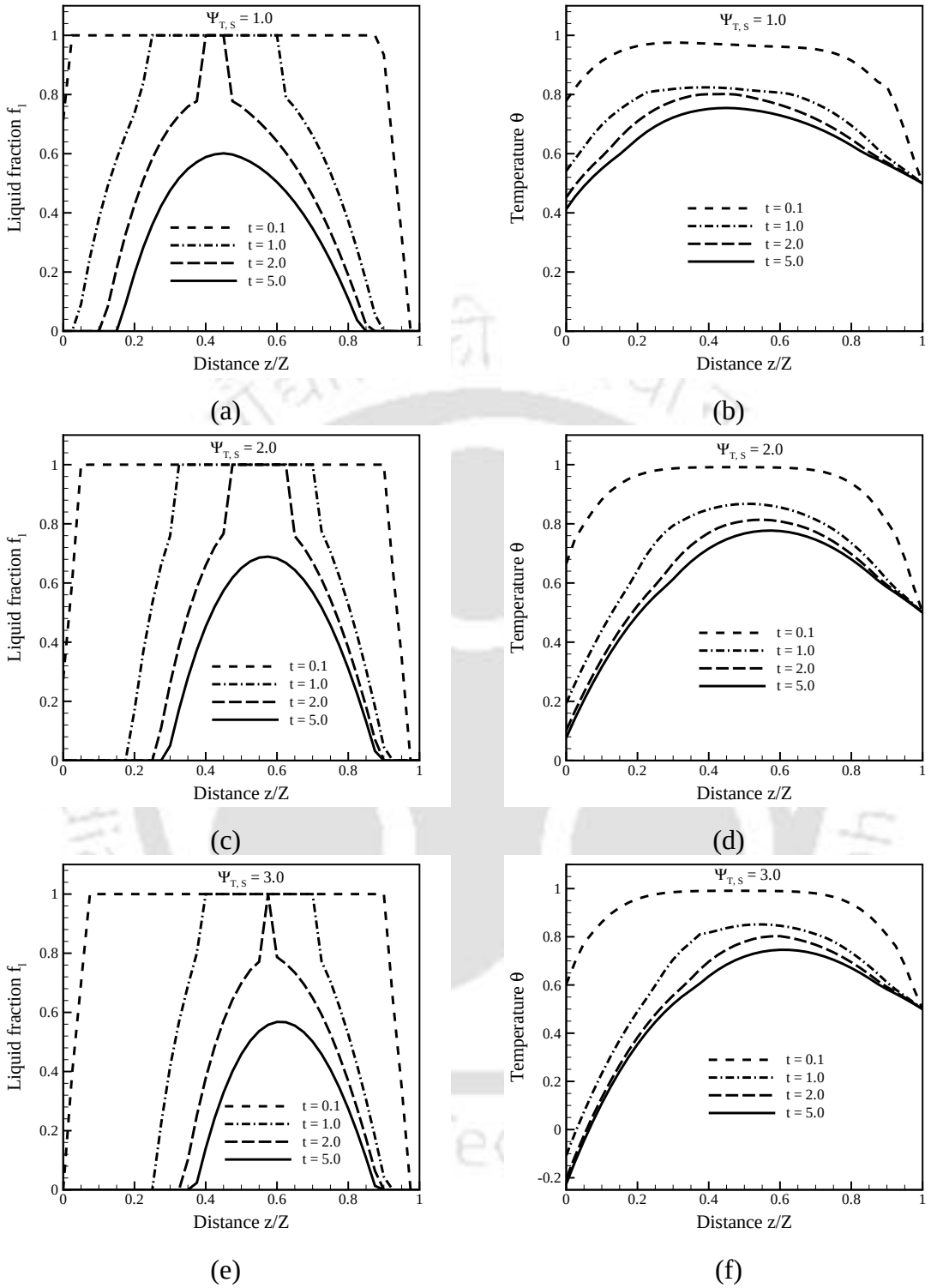

Figure 6.9: Transient value of centre line liquid fraction f_l and temperature θ profiles of the cubical enclosure for $\beta = 1.0$, $N = 0.1$, $\omega = 0.5$, $L = 1.0$ and (a), (b) $\Psi_{T,S} = 1.0$, (c), (d) $\Psi_{T,S} = 2.0$ and (e), (f) $\Psi_{T,S} = 3.0$.

6.4 Summary

Solidification of a 3-D cubical semitransparent absorbing, emitting and scattering semitransparent medium in the presence of volumetric radiation was analyzed. An enthalpy based LBM was used to analyze the solidification process. Radiative information was computed using the FVM. Over a range of temperatures, a distinct liquid-, mushy- and solid- zones were considered. Cases of both Dirichlet and Neumann boundary conditions were taken up. Liquid fraction and temperature distributions in the medium were analyzed for the effects of the extinction coefficient, the scattering albedo, the conduction-radiation parameter and the latent heat.

CHAPTER 7

Natural Convection in the Presence of Volumetric Radiation

7.1 Introduction

Radiation combined with convection and/or conduction finds applications in the analysis and design of combustors, high temperature heat exchangers, spacecrafts, thermal insulations, electronic cooling devices and industrial furnaces. In recent years, analysis of natural convection with and without radiation has received considerable attention [74, 77, 96, 104, 105, 166-171].

Natural convection in the presence of a heat generating body in an air filled vertical enclosure was analyzed by Oh *et al.* [166]. Ha *et al.* [167] studied natural convection in a differentially heated vertical cubic enclosure containing a cubic heat generating body. Interaction between thermal radiation and laminar mixed convection for ascending flows of absorbing and emitting gases in a vertical tube was analyzed by Sediki *et al.* [168]. They considered temperature dependent thermo-physical properties. Balaji and Venkateshan [169] studied interaction of surface radiation with free convection in an air filled open cavity. Steady combined natural convection and surface radiation heat transfer in a two-dimensional side vented open cavity for different aspect ratios, side vent ratios and surface emissivities using air as the fluid medium were studied by Singh and Venkateshan [170]. Conjugate turbulent natural convection and surface radiation in rectangular enclosures heated from below and cooled from other walls was investigated by Sharma *et al*. [171]. They included the effects of various aspect ratios also. Several

other authors [74, 77, 96, 104, 105] have also investigated various aspects of the natural convection in different configurations and they have used different numerical techniques to analyze their problems.

In recent years, the lattice Boltzmann method (LBM) has emerged as a promising computational tool [25]. Owing to its mesoscopic origin, in comparison with conventional fluid dynamics solvers, it offers some advantages like simple calculation procedure, simple and efficient implementation for parallel computation, and easy and robust handling of complex geometries. Like its application to fluid flow problems [23, 25], the LBM has been applied to a wide range of heat transfer problems [18, 22, 24, 27, 100, 150, 151, 172]. Quite recently, natural convection problems have also been investigated using the LBM [74, 77, 96, 104, 105].

Numerical simulation of natural convection in a square cavity on both uniform and non-uniform grids using the LBM was analyzed by Shu *et al*. [74]. Seta *et al*. [77] investigated applicability of the LBM in simulating natural convection in porous media. In their work, temperature field was simulated by a simplified thermal energy distribution function which neglected the compression work done by pressure and viscous heat dissipation. Dixit and Babu [96] used a thermal LBM based on the BGK model to simulate high Rayleigh number natural convection in a square cavity. To avoid requirement of unreasonably high uniform grid for higher Rayleigh numbers, the interpolation supplemented LBM was used in their study. A double population thermal LBM was proposed by Kuznik *et al*. [104] to solve the problem of the heated cavity with imposed temperatures. A non-uniform mesh was used to reduce the computational cost at a high Rayleigh number. A numerical investigation of laminar convective flows in a differentially heated, square enclosure with heat conducting cylinder in its centre was carried out by Jami *et al*. [105]. With suitable coupling accounting for the natural convection, in their work, flow and temperature fields were computed using the LBM and the finite difference method, respectively.

With radiation, natural convection in a rectangular enclosure has not been investigated in much detail. In [169-171], effects of surface radiation on natural convection in a 2-D rectangular geometry were studied and radiation was found to be a significant effect on velocity and temperature distributions in the medium. However, in [169-171], the medium was considered non-participating and radiation appeared only in the form of boundary conditions. In [173], Tan and Howell studied natural convection in a 2-D enclosure containing a radiatively participating medium. They computed radiative information using the product-integral method and the finite difference method was employed to solve the momentum and energy equations. They found that in the presence of radiation, bulk temperature of fluid increased and fluid flow and temperature distributions in the medium were greatly influenced. Banda et al [174] have studied coupled convection-radiation problem and they have used non-oscillatory relaxation scheme in the LBM. Their work stressed on studying the workability of the third order non-oscillatory relaxation scheme in the LBM, and thus effects of radiative parameters were not studied.

The objective of the present work is to use the LBM to simulate natural convection in a 2-D square cavity in the presence of volumetric radiation and, therefore, to study the effects of various parameters such as the extinction coefficient and the scattering albedo on flow filed and temperature distributions. The FVM [120] which is a robust method for computation of radiative information is used to calculate divergence of radiative heat flux required in the energy equation. Formulation for FVM to compute radiative information already explained in chapter 2. The LBM formulation for the velocity field and thermal field are discussed in the following sections.

7.2 Formulation

Let us consider a square cavity as shown in Fig. 7.1. Its bottom and top walls are adiabatic and left and right walls are at temperatures T_H and T_C $(T_H > T_C)$, respectively. Thermo-physical properties, except density, are assumed constant. Density is considered

to vary in the Boussinesq sense. Radiatively, the homogeneous medium in the cavity is absorbing, emitting and scattering, and its optical properties such as the extinction coefficient β and scattering albedo ω are constant. The boundaries of the cavity are considered diffuse-gray.

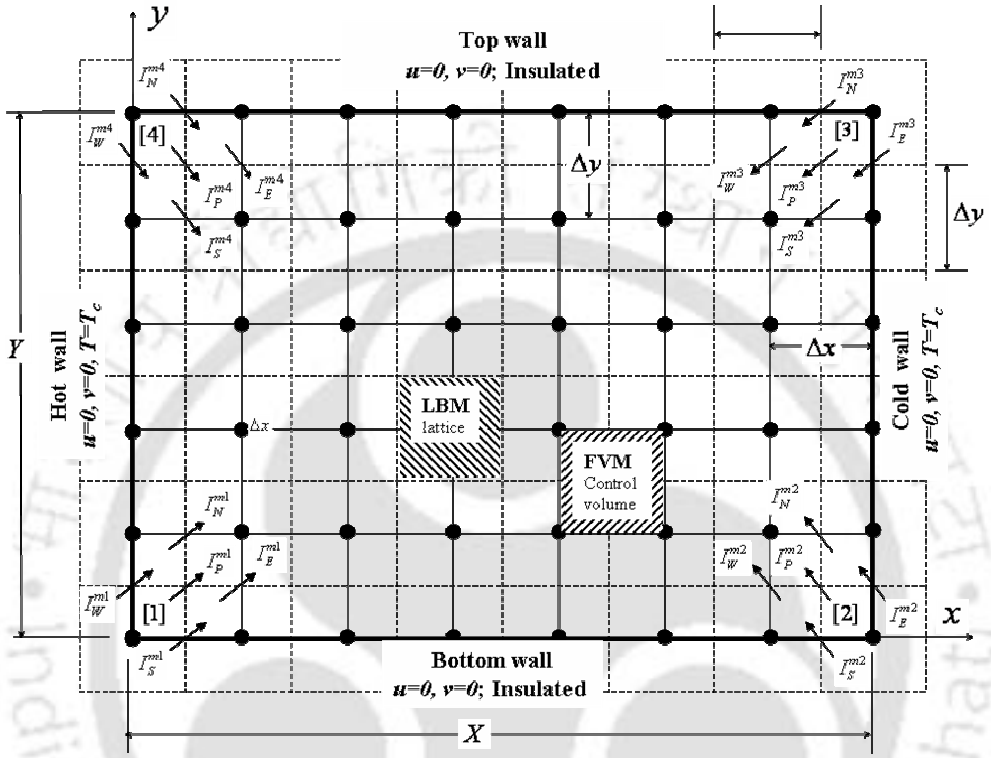

(a)

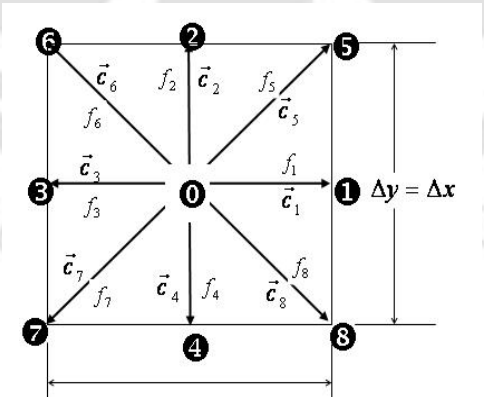

(b)

Figure 7.1: (a) Geometry of the 2-D square cavity under consideration. Arrangement of lattices and control volumes along with the marching scheme in the FVM for four samples equally spaced directions with one in every quadrant are also shown and (b) D2Q9 lattice.

7.2.1 Lattice Boltzmann Equation for Density and Velocity Fields

In the LBM formulation, for computation of density (and velocity) and thermal fields, separate particle distribution functions are used. For computation of density and velocity fields, the governing lattice Boltzmann equation is given by [24, 96]

$$f_i\left(\vec{r}+c_i\Delta t, t+\Delta t\right) = f_i\left(\vec{r},t\right) - \frac{\Delta t}{\tau_v}\left[f_i\left(\vec{r},t\right) - f_i^{(eq)}\left(\vec{r},t\right)\right] + \Delta t \times F \tag{7.1}$$

where f_i is the particle distribution function, c_i is the microscopic velocity, τ_v is the relaxation time, $f_i^{(eq)}$ is the equilibrium distribution function and F is the external force term.

For the D2Q9 lattice (Fig. 7.1c) used in the present work, the relaxation time τ_v is computed from [24,96]

$$\tau_v = \frac{3\nu}{C^2\Delta t} + \frac{1}{2} \tag{7.2}$$

where lattice speed $C = \sqrt{3RT}$ and R is the ideal gas constant.

With Prandtl number Pr and Rayleigh number Ra known, the kinetic viscosity ν appearing in Eq. (7.2) is computed from simultaneously solving the following two equations:

$$\mathrm{Pr} = \frac{\upsilon}{\chi} \tag{7.3}$$

$$Ra = \frac{\beta_t g_0 \left(T_H - T_C\right) \times H^3}{\upsilon\chi} \tag{7.4}$$

where χ is the thermal diffusivity, β_t is the coefficient of thermal expansion, g_0 is the acceleration due to gravity, T_H is the hot wall temperature, T_C is the cold wall temperature and H is height and width of the cavity.

In Eq. (7.4), $\beta_t g_0$ is given by

$$\beta_t g_0 = \frac{|\vec{u}|^2}{\Delta T \times H} \tag{7.5}$$

where in Eq. (7.5), the characteristic velocity of the flow $\vec{u} = Ma \times C/\sqrt{3}$. It is to be noted that to ensure that the flow is fully in the incompressible regime, the Mach number Ma was set to 0.1 in all the calculations.

The 9 velocities $\vec{c}_i$ in the D2Q9 (Fig. 7.1c) lattice are given by:

$$\vec{c}_i = \begin{cases} 0 & i = 0 \\ C\left\{\cos\left[(i-1)\pi/2\right], \sin\left[(i-1)\pi/2\right]\right\} & 1 \le i \le 4 \\ \sqrt{2}C\left\{\cos\left[(i-5)\pi/2 + \pi/4\right], \sin\left[(i-5)\pi/2 + \pi/4\right]\right\} & 5 \le i \le 8 \end{cases} \tag{7.6}$$

The equilibrium function for the density distribution function is given as

$$f_i^{(eq)} = w_i \rho \left[1 + \frac{3(\vec{c}_i \cdot \vec{u})}{C^2} + \frac{9(\vec{c}_i \cdot \vec{u})}{2C^4} - \frac{3\vec{u}^2}{2C^2}\right], \; 0 \le i \le 8 \tag{7.7}$$

For the D2Q9 model, the weights are given as

$$w_i = \begin{cases} 4/9 & i = 0 \\ 1/9 & 1 \le i \le 4 \\ 1/36 & 5 \le i \le 8 \end{cases} \tag{7.8}$$

The external force term F in Eq. (7.1) is given by

$$F = \left[\frac{\vec{G} \cdot (\vec{c}_i - \vec{u})}{RT}\right] f_i^{(eq)} \tag{7.9}$$

In Eq. (7.9), $\vec{G}$ is the external force acting per unit mass and it is given by [96]

$$\vec{G} = \rho \beta_t g (T - T_m) \vec{j} \tag{7.10}$$

where the unit vector $\vec{j}$ is in a direction opposite to gravity. The density ρ varies in Boussinesq sense and it is given by

$$\rho = \bar{\rho}\left[1 - V_c (T - T_m)\right] \tag{7.11}$$

where $\bar{\rho}$ is the density of the fluid at the mean temperature T_m.

7.2.2 Lattice Boltzmann Equation for Thermal Field

For computation of thermal field, in the presence of volumetric radiation, the governing lattice Boltzmann equation is given by [22,100]

$$g_i\left(\vec{r}+\vec{c}_i\Delta t, t+\Delta t\right) = g_i\left(\vec{r},t\right) - \frac{\Delta t}{\tau_t}\left[g\left(\vec{r},t\right) - g_i^{(eq)}\left(\vec{r},t\right)\right] - \left(\frac{\Delta t}{\rho c_p}\right) w_i \nabla\cdot\vec{q}_R \qquad (7.12)$$

where g_i is the particle distribution function denoting the evolution of the internal energy, τ_t is the relaxation time, $g_i^{(eq)}$ is the equilibrium distribution function and $\vec{q}_R$ is the radiative heat flux.

In Eq. (7.12), τ_t is given by

$$\tau_t = \frac{1.5\chi}{C^2\Delta t} + \frac{1}{2} \qquad (7.13)$$

Equilibrium distribution functions for thermal energy are given as

$$g_i^{(eq)} = -w_i\rho e\left(\frac{3}{2}\frac{\vec{u}^2}{C^2}\right), \qquad i=0 \qquad (7.14a)$$

$$g_i^{(eq)} = w_i\rho e\left[\frac{3}{2} + \frac{3\left(\vec{\xi}_i\cdot\vec{u}\right)}{2C^2} + \frac{9\left(\vec{\xi}_i\cdot\vec{u}\right)^2}{4C^4} - \frac{3\vec{u}^2}{2C^2}\right], \; 1\le i\le 4 \qquad (7.14b)$$

$$g_i^{(eq)} = w_i\rho e\left[3 + \frac{6\left(\vec{\xi}_i\cdot\vec{u}\right)}{C^2} + \frac{9\left(\vec{\xi}_i\cdot\vec{u}\right)}{2C^4} - \frac{3\vec{u}^2}{2C^2}\right], \; 5\le i\le 8 \qquad (7.14c)$$

The macroscopic density ρ, velocity $\vec{u}$ and internal energy e are computed from the following:

$$\rho = \sum_i f_i \qquad (7.15a)$$

$$\vec{u} = \frac{1}{\rho}\sum_i \vec{c}_i f_i \qquad (7.15b)$$

$$e = \frac{1}{\rho}\sum_i g_i \tag{7.15c}$$

Temperature is calculated from the equation of state, $e = RT$.

7.2.3 Implementation of Boundary Conditions

In solving the hydrodynamic field, no-slip condition was imposed along all the four walls. In implementing the same in the LBM, unknown distribution functions at a given wall are assumed to be an equilibrium distribution function with a counter-slip velocity. In the LBM, the unknown particle distribution functions are those that are directed into the medium. For example, with D2Q9 lattice shown in Fig. 7.1c, for the lattices along the bottom wall, f_2, f_5 and f_6 are the unknown particle distribution functions. These are computed from the following [36,175]

$$f_2 = \frac{1}{9}\rho' \left\{1 + 3v_w + 4.5v_w^2 - 1.5\left[\left(u_w + u'\right)^2 + v_w^2\right]\right\} \tag{7.16}$$

$$f_5 = \frac{1}{36}\rho' \left\{1 + 3\left(u_w + u' + v_w\right) + 4.5\left(u_w + u' + v_w\right)^2 - 1.5\left[\left(u_w + u'\right)^2 + v_w^2\right]\right\} \tag{7.17}$$

$$f_6 = \frac{1}{36}\rho' \left\{1 + 3\left(-u_w - u' + v_w\right) + 4.5\left(-u_w - u' + v_w\right)^2 - 1.5\left[\left(u_w + u'\right)^2 + v_w^2\right]\right\} \tag{7.18}$$

where u_w and v_w are $x-$ and $y-$components of the wall velocity. In the above equations, there are two unknown parameters namely ρ' and u' which are calculated from the following

$$\rho' = 6\left[\rho_w v_w + \left(f_4 + f_7 + f_8\right) \Big/ \left(1 + 3v_w + 3v_w^2\right)\right] \tag{7.19}$$

$$u' = \frac{1}{1 + 3v_w}\left\{6\left[\rho_w u_w - \left(f_1 - f_3 + f_8 - f_7\right) \Big/ \rho'\right] - u_w - 3u_w v_w\right\} \tag{7.20}$$

Calculations of ρ' and u' require knowledge of the density at the wall ρ_w which is given by

$$\rho_w = 1 \Big/ 1 - v_w\left[f_0 + f_3 + f_3 + 2\left(f_4 + f_7 + f_8\right)\right] \tag{7.21}$$

The two vertical walls are maintained at constant temperatures $(T_H > T_C)$ and the two horizontal walls are adiabatic, $\left.\frac{\partial T}{\partial y}\right|_{(x,0)} = \left.\frac{\partial T}{\partial y}\right|_{(x,H)} = 0$. Eq. (2.20) is used to implement the radiative boundary condition for a diffuse-gray wall at a prescribed temperature. For an adiabatic wall, Eq. (2.20) is used after converting the flux boundary condition to temperature boundary condition. Since in this case, temperature along the wall is an unknown, unlike the known temperature boundary condition, in Eq. (2.20), both the emitted and reflected components of the boundary radiative intensity keep changing as the solution marches towards the steady-state. In implementing the thermal boundary conditions to the LBM, the same no-slip condition that was used for the velocity field was used. The constant heat flux boundary condition was converted to temperature condition by using a second order finite difference approximation.

The unknown distribution functions at the bottom wall for the thermal distribution functions are given by

$$g_2 = \frac{4}{9}\rho' \times \left(e_w + e'\right) \times \left[1.5 - 1.5 \times u' \times u'\right] \tag{7.22}$$

$$g_5 = \frac{1}{36}\rho' \times \left(e_w + e'\right) \times \left[3.0 + 6.0 \times u' + 3.0 \times u' \times u'\right] \tag{7.23}$$

$$g_5 = \frac{1}{36}\rho' \times \left(e_w + e'\right) \times \left[3.0 - 6.0 \times u' + 3.0 \times u' \times u'\right] \tag{7.24}$$

where e' is calculated from the following:

$$e' = \left(3.0 \big/ \rho'\right) \times \left[\left(\rho_w \times e_w\right) - g_0 + g_1 + g_3 + g_4 + g_7 + g_8\right] - e_w \tag{7.25}$$

In similar way, the no-slip boundary conditions can also be applied for other walls.

7.2.4 Solution Procedure

The control volumes of the FVM for the radiative heat transfer in computing the radiative information $\nabla \cdot \vec{q}_R$ and lattices in the LBM for computing the density, velocity and temperature are staggered as shown in Fig. 7.1a. Sizes of the lattices in the LBM and the

control volumes in the FVM are taken the same. In the FVM, in any control volume, intensity distributions are computed at the mid-points of the control surfaces and at the centre of the FVM control volume and thus as required in the LBM, $\nabla \cdot \vec{q}_R$ are not available at the lattice centres. For this, an averaging procedure is used to compute the $\nabla \cdot \vec{q}_R$ information required at the lattice centre.

The procedure to calculate the macroscopic quantities such as density, velocity and temperature is the following:

1. Input constant parameters such as Pr, Ra, β and ω.
2. Calculate relaxation times for density distribution functions and temperature distribution functions using Eqs. (7.2) and (7.13), respectively.
3. Initialize the velocity field and temperature field.
4. Compute the equilibrium density distribution functions $f_i^{(eq)}$ for every lattice (Eq. (7.7)).
5. Compute the equilibrium thermal distribution functions $g_i^{(eq)}$ for every lattice (Eq. (7.14)).
6. With temperature field known, calculate $\nabla \cdot \vec{q}_R$
7. Calculate now the density distribution functions f_i (Eq. (7.1)).
8. Calculate now the thermal distribution functions g_i (Eq. (7.12)).
9. Propagate the particle distributions f_i and g_i to the neighboring lattice centers.
10. Calculate new density, velocity and temperature fields (Eqs. (7.15a-c)).
11. Check for convergence and terminate the process, if appropriate.
12. Modify the particle distribution functions f_i and g_i locally, to satisfy the boundary conditions.
13. Compute the equilibrium density distribution functions $f_i^{(eq)}$ for every lattice.
14. Compute the equilibrium thermal distribution functions $g_i^{(eq)}$ for every lattice.
15. Go to step 6

7.3 Results and Discussion

The numerical code based on the formulation presented in the previous section was first validated against the results available in the literature [96,176] for natural convection without an effect of volumetric radiation. Table 7.1 shows comparison of results of the present work for the maximum horizontal velocity $U_{\max}$ on the vertical mid-plane$\left(\frac{x}{X},\frac{y}{Y}=0.5\right)$, maximum vertical velocity $V_{\max}$ on the horizontal mid-plane$\left(\frac{x}{X}=0.5,\frac{y}{Y}\right)$, average Nusselt number $\bar{N}u=\frac{H}{\chi\left(T_H-T_C\right)}\left(\frac{1}{H^2}\right)\int_0^H\int_0^H\left(uT-\chi\frac{\partial T}{\partial x}\right)dxdy$, Nusselt number $Nu_{1/2}$ along the vertical mid-plane$\left(\frac{x}{X},\frac{y}{Y}=0.5\right)$ and Nu_0 at the hot wall. For Rayleigh number Ra = $10^3,10^4,10^5$ and 10^6 results of the present work have been compared with those obtained by Davis [176] and Babu and Dixit [96]. Results for Ra = $10^3,10^4,10^5$ and 10^6 have been obtained for $64\times64,128\times128,256\times256$ and 512×512 lattices/control volumes, respectively. In both the LBM and the FVM, uniform size lattices/control volumes were used. It is observed from Table 1 that results of the present work are in a very good agreement with those reported in the literature [96, 176].

With inclusion of volumetric radiation, result of the present work for temperature T along the vertical mid-plane$\left(\frac{x}{X},\frac{y}{Y}=0.5\right)$has been compared in Fig. 2 with that of Banda et al [174]. These results have been compared for $Ra=10^4$, extinction coefficient $\beta=1.0$, scattering albedo $\omega=0.0$ and all walls are black. The value of the convection-radiation parameter $R_C=\frac{\kappa_f}{H\sigma T_{\text{ref}}^3}$ was taken to be 250. With 128×128 lattices/control volumes and 4×8 directions, results of the present work compare very well with those given in [174].

Table 7.1: Comparison of numerical results of the present study with results of Vahl Davis [176] and Dixit and Babu [96].

Ra		10^3	10^4	10^5	10^6
Grid used		64×64	128×128	256×256	512×512
U_{max}	Ref. 176	3.469	16.178	34.730	64.630
	Ref. 96	3.6529	16.163	35.521	64.186
	Present	3.6531	16.192	34.738	64.877
V_{max}	Ref. 176	3.697	19.617	68.590	219.36
	Ref. 96	3.682	19.569	68.655	219.866
	Present	3.698	19.637	68.655	220.568
$\overline{Nu}$	Ref. 176	1.118	2.243	4.519	8.800
	Ref. 96	1.121	2.286	4.546	8.652
	Present	1.105	2.220	4.503	8.816
$Nu_{1/2}$	Ref. 176	1.118	2.243	4.519	8.799
	Ref. 96	1.118	2.256	4.519	8.507
	Present	1.112	2.246	4.527	8.842
Nu_0	Ref. 176	1.117	2.238	4.509	8.817
	Ref. 96	1.127	2.247	4.523	8.805
	Present	1.114	2.237	4.507	8.802

It is to be noted that while comparing the results of the present work with those given in [23], $T_H = 0.5$ and $T_C = -0.5$. However, for rest of the results, including the benchmarking done in Table 1, $T_H = 1.0$ and $T_C = 0.0$.

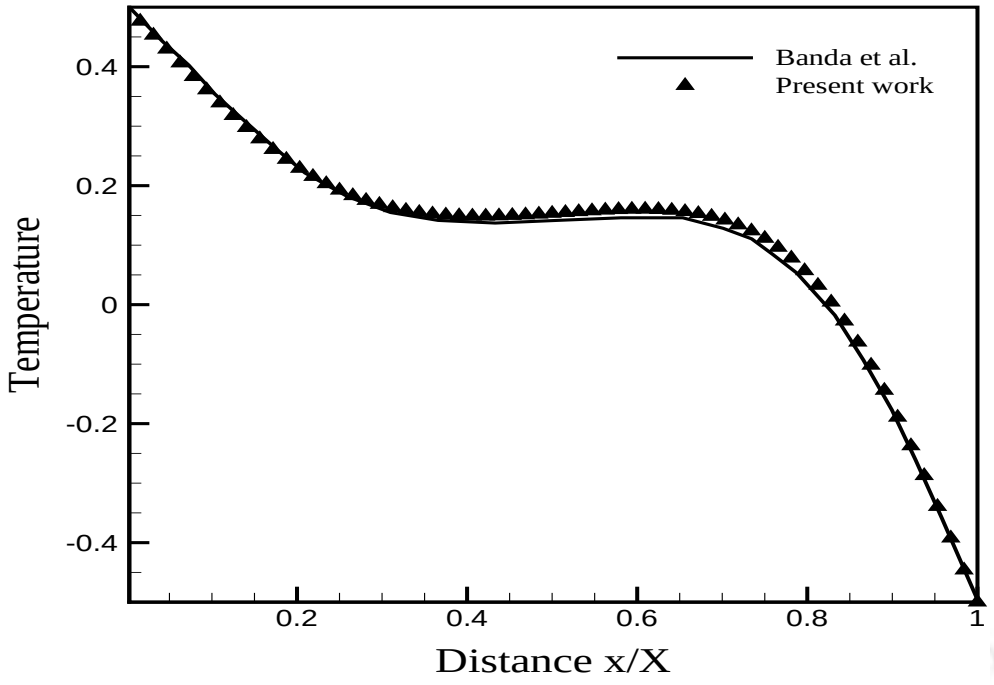

Figure 7.2: Along the vertical mid-plane $\left(\frac{x}{X}, \frac{y}{Y} = 0.5\right)$, comparison of temperature profile of the present work with reference [174].

In Figs. 3 – 6, results of isotherms and streamlines have been given. In Figs. 3-6, results have been given for $Ra = 10^3$, 10^4, 10^5 and 10^6, respectively. In each of these figures, results with and without volumetric radiation have been compared. For the cases with radiation, results have been obtained for $\beta = 1.0$, $\omega = 0.0$ and $R_c = 250$.

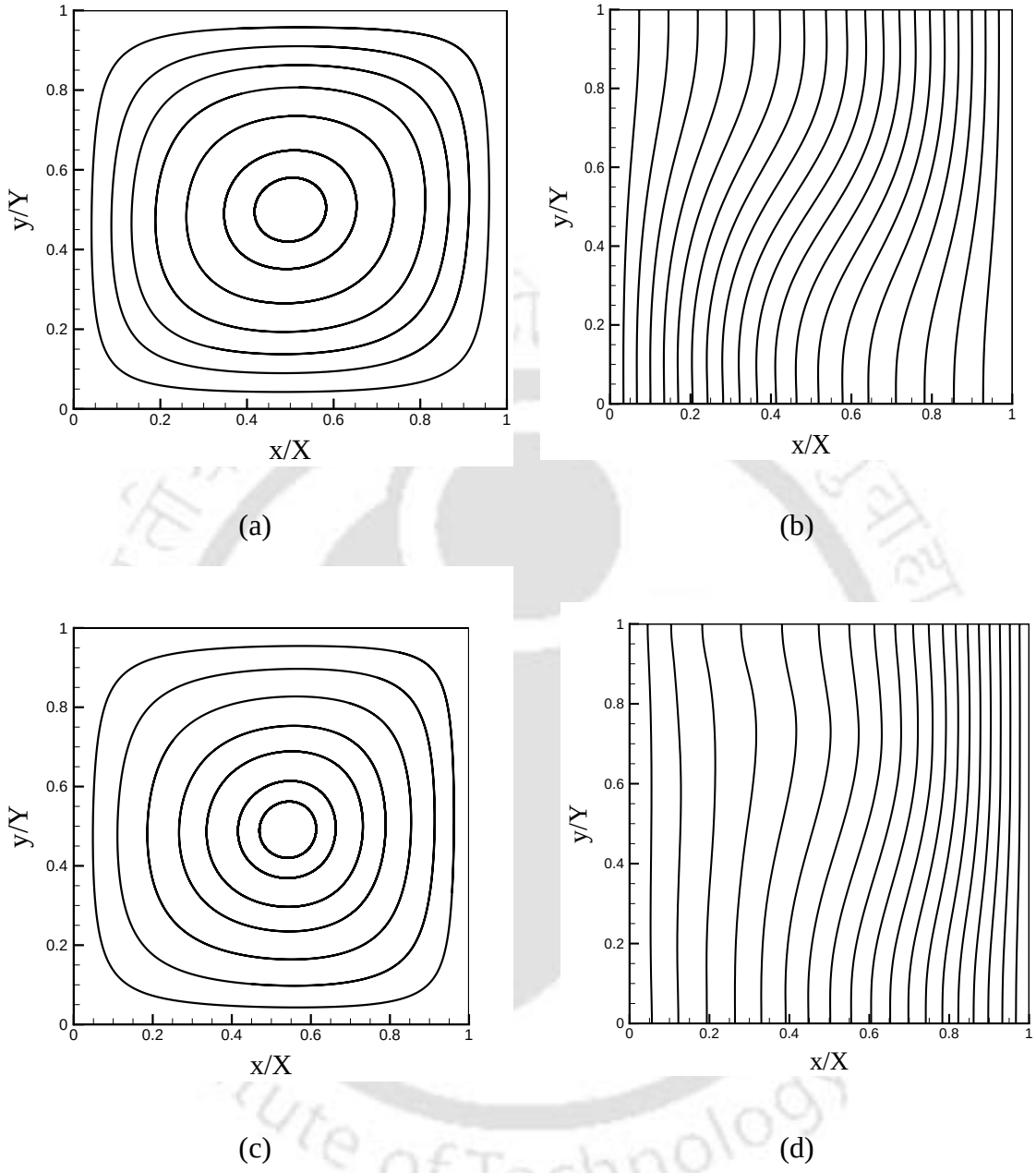

Figure 7.3: Streamlines and isotherms: (a) and (b) without radiation; (c) and (d) with radiation for $Ra = 10^3$.

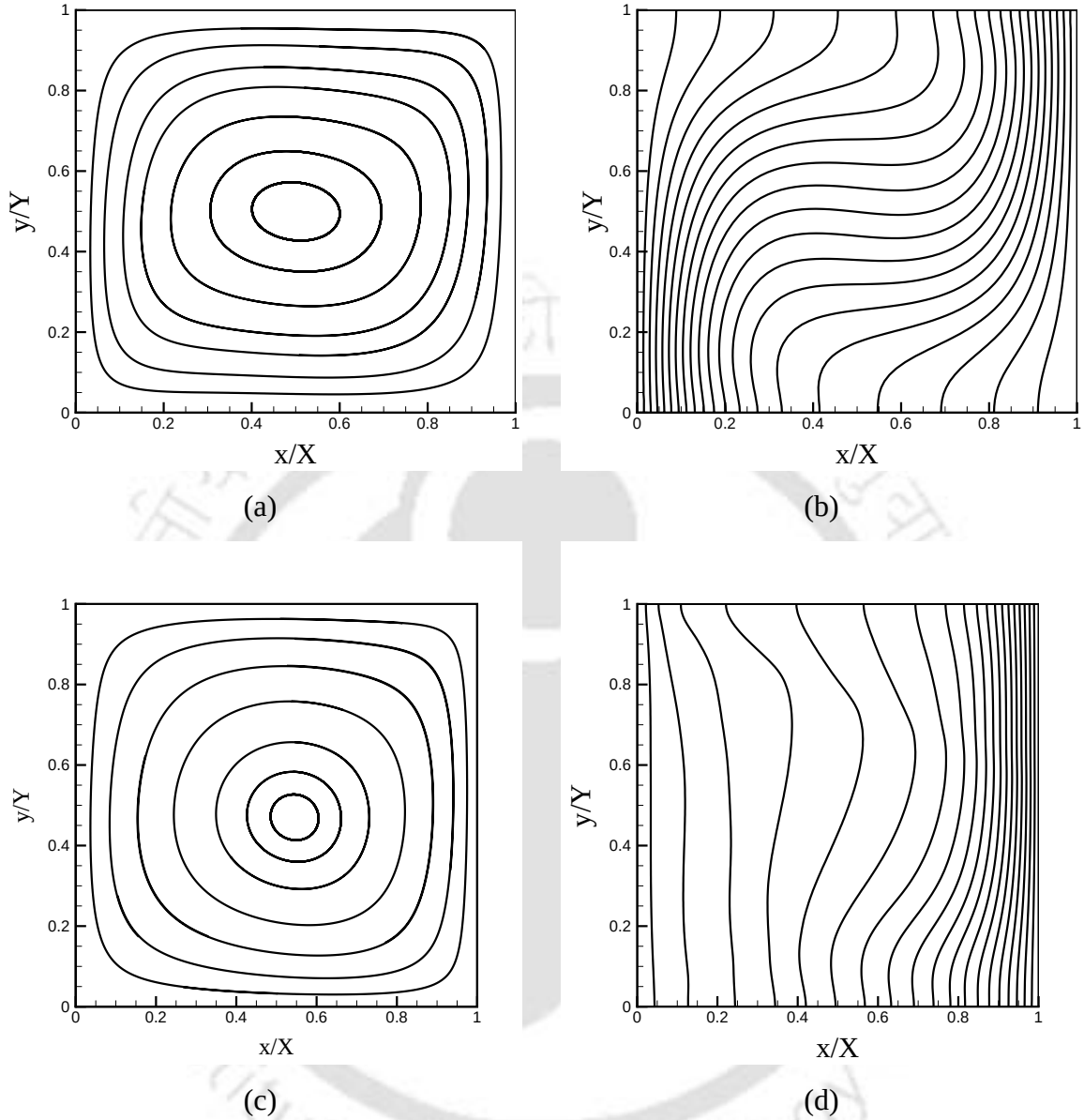

Figure 7.4: Streamlines and isotherms: (a) and (b) without radiation; (c) and (d) with radiation for $Ra = 10^4$.

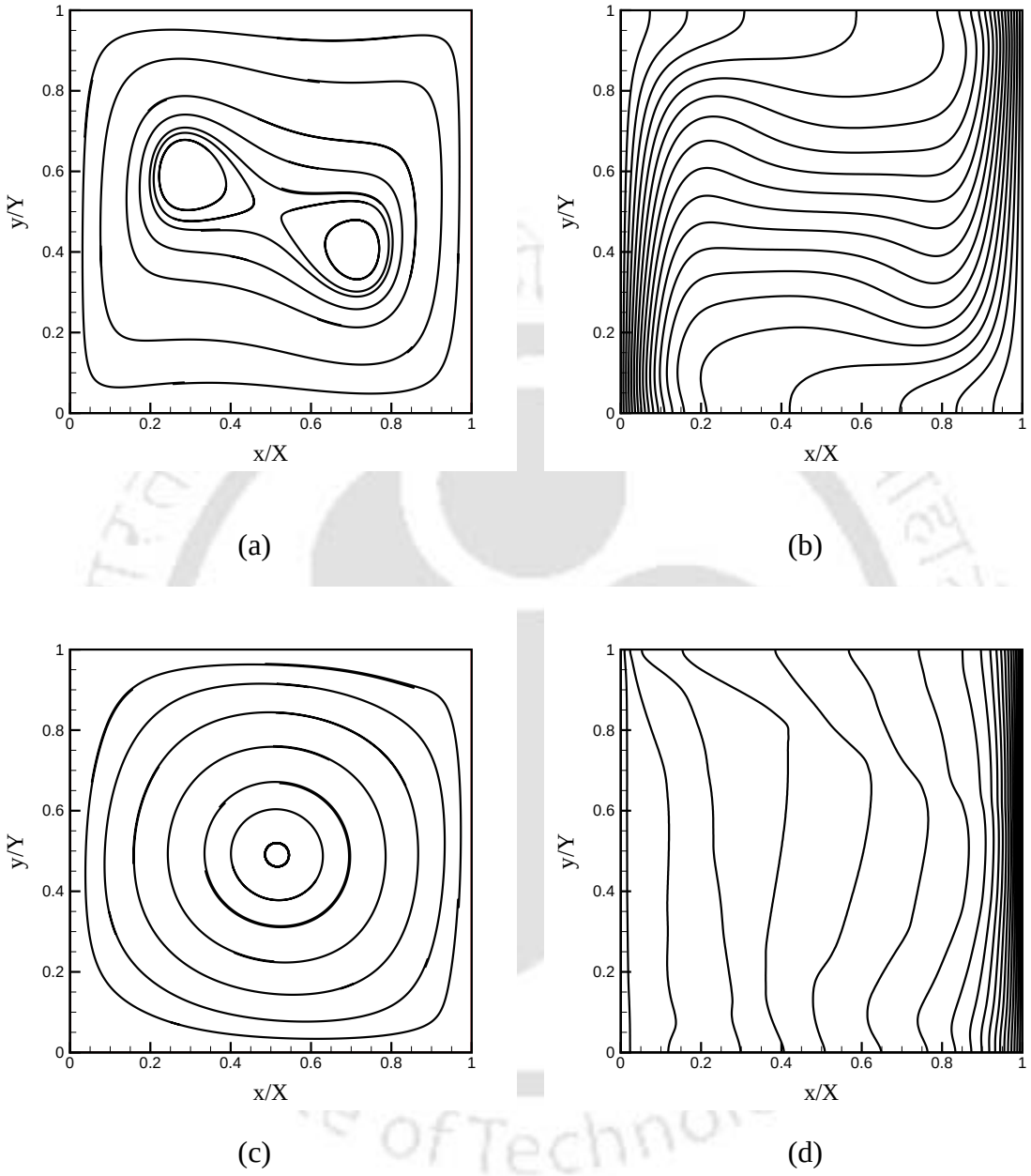

Figure 7.5: Streamlines and isotherms: (a) and (b) without radiation; (c) and (d) with radiation for $Ra = 10^5$.

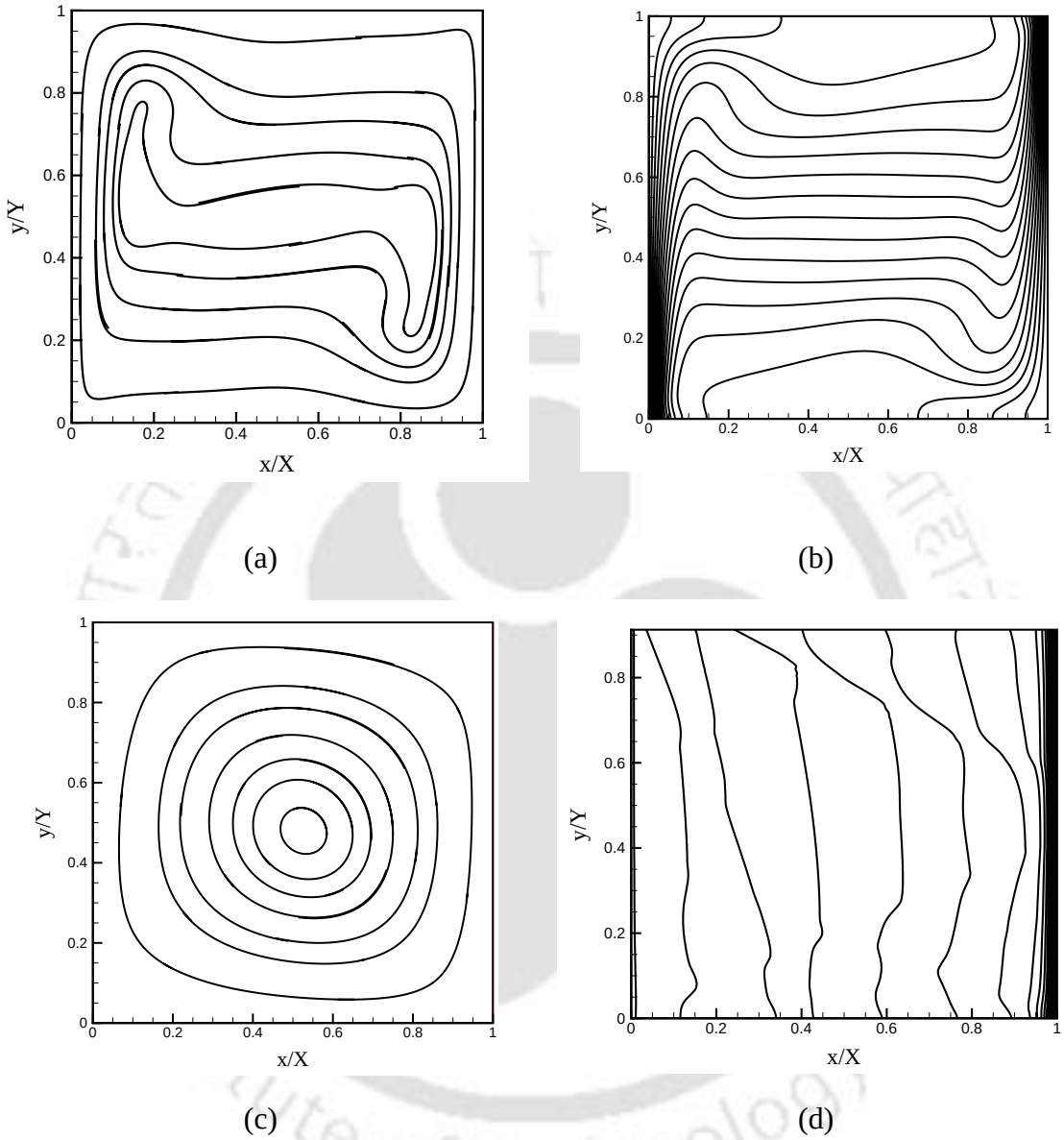

Figure 7.6: Streamlines and isotherms: (a) and (b) without radiation; (c) and (d) with radiation for $Ra = 10^6$.

Figs. 7.3a, 7.4a, 7.5a and 7.6a show streamlines without radiation effect. Similarly, in Figs. 7.3b, 7.4b, 7.5b and 7.6b, isotherms without considering the effects of radiation are shown. By considering the effects of radiation, streamlines are shown in Figs. 7.3c, 7.4c, 7.5c and 7.6c and isotherms are given in Figs. 3d, 4d, 5d and 6d.

For $Ra = 10^3$, effect of radiation on streamlines is not much (Figs. 7.3a and 7.3c). However, its effect on isotherms is noticeable (Figs. 7.3b and 7.3d). Near the cold wall, temperature gradient is observed to be more (Fig. 7.3d). For $Ra = 10^4$, a comparison of Figs. 7.4a and 7.4c show that effect of radiation on streamline is again less but from Figs. 7.4b and 7.4d it is observed that effect of radiation on isotherms is significant. From results given in Figs. 7.5a and 7.5c for $Ra = 10^5$ and in Figs. 7.6a and 7.6c for $Ra = 10^6$, it is evident that radiation has a significant effect on streamlines. In the presence of radiation, the flow field is always symmetric about the mid-planes. A comparison of isotherms given in Figs. 7.5b and 7.5d for $Ra = 10^5$ and in Figs. 7.6b and 7.6d for $Ra = 10^6$ it is clear that with radiation, near the cold wall, temperature gradient increases and there is a homogenization of temperature towards the cold wall. This is owing to the fact that energy in the medium is relatively more uniformly distributed.

In Figs. 7.7-7.14, effects of radiative parameters such as the extinction coefficient β and scattering albedo ω on streamlines and isotherms have been studied. In Figs. 7.7 and 7.8, results are given for $Ra = 10^3$. In Figs. 7.9 and 7.10, the same are given for $Ra = 10^4$. Figs. 7.11 and 7.12 show results for $Ra = 10^5$. For all the results given in Figs, 7.7-7.12, $R_c = 250$.

With $\omega = 0.0$, in Figs. 7.7a-d, effects of β on streamlines and isotherms have been studied. A comparison of results given in Figs. 7.3c, Figs. 7.7a and 7.7c for $\beta = 1.0, 0.1$ and 3.0, respectively shows that β has not much effect on streamlines. However, a comparison of results in Figs. 7.3d, Figs. 7.7b and 7.7d for $\beta = 1.0, 0.1$ and 3.0, respectively show that with an increase in β, effect on isotherms increases. For a higher value of β, temperature gradient near the cold boundary is more. A higher value of β implies that the medium is radiatively more participating and thus radiation effect is more.

Effects of the scattering albedo ω on streamlines and isotherms have been given in Figs. 7.8a-d. In this figure, results are given for $\beta = 1.0$. In Figs. 7.8a and 7.8c, streamlines have been plotted for $\omega = 0.5$ and 0.9, respectively. In Figs. 7.8b and 7.8d, results of isotherms have been presented for $\omega = 0.5$ and 0.9, respectively. A comparison of streamlines results given in Figs. 7.3c (for $\omega = 0$), 7.8a and 7.8c show that ω has no significant effect on streamlines. However, results given in Figs. 7.3d, 7.8b and 7.8d show that with increase in ω, radiation effect decreases and isotherms are similar to the case without the effect of radiation (Fig. 7.3b).

It is seen from Figs. 7.9 and 7.10 that for $Ra = 10^4$, β and ω have not much effects on streamlines. A comparison of Figs. 7.4d (for $\beta = 1.0$), 7.9b (for $\beta = 0.1$) and 7.9d (for $\beta = 3.0$) show that with an increase in β, temperature gradient near the cold wall increases. Further it is observed from Figs. 7.7 and 7.9 that for a higher value of Ra, effects of β on isotherm are more pronounced. A comparison of Figs. 7.4d (for $\omega = 0.0$), 7.10b (for $\omega = 0.5$) and 7.10d (for $\omega = 0.9$) show that with an increase in the value of ω, radiation effect on isotherms decreases.

For $Ra = 10^5$, effects of β and ω on streamlines and isotherms have been studied in Figs. 7.11 and 7.12, respectively. In Figs. 7.11a and 7.11c, streamline results are given for $\beta = 0.1$ and 3.0, respectively. Isotherm results for $\beta = 0.1$ and 3.0 are given in Figs. 7.11b and 7.11d, respectively. A comparison of Figs. 7.5c (for $\beta = 1$), Fig. 7.11a and 7.11c show that with increase in β, streamline profiles tend to be more symmetric. From Figs. 7.5d (for $\beta = 1$), Fig. 7.11b and 7.11d, it is seen that with an increase in β, temperature gradient is very high near the cold wall. Even for $Ra = 10^5$, from Figs. 7.5c (for $\omega = 0.0$), 7.12b and 7.12d it is seen that ω is not seem to have any noticeable effect on streamlines. However, a comparison of Figs. 7.5d (for $\omega = 0.0$), Figs.7.12b and 7.12d, it is evident that with an increase in ω, radiation effect on isotherms decreases.

In generating results of the present work, the program was terminated when for every node, error in temperature was $\left|T^{k}-T^{k-1}\right| \le 10^{-8}$. Depending upon the parameters, for the prescribed error limit, the number of iterations ranged from 15000 to 120000. All the computations in the present work were carried out with $\Delta t = 1.0$. All the runs were taken on Two AMD Opteron Dual Core Processor, 2.6 GHz, 8 GB DDR2 SDRAM RDIMM and CPU time ranged from 4 hours to 16 days. With 512×512 lattices/control volume and 4×8 ray directions, per minute 5 iterations were achieved.

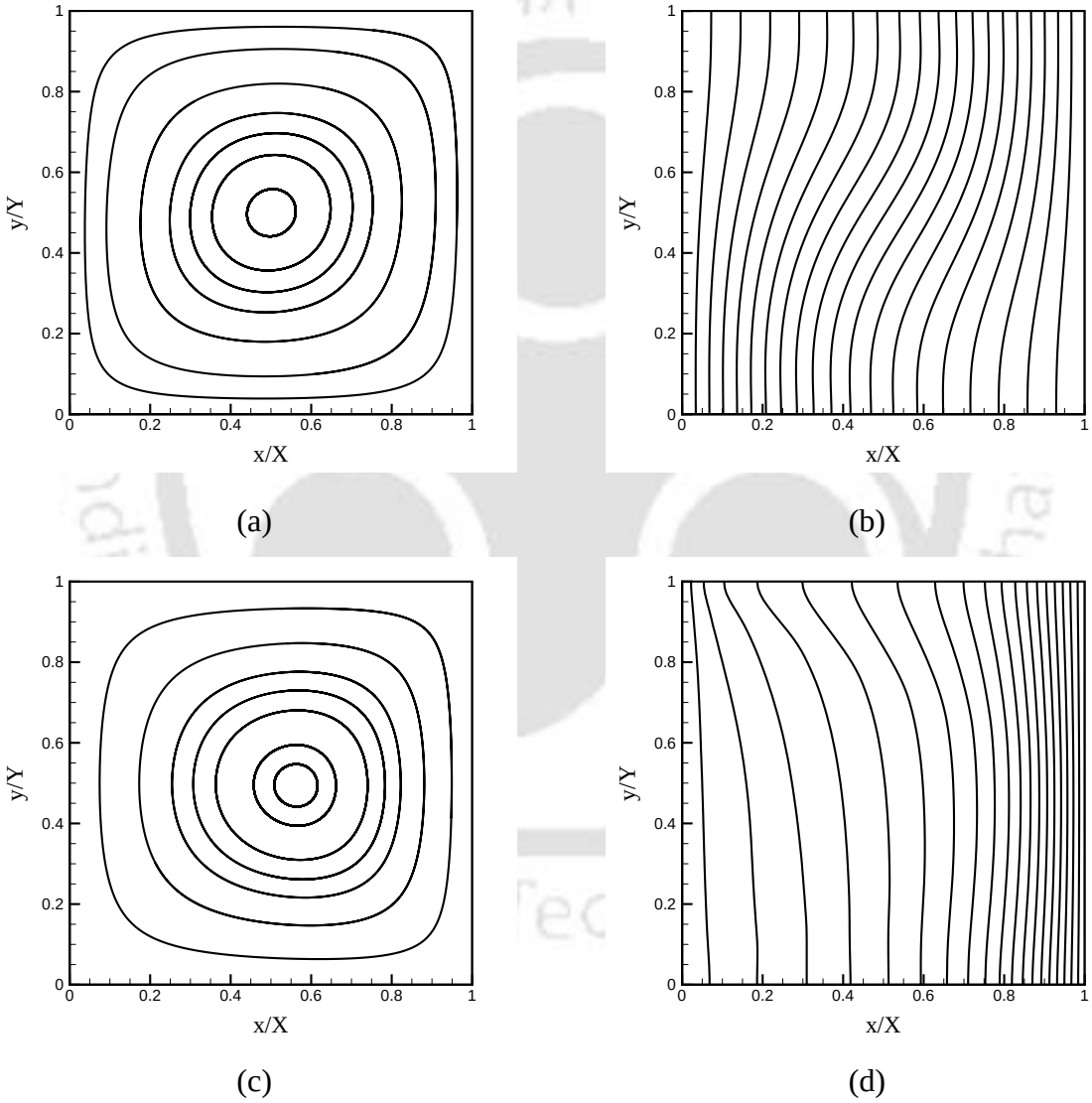

Figure 7.7: Effects of extinction coefficient β on streamlines and isotherms for $Ra = 10^3$: (a) and (b) $\beta = 0.1$; (c) and (d) $\beta = 3.0$.

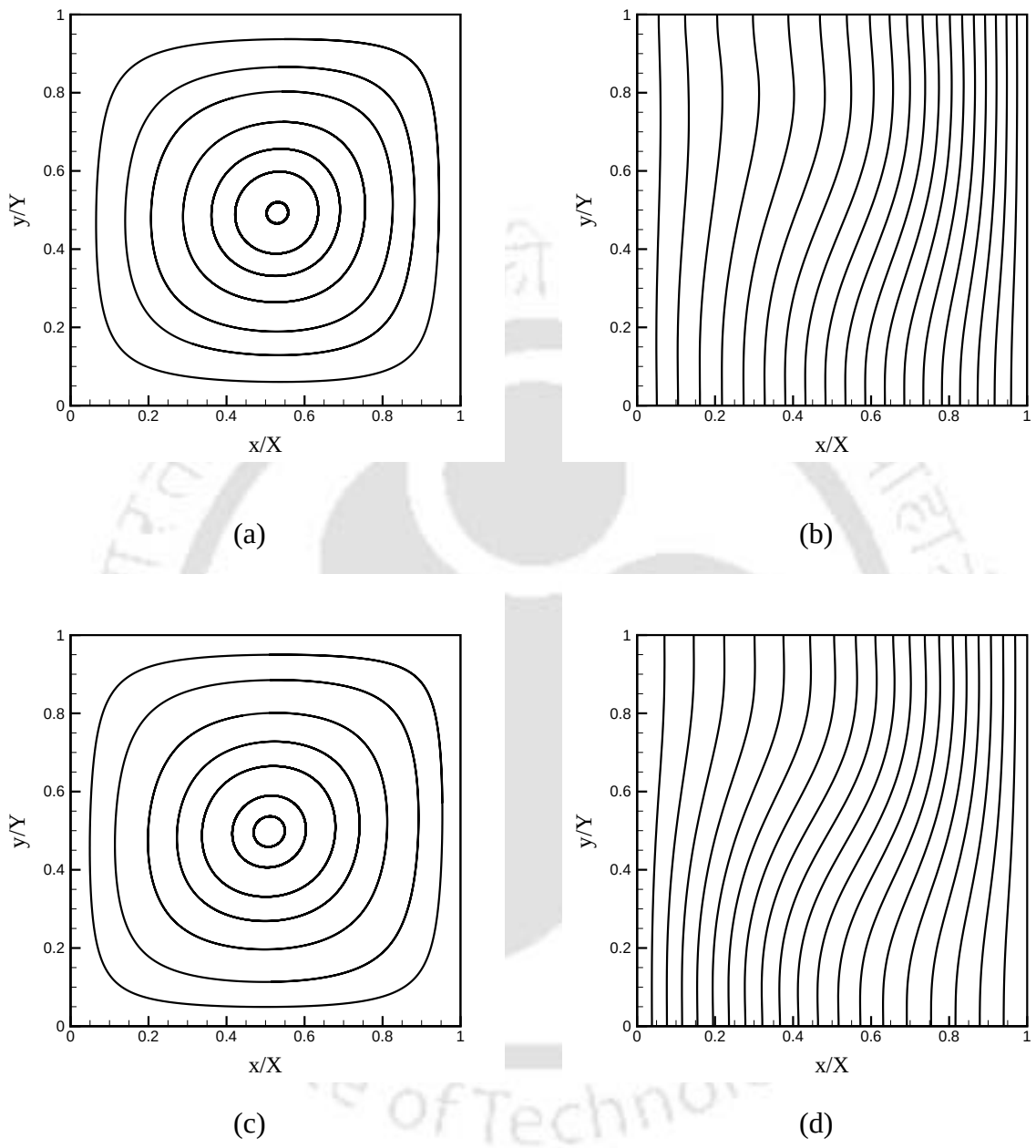

Figure 7.8: Effects of scattering albedo ω on streamlines and isotherms for $Ra = 10^3$: (a) and (b) $\omega = 0.5$; (c) and (d) $\omega = 0.9$.

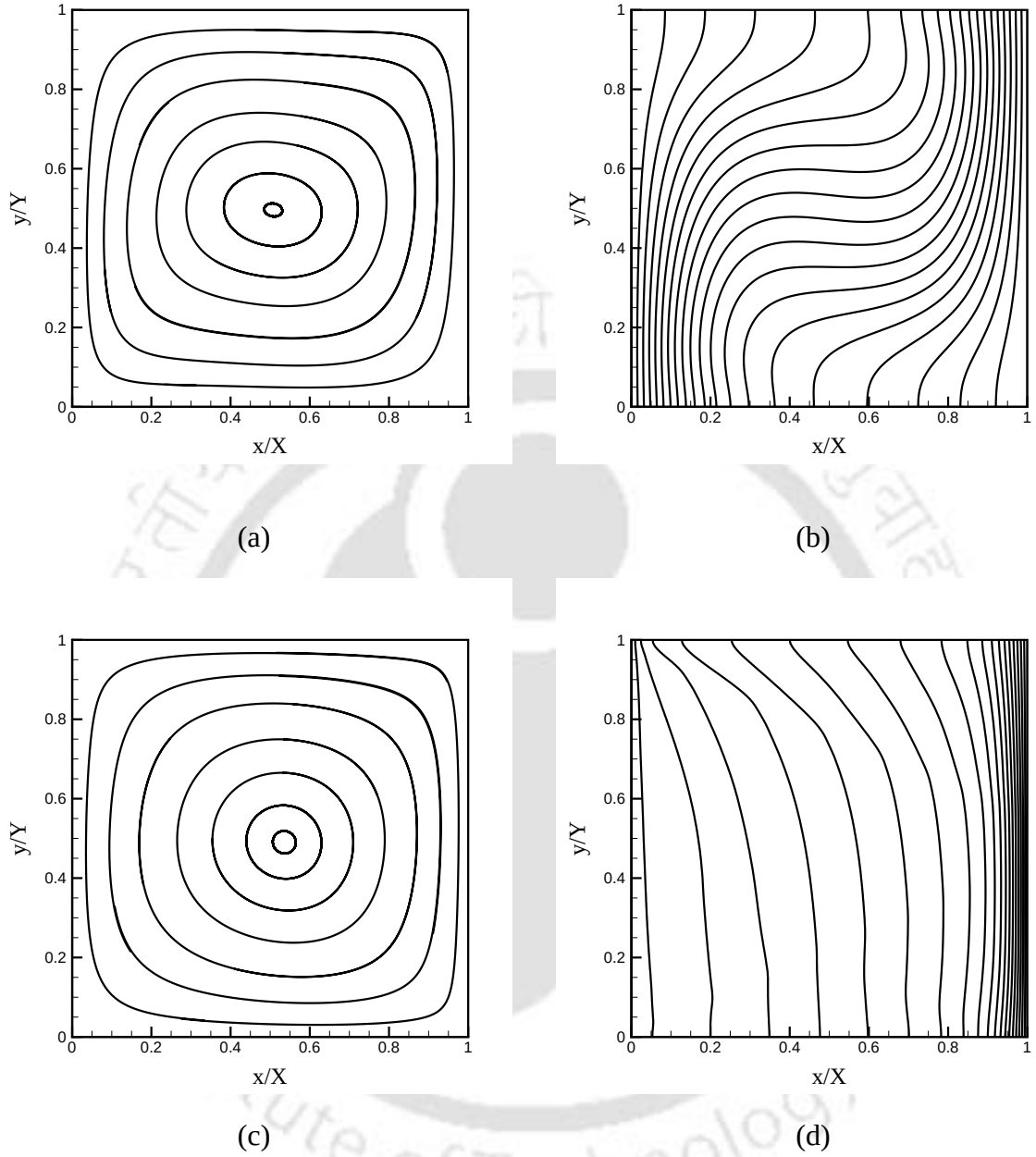

Figure 7.9: Effects of extinction coefficient β on streamlines and isotherms for $Ra = 10^4$: (a) and (b) $\beta = 0.1$; (c) and (d) $\beta = 3.0$.

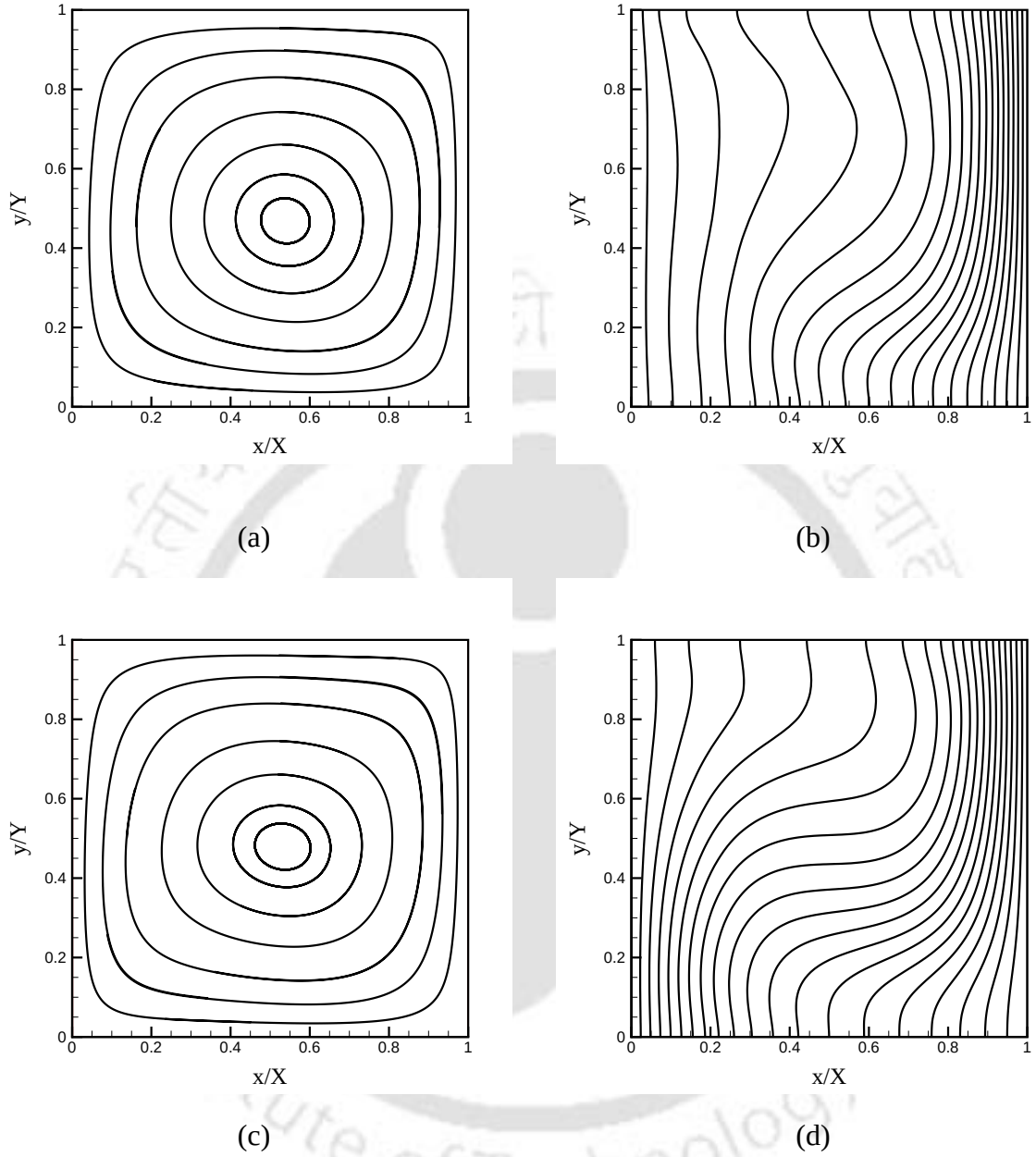

Figure 7.10: Effects of scattering albedo ω on streamlines and isotherms for $Ra = 10^4$: (a) and (b) $\omega = 0.5$; (c) and (d) $\omega = 0.9$.

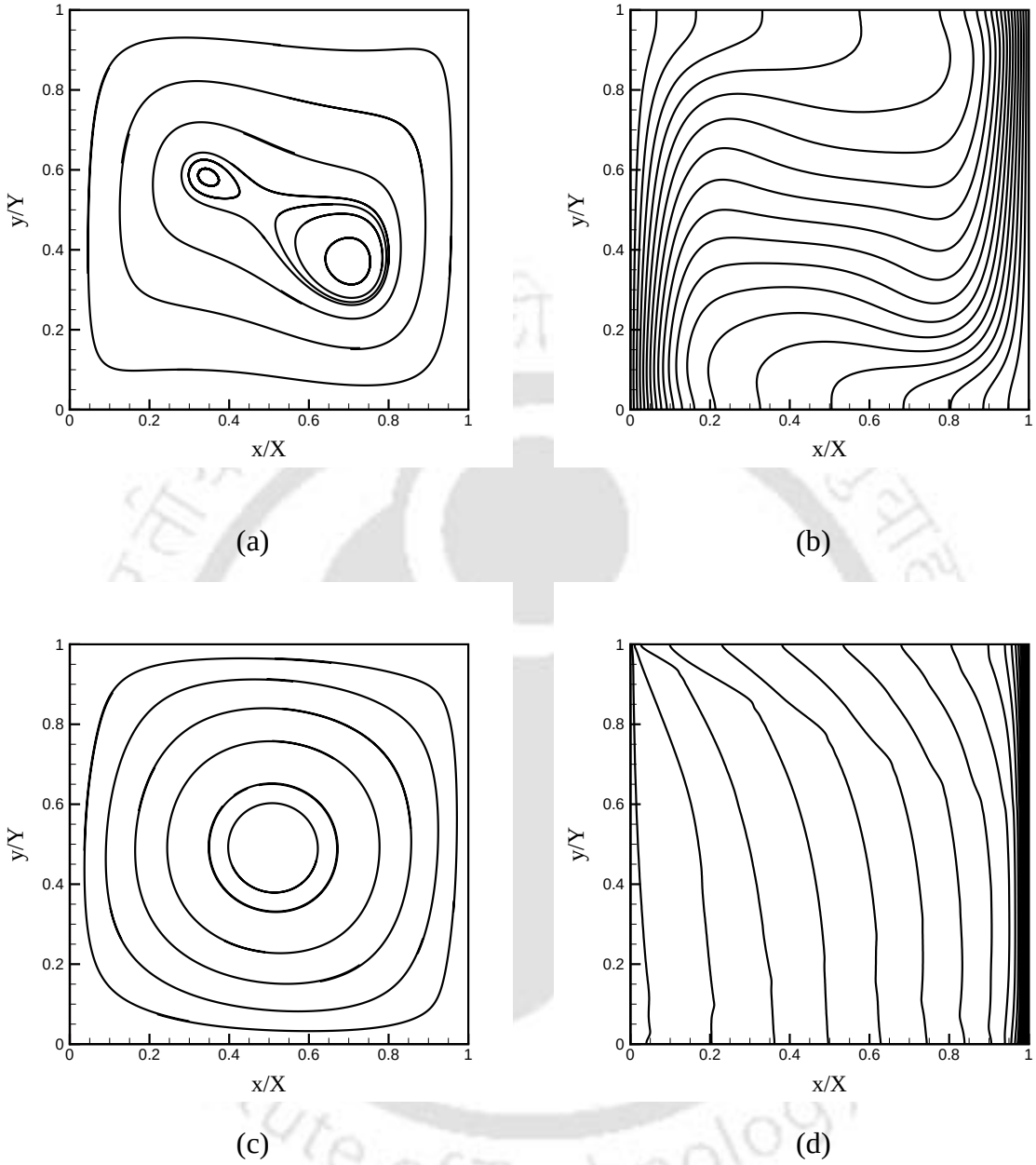

Figure 7.11: Effects of extinction coefficient β on streamlines and isotherms for $Ra = 10^5$: (a) and (b) $\beta = 0.1$; (c) and (d) $\beta = 3.0$.

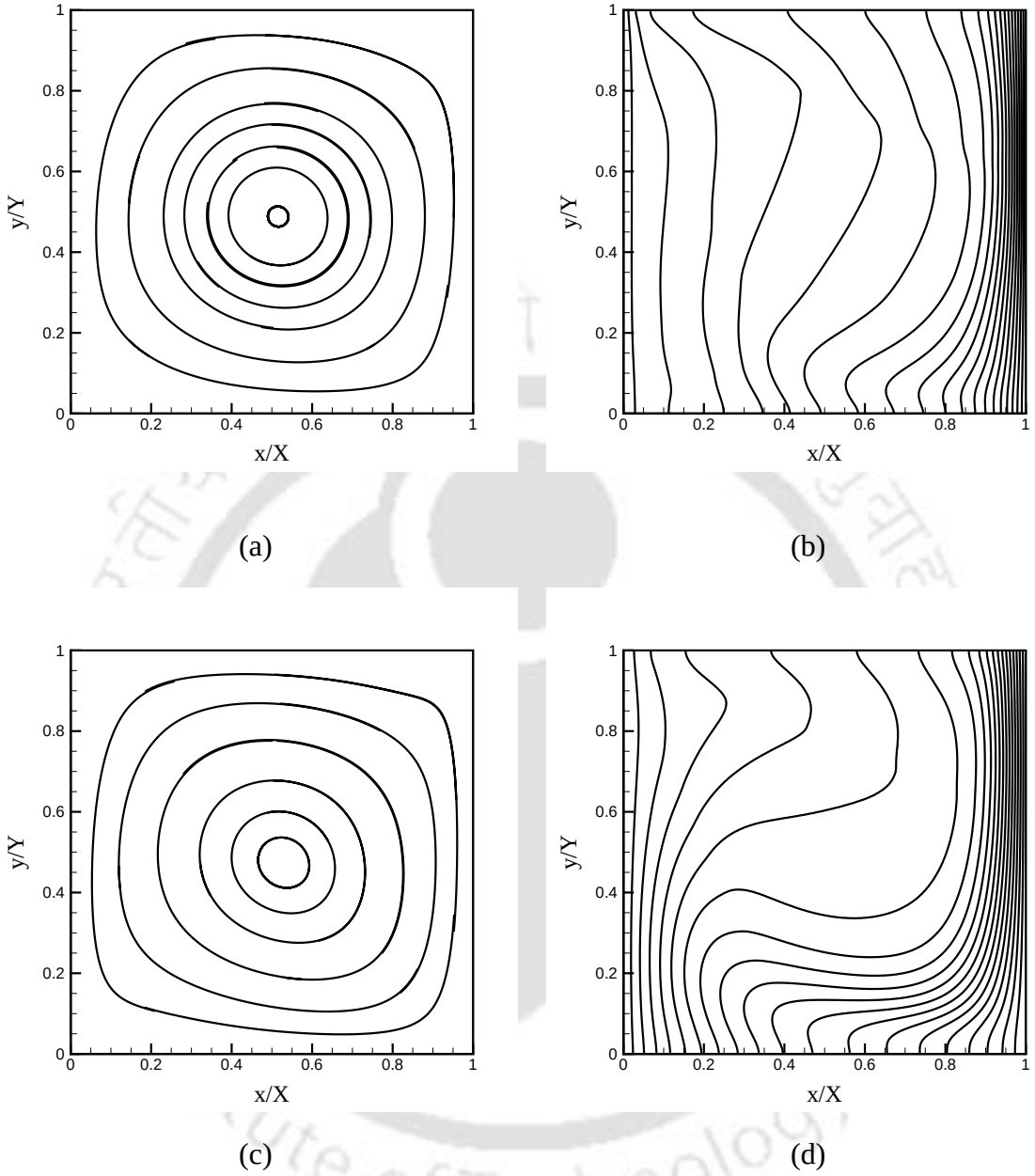

Figure 7.12: Effects of scattering albedo ω on streamlines and isotherms for $Ra = 10^5$: (a) and (b) $\omega = 0.5$; (c) and (d) $\omega = 0.9$.

7.4 Summary

The LBM was used to analyze natural convection in the presence of volumetric radiation in a square cavity containing an absorbing, emitting and scattering medium. Separate particle distribution functions in the LBM were used to calculate the density and velocity fields, and the thermal field. The radiative term of the energy equation was computed using the FVM. Streamlines, isotherms and Nusselt number were analyzed for different parameters such as Rayleigh number, convection-radiation parameter, extinction coefficient and scattering albedo. The next chapter deals with the analysis of a localized fire in a 3-D tunnel.

CHAPTER 8

Analysis of a Localized Fire in a 3-D Tunnel

8.1 Introduction

In the recent years, analysis of natural convection with and without radiation in enclosures has received considerable attention [166-169, 177-181]. This has practical applications in areas such as thermal insulation, cooling of electronic components, building design, etc. Natural convection in a single or partitioned enclosure was reported in [166-169, 178]. House et al. [177] analyzed the effects of a centrally located conducting body on the heat transfer in an air filled vertical enclosure. The same geometry was also considered by Oh et al. [166]. They considered the effect of heat generation. Ha et al. [167] investigated steady state natural convection in a differentially heated vertical cubic enclosure containing a cubic heat generating body. A numerical study of the interaction between thermal radiation and laminar mixed convection for ascending flows of absorbing and emitting gases in a vertical tube was studied by Sediki et al. [168]. In their analysis, they considered the effect of temperature dependent thermo-physical properties. Balaji and Venkateshan [169] reported numerical results of interaction of surface radiation with free convection in an air filled open cavity. In most of the previous studies on natural convection in a cavity with or without heat generating partitions, the effect of volumetric radiation was not considered [166-169, 178]. Radiation was only considered as the boundary conditions [169].

In a partitioned enclosure, literature dealing with combined convection and volumetric radiation is scarce. Chang et al. [178] considered interaction of radiation and natural convection in a square enclosure having vertical partitions of equal lengths and finite thicknesses located at the centre of the ceiling and floor. They considered an idealized configuration. In real life, geometries involved are more complex. In the present work, therefore, a combined mode natural convection and volumetric radiation in a practical geometry representing a road tunnel is considered.

The fire on 24th March 1999 in the Mont Blanc Tunnel in Europe (boarder of Italy and France) was one of the most severe accidents [179,180]. Many lost their lives. During the accident, due to a large fire, the ventilation system was less effective. The safety systems did not work properly. The operator did not observe the onset of the fire and thus could not signal the same and took safety precautions to save the passengers trapped in the tunnel.

To detect the onset of a fire, thermal sensors are installed in the tunnel. In case of a fire, the temperature and heat flux profiles within the tunnel change abruptly. The extent of a possible damage can be assessed with the knowledge of temperature and heat flux profiles. Thus, numerical and experimental investigations bear significance.

To minimize/avoid casualties in tunnels, researchers undertook heat transfer analysis by simulating a fire in the tunnel. The control of fire in the Mont Blanc Tunnel with a special emphasis on the effect of ventilation has remained a very important aspect of investigation [179-182]. Both numerical and experimental studies have been carried out to propose recommendations for the operator and assess damages in case of a fire [179-182].

Earlier investigations [179-182] on analysis of fire in the tunnel have not considered the effect of volumetric radiation. The present work, therefore, deals with the numerical analysis of fire considering the effect of radiation in a 3-D tunnel representing the Mont Blanc Tunnel.

The LBM is one of the promising numerical techniques [1, 19, 20, 22, 23, 24, 25, 87, 88, 96, 100, 183-186]. In comparison with the conventional CFD solvers, advantages of LBM include simple calculation procedure, simple and efficient implementation for parallel computation, easy and robust handling of complex geometries. Although the LBM has found wide usage in fluid mechanics [1, 23, 25, 183,185], its application to heat transfer problems has also received attention [19, 20, 22, 24, 25, 87, 88, 96, 100].

In the present work, the LBM and the finite difference method (FDM) in conjunction with the FVM for radiation are used to analyze heat transfer in a 3-D tunnel caused by a localized fire. The density and the velocity fields are computed using the LBM. The FVM is used to compute the radiative information required in the energy equation which is solved using the FDM based upwind scheme. Boussinesq approximation is considered to take into account the buoyancy effects. One of the other objectives of the present work is also, therefore, to check the workability of three different classes of solvers on a common platform.

8.2 Physical Geometry of the Problem

In this study, the combined effect of natural convection and radiation is analyzed due to a localized fire inside a 3-D tunnel (Fig 8.1). A fire is assumed to take place in the middle of the tunnel. The dimensions of the tunnel are as follows: length $X = 840\ m$ (Fig. 8.1a, b), width $Y = 8.8\ m$ (Fig. 8.1c) and height $Z = 7.9\ m$ (Fig. 8.1c). From both entrance and exit sides: a flat ceiling up to a distance of 4.8 m (Fig. 8.1a), an arch ceiling (Fig. 8.1c) for rest of the length (830.04 m), coordinates of the centre of the half-circle (4.38 m., 3.48 m.) (Fig. 8.1c), radius of the half-circle 4.41 m (Fig. 8.1c); basement size along the length of the tunnel 0.7906 m (Fig. 8.1c).

In the present work, computations were performed on a simpler model problem, because the main goal is to successfully establish that three different classes of solvers (LBM, FD

up-wind and FVM) could be coupled. For this reason, only a portion of roughly $X = 68.4\ m$ of the total tunnel length (including the fire region) has been considered.

8.3 Formulation

When the fire is caused in a tunnel, air and smokes are the two main species having different properties. Particulate matters also result from fire outbreak and for the sake of simplicity; they are considered as a part of the smoke. Thus, in the problem under consideration, we have two species, viz., air and smoke, and the governing energy equation for the generic species σ, is given by

$$\rho_\sigma \frac{\partial T_\sigma}{\partial t} + \rho U_j^\sigma \frac{\partial T_\sigma}{\partial x_j} = \frac{\partial}{\partial x_j}\left(\Gamma_\sigma \frac{\partial T_\sigma}{\partial x_j}\right) + \frac{1}{C_p^\sigma}\nabla \cdot \boldsymbol{q}_R^\sigma + \sum_\zeta \rho_\zeta \Omega_{\sigma\xi}\left(T_\zeta - T_\sigma\right), \tag{8.1}$$

where for species σ, ρ_σ is the density, c_p^σ is the specific heat, Γ_σ is the diffusion transport coefficient, U_j^σ is the velocity vector and $\Omega_{\sigma\zeta}$ is the thermal transfer kernel which takes into account the transfer between species σ and species ζ. In the above equation, $\boldsymbol{q}_R$ is the radiative heat flux.

In the problem under consideration, a distinct interface between air and smoke is considered to exist. Thus since there is no direct contact except at the interface between species air σ and species smoke ζ, the last term in energy equation (8.1) that accounts for coupling term between two species is neglected. The two species are coupled through radiative exchange. In the light of the above, after dropping the subscripts identifying the species, the energy equation becomes

$$\rho \frac{\partial T}{\partial t} + \rho U_j \frac{\partial T}{\partial x_j} = \frac{\partial}{\partial x_j}\left(\Gamma \frac{\partial T}{\partial x_j}\right) + \frac{1}{C_p}\nabla . \boldsymbol{q}_R \tag{8.2}$$

The solution of energy equation (8.2) requires determination of divergence of radiative heat flux $\nabla . \bar{q}_R$ and knowledge of the velocity field U_j. In the present work, $\nabla . \boldsymbol{q}_R$ is

computed using the FVM. Density ρ and velocity U_j are determined using the LBM. The energy equation (Eq. (8.2)) is then finally solved using the FDM based fully explicit upwind scheme. Selection of three classes of methods namely viz. the FVM for $\nabla.\boldsymbol{q}_R$, LBM for ρ and U_j and FDM for calculation of temperature field T is based on suitable methods which are compatible to each other to exchange the information.

In the following pages, we are not providing the formulation for the determination of the divergence of radiative heat flux $\nabla.\boldsymbol{q}_R$ using the FVM. Its details already described in chapter 2. We provide LBM formulation for determination of density ρ and velocity field U_j. The FDM based upwind scheme to solve energy equation (Eq. (8.2)) is described next.

8.3.1 The Lattice Boltzmann Method

A multi–component flow can be modelled by means of two possible approaches: (1) multi-fluid (i.e. a set of equations for each species), (2) single-fluid i.e. a set of equations for the mixture barycentric velocity and for the smoke concentration. In terms of the kinetic elementary equations (like those considered by the LBM), the first approach is most natural. In this case, we have to solve the following equations:

1. a discrete set of equations for continuity and momentum equations for air,
2. a discrete set of equations for continuity and momentum equations for smoke,
3. a discrete set of equations for energy equation (advection – diffusion – source equation) for air (coupled with the barycentric fluid flow equations and smoke equation),
4. a discrete set of equations for energy equation (advection – diffusion – source equation) for smoke (coupled with the barycentric fluid flow equations and smoke equation),
5. a discrete set of equations for the full radiation transfer equation (including the effects due to the participating media).

In particular, we use the multi-species approach for solving the continuity and momentum equations for both air and smoke. Under some proper assumptions, this is equivalent to solving a barycentric equation for the mixture (mass-averaged), velocity and diffusion equations for the smoke concentration [185]. This set of equations is solved by means of the LBM.

Following the derivation of the Boltzmann equation for a simple system with a single species, the kinetic equations for a mixture can be derived in a similar way [189]. Let us consider a mixture composed of only two types of particles labeled *a* and *b*. The Boltzmann equations for the binary system are

$$\frac{\partial f_a}{\partial t} + \mathbf{v} \cdot \nabla f_a + \mathbf{g}_a \cdot \nabla_{\mathbf{v}} f_a = Q_{aa} + Q_{ab}, \tag{8.3}$$

$$\frac{\partial f_b}{\partial t} + \mathbf{v} \cdot \nabla f_b + \mathbf{g}_b \cdot \nabla_{\mathbf{v}} f_b = Q_{ba} + Q_{bb}, \tag{8.4}$$

where $f_a(\mathbf{x}, \mathbf{v}, t)$ is the continuous single particle distribution function for the *a* species, $\mathbf{v}$ is the microscopic velocity, $\mathbf{g}_a$ is the acceleration due to an external field (buoyancy) for species *a*. A similar definitions hold for the species *b* too. The quadratic expressions Q_{aa} and Q_{bb} are the collision terms which describe the collisions among particles of the same type (*self-collisions*), while Q_{ab} and Q_{ba} are the collision terms due to the interactions among different species (*cross-collisions*).

Each collision terms in Eqs. (8.3) and (8.4) has a well–known structure similar to the collision operator involved in the Boltzmann equation for a single fluid [189]. The time evolution of the distribution function for each species is affected both by collisions with particles of the same type and with particles of different type. These two phenomena are the kinetic driving forces of the equilibration process for the whole mixture.

A simplified kinetic model which allows one to separately describe both the driving forces, as they appear in the original Boltzmann equations, would be desirable. Essentially the key idea is to substitute the previous collision terms with simplified ones,

which are selected with a BGK–like structure. The model obtained is due to Hamel [190]. In the following, only the equation for a generic species $\sigma = a, b$ will be considered. The simplified kinetic equation has the general form

$$\frac{\partial f_\sigma}{\partial t} + \mathbf{v}\cdot\nabla f_\sigma + \mathbf{g}_\sigma \cdot \nabla_{\mathbf{v}} f_\sigma = -\frac{1}{\tau_\sigma}\left[f_\sigma - f_\sigma^e\right] - \frac{1}{\tau_m}\left[f_\sigma - f_{\sigma(m)}^e\right] \tag{8.5}$$

where τ_σ is the relaxation time constant for self-collisions, τ_m is the relaxation time constant for cross-collisions, f_σ^e is a Maxwellian distribution function centered on the specific velocity, while $f_{\sigma(m)}^e$ is a Maxwellian distribution function centered on a characteristic velocity for the mixture. The explicit expressions of these Maxwellians are

$$f_\sigma^e = \frac{\rho_\sigma / m_\sigma}{(2\pi e_\sigma)^{D/2}} \exp\left[-\frac{1}{2}\frac{(\mathbf{v}-\mathbf{u}_\sigma)^2}{e_\sigma}\right], \tag{8.6}$$

$$f_{\sigma(m)}^e = \frac{\rho_\sigma / m_\sigma}{(2\pi e_\sigma)^{D/2}} \exp\left[-\frac{1}{2}\frac{(\mathbf{v}-\mathbf{u})^2}{e_\sigma}\right]. \tag{8.7}$$

where ρ_σ is the single species density, m_σ the particle mass, $\mathbf{u}_\sigma = [U_1^\sigma, U_2^\sigma, U_3^\sigma]^T$ is the macroscopic velocity, $\mathbf{u} = [U_1, U_2, U_3]^T$ is the macroscopic barycentric (mass – averaged) velocity, e_σ is the internal energy, and D the number of physical dimensions. The barycentric (mass – averaged) velocity is defined as

$$\mathbf{u} = \sum_\sigma x_\sigma \mathbf{u}_\sigma = \sum_\sigma \rho_\sigma \mathbf{u}_\sigma / \sum_\sigma \rho_\sigma \tag{8.9}$$

where x_σ is the mass concentration (mass fraction) for the generic species. Local momentum conservation implies that the relaxation time constant τ_m for the cross-collisions must be the same for all species.

Macroscopic quantities, such as the density $\rho_\sigma(\mathbf{x}, t)$, the macroscopic specific velocity $\mathbf{u}_\sigma(\mathbf{x}, t)$, and, consequently, the macroscopic barycentric velocity $\mathbf{u}(\mathbf{x}, t)$ can be calculated as the moments of the density distribution function, i.e.

$$\rho_\sigma(\mathbf{x}, t) = \int_{-\infty}^{+\infty} m_\sigma \, f_\sigma \, d\mathbf{v}\,, \tag{8.10}$$

$$\rho_\sigma \, \mathbf{u}_\sigma(\mathbf{x}, t) = \int_{-\infty}^{+\infty} m_\sigma \, \mathbf{v} \, f_\sigma \, d\mathbf{v}\,. \tag{8.11}$$

Unfortunately, the Hamel model (and all those resulting by a proper linearization of it) is not completely self-consistent [185,191]. In fact, if one sums over the species equations, one does not exactly recover the momentum equations (as one should). For this reason, a new lattice Boltzmann model was, thus, developed [185] for recovering the transport coefficients. The continuous (pseudo–) kinetic model used as the theoretical starting point is a proper simplification of the BGK model proposed by Aoki et al. [192]. The simplified kinetic equation has the general form

$$\frac{\partial f_\sigma}{\partial t} + \mathbf{v} \cdot \nabla f_\sigma + \mathbf{g}_\sigma \cdot \nabla_{\mathbf{v}} f_\sigma = -\frac{1}{\tau_m}\left[f_\sigma - f^{e}_{\sigma(m)}\right] \tag{8.12}$$

To solve the continuous kinetic equation (Eq. (8.12)), the discrete ordinates method can be applied [193, 194]. According to this method, a set of discrete microscopic velocities $\mathbf{v}_i$ must be defined for which the distribution function is evaluated. The generic function $f^i_\sigma(\mathbf{x}, t)$ is the single particle distribution function evaluated for velocity $\mathbf{v}_i$ at $(\mathbf{x}, t)$. In the present paper, a three-dimensional lattice called D3Q19, which makes use of nineteen discrete velocities (Q), is considered [195]. The specific lattice used in the calculation is identified by the magnitude c (all the lattices in the same set have the same proportions among the elements, but they are all scaled to the physical microscopic velocity c called the lattice speed).

This assumption simplifies the development of the numerical code, and it is essential for the physical model, because the discrete lattice is used for overcoming the intrinsic constraints of the continuous simplified model. Thus, the kinetic equation, which is an integro-differential equation, reduces to a system of differential equations. Since the reference lattice has been defined, it is possible to write the operative formula in vectorial form, namely,

$$\frac{\partial \mathbf{f}_\sigma}{\partial t} + \mathbf{V} \cdot \nabla \mathbf{f}_\sigma = \mathbf{A}_m \left[\mathbf{f}^e_{\sigma(m)} - \mathbf{f}_\sigma \right], \tag{8.13}$$

where $\mathbf{V}$ is the matrix collecting all the lattice components ($\mathbf{V}$ has dimensions Q x D, i.e. 19 x 3) and the scalar product between matrices must be thought of as saturating the second index (in fact $\nabla \mathbf{f}_\sigma$ has dimensions 19 x 3 and consequently $\mathbf{V} \cdot \nabla \mathbf{f}_\sigma$ is a column vector 19x1). Since only the distribution functions for discrete microscopic velocities are considered, an interpolation test function must be adopted to calculate the macroscopic quantities. In this way, the previous integrals which define the macroscopic moments reduce to weighted summations of the considered discrete functions. The interpolation test function should be as similar to the local Maxwellian distribution function as possible in order to easily include the equilibrium conditions. If we consider a low Reynolds number, the equilibrium distribution function can be linearized around the state at rest [194]. This assumption allows one to compute the lattice weights for performing the calculation of the macroscopic quantities. The final result is that all the macroscopic (both hydrodynamic and not-conserved) moments are proper linear combinations of the discrete distribution functions (modified in order to directly included the selected quadrature weights); or, equivalently, a linear mapping exists between the macroscopic moments and the discrete distribution functions. In the present application, the term that takes into account the effect of the external force field (buoyancy) can be modeled by simply modifying the definition of the discrete macroscopic momentum, namely

$$\rho_\sigma(\mathbf{x}, t) = \sum_{i=1}^{Q} [\mathbf{f}_\sigma]_i \,, \tag{8.14}$$

$$\rho_\sigma \, \mathbf{u}_\sigma(\mathbf{x}, t) = \sum_{i=1}^{Q} [\mathbf{V}_\sigma]_i [\mathbf{f}_\sigma]_i + \tau_m \, \mathbf{b}_\sigma \,, \tag{8.15}$$

where the additional term can be expressed by means of the Boussinesq approximation for modeling buoyancy effects in small density varying flows, namely

$$\mathbf{b}_\sigma = (\rho_\sigma - \rho_0)\, \mathbf{g} = -\rho_0 \beta \, (T_\sigma - T_0)\, \mathbf{g} \,, \tag{8.16}$$

where ρ_0 is the (roughly constant) density of the flow, T_0 is the operating temperature, β is the thermal expansion coefficient and $\mathbf{g}$ is the gravitational acceleration.

Comparing the previous expressions with the original continuous one, the collisional matrix should be diagonal, namely $\mathbf{A}_m = 1/\tau_m \, \mathbf{I}$. However, in order to increase the number of tunable parameters, the collisional matrix is assumed to be

$$\mathbf{A}_m = \mathbf{M}_D^{-1} \mathbf{D}_m \mathbf{M}_D , \tag{8.17}$$

where $\mathbf{M}_D$ defines a proper orthonormal basis for the D3Q19 lattice and $\mathbf{D}_m$ is the diagonal matrix, namely,

$$\begin{aligned} diag(\mathbf{D}_m) = [0, &\lambda_m^I, \lambda_m^I, \lambda_m^I, \lambda_{m1}^{II}, \lambda_{m1}^{II}, \lambda_{m1}^{II}, \lambda_{m1}^{II}, \lambda_{m1}^{II}, \lambda_{m1}^{II}, \lambda_{m2}^{II}, \\ &\lambda_m^{III}, \lambda_m^{III}, \lambda_m^{III}, \lambda_m^{III}, \lambda_m^{III}, \lambda_m^{III}, \lambda_m^{IV}, \lambda_m^{IV}, \lambda_m^{IV}] \end{aligned} , \tag{8.18}$$

collecting the generalized relaxation frequencies for self and cross collisions. As will be clear later on, λ_m^I controls the molecular diffusivity, λ_{m1}^{II} and λ_{m2}^{II} control the mixture kinematic and bulk viscosity respectively, while λ_m^{III} and λ_m^{IV} are free parameters affecting the stability of the model (usually $\lambda_m^{III} = \lambda_m^{IV} = 1$).

Once the hydrodynamic moments are computed, it is necessary to verify that they satisfy the desired macroscopic transport equations. For achieving this goal, diffusive scaling [196] can be properly applied. There are three characteristic time scales in this system: the time scale which properly describes the collision phenomenon; the time scale which properly describes the particle dynamics on the lattice and, finally, the time scale which properly describes the slow fluid dynamics. The fast fluid dynamics (acoustic waves) is neglected. Since a lot of collisions are needed in order to travel across the system, it is possible to apply an asymptotic analysis of the previous scheme by investigating the solutions which are much slower than the characteristic collision time. Once the characteristic time scales are defined, the basic idea is to express the previous equation in terms of some normalized quantities in order to analyze the slow fluid dynamics only. Application of the diffusive scaling to equation (8.13) for a binary mixture yields

$$\frac{\partial \rho_\sigma}{\partial t} + \nabla \cdot (\rho_\sigma \mathbf{u}_\sigma) = 0 , \tag{8.19}$$

$$\rho_\sigma (\mathbf{u}_\sigma - \mathbf{u}) = -D_\sigma \nabla \rho_\sigma , \tag{8.20}$$

$$\frac{\partial \mathbf{u}}{\partial t} + \nabla \cdot \left(\mathbf{u} \otimes \mathbf{u} \right) = -\frac{1}{\rho} \nabla p + \nu \nabla^2 \mathbf{u} + \frac{1}{\rho} \sum_{\sigma} \mathbf{b}_{\sigma} , \tag{8.21}$$

where $D_{\sigma} = e_{\sigma} / \lambda_{\sigma}^{I}$, $\nu = c^2 / \left(3 \lambda_{m1}^{II} \right)$, $p = \sum_{\sigma} p_{\sigma}$ and $p_{\sigma} = e_{\sigma} \rho_{\sigma}$. The internal energies can be expressed by means of the molecular weights, namely $e_{\sigma} = RT_{\sigma} / M_{\sigma}$ where R is the universal gas constant (8.31441 J mol^{-1} K^{-1}). Consequently, it is possible to define an equivalent molecular weight for the mixture in such a way that $p / \rho = RT / M$, i.e.

$$M = \frac{1}{\sum_{\sigma} x_{\sigma} / M_{\sigma}} . \tag{8.22}$$

This equivalent molecular weight for the mixture depends on the local mass concentrations ($x_{\sigma} = \rho_{\sigma} / \rho$), because it is not an intrinsic property of the components. By selecting the relaxation frequency such as

$$\lambda_{m}^{I} = \frac{M^2}{M_a M_b} \frac{p}{\rho D} , \tag{8.23}$$

where D is the mutual diffusivity of the binary mixture, which is a molecular property due to the molecular interaction potentials, the species velocity difference can be rewritten as

$$\mathbf{u}_a - \mathbf{u}_{\mathbf{b}} = -\frac{D}{y_a y_b} \left[\nabla y_a + \frac{y_a y_b \left(M_b - M_a \right)}{M} \nabla \ln \left(\frac{p}{p_0} \right) \right] , \tag{8.24}$$

where $y_{\sigma} = p_{\sigma} / p$ are the volume/molar concentrations. The previous expression is fully consistent with the Maxwell – Stefan macroscopic model (in case of binary mixtures, the Maxwell – Stefan model is equivalent to the Fick model), which is actually quite popular for modeling multi – component fluid flow. This is an important result because it proves that, in the continuous limit (i.e. if a sufficiently large number of particles is considered), the developed mesoscopic model recovers the Maxwell – Stefan macroscopic model.

This last confirmation completes the proposed hybrid numerical scheme, which is based on LBM in order to compute the mixture barycentric velocity and diffusion process (consistently with Stefan – Maxwell model); the fully explicit upwind scheme for the convective transport and the FVM for the radiation transfer equation.

8.3.2 The Upwind Scheme

The density and velocity fields result from the solution of the continuity and momentum equations or in the present work from its LBM equivalent. The solution of density and velocity fields is obtained using the multiple–relaxation–time LBM for multi – component flows [185]. Once the flow field has been computed using the LBM, the temperature filed is calculated by solving Eq. (8.2) by the fully explicit upwind scheme. In the centre difference, the convection property at the interface is considered as the average of its values at two the consecutive nodes. This is considered a weak point for the central difference scheme and the upwind scheme proposes a better prescription [187, 188]. In the upwind scheme, the diffusion term is discretized by means of the central difference approximation, but the convective term is calculated using the following assumption.

The convection – diffusion part of Eq. (8.2) is

$$\rho \frac{\partial T}{\partial t} + \rho U_j \frac{\partial T}{\partial x_j} = \frac{\partial}{\partial x_j}\left(\Gamma \frac{\partial T}{\partial x_j} \right) \tag{8.25}$$

The density and velocity are considered to vary in each direction. Since density is always positive, there is no need to consider the value of density for the upwind scheme. Mainly depending upon the velocity, Eq. (8.25) is discretized using upwind scheme. In the present 3-D geometry, the 8 combinations of velocity directions are the following:

$$U_x > 0,\ U_y > 0 \text{ and } U_z > 0 \tag{8.26 a}$$

$$U_x > 0,\ U_y < 0 \text{ and } U_z > 0 \tag{8.26 b}$$

$$U_x > 0,\ U_y < 0 \text{ and } U_z < 0 \tag{8.26 c}$$

$$U_x > 0,\ U_y > 0 \text{ and } U_z < 0 \tag{8.26 d}$$

$$U_x < 0,\ U_y > 0 \text{ and } U_z > 0 \tag{8.26 e}$$

$$U_x < 0,\ U_y > 0 \text{ and } U_z < 0 \tag{8.26 f}$$

$$U_x < 0,\ U_y < 0 \text{ and } U_z > 0 \tag{8.26 g}$$

$$U_x < 0,\ U_y < 0 \text{ and } U_z < 0 \tag{8.26 h}$$

In the upwind scheme, for each of the velocity combinations, discretization of Eq. (8.2) is done differently. For the above 8 combinations, discretization are given in the Appendix.

8.4 Results and Discussion

As previously pointed out, a simpler model problem has been defined by considering a shorter tunnel with actual size $68.4 \times 8.8 \times 7.9\ m$. In the present work, the computations were done for $101 \times 15 \times 15$ control volumes. Since some proper ghost cells must be considered at the boundary of the physical domain in order to impose some proper boundary conditions, the actual mesh size is $\delta = 8.8/(15-2)\ m = 0.68 m$. Considering the size of the geometry, a finer mesh was desirable. However since, one of the objectives of the present work was to see how three different types of solvers work together, as a preliminary work in this direction, results in the following pages are presented with a relatively rough mesh. With the finer mesh, because of the exorbitant computational time (a few days), parallelization of the hybrid solver becomes inevitable.

A simple fire is assumed in the middle of the tunnel. The fire volume is $1.36 \times 2.04 \times 0.68\ m^3$ (please note that the size of the fire in Fig. 8.1(a) is not to the scale), which means $2 \times 3 \times 1$ in grid spacing, and it starts from the ground floor ($Z = 7.89\,\text{m}$). The initial temperature of air was taken as the environmental temperature (300K) and the temperature of the smoke originating from fire was taken as 1200 K. The computations were made for 1000 collisions (time steps with $\Delta t = 1.0$) which corresponds to the arrival of the smoke to the entrance and exit of the tunnel.

In the following pages, we provide isotherms in three planes, viz., Y-Z, X-Y and X-Z. These isotherms are provided for with and without the effect of radiation. With radiation, isotherms are given for the effect of the scattering albedo ω, the conduction-radiation parameter $N = K\beta / 4\sigma T_{ref}^3$ and the emissivities ε of the tunnel walls.

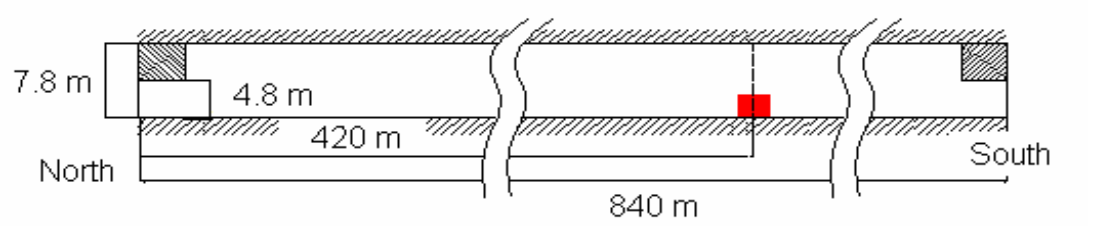

(a)

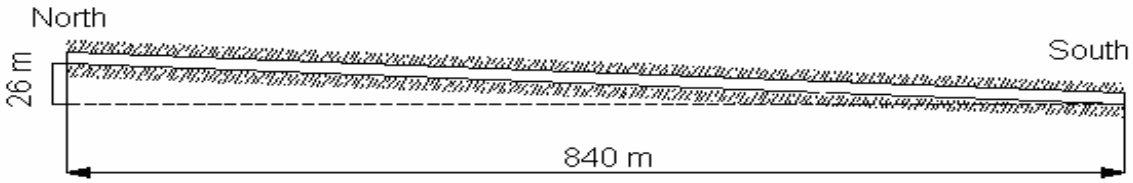

(b)

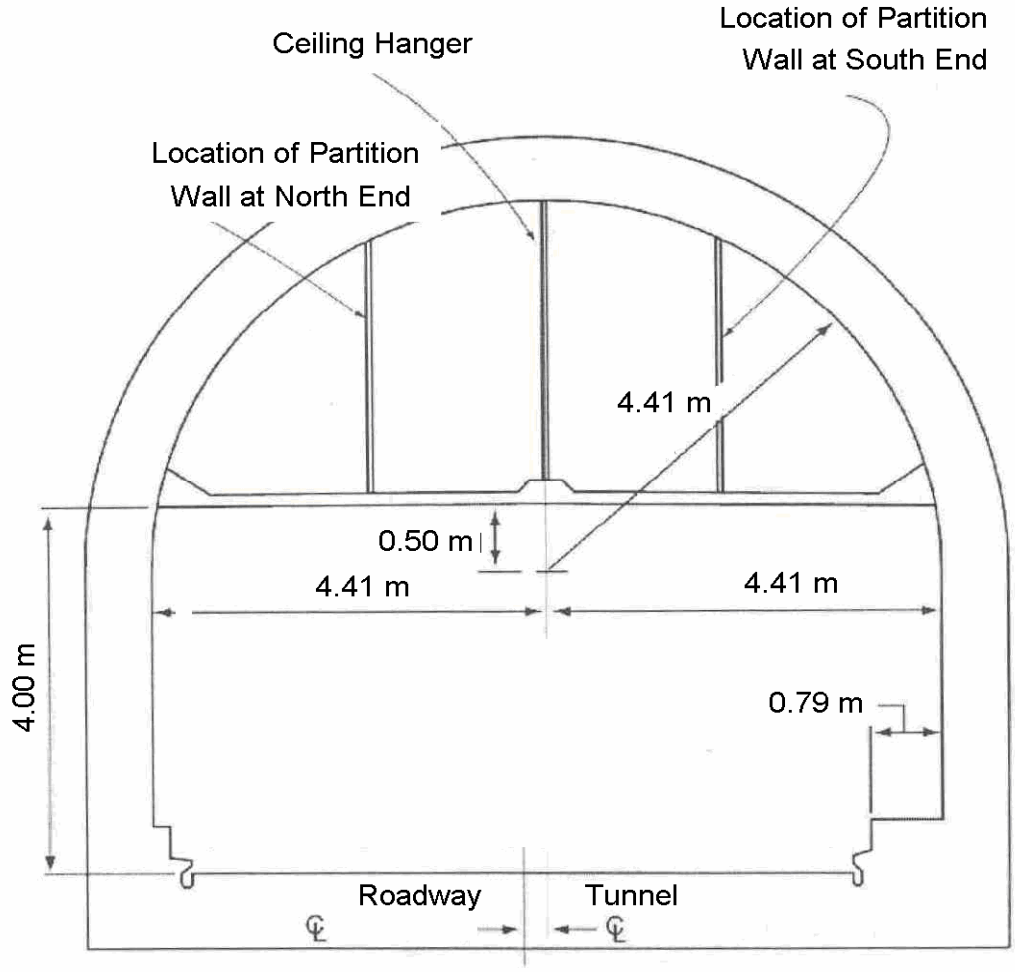

(c)

Figure 8.1: (a) The view (X-Z Plane) along the length of the tunnel; (b) the head difference along the length of the tunnel; (c) the cross section (Y-Z Plane) of the tunnel.

Isotherms in the Y-Z (vertical) plane in the middle $(x = 420\,\mathrm{m})$ of the tunnel are shown in Fig. 8.2. For results in Fig. 8.2, the boundaries of the tunnel have been assumed black.

In Figs. 8.2a and 8.2b isotherms are shown for the case without and with the effect of radiation, respectively. In Fig. 2b, isotherms are shown for extinction coefficient $\beta = 1.0$, scattering albedo $\omega = 0.0$ and conduction-radiation parameter $N = 170.0$. It is observed that in the absence of radiation, temperature close to the ceiling in the central region is about 0.55 (Fig. 8.2a) which is lower than that for the case with the effect of radiation (Fig. 8.2b). It is seen from Figs. 8.2a and 8.2b that temperature in the Y-Z plane is more intense in the presence of radiation.

With extinction coefficient $\beta = 1.0$ and conduction-radiation parameter $N = 170.0$, for scattering albedo $\omega = 0.5$ and 0.9, isotherms have been compared in Figs. 8.2c and 8.2d, respectively. A comparison of Figs. 8.2b, 8.2c and 8.2d show that when the medium is more scattering, effect of radiation on temperature gradients are more pronounced. For a higher value of ω, temperature in the region close to the ceiling is less.

With extinction coefficient $\beta = 1.0$ and scattering albedo $\omega = 0.0$, for the two values of conduction-radiation parameter $N = 220.0$ and 300.0, isotherms are shown in Figs. 8.2e and 8.2f. When the conduction-radiation parameter $N = 220.0$, the isotherms very close to the ceiling are 0.717 (Fig. 8.2e) and for $N = 300.0$, the same are 0.67 (Fig. 8.2f). As seen from Figs. 8.2b, 8.2e and 8.2f, it is clear that for a higher value of N, the radiation effect is less and thus the temperature gradient is more near the fire zone.

Isotherms in the X-Y (horizontal) plane at a height $z = 3.945\,\mathrm{m}$ of the tunnel are shown in Fig. 8.3. For results in Fig. 8.3, the boundaries of the tunnel have been assumed black.

Fig. 8.3a and 8.3b show contours without and with the effect of radiation, respectively. Cases in Figs. 8.3a and 8.3b are analogous to Figs. 8.2a and 8.2b, respectively. Considering the effect of radiation, with $\beta = 1.0$, $\omega = 0.0$ and $N = 170.0$, isotherms are

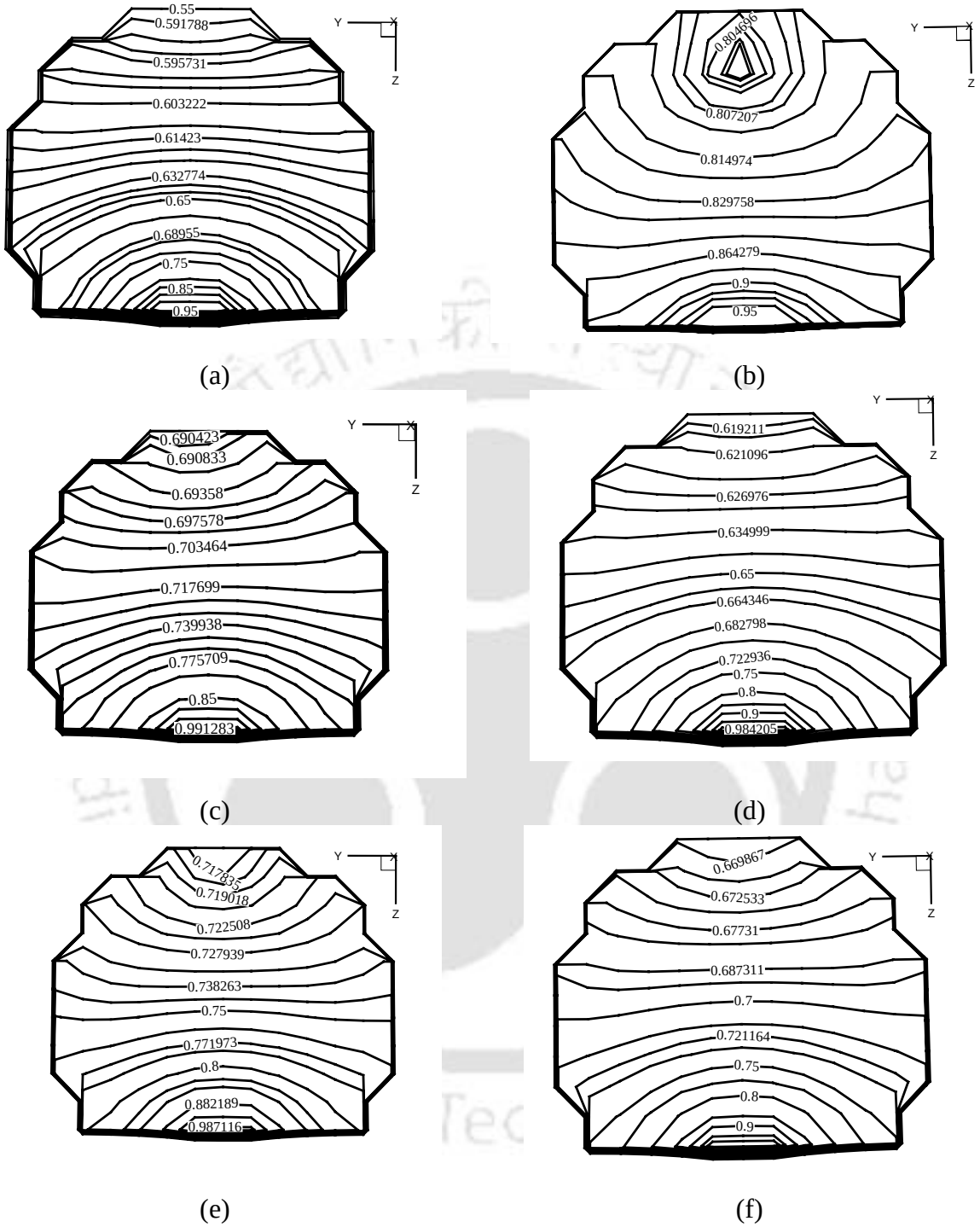

Figure 8.2: Isotherms at the middle $(x = 420\,\text{m})$ of the tunnel in Y-Z plane (a) without radiation, with radiation for $\beta = 1.0$ (b) $\omega = 0.0$ and $N = 170$, (c) $\omega = 0.5$ and $N = 170$, (d) $\omega = 0.9$ and $N = 170$, (e) $\omega = 0.0$ and $N = 220$ and (f) $\omega = 0.0$ and $N = 300$.

shown in Fig. 8.3b. It is observed from Figs. 8.3a and 8.3b that in case of radiation, temperature in the tunnel in the axial (x) direction is more than the case without radiation. Further in the central region of the X-Y plane, because of the fire, temperature is more.

The effect of scattering albedo on isotherms in the X-Y plane is shown in Figs. 8.3c and 8.3d. With $\beta = 1.0$ and $N = 170.0$, results are given for $\omega = 0.5$ and 0.9 in Figs. 8.3c and 8.3d, respectively. At the central region of the X-Y plane, the isotherms value for $\omega = 0.0$, $\omega = 0.5$ and $\omega = 0.9$ are very close to the 0.83, 0.72 and 0.65 respectively. It is observed from Figs. 8.3b, 8.3c and 8.3d that when scattering is more, temperature in the central region and also along the axial (x) direction is less. This observation is similar to that of Fig. 8.2b, 8.2c and 8.2d.

Figs. 8.3e and 8.3f show the effect conduction-radiation parameter on isotherm in the X-Y plane at the middle of height of the tunnel. Isotherms for two values of $N = 220.0$ and 300.0 are shown in Figs. 8.3e and 8.3f respectively with $\beta = 1.0$ and $\omega = 0.0$. It is clear from Figs. 8.3b, 8.3e and 8.3f, the effect of radiation is very much dependent upon the conduction-radiation parameter. At the central region of the X-Y plane, the isotherm value is 0.836 for $N = 170.0$ (Fig. 8.3b), 0.751 for $N = 220.0$ (Fig. 8.3e) and 0.709 for $N = 300.0$ (Fig. 8.3f).

Isotherms in the X-Z (vertical) plane at $y = 4.41\text{m}$ are shown in Fig. 8.4. Results are presented for black boundaries. In Figs. 8.4a and 8.4b, isotherms are shown for the case without and with the effect of radiation and they correspond to the cases shown in Figs. 8.2a, 8.2b, 8.3a and 8.3b. It is observed that in the absence of radiation, temperature close to the ceiling in the central region is about 0.59 (Fig. 8.4a) which is lower than that for the case with the effect of radiation (Fig. 8.4b). Further in the axial (x) direction, temperature is more in the presence of radiation.

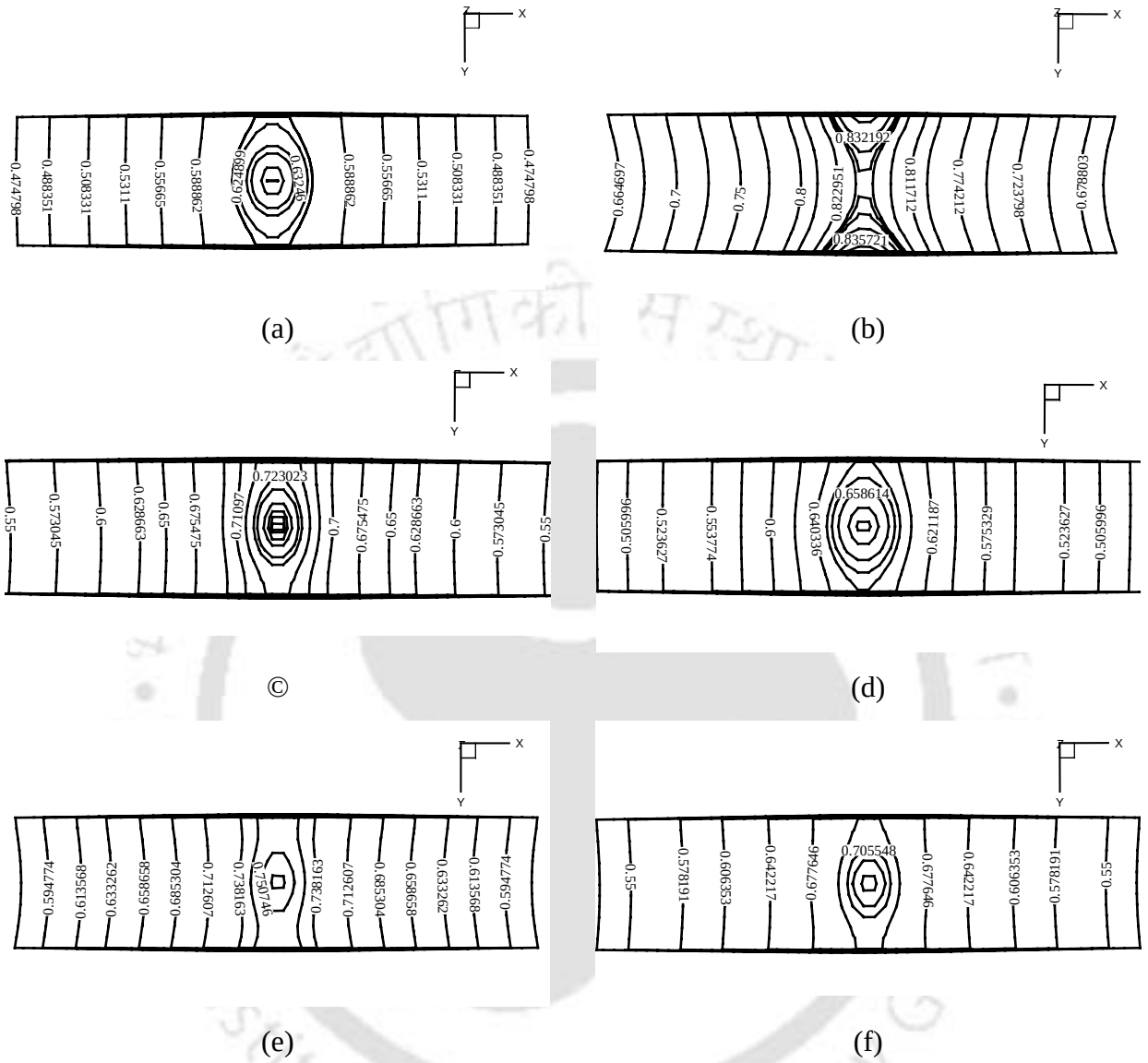

Figure 8.3: Isotherms at the middle ($z = 3.945\,\text{m}$) of the tunnel in X-Y plane (a) without radiation, with radiation for $\beta = 1.0$ (b) $\omega = 0.0$ and $N = 170$, (c) $\omega = 0.5$ and $N = 170$, (d) $\omega = 0.9$ and $N = 170$, (e) $\omega = 0.0$ and $N = 220$ and (f) $\omega = 0.0$ and $N = 300$.

The effect of the scattering albedo ω on isotherms in the X-Z plane is shown in Figs. 8.4c and 8.4d. At the middle of the tunnel, near the ceiling, the approximate values of isotherms are 0.8 (Fig. 8.4b), 0.69 (Fig. 8.4c) and 0.62 (Fig. 8.4d)

for $\omega = 0.0$, $\omega = 0.5$ and $\omega = 0.9$ respectively. A comparison of Figs. 8.4b, 8.4c and 8.4d show that temperature close to the ceiling is less when the scattering of radiation is more, thus in the z – direction, the gradient in temperature increases with increase in ω.

Effect of conduction-radiation parameter N on the isotherms in the X-Z plane is shown in Figs. 8.4e and 8.4f. Observation of Figs. 8.4b, 8.4e and 8.4f show that with increase in N, radiation effect decreases. For $N = 170, 220$ and 300, in the central region, near the ceiling, the approximate values of temperatures are 0.8 (Fig. 8.4b), 0.7 (Fig. 8.4e) and 0.66 (Fig. 8.4f), respectively. Further in the axial (x) direction away from the centre, for higher values of N, temperature decreases.

Effects of the emissivity of the boundaries of the tunnel on isotherms in different planes have been shown in Figs. 8.5a-8.5f. At the middle $(x = 420\,\text{m})$ of the tunnel in Y-Z plane with $\beta = 1.0$, $\omega = 0.0$ and $N = 170.0$, for $\varepsilon = 0.1$ and 0.5, isotherms have been shown in Figs. 8.5a and 8.5b, respectively. It is observed from these figures that the radiation effect is more for higher value of ε. When the emissivity of walls of the tunnel is $\varepsilon = 0.1$, the isotherms very close to the ceiling are 0.665 (Fig. 8.5a) and for $\varepsilon = 0.5$, the values are slightly above 0.723 (Fig. 8.5b). From these figures it is clear that temperature gradient near the ceiling of the tunnel is less than that near the floor.

With $\beta = 1.0$, $\omega = 0.0$ and $N = 170.0$, for $\varepsilon = 0.1$ and 0.5, isotherms in the X-Y plane at the middle $(z = 3.945\,\text{m})$ of the tunnel have been shown in Figs. 8.5c and 8.5d, respectively. When the emissivity of walls of the tunnel is $\varepsilon = 0.1$, the isotherm very close to the central region is slightly more than 0.711 (Fig. 8.5c). When the emissivity of the walls is increased to a value of $\varepsilon = 0.5$, the isotherm value at the central region of X-Y plane is found to be 0.762 (Fig. 8.5b). From these figures it is clear that temperature gradient near the central region of the X-Y plane is less.

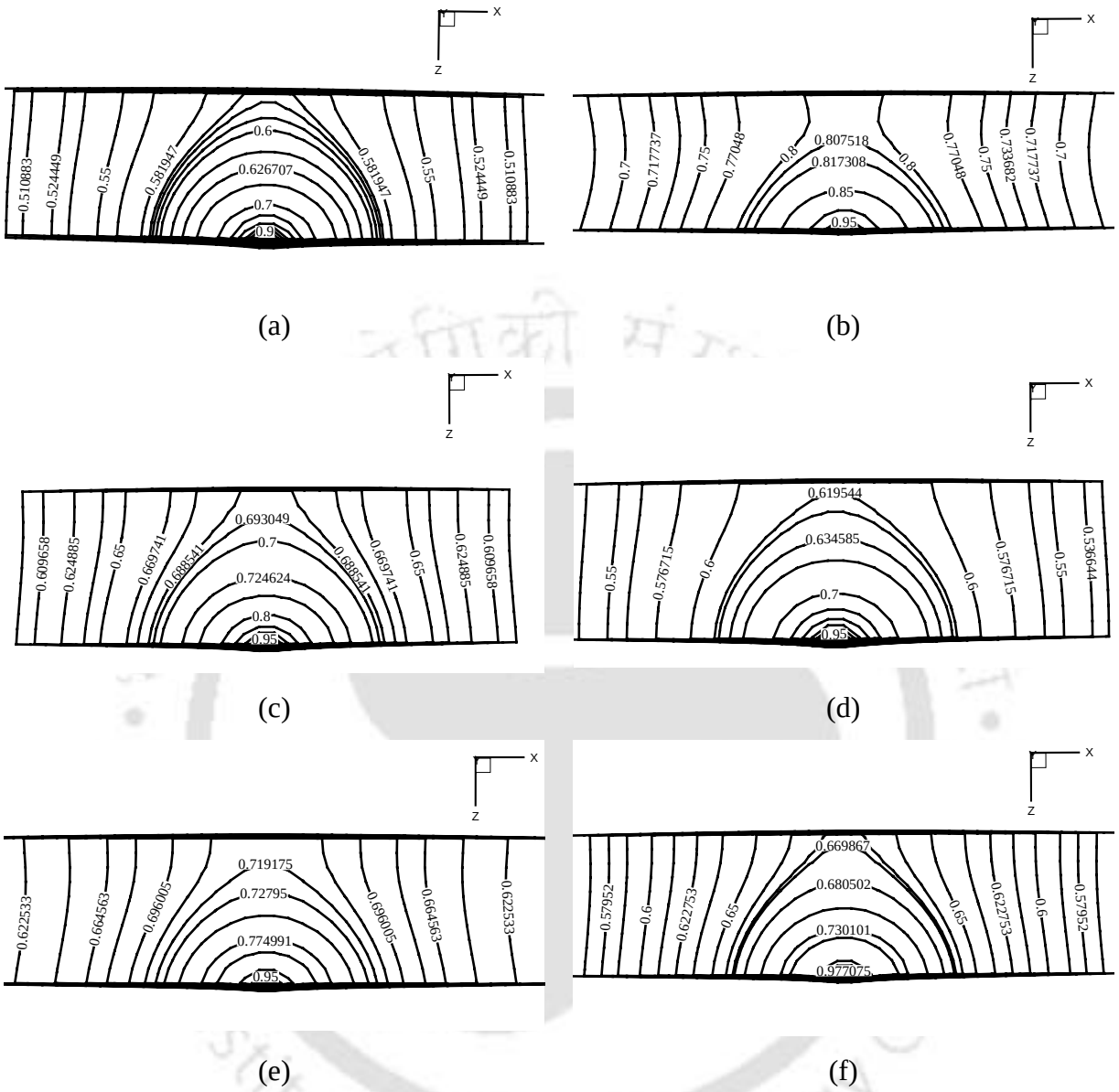

Figure 8.4: Isotherms at the middle ($y = 4.41\text{m}$) of the tunnel in X-Z plane (a) without radiation, with radiation for $\beta = 1.0$ (b) $\omega = 0.0$ and $N = 170$, (c) $\omega = 0.5$ and $N = 170$, (d) $\omega = 0.9$ and $N = 170$, (e) $\omega = 0.0$ and $N = 220$ and (f) $\omega = 0.0$ and $N = 300$.

Effects of wall emissivity on isotherms in the X-Z plane at the middle $(y = 4.41\text{m})$ of the tunnel are shown in Figs.8.5e and 8.5f for $\varepsilon = 0.1$ and 0.5, respectively. These results are shown for $\beta = 1.0$, $\omega = 0.0$ and $N = 170.0$. It is observed from these two figures that when

the walls become more reflecting, in the central region, near the ceiling and also in the axial (x) direction, temperature rise is more.

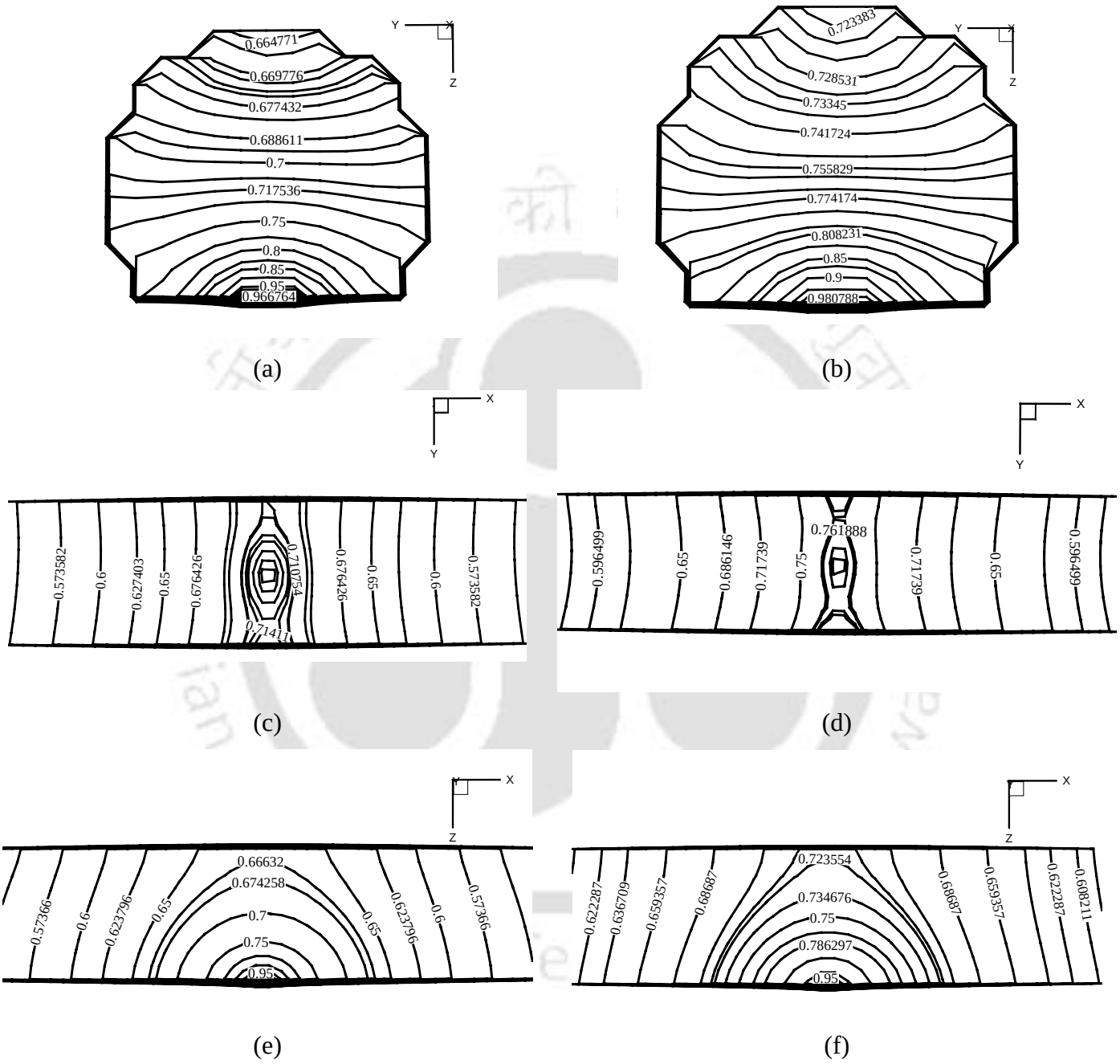

Figure 8.5: Isotherms with radiation for $\beta = 1.0$, $\omega = 0.0$ and $N = 170$ at the middle $(x = 420\,\text{m})$ of the tunnel in Y-Z plane (a) $\varepsilon = 0.1$ (b) $\varepsilon = 0.5$; at the middle $(z = 3.945\,\text{m})$ of the tunnel in X-Y plane (c) $\varepsilon = 0.1$ (d) $\varepsilon = 0.5$; at the middle($y = 4.41\,\text{m}$) of the tunnel in X-Z plane (e) $\varepsilon = 0.1$ (f) $\varepsilon = 0.5$.

8.5 Summary

The localized fire in a 3-D tunnel was analyzed by solving a combined mode natural conduction and radiation problem. Non-local thermal equilibrium between air and smoke was considered. Separate energy equations were used for the two species. The density and temperature fields required for the solution of the energy equation were computed using the lattice Boltzmann method. The finite volume method was used to compute radiative information. The energy equations were solved using the fully explicit upwind scheme. Boussinesq approximation is used to account for the buoyancy effect. Effects of the scattering albedo, the conduction-radiation parameter and the wall emissivities on temperature profiles in the tunnel were studied.

CHAPTER 9

Conclusions and Scope for Future Work

9.1 Conclusions

In the present thesis, applications of the LBM to analyze radiation, conduction and/or convection heat transfer problems in 1-D, 2-D and 3-D Cartesian geometries were considered. The formulation of the governing energy equation was done using the LBM. The FVM was used to compute the radiative information. To extend the applicability of the LBM to different types of heat transfer problems, a total of six problems were considered.

A detailed literature review about the developments and applications of the LBM to various problems in the area of fluid mechanics and heat transfer was presented in Chapter 1. The literature review started with a historical development of the LBM and subsequently its applications to various problems were presented. The year-wise developments were taken as the basis of reviewing the papers on the LBM. Importance of consideration of radiative heat transfer was presented in Chapter 1. Strong and weak points of different numerical radiative transfer methods were briefly discussed. Objectives and organization of the thesis were presented at the end of Chapter 1.

Mathematical formulation to solve a 3-D conduction-radiation problem using the LBM was given in Chapter 2. The kinetic equation to be used in the LBM was derived from Boltzmann equation. A generation formulation to obtain radiative information using the

FVM was presented. With radiative information known, solution procedure in the LBM was discussed.

Application of the LBM to 1-D conduction-radiation heat transfer problems earlier applied on uniform lattices was extended to non-uniform lattices in Chapter 3. The LBM was also implemented to a conduction-radiation problem with flux boundary condition. With non-uniform lattices/control volumes, to facilitate collisions to take place at the same instant, interpolations of the particle distribution functions were done and the single relaxation time based on the smallest size lattice was used for all the lattices. With variable relaxation time, the results with non-uniform size lattices/control volumes were found to compare very well with those with the uniform size lattices/control volumes. For various radiative parameters such as the extinction coefficient, scattering albedo, conduction-radiation parameter and clustering parameter, results of the uniform and non-uniform lattices/control volumes were found in good agreement. In case of heat generation in the medium, effects of various parameters were also studied on temperature distribution θ, conductive heat flux Ψ_C, radiative heat flux Ψ_R and total heat flux Ψ_T. With heat generation, results were found to converge fast. Comparison of results showed very good agreement with those available in the literature. The LBM-FVM with non-uniform lattices/control volumes were found to take less number of iterations for the steady-state solutions.

In Chapter 4, the LBM was applied to solve a transient conduction and radiation problem in a 2-D rectangular enclosure containing absorbing, emitting and scattering medium. Three different cases were considered to validate the usage of the LBM in solving transient conduction and radiation heat transfer problems. To facilitate collisions to take place at the same instant for non-uniform lattices, quadratic interpolations of the particle distribution functions were done.

The results with non-uniform size lattices/control volumes were found to compare very well with those with the uniform size lattices/control volumes. For various parameters including the clustering parameter, results of the uniform and non-uniform

lattices/control volumes were found in good agreements. In case of the 2-D geometry also, the LBM in conjunction with the FVM was implemented for the solution of combined conduction-radiation problems with flux boundary conditions. The validity of the formulation was established first by comparing the results of the inverse problems with that of the direct ones. For different sets of parameters, temperature distributions were analyzed. In the present work, having shown successful implementation of the LBM in conjunction with the FVM to a more general class problem having temperature and flux boundary conditions, we recommend further exploration of the LBM–FVM to other heat transfer problems involving thermal radiation having temperature as well as flux boundary conditions. The effects of heat generation were also analyzed.

The LBM in conjunction with the FVM was used for the solution of combined conduction-radiation problems in a 3-D cubical absorbing, emitting and isotropically scattering medium in Chapter 5. Both temperatures as well as flux boundary conditions were considered. Problems were solved for both uniform and non-uniform lattices/control volumes. Volumetric heat generation was taken into account. Centreline non-dimensional temperature distributions were studied for various parameters such as the extinction coefficient, the scattering albedo, the conduction-radiation parameter, the south boundary emissivity and the south boundary heat flux. With all boundaries at prescribed temperatures, in all the cases, results of uniform and non-uniform lattices/control volumes were also compared and steady-state results were compared with those available in the literature. Results were found in good agreement. Numbers of iterations for steady-state solutions were comparable for both uniform and non-uniform lattices. With south boundary at a prescribed heat flux, the LBM-FVM formulation was validated by comparing temperature results of both the direct and inverse methods. In this, in the inverse method, the number of iterations for the steady-state solution was found less. In conduction dominated case, heat generation was found to have a significant effect on temperature.

Solidification of a 3-D cubical semitransparent absorbing and isotropically scattering medium was analyzed in Chapter 6. An enthalpy based formulation in the LBM was used

to simulate the solidification process. Radiative information was computed using the FVM. Distributions of liquid fraction and temperature were studied for the effects of the extinction coefficient, the scattering albedo, the conduction radiation parameter and the latent heat. In radiation dominated case (low value of the conduction-radiation parameter) and a strongly participating medium situation (high value of the extinction coefficient), the thickness of the mushy zone was observed to be less and its movement was slow. With increase in scattering (high value of scattering albedo), the mushy zone thickness was found to be more. A high value of the latent heat was found to yield a thinner mushy zone. Increase in heat flux extraction from the south boundary resulted in rapid solidification. With a thicker mushy zone, temperature profiles in the medium were found to be steeper.

In Chapter 7, natural convection in the presence of volumetric radiation was analyzed using the LBM. Separate particle distribution functions were used for the computations of velocity and temperature fields. The radiative information required for the energy equation was computed using the FVM. Results of the present work were compared with those available in the literature. A good agreement was achieved. For Ra in the range $10^3 - 10^6$, effects of radiative parameters such as the extinction coefficient and the scattering albedo were analyzed on streamlines and isotherms in the medium. Results with the effects of radiation were also compared with those without radiation. For a high value of the Ra, velocity field was found to be significantly affected by radiation. The flow field was found to be symmetric in the presence of radiation. For a low value of the extinction coefficient, even at a high Ra, the flow field was found similar to that without the effect of radiation. The scattering coefficient was not found to have significant effect on the streamlines. Extinction coefficient was found to have a pronounced effect on temperature distributions in the medium. When the medium is more participating, temperature gradient near the cold boundary was found to be more.

Temperature field in a 3-D tunnel owing to a localized fire was analyzed in Chapter 8. Separate energy equations for air and smoke were considered. Buoyancy effect was considered in the combined mode convection-radiation problem. Velocity and density

fields required in the energy equations for the two species were computed using the LBM. Radiative information for the energy equation was computed using the FVM. With velocity, density and radiative terms known, energy equation was solved using the fully explicit upwind scheme. Three different classes of solvers, viz., LBM for density and velocity fields, FVM for volumetric radiation and FDM based fully explicit upwind schemes were found compatible. For different values of the scattering albedo, the convection-radiation parameter and wall emissivities, isotherms were obtained in Y-Z, X-Y and X-Z planes. Isotherms were also obtained without considering the effect of radiation. In the presence of radiation, temperature was found to be more in the tunnel. When the scattering was more, temperature in the tunnel was less. With increase in convection-radiation parameter, a similar trend was observed. However, with decrease in the emissivities of tunnel boundaries, temperature was found to increase.

Although in the present work, computations were performed on the course grid, the work could successfully establish that three different classes of solvers could be coupled and incorporation of volumetric radiation effect in the fire simulation is inevitable. Since the tunnel size was very big, a precise computation required a huge amount of fine grids and because of the involvement of volumetric radiation, the computational requirement became enormous. This type of practical computations cannot be achieved without parallelization of the codes and running the same on a high end computational platform.

9.2 Scope for Future Work

In the present work, the LBM was applied to the solution of radiation, conduction and/or convection problems in 1-D, 2-D and 3-D Cartesian geometries. Further, the 2-D and 3-D Cartesian geometries considered in the present work did not contain any inhomogeneity in terms of a solid object and they were of regular shapes. One of the important features of the LBM is that it is suitable for a parallel architecture. In fluid mechanics problems, it has also been applied to unstructured grids. Thus keeping above into mind, the following are the scopes for future work:

- The application of the LBM can be applied to radiation, conduction and/or convection problems in 2-D and 3-D Cartesian geometries containing solid inhomogeneties of different shapes and sizes. In case of convective heat transfer, one or more boundaries of the enclosure could be partially open.

- With volumetric radiation, the application of the LBM to combined mode problems can be extended to 1-D, 2-D and 3-D cylindrical geometries.

- With natural convection in the presence of volumetric radiation, computational time without parallelization has been exorbitant. Thus, with simple as well as complex geometries, the radiation, conduction and/or convection problems using the LBM in conjunction with the FVM should be solved on a parallel architecture.

- In the present work, in some problems, the LBM was used on non-uniform lattices. There are many problems which necessitate use of unstructured grids/lattices. Therefore, in future work, use of the LBM to radiation, conduction and/or convection mode problems on unstructured lattices should be taken up.

- As a move towards application of the LBM to more complex problems involving thermal radiation, problems of heat transfer in porous media, free-flame combustion as well as porous media combustion can be taken up.

- In solution of problems dealing with radiation, conduction and/or convection using the LBM, the radiative information so far have been computed using the DTM, DOM, CDM and the FVM. It will be a substantial step if the LBM can be used to compute radiative information also.

Bibliography

1. D. A. Wolf-Gladrow, Lattice-gas cellular automata and lattice Boltzmann models: An Introduction, Springer-Verlag, Berlin-Heidelberg, 2000.
2. G.D. Doolen, Lattice gas method for partial differential equations, Addison-Wesley, 1990.
3. T. Toffoli and N. Margolus, Cellular automata machines: a new environment for modeling, The MIT Press, 1987
4. S. Wolfram, Cellular automata and complexity, Addison-Wesley, Reading MA, 1994.
5. B. Chopard and M. Droz, Cellular automata modeling of physical systems, Cambridge University Press, 1998.
6. L. Kadanoff, On two levels, Phys. Today, 39, 9, pp. 7-9, 1986.
7. W.D. Hillis, Richard Feynman and the connection machine, Phys. Today, 42, 2, pp. 72, 1989.
8. J. Hardy, Y. Pomeau and O. de Pazzis, Time evolution of a two dimensional model systems, I. Invariants states and time correlation functions, J. Math. Phys., 14, 12, pp. 1746-1759, 1973.
9. U. Frisch, B. Hasslacher and Y. Pomeau, Lattice gas automata for the Navier-Stokes equations, Phys. Rev. Lett. 56, pp. 1505, 1986.
10. G.R. McNamara and G. Zanetti, Use of the Boltzmann equation to simulate lattice-gas automata, Phys. Rev. Lett. 61, 20, pp. 2332-2335, 1988.
11. K. Gunstensen, D.H. Rothman, S. Zaleski and G. Zanetti, Lattice Boltzmann model of immiscible fluids, Phys. Rev. A 43, pp.4320 – 4327, 1991.
12. D. Grunau, S. Chen and K. Eggart, A lattice Boltzmann model for multi-phase fluid flows, Phys. Fluids A 5, pp. 2557-2562, 1993.
13. S. Chen, H. Chen, D. Martnez, and W. Matthaeus, Lattice Boltzmann model for simulation of magnetohydrodynamics, Phys. Rev. Lett. 67, pp. 3776 – 3779, 1991.

14. D.O. Martnez, S. Chen and W. Matthaeus, Lattice Boltzmann magneto-hydrodynamics, Phys. Plasma, 1, 6, pp. 1850-1867, 1994.
15. S.P. Dawson, S. Chen and G.D. Doolen, Lattice Boltzmann computations for reaction-diffusion equations, 98, 2, pp. 1514-1523, 1993.
16. S. Succi, R. Benzi and F. Higuera, The Lattice Boltzmann Equation: a new tool for computational fluid dynamics, Physica D, 47, pp. 219, 1991.
17. S. Chen, Z. Wang, X. Shan and G.D. Doolen, Lattice Boltzmann computational fluid dynamics in three dimensions J. Stat. Phys., 68, 3-4, pp. 379-400,1992.
18. W.-S. Jiaung, J.R. Ho and C.-P. Kuo, Lattice Boltzmann method for heat conduction problem with phase change, Numer. Heat Transfer, Part B, 39, pp. 167-187, 2001.
19. J.R. Ho, C.-P. Kuo, W.-S. Jiaung, and C. –J. Twu, Lattice Boltzmann scheme for hyperbolic heat conduction equation, Numer. Heat Transfer, Part B, 41, pp. 591-607, 2002.
20. J.R. Ho, C.-P. Kuo, and W.-S. Jiaung, Study of heat transfer in multilayered structure within the framework of dual-phase-lag heat conduction model using lattice Boltzmann method, Int. J. Heat Mass Transfer, 46, pp. 55-69, 2003.
21. D. Chatterjee, and S. Chakraborty, An Enthalpy-based lattice Boltzmann model for diffusion dominated solid-liquid phase transformation, Physics Letters A., 341, pp. 320-330, 2005.
22. S.C. Mishra and A. Lankadasu, Transient conduction-radiation heat transfer in participating media using the lattice Boltzmann method and the discrete transfer method, Numer. Heat Transfer, A, 47, 9, pp. 935-954, 2005.
23. S. Chen and G.D. Doolen, Lattice Boltzmann method for fluid flows, Annu. Rev. Fluid Mech., 30, pp. 329-364, 1998.
24. X. He, S. Chen, and G.D. Doolen, A novel thermal model for the lattice Boltzmann method in incompressible limit, J. Comput. Phys, 146, pp. 282-300, 1998.
25. S. Succi, The lattice Boltzmann method for fluid dynamics and beyond, Oxford University Press, 2001.
26. R.R. Nourgaliev, T.N. Dinh, T.G. Theofanous, and D. Joseph, The lattice

Boltzmann equation method: Theoretical interpretation, numeric and implications, Int. J. Multiphase flow, 29, pp. 117-169, 2003.

27. L. Zhu, D. Tretheway, L. Petzold, and C. Meinhart, Simulation of fluid slip at 3D hydrophobic micro channel walls by the lattice Boltzmann method, J. Comput. Phys, 202, pp. 181-195, 2005.
28. H. Xi, G. Peng, and S.-H. Chou, Finite-volume lattice Boltzmann schemes in two and three dimensions, Phy. Rev. E, 60, 3, pp. 3380-3388, 1999.
29. S. Succi, M. Vergassola and R. Benzi, Lattice Boltzmann scheme for two-dimensional magnetohydrodynamics, Phys. Rev. A, 43, 8, pp. 4521-4524, 1991.
30. F.J. Alexander, S. Chen and J.D. Sterling, Lattice Boltzmann thermo-hydrodynamics, Phys. Rev. E, 47, 8, pp. 2249-2252, 1993.
31. P.A. Skordos, Initial and boundary conditions for the lattice Boltzmann method, Phys. Rev. E, 48, 6, pp. 4823-4842, 1993.
32. S. Chen, S.P. Dawson, G.D. Doolen, D. R. Janecky and A. Lawniczar, Lattice methods and their applications to reacting systems, Comp. Chem. Engg, 19, 6/7, pp. 617-646, 1995.
33. D.R. Noble, S. Chen, J.G. Georgiadis and R.O. Buckius, A consistent hydrodynamic boundary condition for the lattice Boltzmann method, Phys. Fluids, 7, 1, pp. 203-209, 1995.
34. S. Hou, Q. Zou, S. Chen, G.D. Doolen and A.C. Cogley, Simulation of cavity flow by the lattice Boltzmann method, J. Comp. Phys., 118, pp. 329-347, 1995.
35. W. Miller, Flow in the driven cavity calculated by the lattice Boltzmann method, Phys. Rev. E, 51, 4, pp. 3659-3671, 1995.
36. T. Inamuro, M. Yoshino and F. Ogino, A non-slip boundary condition for lattice Boltzmann method, Phys. Fluids, 7, 12, pp. 2928-2930, 1995.
37. J.G. M. Eggels and J.A. Somers, Numerical simulation of free convective flow using the lattice Boltzmann scheme, Int. J. Heat Fluid Flow, 16, pp. 357-364, 1995.
38. X. He, L.S. Luo, and M. Dembo, Some progress in lattice Boltzmann method. Part I. Non-uniform mesh grids, J. Comput. Phys. 129, pp. 357-363, 1996.
39. X. Shan, Simulation of Rayleigh-Benard convection using a lattice Boltzmann

method, Phys. Rev., E, 55, 3, pp. 2780-2788, 1997.

40. X. He, L.S. Luo, and M. Dembo, Some progress in lattice Boltzmann method: Reynolds number enhancement in simulations, Physica A, 239, pp. 276-285, 1997.
41. X. He and G. Doolen, Lattice Boltzmann method on a curvilinear coordinate system: Vortex shedding behind a circular cylinder, Phys. Rev. E, 56,1, pp. 434-440, 1997.
42. R. Mei and W. Shyy, On the finite difference-based lattice Boltzmann method in curvilinear coordinates, J. Comp. Phys., 143, pp. 426-448, 1998.
43. X. He and G. Doolen, Lattice Boltzmann method on a curvilinear coordinate system: Flow around a circular cylinder, J. Comp. Phys, 134, pp. 306-315, 1997.
44. G. Peng, H. Xi and C. Duncan, Lattice Boltzmann method on irregular meshes, Phys. Rev. E, 58,4, pp. 4124-4127, 1998.
45. M. Soe, G. Vahala, P. Pavlo, L. Vahala and H. Chen, Thermal lattice Boltzmann simulations of variable Prandtl number turbulent flows, Phys. Rev. E, 57,4, pp. 4227-4237, 1998.
46. C. Sun, Lattice-Boltzmann models for high speed flows, Phys. Rev. E, 58, 6, pp. 7283-7287, 1997.
47. O. Fillipova and D. Hanel, Grid refinement for lattice-BGK models, J. Comp. Phys, 147, pp. 219-228, 1998.
48. P. Pavlo, G. Vahala, L. Vahala and M. Soe, Linear stability analysis of thermo-lattice Boltzmann models, J. Comp. Phys, 139, pp. 79-91, 1998.
49. H. Xi and C. Duncan, Lattice Boltzmann simulations of three-dimensional single droplet deformation and breakup under simple shear flow, Phys. Rev. E, 59, 3, pp. 3022-3026, 1999.
50. V. Karlin, S. Succi and S. Orszag, Lattice Boltzmann method for irregular grids, Phys. Rev. Lett., 82, 26, pp. 5245-5248, 1999.
51. R. Verberg and A.J.C. Ladd, Simulation of low –Reynolds-number flow via a time-independent lattice-Boltzmann method, Phys. Rev. E, 60, 3, pp. 3366-3373, 1999.
52. R. Mei, L.S. Luo and W. Shyy, An accurate curved boundary treatment in the lattice Boltzmann method, J. Comp. Phys, 155, pp. 307-330, 1999.

53. K. Sankaranarayanan, X. Shan, I.G. Kevrekidis and S. Sundaresan, Bubble flow simulations with the lattice Boltzmann method, Chem. Engg. Sci., 54, pp. 4817-4823, 1999.
54. B.J. Palmer and D.R. Rector, Lattice Boltzmann algorithm for simulating thermal flow in compressible fluids, J. Comp. Phys, 161, pp. 1-20, 2000.
55. D. Qi, Lattice Boltzmann simulations of fluidization of rectangular particles, Int. J. Multiphase Flow, 26, pp. 421-433, 2000.
56. C. Sun, Adaptive lattice Boltzmann model for compressible flows: Viscous and conductive properties, Phys. Rev. E, 61, 3, pp. 2645-2653, 2000.
57. H. Yu and K. Zhao, Lattice Boltzmann method for compressible flows with high Mach numbers, Phys. Rev. E, 61, 4, pp. 3867-3870, 2000.
58. O. Filippova and D. Hanel, A nobel lattice BGK approach for low Mach number combustion, J. Comp. Phys, 158, pp. 139-160, 2000.
59. C.L. Lin and Y.G. Lai, Lattice Boltzmann method on composite grids, Phys. Rev. E, 62, 2, pp. 2219-2225, 2000.
60. R. Mei, W. Shyy, D. Yu and L.S. Luo, Lattice Boltzmann method for 3-D flows with curved boundary, J. Comp. Phys, 161, pp. 680-699, 2000.
61. K. Kono, T. Ishizuka, H. Tsuda and A. Kurosawa, Application of lattice Boltzmann model to multiphase flows with phase transition, Comp. Phys. Communications, 129, pp. 110-120, 2000.
62. J. Bernsdrof, G. Brenner and F. Durst, Numerical analysis of the pressure drop in porous media flow with lattice Boltzmann (BGK) automata, Comp. Phys. Communications, 129, pp. 247-255, 2000.
63. N. Takada, M. Misawa, A. Tomiyama and S. Fujiwara, Numerical simulation of two-and three-dimensional two-phase fluid motion by lattice Boltzmann method, Comp. Phys. Communications, 129, pp. 233-246, 2000.
64. R. Zhang, H. Chen, Y.H. Qian and S. Chen, Effective volumetric lattice Boltzmann scheme, Phys. Rev. E, 63, 5, pp. 1-6, 2001.
65. W. Miller, The lattice Boltzmann method: a new tool for numerical simulation of the interaction of growth kinetics and melt flow, J. Crystal Growth, 230, pp. 263-269, 2001.

66. C. Denniston, E. Orlandini and J. M. Yeomans, Simulations of liquid crystals in Poiseuille flow, Comput. Theor. Polymer Sci., 11, pp. 389-395, 2001.
67. Z.L. Yang, T.N. Dinh, R.R. Nourgaliev and B. R. Sehgal, Numerical investigation of boiling regime transition mechanism by a lattice Boltzmann model, Nuclear Engg Design, 204, pp. 143-153, 2001.
68. O. Filippova, S. Succi, F. Mazzocco, C. Arrighetti, G. Bella and D. Hanel, Multiscale lattice Boltzmann schemes with turbulence modeling, J. Comp. Phys, 170, pp. 812-829, 2001.
69. J.C. desplat, I. Pagonabarraga and P. Bladon, LUDWIG: a parallel lattice Boltzmann code for complex fluids, Comp. Phys. Commun., 134, pp. 273-290, 2001.
70. C. SHu, Y.T. Chew and X. D. Niu, Least-square-based lattice Boltzmann method: a meshless approach for simulation of flows with complex geometry, Phys. Rev. E, 64, 4, pp. 045701-4, 2001.
71. M. Bouzidi, D. d'Humieres, P. Lallemand and L.S. Luo, Lattice Boltzmann equation on a two-dimensional rectangular grid, J. Comp. Phys, 172, pp. 704-717, 2001.
72. Y.G. Lai, C.L. Lin and J. Huang, Accuracy and efficiency study of lattice Boltzmann method for steady-state flow simulations, Numer. Heat Transfer, B, 39, pp. 21-43, 2001.
73. X. He and G. D. Doolen, Thermodynamic foundations of kinetic theory and lattice Boltzmann models for multiphase flows, J. Stat. Phys., 107, 112, pp. 309-328, 2002.
74. C. Shu, Y. Peng and Y.T. Chew, Simulation of natural convection in a square cavity by taylo series expansion- and least square based lattice Boltzmann method, Int. J. Modern Phys., 13, 10, pp. 1399-1414, 2002.
75. Y.T. Chew, C. Shu and Y. Peng, On implementation of boundary conditions in the application of finite volume lattice Boltzmann method, J. Stat. Phys., 107, 112, pp. 539-556, 2002.
76. X. Zhang, J.W. Crawford, A.G. Bengpugh and I. M. Young, On boundary conditions in the lattice Boltzmann model for advection and anisotropic dispersion

equation, Advances in Water Resources, 25, pp. 601-609, 2002.

77. T. Seta and R. Takahashi, Numerical stability analysis of FDLBM, J. Stat. Phys., 107, 112, pp. 557-572, 2002.
78. Z. Lu, Y. Liao, D. Qian, J.B. McLaughlin, J. J. Derksen and K. Kontomaris, Large Eddy Simulations of a stirred tank using the Lattice Boltzmann method on a non uniform grid, J. Comp. Phys., 181, pp. 675-704, 2002.
79. T. Inamuro, M. Yoshino, H. Inoue, R. Mizono and F. Ogino, A lattice Boltzmann method for a binary miscible fluid mixture and its application to a heat-transfer problem, J. Comp. Phys., 179, pp. 201-215, 2002.
80. I. Ginzburg and K. Steiner, Lattice Boltzmann model for free-surface flow and its application to filling process in casting, , J. Comp. Phys., 185, pp. 61-99, 2003.
81. V. Sofonea and R.F. Sekerka, Viscosity of finite difference lattice Boltzmann models, J. Comp. Phys., 184, pp. 422-434, 2003.
82. Y. Peng, C. Shu and Y.T. Chew, Simplified thermal lattice Boltzmann model for incompressible thermal flows, Phys. Rev. E, 68, 2, pp. 026701-8, 2003.
83. T. Inamuro, T. Ogata, S. Tajima and N. Konishi, A lattice Boltzmann method for incompressible two-phase flows with large density differences, J. Comp. Phys., 198, pp. 628-644, 2004.
84. T. Inamura, K. Suzuki, T. Nakamura and M. Yoshida, Acceleration of steady-state lattice Boltzmann simulations on non-uniform mesh using local time step method, J. Comp. Phys., 202, pp. 645-663, 2005.
85. S.C. Mishra, A. Lankadasu and K. Beronov, Application of the lattice Boltzmann method for solving the energy equation of a 2-D transient conduction-radiation problem, Int. J. Heat Mass Transfer, 48: 3648-3659, 2005.
86. Y. Liu, R.M.C. So and Z.X. Cui, Bluff body flow simulation using lattice Boltzmann equation with multiple relaxation time, Comp. Fluids, 35, pp. 951-956, 2006.
87. R. Raj, A. Prasad, P.R. Parida and S.C. Mishra, Analysis of solidification of a semitransparent planar layer using the lattice Boltzmann method and the discrete transfer method, Numer. Heat Transfer, A, 49, pp. 279-299, 2006.

88. N.Gupta, G.R. Chaitanya and S.C. Mishra, Lattice Boltzmann method applied to variable thermal conductivity conduction radiation problems, J. Thermophys. Heat Transfer, 20, pp. 895-902, 2006.
89. W. C. Hung and Y. Ru, A numerical study for slip flow heat transfer, Applied Math. Comp., 173, pp. 1246-1264, 2006.
90. J. Onishi, Y. Chen and H. Ohashi, Dynamic simulation of multi-component visco-elastic fluids using the lattice Boltzmann method, Physica A, 362, pp. 84-92, 2006.
91. S. Ansumali, I.V. Karlin, C.E. Frouzakis and K.B. Boulouchos, Entropic lattice Boltzmann method for microflows, Physica A, 359, pp. 289-305, 2006.
92. C. K. Chen, T.S. yen and Y.T. Yang, Lattice Boltzmann method simulation of backward-facing step on convective heat transfer with field synergy principle, Int. J. heat Mass Transfer, 49, pp. 1195-1204, 2006.
93. T. Seta, E. Takegoshi and K. Okui, Lattice Boltzmann simulation of natural convection in porous media, Math. Comp. Simulations, 72, pp. 195-200, 2006.
94. A. Tentner, H. Chen and R. Zhang, Simulation of two-phase flow and heat transfer phenomena in a boiling water reactor using the lattice Boltzmann method, Physica A, 362, pp. 98-104, 2006.
95. Y. Zhou, R. Zhang, I. Staroselsky, H. Chen, W. T. Kim and M. S. Jhon, Simulation of micro- and nano-scale flows via the lattice Boltzmann method, Physica A, 362, pp. 68-77, 2006.
96. H.N. Dixit and V. Babu, Simulation of high Rayleigh number natural convection in a square cavity using the lattice Boltzmann method, Int. J. Heat Mass Transfer 49, pp. 727-739, 2006.
97. D. Yu and S.S. Girimaji, Multi-block lattice Boltzmann method:Extension to 3D and validation in turbulence, Physica A, 362, pp. 118-124, 2006.
98. K. Yamamoto and N. Takada, LB simulation on soot combustion in porous media, Physica A, 362, pp. 111-117, 2006.
99. J. Wang, M. Wang and Z. Li, A lattice Boltzmann algorithm for fluid-solid conjugate heat transfer, Int. J. Thermal Sci. 46, pp. 228-234, 2007.
100. S.C. Mishra and H.K. Roy, Solving transient conduction and radiation heat

transfer problems using the lattice Boltzmann method and the finite volume method, J. Comput. Phys.233, pp. 89-107, 2007.

101. Y.Y. Yan and Y.Q. Zu, Numerical simulation of heat transfer and fluid flow past a rotating isothermal cylinder- a LBM approach, Int. J. Heat Mass Transfer, 51, 9-10, pp. 2519-2536, 2007.
102. Z.W. Tian, C. Zou, H.J. Liu, Z.L. Guo, Z. H. Liu and C. G. Zheng, lattice Boltzmann scheme for simulating thermal micro-flow, Physica A, 385, pp. 59-68, 2007.
103. P.H. Kao, T.F. Ren and R.J. Yang, An investigation into fixed-bed micro-reactors using lattice Boltzmann method simulations, Int. J. Heat Mass Transfer, 50, pp. 4243-4255, 2007.
104. F. Kunzik, J. Vereilles, G. Rusaouen and G. Krauss, A double-population lattice Boltzmann method with non-uniform mesh for the simulation of natural convection in a square cavity, Int. J. Heat Fluid Flow, 28, pp. 862-870, 2007.
105. M. Jami, A. Mezrhab, M. Bouzidi and P. Lallemand, Lattice Boltzmann method applied to the laminar natural convection in an enclosure with a heat-generating cylinder conducting body, Int. J. Thermal Sci. 46, pp. 38-47, 2007.
106. J. Bernsdrof, S.E. Harrison, S.M. Smith, P.V. Lawford and D.R. Hose, Applying the lattice Boltzmann technique to biofluids: a novel approach to simulate blood coagulation, Comp. Math. Applications, 55, pp. 1408-1414, 2008.
107. E. Seema, M.E. Ganaoui, R. Bennacer and A.A. Mohamad, Investigation of flows in solidification by using the lattice Boltzmann method, Int. J. Thermal Sci. 47, pp. 201-208, 2008.
108. C. Sun and L.L. Munn, Lattice Boltzmann simulation of blood flow in digitized vessel networks, Comp. Math. Applications, 55, pp. 1594-1600, 2008.
109. M.F. Modest, Radiative Heat Transfer, 2nd Edition, Academic Press, New York, 2003.
110. R. Siegel and J. Howell, Thermal Radiation Heat Transfer, 4th edition, Taylor & Francis, New York, 2002.
111. P. Talukdar, Combined radiation, conduction and/or convection heat transfer in participating media, PhD thesis, Indian Institute of Technology Guwahati, India,

2004.

112. S. Rosseland, Theoretical astrophysics; atomic theory and the analysis of stellar atmosphere and envelopes, Clarendon Press, Oxford, 1936.
113. H.C. Hottel and E.S. Cohen, Radiant heat exchange in a gas-filled enclosure: allowance for non-uniformity of gas temperature, AIChE Journal, 4, pp. 3-14, 1958.
114. J.A. Fleck, The calculation of nonlinear radiation transport by a Monte Carlo method: statistical physics, Methods in Comp. Phys. 1, pp. 43-65, 1961.
115. T.M. Shih and Y.N. Chen, A discretized intensity method proposed for two-dimensional systems enclosing radiative and conductive media, Numer. Heat Transfer, 6, pp. 117-134, 1983.
116. F.A. Milne, Thermodynamics of the stars, in handbook of astrophysics, Springer-Verlag, OHG, Berlin, pp.65-255, 1930.
117. V. Kourganoff, Basic methods in Transfer problems, Dover Publications, New York, 1963.
118. G.D. Raithby and E.H. Chui, A finite volume method for predicting radiant heat transfer in enclosures with participating media. ASME J Heat Transfer, 112: 415-423, 1990.
119. J.C. Chai, H.S. Lee and S.V. Patankar, Finite volume method for radiation heat transfer, AIAA J thermophys Heat Transfer, 8(3): 419-425, 1994.
120. J. C. Chai and S. V. Patankar, Finite volume method for radiation Heat Transfer, Adv. Numer. Heat Transfer, 2, 110-135, 2000.
121. P. Mahanta and S.C. Mishra, Collapsed dimension method applied to radiative transfer problems in complex enclosures with participating medium, Numer. Heat Transfer, B, 42, 4, pp. 367-38, 2002.
122. P. Talukdar and S.C. Mishra, Analysis of conduction-radiation problem in absorbing, emitting and anisotropically scattering media using the collapsed dimension method, Int. J. Heat Mass Transfer, 45, pp. 2159-2168, 2002.
123. J. R. Howell, Radiative transfer in multi-dimensional enclosures with participating media, ASME, 83-HT-32, 1983.

124. K.T. Yang, Numerical modeling of natural convection-radiation interactions in enclosures, In Proceedings of the 8th International Heat Transfer Conference, 1, pp. 131-140, 1986.
125. P.L. Bhatnagar, E.P. Gross and M. Krook, A model for collusion process in gases. I. small amplitude processes in charged and neutral one-component systems, Phys. Rev., 94, 3, pp. 511-525, 1954.
126. X. He and L.S. Luo, Theory of the lattice Boltzmann method: From the Boltzmann equation to the lattice Boltzmann equation, Phy. Rev. E, 56, 6, pp. 6811-6817, 1997.
127. R.R. Nourgaliev, T.N. Dinh, T.G. Theofanous, and D. Joseph, The lattice Boltzmann equation method: Theoretical interpretation, numeric and implications, Int. J. Multiphase flow, 29, 117-169, 2003.
128. S. Suci, G. Amati and R. Benzi, Challenges in lattice Boltzmann computing, J. Stat. Phys., 81, pp. 5-16, 2005.
129. S. Ubertini and S. Succi, Recent advances of lattice Boltzmann techniques on unstructured grid, Progress in Computational Fluid Dynamics, 5, 85-96, 2005.
130. H. D. Chen, Finite volume lattice Boltzmann method, Phys. Rev. E, 59, pp. 6202-6205, 1999.
131. R. Viskanta and R.J. Grosh, Heat transfer by simultaneous conduction and radiation in an absorbing medium. J. Heat Transfer, 84: 63-72, 1962.
132. R. Fernandes and J. Francis, Finite element analysis of planer conductive and radiative heat transfer with flux boundary. In Paper No. 82-0910, 3rd AIAA/ASME Joint Thermophysics, Fluids, Plasma and Heat Transfer Conf., Saint Louis, MO, June 7-11, 1992.
133. J.D. Lin and J.H. Tsai, Radiation-conduction interaction in a planer, anisotropically scattering medium with flux boundary. Numer. Heat Transfer, A, 16: 119-128, 1989.
134. C. Barker and W.H. Sutton, The transient radiation and conduction heat transfer in a gray participating medium with semi-transparent boundaries, Radiation Heat Transfer, ASME J. Radiation Heat Transfer, 49:25-36, 1985.
135. W.H. Sutton, A short time solution for coupled conduction and radiation in a

participating slab geometry, J. Heat Transfer, 108: 465-466, 1986.

136. C.C. Lii and M.N. Ozisik, Transient radiation and conduction in an absorbing, emitting and scattering slab with reflective boundaries. Int. J. Heat Mass Transfer, 15: 1175-1179, 1972.
137. J.R. Tsai and M.N. Ozisik, Transient, combined conduction and radiation in an absorbing, emitting and isotropically scattering solid sphere. J. Quant. Spectros. Radiat. Transfer, 38(4): 243-251, 1987.
138. R. Viskanta, Heat transfer by conduction and radiation in absorbing and scattering materials. J. Heat Transfer, 87(1): 143-150, 1965.
139. C.H. Ho and M.N. Ozisik, Combined conduction and radiation in a two layer planer medium with flux boundary condition, Numer. Heat Transfer, 11(3): 321, 1987.
140. P.R. Parida, R. Raj, A. Prasad and S.C. Mishra, Solidification of a semitransparent planar layer subjected to radiative and convective cooling, J. Quant. Spectrosc. Radiat. Transfer, 107, pp. 226-235, 2007.
141. B. Mondal and S.C. Mishra, Application of the lattice Boltzmann method and discrete ordinate method for solving transient conduction and radiation heat transfer problems, Numerical Heat Transfer, Part A , 52, 8, pp. 757-775, 2007.
142. F. Massaioli, R. Benzi and S. Succi, Exponential tails in two-dimensional Rayleigh-Bénard convection, Europhys. Lett., 21(1993), 305-310.
143. W.W. Yuen and E.E. Takara, Analysis of combined conductive-radiative heat transfer in a two-dimensional rectangular enclosure with a gray medium, J. Heat Transfer, 110, 468-474, 1988.
144. C.Y. Wu and N.R. Ou, Transient two-dimensional radiative and conductive heat transfers in a scattering medium, Int. J. Heat Mass Transfer, 37, 2675-2686, 1994.
145. S.C. Mishra, P. Talukdar, D. Trimis and F. Durst, Computational efficiency improvements of the radiative transfer problems with or without conduction – a comparison of the collapsed dimension method and the discrete transfer method, Int. J. Heat Mass Transfer, 46, 3083-3095, 2003.
146. H. S. Chu and C. J. Tseng, Conduction-radiation interaction in absorbing, emitting and scattering media with variable thermal conductivity, J. Thermophys. Heat

Transfer, 6, 3, pp. 537-540, 1992.

147. C.N. Sokman and M.M. Razzaque, Finite element analysis of conduction radiation heat transfer in an enclosure with heat flux boundary conditions, In Radiation, Phase Change Heat Transfer and Thermal Systems, ASME HTD, 81, 1, pp. 17-23, 1987.
148. L. H. Liu, H. P. Tan and T.W. Tong, Non-Fourier effects on transient temperature response in semitransparent medium caused by laser pulse, Int. J. Heat Mass Transfer, 44, pp. 3335-3344, 2001.
149. D. Chatterjee and S. Chakraborty, An Enthalpy-Source Based Lattice Boltzmann Model for Conduction Dominated Phase Change of Pure Substances, Int. J. Thermal Sci., 47, 5, pp. 552-559, 2008.
150. D. Chatterjee and S. Chakraborty, A Hybrid Lattice Boltzmann Model for Solid-Liquid Phase Transition in Presence of Fluid Flow, Phys. Lett., *A*, 351, pp. 359-367, 2005.
151. S. Chakraborty and D. Chatterjee, An Enthalpy-Based Hybrid Lattice-Boltzmann Method for Modelling Solid–Liquid Phase Transition in the Presence of Convective Transport, J. Fluid Mechanics, 592, pp. 155-175, 2007.
152. P. Talukdar, F. V. Issendrorff, D. Trimis, and C.J. Simonson, "Conduction-radiation interaction in 3-D irregular enclosures using the finite volume method," Heat and Mass Transfer, 44, 6, pp.695-704, 2008.
153. O. Wellele, H.R.B. Orlande, N. Jr. Ruperti, M. J. Colaco and A. Delmas, Coupled conduction-radiation in semi-transparent materials at high temperatures, J. Phys. Chem. Solids, 67, pp. 2230-2240, 2006.
154. S. H. Co and J.E. Sunderland, Heat conduction problems with melting or freezing, J. Heat Transfer 91, pp. 421-426, 1969.
155. I.S. Habib, Solidification of semitransparent materials by conduction and radiation, Int. J. Heat Mass Transfer,14, pp. 2161–2164, 1971.
156. M. Abrams, R. Viskanta, The effects of radiative heat transfer upon the melting and solidification of semitransparent crystals, J. Heat Transfer 96, pp. 184–190, 1974.

157. F.O. Oruma, M.N. Ozisik, M.A. Boles, Effects of anisotropic scattering on melting and solidification of a semiinfinite semi-transparent medium, Int. J. Heat Mass Transfer 28, pp. 441–449, 1985.
158. V.S. Yuferev, Z. Chvoj, E.N. Kolesnikova, The effect of radiative heat transfer on morphological stability during directional solidification of a binary melt, J. Cryst. Growth 108, pp. 367–376, 1991.
159. Y. Shu, B.Q. Al, L. A1, K.G. Lynn, Numerical modeling of internal radiation and solidification in semitransparent melts in magnetic fields. Numer. Heat Transfer, B 45, pp. 957-976, 2004.
160. S.C. Mishra, N.C. Behera, A.K. Garg and A. Mishra, Solidification of a 2-D semitransparent medium using the lattice Boltzmann method and the finite volume method, Int. J. Heat Mass Transfer (doi:10.1016/j.ijheatmasstransfer.2008.02.003) 2008.
161. E.M. Genies, M. Lapkowski, C. Santier and E. Vieil, Polyaniline, spectrochemistry, dsisplay and battery, Synth. Met. 18, pp. 631-636, 1987.
162. B. Scosati, Conducting polymers: new frontiers and prospective, Mat. Sci. Eng. 12, pp. 369-373, 1992.
163. J. Chen, A.K. Burrell, G.E. Callis, D.L Officer, G. F. Swiegers, Preparation, characterization and biosensor application of conditioning polymers based on ferrocene substituted thiopene and terthiophene, Electrochim. Acta, 47, pp. 2715-2724, 2002.
164. K. Gurunathan, D. Amalnerkar, D. Triovedi, Synthesis and characterization of conducting polymer composite for cathode material in rechargeable battery, Mat. Lett. 57, pp. 1642-1648, 2003.
165. P. Sadooghi, Transient coupled radiative and conductive heat transfer in a semitransparent layer of ceramic, J. Quant. Spectros. Radiat. Transfer, 92, pp. 403-416, 2005.
166. J.Y. Oh, M.Y. Ha, T.F. Kim, A numerical study of heat transfer and flow of natural convection in an enclosure with a heat generating conducting body, Numer Heat Transfer A, Vol.31, pp. 289-304, 1997.
167. M.Y. Ha, M.J. Jung, A numerical study on three-dimensional conjugate heat-

transfer of natural convection and conduction in a differentially-heated cubic enclosure with a heat generating cubic conducting body, Int J Heat Mass Transfer, Vol.43, pp. 4229-48, 2000.

168. E. Sediki, A. Soufiani, M.S. Sifaoui, Combined gas radiation and laminar mixed convection in vertical circular tubes, Int J Heat and Fluid Flow, Vol. 24, pp. 736-746, 2003.
169. C. Balaji, S.P. Venkateshan, Combined conduction, convection and radiation in a slot, Int J Heat and Fluid Flow, Vol.16, pp. 139-144, 1995.
170. S.N. Singh and S. P. Venkateshan, Numerical study of natural convection with surface radiationin side-vented open cavities, Int. J. Thermal Sciences, Vol. 43, pp. 865-876, 2004.
171. A.K. Sharma. K. Velusamy, C. Balaji and S.P. Venkateshan, Conjugate turbulent natural convection with surface radiation in air filled rectangular enclosures, Int. J. Heat Mass Transfer, Vol. 50, pp. 625-639, 2007.
172. W.W. Yan, Y. Liu, Z.L. Guo, and Y.S. Xu, "Lattice Boltzmann simulation on natural convection heat transfer in a two-dimensional cavity filled with heterogeneously porous medium", Int. J. Modern Phys., Vol. 17, pp. 771-783, 2006.
173. Z. Tan, and J.R. Howell, "Combined radiation and natural convection in a two dimensional participating square medium", Int. J. Heat Mass Transfer, Vol. 34, pp. 785-791, 1991.
174. M.K. Banda, A. Klar, and M. Seaid, "A lattice-Boltzmann relaxation scheme for coupled convection-radiation systems", J. Comp. Phys. Vol. 206, pp. 1408-1431, 2007.
175. X. He, Q. Zou, L.S. Luo, and M. Dembo, "Analytic solutions of simple flows and analysis of non-slip boundary condition for the lattice Boltzmann BGK model", J. Stat. Phys., Vol. 87, pp. 115-136, 1997.
176. G.D.V. Davis, "Natural convection of air in a square cavity: a benchmark numerical solution", Int. J. Numer. Meth. Fluids, Vol. 3, pp. 249-264, 1983.
177. J.M. House, C. Beckermann and T.F. Smith, Effect of a centred conducting body on natural convection heat transfer in an enclosure, Numer Heat Transfer A, 18,

pp. 213-225, 1990.

178. L.C. Chang, K.T. Yang and J.R. Lloyd, Radiation- natural convection interactions in two-dimensional complex enclosures, J Heat Transfer , 105, pp. 89-95, 1983.
179. W.M.S. Bradbury, W.S. Atkins, The Mont Blanc tunnel fire of 24 March 1999 simulations of alternative ventilation configurations, Third International Conference “Tunnel fires and Escape from Tunnels ”, 9-11 October 2001, Washington;113-124.
180. B. Brousse, A. Voeltzel, Y.Le Botlan and E. Ruffin, Mont Blanc tunnel ventilation and fire tests, Tunnel Management International, 5, pp.1, 2002.
181. V. Ferro, R. Borchiellini and V. Giaretto, Description and application of a tunnel simulation model, Aerodynamic and Ventilation of Vehicle Tunnels, Elsevier Applied Science, pp. 487-512, 1991.
182. P. Chase and J.M. Apvrille, A new ID computer model for fires in complex under ground networks, Fire in Tunnel, pp. 201-202, 1999 .
183. B. Chopard, P.O. Luthi, Lattice Boltzmann computations and applications to physics, Theor. Comput. Phys. 217, pp.115–130, 1999.
184. R.G.M. von der Sman, M.H. Ernst, A.C. Berkerbosch, Lattice Boltzmann scheme for cooling of packed cut flowers, Int. J. Heat Mass Transfer, 43, pp. 577–587, 2000.
185. P. Asinari, Semi-implicit-linearized multiple-relaxation time formulation of lattice Boltzmann schemes for mixture modeling, Physical Review E, 73, 5, pp. 056705-056728, 2006.
186. B. Mondal and S.C. Mishra, Lattice Boltzmann method Applied to the solution of the energy equations of the transient conduction and radiation problems on non-uniform lattices, Int. J. Heat Mass Transfer, 51, pp. 68-82, 2008.
187. S.V. Patankar, Numerical Heat Transfer and Fluid Flow, McGraw-Hill, 1981.
188. Ferziger J.H., Peric M., Computational Methods for Fluid Dynamics, Springer, Germany 1996.
189. S. Chapman, T.G. Cowling, The Mathematical Theory of Non-Uniform Gases, Cambridge University Press, Cambridge, 1970.

190. B.B. Hamel, Boltzmann Equations for Binary Gas Mixtures, Ph.D. dissertation, Princeton University, 1963.
191. P. Asinari, Asymptotic analysis of multiple-relaxation-time lattice Boltzmann schemes for mixture modeling, Computers and Mathematics with Applications, 55, pp. 1392-1407, 2008.
192. P. Andries and K. Aoki and B. Perthame, A consistent BGK-type model for gas mixtures, Journal of Statistical Physics, 106 pp.993-1018, 2002.
193. C. Cercignani, Theory and applications of the Boltzmann equation, Scottish Academic Press, Edinburgh and London, UK, 1975.
194. T. Abe, Derivation of the lattice Boltzmann method by means of the discrete ordinate method for the Boltzmann equation, J. Comput. Phys., 131, pp. 241-246, 1997.
195. Y. H. Qian, D. D'Humieres, P. Lallemand, Lattice BGK models for Navier-Stokes equations, Europhysics Letters, 17, pp. 479-484, 1992.
196. Y. Sone, Kinetic Theory and Fluid Dynamics, Birkhauser, Boston, 2002.

Appendix

For 3-D geometry considered in the present work, Eq. (8.25) is written as

$$\rho\frac{\partial T}{\partial t}+\rho U_x\frac{\partial T}{\partial x}+\rho U_y\frac{\partial T}{\partial y}+\rho U_z\frac{\partial T}{\partial z}=\Gamma\left(\frac{\partial^2 T}{\partial x^2}+\frac{\partial^2 T}{\partial y^2}+\frac{\partial^2 T}{\partial z^2}\right)$$

and for the 8 velocity combinations given in Eq. (8.26), the above equation is discretized in the following way in the upwind scheme:

Condition 1: $U_x>0$, $U_y>0$ and $U_z>0$ (refer to Eq. (8.26a)):

$$\rho\frac{T_{i,j,k}^{n+1}-T_{i,j,k}^{n}}{\Delta t}=-(\rho U)_x\frac{T_{i,j,k}^{n}-T_{i-1,j,k}^{n}}{\Delta x}-(\rho U)_y\frac{T_{i,j,k}^{n}-T_{i,j-1,k}^{n}}{\Delta y}-(\rho U)_z\frac{T_{i,j,k}^{n}-T_{i,j,k-1}^{n}}{\Delta z}$$
$$+\Gamma\left[\frac{T_{i+1,j,k}^{n}-2T_{i,j,k}^{n}+T_{i-1,j,k}^{n}}{\Delta x^2}+\frac{T_{i,j+1,k}^{n}-2T_{i,j,k}^{n}+T_{i,j-1,k}^{n}}{\Delta y^2}+\frac{T_{i,j,k+1}^{n}-2T_{i,j,k}^{n}+T_{i,j,k-1}^{n}}{\Delta z^2}\right]$$

$$T_{i,j,k}^{n+1}=\left(1-\frac{(\rho U)_x\Delta t}{\Delta x\rho}-\frac{(\rho U)_y\Delta t}{\Delta y\rho}-\frac{(\rho U)_z\Delta t}{\Delta z\rho}-3\times 2\frac{\Gamma\Delta t}{\rho\Delta x^2}\right)T_{i,j,k}^{n}$$
$$+\left(\frac{\Gamma\Delta t}{\rho\Delta x^2}\right)T_{i+1,j,k}^{n}+\left(\frac{\Gamma\Delta t}{\rho\Delta x^2}+\frac{(\rho U)_x\Delta t}{\Delta x\rho}\right)T_{i-1,j,k}^{n}$$
$$+\left(\frac{\Gamma\Delta t}{\rho\Delta x^2}\right)T_{i,j+1,k}^{n}+\left(\frac{\Gamma\Delta t}{\rho\Delta x^2}+\frac{(\rho U)_y\Delta t}{\Delta x\rho}\right)T_{i,j-1,k}^{n}$$
$$+\left(\frac{\Gamma\Delta t}{\rho\Delta x^2}\right)T_{i,j,k+1}^{n}+\left(\frac{\Gamma\Delta t}{\rho\Delta x^2}+\frac{(\rho U)_z\Delta t}{\Delta x\rho}\right)T_{i,j,k-1}^{n}$$

Condition 2: $U_x>0$, $U_y<0$ and $U_z>0$ (refer to Eq. (8.26b)):

$$\rho\frac{T_{i,j,k}^{n+1}-T_{i,j,k}^{n}}{\Delta t}=-(\rho U)_x\frac{T_{i,j,k}^{n}-T_{i-1,j,k}^{n}}{\Delta x}-(\rho U)_y\frac{T_{i,j+1,k}^{n}-T_{i,j,k}^{n}}{\Delta y}-(\rho U)_z\frac{T_{i,j,k}^{n}-T_{i,j,k-1}^{n}}{\Delta z}$$
$$+\Gamma\left[\frac{T_{i+1,j,k}^{n}-2T_{i,j,k}^{n}+T_{i-1,j,k}^{n}}{\Delta x^2}+\frac{T_{i,j+1,k}^{n}-2T_{i,j,k}^{n}+T_{i,j-1,k}^{n}}{\Delta y^2}+\frac{T_{i,j,k+1}^{n}-2T_{i,j,k}^{n}+T_{i,j,k-1}^{n}}{\Delta z^2}\right]$$

$$T_{i,j,k}^{n+1} = \left(1 - \frac{(\rho U)_x \Delta t}{\rho \Delta x} + \frac{(\rho U)_y \Delta t}{\rho \Delta y} - \frac{(\rho U)_z \Delta t}{\rho \Delta z} - 3 \times 2 \frac{\Gamma \Delta t}{\rho \Delta x^2}\right) T_{i,j,k}^n$$
$$+ \left(\frac{\Gamma \Delta t}{\rho \Delta x^2}\right) T_{i+1,j,k}^n + \left(\frac{\Gamma \Delta t}{\rho \Delta x^2} + \frac{(\rho U)_x \Delta t}{\rho \Delta x}\right) T_{i-1,j,k}^n$$
$$+ \left(\frac{\Gamma \Delta t}{\rho \Delta x^2} - \frac{(\rho U)_y \Delta t}{\Delta x \rho}\right) T_{i,j+1,k}^n + \left(\frac{\Gamma \Delta t}{\rho \Delta x^2}\right) T_{i,j-1,k}^n$$
$$+ \left(\frac{\Gamma \Delta t}{\rho \Delta x^2}\right) T_{i,j,k+1}^n + \left(\frac{\Gamma \Delta t}{\rho \Delta x^2} + \frac{(\rho U)_z \Delta t}{\rho \Delta x}\right) T_{i,j,k-1}^n$$

Condition 3: $U_x > 0$, $U_y < 0$ and $U_z < 0$ (refer to Eq. (8.26c)):

$$\rho \frac{T_{i,j,k}^{n+1} - T_{i,j,k}^n}{\Delta t} = -(\rho U)_x \frac{T_{i,j,k}^n - T_{i-1,j,k}^n}{\Delta x} - (\rho U)_y \frac{T_{i,j+1,k}^n - T_{i,j,k}^n}{\Delta y} - (\rho U)_z \frac{T_{i,j,k+1}^n - T_{i,j,k}^n}{\Delta z}$$
$$+ \Gamma \left[\frac{T_{i+1,j,k}^n - 2T_{i,j,k}^n + T_{i-1,j,k}^n}{\Delta x^2} + \frac{T_{i,j+1,k}^n - 2T_{i,j,k}^n + T_{i,j-1,k}^n}{\Delta y^2} + \frac{T_{i,j,k+1}^n - 2T_{i,j,k}^n + T_{i,j,k-1}^n}{\Delta z^2}\right]$$

$$T_{i,j,k}^{n+1} = \left(1 - \frac{(\rho U)_x \Delta t}{\rho \Delta x} + \frac{(\rho U)_y \Delta t}{\rho \Delta y} + \frac{(\rho U)_z \Delta t}{\rho \Delta z} - 3 \times 2 \frac{\Gamma \Delta t}{\rho \Delta x^2}\right) T_{i,j,k}^n$$
$$+ \left(\frac{\Gamma \Delta t}{\rho \Delta x^2}\right) T_{i+1,j,k}^n + \left(\frac{\Gamma \Delta t}{\rho \Delta x^2} + \frac{(\rho U)_x \Delta t}{\rho \Delta x}\right) T_{i-1,j,k}^n$$
$$+ \left(\frac{\Gamma \Delta t}{\rho \Delta x^2} - \frac{(\rho U)_y \Delta t}{\rho \Delta x}\right) T_{i,j+1,k}^n + \left(\frac{\Gamma \Delta t}{\rho \Delta x^2}\right) T_{i,j-1,k}^n$$
$$+ \left(\frac{\Gamma \Delta t}{\rho \Delta x^2} - \frac{(\rho U)_z \Delta t}{\rho \Delta x}\right) T_{i,j,k+1}^n + \left(\frac{\Gamma \Delta t}{\rho \Delta x^2}\right) T_{i,j,k-1}^n$$

Condition 4: $U_x > 0$, $U_y > 0$ and $U_z < 0$ (refer to Eq. (8.26d)):

$$\rho \frac{T_{i,j,k}^{n+1} - T_{i,j,k}^n}{\Delta t} = -(\rho U)_x \frac{T_{i,j,k}^n - T_{i-1,j,k}^n}{\Delta x} - (\rho U)_y \frac{T_{i,j,k}^n - T_{i,j-1,k}^n}{\Delta y} - (\rho U)_z \frac{T_{i,j,k+1}^n - T_{i,j,k}^n}{\Delta z}$$
$$+ \Gamma \left[\frac{T_{i+1,j,k}^n - 2T_{i,j,k}^n + T_{i-1,j,k}^n}{\Delta x^2} + \frac{T_{i,j+1,k}^n - 2T_{i,j,k}^n + T_{i,j-1,k}^n}{\Delta y^2} + \frac{T_{i,j,k+1}^n - 2T_{i,j,k}^n + T_{i,j,k-1}^n}{\Delta z^2}\right]$$

$$T_{i,j,k}^{n+1} = \left(1 - \frac{(\rho U)_x \Delta t}{\rho \Delta x} - \frac{(\rho U)_y \Delta t}{\rho \Delta y} + \frac{(\rho U)_z \Delta t}{\rho \Delta z} - 3 \times 2 \frac{\Gamma \Delta t}{\rho \Delta x^2}\right) T_{i,j,k}^{n}$$
$$+ \left(\frac{\Gamma \Delta t}{\rho \Delta x^2}\right) T_{i+1,j,k}^{n} + \left(\frac{\Gamma \Delta t}{\rho \Delta x^2} + \frac{(\rho U)_x \Delta t}{\rho \Delta x}\right) T_{i-1,j,k}^{n}$$
$$+ \left(\frac{\Gamma \Delta t}{\rho \Delta x^2}\right) T_{i,j+1,k}^{n} + \left(\frac{\Gamma \Delta t}{\rho \Delta x^2} + \frac{(\rho U)_y \Delta t}{\rho \Delta x}\right) T_{i,j-1,k}^{n}$$
$$+ \left(\frac{\Gamma \Delta t}{\rho \Delta x^2} - \frac{(\rho U)_z \Delta t}{\rho \Delta x}\right) T_{i,j,k+1}^{n} + \left(\frac{\Gamma \Delta t}{\rho \Delta x^2}\right) T_{i,j,k-1}^{n}$$

Condition 5: $U_x < 0$, $U_y > 0$ and $U_z > 0$ (refer to Eq. (8.26e)):

$$\rho \frac{T_{i,j,k}^{n+1} - T_{i,j,k}^{n}}{\Delta t} = -(\rho U)_x \frac{T_{i+1,j,k}^{n} - T_{i,j,k}^{n}}{\Delta x} - (\rho U)_y \frac{T_{i,j,k}^{n} - T_{i,j-1,k}^{n}}{\Delta y} - (\rho U)_z \frac{T_{i,j,k}^{n} - T_{i,j,k-1}^{n}}{\Delta z}$$
$$+ \Gamma \left[\frac{T_{i+1,j,k}^{n} - 2T_{i,j,k}^{n} + T_{i-1,j,k}^{n}}{\Delta x^2} + \frac{T_{i,j+1,k}^{n} - 2T_{i,j,k}^{n} + T_{i,j-1,k}^{n}}{\Delta y^2} + \frac{T_{i,j,k+1}^{n} - 2T_{i,j,k}^{n} + T_{i,j,k-1}^{n}}{\Delta z^2}\right]$$

$$T_{i,j,k}^{n+1} = \left(1 + \frac{(\rho U)_x \Delta t}{\rho \Delta x} - \frac{(\rho U)_y \Delta t}{\rho \Delta y} - \frac{(\rho U)_z \Delta t}{\rho \Delta z} - 3 \times 2 \frac{\Gamma \Delta t}{\rho \Delta x^2}\right) T_{i,j,k}^{n}$$
$$+ \left(\frac{\Gamma \Delta t}{\rho \Delta x^2} - \frac{(\rho U)_x \Delta t}{\rho \Delta x}\right) T_{i+1,j,k}^{n} + \left(\frac{\Gamma \Delta t}{\rho \Delta x^2}\right) T_{i-1,j,k}^{n}$$
$$+ \left(\frac{\Gamma \Delta t}{\rho \Delta x^2}\right) T_{i,j+1,k}^{n} + \left(\frac{\Gamma \Delta t}{\rho \Delta x^2} + \frac{(\rho U)_y \Delta t}{\rho \Delta x}\right) T_{i,j-1,k}^{n}$$
$$+ \left(\frac{\Gamma \Delta t}{\rho \Delta x^2}\right) T_{i,j,k+1}^{n} + \left(\frac{\Gamma \Delta t}{\rho \Delta x^2} + \frac{(\rho U)_z \Delta t}{\rho \Delta x}\right) T_{i,j,k-1}^{n}$$

Condition 6: $U_x < 0$, $U_y > 0$ and $U_z < 0$ (refer to Eq. (8.26f)):

$$\rho \frac{T_{i,j,k}^{n+1} - T_{i,j,k}^{n}}{\Delta t} = -(\rho U)_x \frac{T_{i+1,j,k}^{n} - T_{i,j,k}^{n}}{\Delta x} - (\rho U)_y \frac{T_{i,j,k}^{n} - T_{i,j-1,k}^{n}}{\Delta y} - (\rho U)_z \frac{T_{i,j,k+1}^{n} - T_{i,j,k}^{n}}{\Delta z}$$
$$+ \Gamma \left[\frac{T_{i+1,j,k}^{n} - 2T_{i,j,k}^{n} + T_{i-1,j,k}^{n}}{\Delta x^2} + \frac{T_{i,j+1,k}^{n} - 2T_{i,j,k}^{n} + T_{i,j-1,k}^{n}}{\Delta y^2} + \frac{T_{i,j,k+1}^{n} - 2T_{i,j,k}^{n} + T_{i,j,k-1}^{n}}{\Delta z^2}\right]$$

$$T_{i,j,k}^{n+1}=\left(1+\frac{(\rho U)_x\Delta t}{\rho\Delta x}-\frac{(\rho U)_y\Delta t}{\rho\Delta y}+\frac{(\rho U)_z\Delta t}{\rho\Delta z}-3\times 2\frac{\Gamma\Delta t}{\rho\Delta x^2}\right)T_{i,j,k}^{n}$$
$$+\left(\frac{\Gamma\Delta t}{\rho\Delta x^2}-\frac{(\rho U)_x\Delta t}{\rho\Delta x}\right)T_{i+1,j,k}^{n}+\left(\frac{\Gamma\Delta t}{\rho\Delta x^2}\right)T_{i-1,j,k}^{n}$$
$$+\left(\frac{\Gamma\Delta t}{\rho\Delta x^2}\right)T_{i,j+1,k}^{n}+\left(\frac{\Gamma\Delta t}{\rho\Delta x^2}+\frac{(\rho U)_y\Delta t}{\rho\Delta x}\right)T_{i,j-1,k}^{n}$$
$$+\left(\frac{\Gamma\Delta t}{\rho\Delta x^2}-\frac{(\rho U)_z\Delta t}{\rho\Delta x}\right)T_{i,j,k+1}^{n}+\left(\frac{\Gamma\Delta t}{\rho\Delta x^2}\right)T_{i,j,k-1}^{n}$$

Condition 7: $U_x<0$, $U_y<0$ and $U_z>0$ (refer to Eq. (8.26g)):

$$\rho\frac{T_{i,j,k}^{n+1}-T_{i,j,k}^{n}}{\Delta t}=-(\rho U)_x\frac{T_{i+1,j,k}^{n}-T_{i,j,k}^{n}}{\Delta x}-(\rho U)_y\frac{T_{i,j+1,k}^{n}-T_{i,j,k}^{n}}{\Delta y}-(\rho U)_z\frac{T_{i,j,k}^{n}-T_{i,j,k-1}^{n}}{\Delta z}$$
$$+\Gamma\left[\frac{T_{i+1,j,k}^{n}-2T_{i,j,k}^{n}+T_{i-1,j,k}^{n}}{\Delta x^2}+\frac{T_{i,j+1,k}^{n}-2T_{i,j,k}^{n}+T_{i,j-1,k}^{n}}{\Delta y^2}+\frac{T_{i,j,k+1}^{n}-2T_{i,j,k}^{n}+T_{i,j,k-1}^{n}}{\Delta z^2}\right]$$

$$T_{i,j,k}^{n+1}=\left(1+\frac{(\rho U)_x\Delta t}{\rho\Delta x}+\frac{(\rho U)_y\Delta t}{\rho\Delta y}-\frac{(\rho U)_z\Delta t}{\rho\Delta z}-3\times 2\frac{\Gamma\Delta t}{\rho\Delta x^2}\right)T_{i,j,k}^{n}$$
$$+\left(\frac{\Gamma\Delta t}{\rho\Delta x^2}-\frac{(\rho U)_x\Delta t}{\rho\Delta x}\right)T_{i+1,j,k}^{n}+\left(\frac{\Gamma\Delta t}{\rho\Delta x^2}\right)T_{i-1,j,k}^{n}$$
$$+\left(\frac{\Gamma\Delta t}{\rho\Delta x^2}-\frac{(\rho U)_y\Delta t}{\rho\Delta x}\right)T_{i,j+1,k}^{n}+\left(\frac{\Gamma\Delta t}{\rho\Delta x^2}\right)T_{i,j-1,k}^{n}$$
$$+\left(\frac{\Gamma\Delta t}{\rho\Delta x^2}\right)T_{i,j,k+1}^{n}+\left(\frac{\Gamma\Delta t}{\rho\Delta x^2}+\frac{(\rho U)_z\Delta t}{\rho\Delta x}\right)T_{i,j,k-1}^{n}$$

Condition 8: $U_x<0$, $U_y<0$ and $U_z<0$ (refer to Eq. (8.26h))

$$\rho\frac{T_{i,j,k}^{n+1}-T_{i,j,k}^{n}}{\Delta t}=-(\rho U)_x\frac{T_{i+1,j,k}^{n}-T_{i,j,k}^{n}}{\Delta x}-(\rho U)_y\frac{T_{i,j+1,k}^{n}-T_{i,j,k}^{n}}{\Delta y}-(\rho U)_z\frac{T_{i,j,k+1}^{n}-T_{i,j,k}^{n}}{\Delta z}$$
$$+\Gamma\left[\frac{T_{i+1,j,k}^{n}-2T_{i,j,k}^{n}+T_{i-1,j,k}^{n}}{\Delta x^2}+\frac{T_{i,j+1,k}^{n}-2T_{i,j,k}^{n}+T_{i,j-1,k}^{n}}{\Delta y^2}+\frac{T_{i,j,k+1}^{n}-2T_{i,j,k}^{n}+T_{i,j,k-1}^{n}}{\Delta z^2}\right]$$

$$T_{i,j,k}^{n+1} = \left(1 + \frac{(\rho U)_x \Delta t}{\rho \Delta x} + \frac{(\rho U)_y \Delta t}{\rho \Delta y} - \frac{(\rho U)_z \Delta t}{\rho \Delta z} - 3 \times 2 \frac{\Gamma \Delta t}{\rho \Delta x^2}\right) T_{i,j,k}^{n}$$
$$+ \left(\frac{\Gamma \Delta t}{\rho \Delta x^2} - \frac{(\rho U)_x \Delta t}{\Delta x \rho}\right) T_{i+1,j,k}^{n} + \left(\frac{\Gamma \Delta t}{\rho \Delta x^2}\right) T_{i-1,j,k}^{n}$$
$$+ \left(\frac{\Gamma \Delta t}{\rho \Delta x^2} - \frac{(\rho U)_y \Delta t}{\rho \Delta x}\right) T_{i,j+1,k}^{n} + \left(\frac{\Gamma \Delta t}{\rho \Delta x^2}\right) T_{i,j-1,k}^{n}$$
$$+ \left(\frac{\Gamma \Delta t}{\rho \Delta x^2} - \frac{(\rho U)_z \Delta t}{\rho \Delta x}\right) T_{i,j,k+1}^{n} + \left(\frac{\Gamma \Delta t}{\rho \Delta x^2}\right) T_{i,j,k-1}^{n}$$